Universiteit Gent
Faculteit Toegepaste Wetenschappen
Vakgroep Chemische Proceskunde en Technische Chemie

Productie van Aromaatarme Brandstoffen: Kinetiek en Industriële Toepassing van Hydrokraken

Production of Low-Aromate Fuels: Kinetics and Industrial Application of Hydrocracking

---

Joris Thybaut

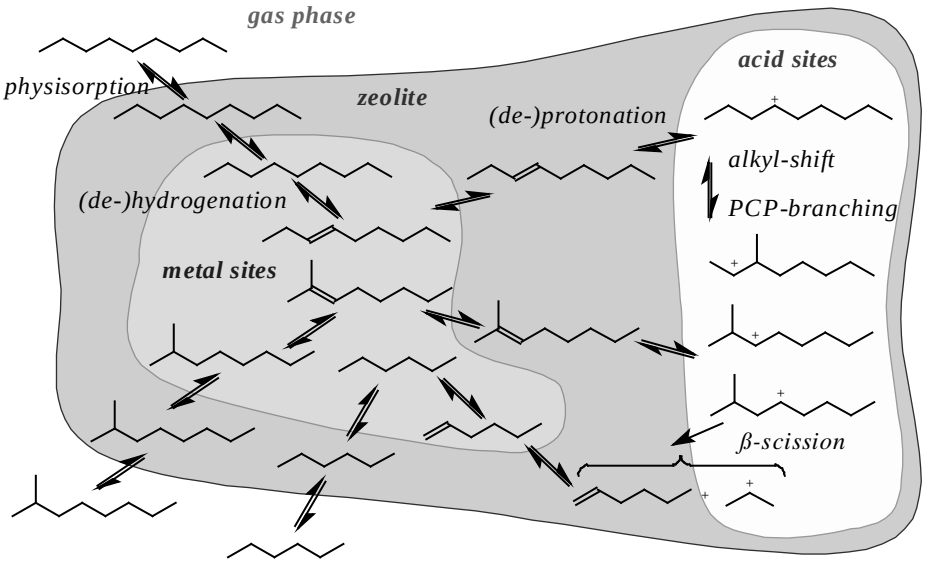

Promotor: prof. dr. ir. Guy B. Marin

Laboratorium voor
Petrochemische Techniek
Directeur:
prof. dr. ir. Guy B. Marin

Proefschrift tot het verkrijgen van de graad van
Doctor in de Toegepaste Wetenschappen:
Scheikunde
Academiejaar 2002-2003

Promotor:

prof. dr. ir. Guy B. Marin	Universiteit Gent

Examencommissie:

prof. dr. ir. J. Van Campenhout, voorzitter	Universiteit Gent
prof. dr. ir. J. Debacker, secretaris	Universiteit Gent
prof. dr. ir. J. Defrancq	Universiteit Gent
prof. dr. I. De Vynck	Universiteit Gent
dr. ir. P. Galtier	Institut Français du Pétrole
prof. dr. ir. Z. Hens	Universiteit Gent
prof. dr. ir. G. Heynderickx	Universiteit Gent
prof. dr. ir. J. Martens	Katholieke Universiteit Leuven
prof. dr. ir. R. Van Veen	Shell – Technische Universiteit Eindhoven

Universiteit Gent
Faculteit Toegepaste Wetenschappen
Vakgroep Chemische Proceskunde en Technische Chemie
Krijgslaan 281, gebouw S 5
B-9000 Gent
België
Tel.: ++32 (0)9 264 45 16
Fax: ++32 (0)9 264 49 99

Dit werk kwam tot stand in het kader van het programma Interuniversitaire Attractie Polen gesponsord door de Belgische regering en de Federale Dienst voor Wetenschappelijke, Technische en Culturele aangelegenheden (DWTC)

Dit proefschrift is elektronisch beschikbaar op volgende URL:
http://allserv.rug.ac.be/~jthybaut/proefschrift

Dankwoord

Met het einde van mijn doctoraat in zicht, is het gepast eens stil te staan en allen te bedanken die een onmisbare, rechtstreekse of onrechtstreekse bijdrage geleverd hebben bij dit werk.
Vooreerst uiteraard mijn promotor, Guy Marin. Guy, je hebt mij de kans geboden om alvast de eerste jaren van mijn carrière aan de wetenschap in het algemeen en hydrokraken in het bijzonder te wijden. Onder jouw leiding heb ik zowel mijn theoretische kennis als mijn experimentele vaardigheden verder kunnen ontplooien en alleen dankzij jouw geduld sta ik waar ik nu ben wat betreft het schrijven van wetenschappelijke teksten. Nog eens bedankt.
Ook aan Geraldine Heynderickx ben ik dank verschuldigd. Geraldine, jij hebt mij immers als eerste aangesproken om aan het labo te doctoreren en op die manier mij de nodige duw in de juiste richting gegeven om het werk aan te vatten.
Johan Martens en Gino Baron, jullie kijk op dit werk maakt ontegensprekelijk een belangrijk deel uit in de ontwikkeling ervan. De periodieke IAP vergaderingen waren keer op keer aangename ontmoetingen waar in een open sfeer over de wetenschap en aanverwante zaken gediscussieerd werd. Gina, jou wil ik hierbij ook vermelden, en niet in het minst voor het opmeten van nieuwe experimentele gegevens en het grasduinen in de reeds bestaande!
Zonder de collega's wetenschappers medewerkers zou het leven op het labo ook niet zijn wat het is. Jullie zijn met te veel om jullie allen persoonlijk te vermelden en daarom beperk ik mij hier tot de volgende personen. Gert, je was al mijn begeleider tijdens mijn ingenieursthesis en in de aanvangsjaren van mijn doctoraat heb je mij nog heel wat theoretische en praktische dingen geleerd. Ook nu weer heb je je bijdrage geleverd met het nalezen van de tekst. Antonio *no problem* Muñoz, your Mexican life style has learned me to enjoy things, but still to deliver high quality work. Gorik, eerst kende ik je als student, nadien deelden we hetzelfde bureel en nu word je ook assistent. Ik hoop dat we onze samenwerking goed kunnen voortzetten. My present 'roommates': Carlos, after Antonio, you are now helping me not to forget that life has to be enjoyable, even when one is working hard. Narasimhan, not only a 'roommate', but also scientifically a close co-worker. I hope to continue our prize winning cooperation!
Het administratief en technisch personeel draag ik eveneens een warm hart toe. Etienne *komt u of gaat u?* Van Damme, awel Etienne, ik blijf nog! Marcel Vervust en Gilbert Van Oost, bedankt voor jullie praktische en technische hulp bij de experimentele installaties. Bedankt ook alle andere leden van het administratief en technisch personeel.
De studenten die onder mijn begeleiding hun ingenieursthesis gemaakt hebben: Lynn De Moor, Isabelle Fovel, Kevin Van Geem, Ben De Waele en Irene Llano. Jullie geduld bij het experimentele werk was vereist om dit doctoraat te verwezenlijken. Ook de discussies bij de verwerking en de interpretatie van de resultaten hebben dit werk goed vooruit geholpen.
En tenslotte, uiteraard, mijn familie. Mijn ouders, bedankt voor de mogelijkheid die jullie mij gegeven hebben om mijn talenten ten volle te ontwikkelen aan de universiteit zonder dat ik me daarvoor om veel dingen hoefde te bekommeren. Mijn zussen en broer, samen met onze ouders hebben jullie gezorgd voor een aangename en stimulerende sfeer, waarin het mogelijk was uit te groeien tot wie ik nu ben. Het meest welgemeende woord van dank heb ik opgespaard tot het laatst, voor jou Leen, mijn vrouw(tje). Vooral het laatste jaar is veeleisend geweest en heb ik niet altijd de nodige tijd voor jou en Marliesje kunnen vrijmaken. Bij deze wil ik je dan ook nogmaals bedanken voor het begrip en het geduld dat je gedurende de hele periode hebt opgebracht en voor de liefdevolle omgeving waarin ik heb kunnen werken!

Joris augustus 2002

Table of Contents

List of Tables

List of Figures

Notation

Roman Symbols

*	active site
A_i	chromatogram peak surface area for component *i*
A_i *(i=0,…,9)*	Chao-Seeder coefficients in the calculation of the pure liquid fugacity
A_i	aromatic component *i*
AH_i	partially hydrogenated species corresponding with aromatic component *A* with *i* H atoms added
A_r	affinity for reaction *r* [J mol^{-1}]
AS	alkyl shift
a_i	generalized activity for component *i* [-]
as, at	allylic secondary or tertiary carbon atom
a'_v	volumetric gas liquid interphase area [m_i^2 m_r^{-3}]
B	benzene
B	model parameter related to the coverage of the surface by partially hydrogenated species [-]
BAL	balance
$\boldsymbol{b}$	model parameter vector
b_i	i^{th} model parameter
C	concentration [$\mathrm{mol\,kg_{cat}^{-1}}$]
C_A^M	concentration of component *A* on the metal surface [$\mathrm{mol\,kg_{cat}^{-1}}$]
C_t^A	total concentration acid sites [$\mathrm{mol\,kg_{cat}^{-1}}$]
C_t^M	total concentration metal sites [$\mathrm{mol\,kg_{cat}^{-1}}$]
$C_{n/m}$	molar ratio between alkane with *n* and *m* carbon atoms [mol mol^{-1}]
C_p	specific heat capacity [J kg^{-1} K^{-1}]
$C_{sat,A}$	saturation concentration of component *A* [$\mathrm{mol\,kg_{cat}^{-1}}$]
CF_i^A	calibration factor for component *i* on detector of type *A*
CHA	cyclohexane

CHD	cyclohexadiene
CHE	cyclohexene
CN	carbon number
cr	cracked product
$D_{(e)}$	(effective) diffusivity [$m^2\ s^{-1}$]
d_p	diameter catalyst particle [m_p]
E	error function
$E_{0,i}$	reference activation energy in the Evans-Polanyi relationship for reaction family *i* [J mol^{-1}]
$E_A^{(B)}$	activation energy (for reaction *B*) [J mol^{-1}]
EP_A^+	fraction in stream A boiling above a specified temperature [-]
E_{distr}	acid strength distribution function [mol J^{-1}]
E_{zi}	Zwitter ion stabilization energy [J mol^{-1}]
$F_{regress}$	*F*-value for the significance of the regression [-]
F	molar flow rate [mol s^{-1}]
$f^{(F)}$	fugacity (in aggregation state *F*) [Pa]
$\Delta G_f^0(A)$	standard Gibbs energy of formation of component *A* [J mol^{-1}]
ΔH^0	standard enthalpy difference [J mol^{-1}]
ΔH^+	model parameter reflecting the catalyst average acid strength [J mol^{-1}]
$\Delta_r H_j^0$	standard reaction enthalpy of reaction *j* [J mol^{-1}]
$\Delta_v H^0$	enthalpy of vapourization [J mol^{-1}]
H^+	proton
H	Henry coefficient [mol kg_{cat}^{-1} Pa^{-1}]
HN	number of hydrogen atoms
h_F	heat transfer coefficient in phase *F* [W m_i^{-2} K^{-1}]
iso	isomer
J_i	Jacobian matrix for response *j*
K	equilibrium coefficient [$Pa^{n_p - n_r}$]
$K(A_1;A_2)$	equilibrium coefficient between A_1 and A_2 [-]
$K_g^*(n;T)$	factor in the calculation of $LC_{m;n}^B(g;h)$ accounting for the formation of all alkanes belonging to lump *g* [Pa^{-1}]

$K^{(n)}$	partition coefficient (in the n^{th} iteration) [-]
K_i	surface equilibrium coefficient for the addition of the i^{th} H atom [-]
K_L	overall gas liquid mass transfer coefficient [$m^3\ m_i^{-2}\ s^{-1}$]
$K_{L,A}$	Langmuir physisorption coefficient for component A [Pa^{-1}]
$K^M_{deh,f}$	Dehydrogenation equilibrium coefficient on the metal surface [-]
K^A_f	chemisorption (= protonation) coefficient for lump f on acid sites [$kg_{cat}\ mol^{-1}$]
K^M_f	chemisorption coefficient for lump f on metal sites [$kg_{cat}\ mol^{-1}$]
$K^*_{ref,g}(n;T)$	factor in the calculation of $LC^B_{m;n}(g;h)$ accounting for the formation of hydrogen and the reference alkene from the elements [-]
$k^{(B)}$	rate coefficient (of reaction family B) with total reaction order n [$(mol\ kg^{-1})^{n-1}\ s^{-1}$]
$k_0^{(B)}$	preexponential factor (of the rate coefficient of reaction family B) with total reaction order n [$(mol\ kg^{-1})^{n-1}\ s^{-1}$]
$k_{0,(i)}$	preexponential factor (of the rate coefficients in reaction family i) with total reaction order n [$(mol\ kg^{-1})^{-1}\ s^{-1}$]
k_F	mass transfer coefficient in phase F [$m^3\ m_i^{-2}\ s^{-1}$]
k_i	rate coefficient for the addition of the i^{th} H atom [s^{-1}]
$k_{i,j}$	rate coefficient for reaction j in reaction family i with total reaction order n [$(mol\ kg^{-1})^{n-1}\ s^{-1}$]
$k^B_{lump}(g;h)$	lumped rate coefficient for reaction family B from lump g to lump h [$mol\ kg_{cat}^{-1}\ s^{-1}$]
$LC^B_{m;n}(g;h)$	lumping coefficient for the reactions of family B converting carbenium ions of type m from lump g into carbenium ions of type n of lump h [Pa]
MW_i	molecular weight of component i [$mol\ kg^{-1}$]
m	carbon atom type
m	reaction order
$m_{i,k}$	type of carbenium ion k corresponding with alkane i
N_i	cycloalkane i
N	molar flux [$mol\ m^{-2}\ s^{-1}$]
$N^B_{m;n}(g;h)$	factor contributing to $LC^B_{m;n}(g;h)$ accounting for symmetry effects [-]

$NO_{i,j}$	cycloalkene *j* corresponding with cycloalkane *i*
$N(x_1;x_2)$	number of moles of components for which the property *x* is between x_1 and x_2 [mol]
n	composition density function
n	number of components
n	carbon atom type
n	(total) reaction order
n	normal alkane
n	number of iterations
n_e	number of single events
$n_{q,r}$	type of carbenium ion *r* corresponding with alkane *q*
n_s	number of identical transformations
nob	number of observations
npar	number of parameters
nresp	number of responses
$O_{(i,j)}$	alkene (*j* corresponding with alkane *i*)
Pr	Prandtl number $\mu\ C_p\ \lambda^{-1}$
PA	proton affinity [J mol^{-1}]
$P_{(i)}$	alkane (*i*)
PCP	protonated cyclopropane
p	primary carbon atom
$p_{(A)}$	(partial) pressure (of component *A*) [Pa]
Q	volumetric flow rate [$m^3\ s^{-1}$]
Q_p	proton transfer energy [J mol^{-1}]
q_F	conductive heat flux in phase *F* [W m^{-2}]
R	gas constant [8.31451 J mol^{-1} K^{-1}]
$R_A^{(B)}$	net production rate of component *A* (via reaction family *B*) [mol kg_{cat}^{-1} s^{-1}]
RDS	rate-determining step
$R^+_{(i,k)}$	carbenium ion (*k* corresponding with alkane *i*)
r_j	reaction rate (of reaction *j*) with reaction order *n* [mol $(kg_{cat}\ s)^{-n}$]
$r^B(m;n)$	elementary reaction rate of reaction family *B* converting a carbenium ion of type *m* into a carbenium ion of type *n* [$(mol\ kg_{cat}^{-1})^{n-1}\ s^{-1}$]

$r^B(g;h)$	lumped reaction rate of reaction family *B* from lump *g* to lump *h* [(mol kg_{cat}^{-1})$^{n-1}$ s^{-1}]
Sc	Schmidt number $\mu\ \rho^{-1}D_i^{-1}$
$S_{j,i}$	Stoechiometric coefficient for component *i* in reaction *j*
SSQ	sum of squared residual between experimental and model calculated molar outlet flow rates [mol^2 s^{-2}]
s	secondary carbon atom
T	temperature [K]
TBP	True Boiling Point [K]
t_n	Student's *t*-value for *n* degrees of freedom
t	tertiary carbon atom
$u_{s(,F)}$	superficial velocity (in phase *F*) [m_F^3 m_r^2 s^{-1}]
$V(b)_{i,j}$	element on row *i* and column *j* of the covariance matrix of the parameter estimates
V_m	molar volume [m^3 mol^{-1}]
W	catalyst mass [kg_{cat}]
w_i	weighting factor for response *i* [-]
X	liquid-phase mole fraction condition [-]
X_i	conversion of component *i* [-]
x	physical property of a petroleum fraction
x_i	liquid-phase mole fraction of component *i* [-]
Y	gas-phase mole fraction condition
Y	yield [kg kg_{feed}^{-1}]
y_i	gas-phase mole fraction of component *i* [-]
z	axial reactor coordinate [m]
z_i	global mole fraction of component *i* [-]

Greek Symbols

α	model parameter
α_i	Evans-Polanyi coefficient for reaction family *i*
β	real parameter value vector
β	β-scission
Φ	fugacity coefficient [-]

γ	molar hydrogen to hydrocarbon ratio [mol mol^{-1}]
δ_F	frictional pressure drop per unit length for flow of phase *F* only [Pa m_r^{-1}]
ε	void fraction [m_f^3 m_p^{-3}]
$\varphi_{(n)}$	molar vapour fraction (in the n^{th} iteration)
λ	thermal conductivity [W m^{-1} K^{-1}]
η_i	effectiveness factor for reaction *i*
μ	dynamic viscosity [Pa s]
$\mu_i^{(F)}$	chemical potential of component *i* (in aggregation state *F*) [J mol^{-1}]
ν	pure liquid fugacity coefficient [-]
θ	fractional surface coverage [-]
θ	normalized true boiling point [-]
ρ_B	catalyst bulk density [kg m_r^{-3}]
ρ_F	density of phase *F* [kg m_F^{-3}]
$\rho_{i,j}$	linear correlation coefficient between parameter *i* and *j* [-]
σ	global symmetry number
τ	catalyst tortuosity
ξ	pellet coordinate [m_p]
Ω	reactor cross section [m^2]
ω	acentric factor

Superscript

_	mean value
=	double bond
*	mole fraction before normalization
*	composite dehydrogenation, isomerization or cracking rate coefficient
*	pure form
˘	effluent after mixing with internal standard
^	model calculated value
~	single-event
0	inlet

0	standard state
(0)	intermediate value
(1)	intermediate value
A	acid site
ave	average
comp	composite
e	effluent
F	aggregation state: *V* vapour or *L* liquid
f	expressed in terms of fugacities
g	gas
hyd	hydrogenation
L	liquid
l	liquid
lg	flashed gas
ll	flashed liquid
M	metal site
v	vapour

Subscript

$\neq$	activated complex
C	carbon
C_i	alkane with *i* carbon atoms
c1	cracking from monobranched isomers
chem	chemisorption / chemical interactions
cr	cracking (from multibranched isomers)/cracked products
$deh_{i,j}$	dehydrogenation of alkane *i* into alkene *j*
f	forward
f	lump *f*
G	gas
g	lump *g*
gch	gauche
-H	species with one hydrogen atom abstracted
H	hydrogen atom

$hyd_{i,j}$	hydrogenation of alkene *j* into alkane *i*
I	interphase
i	alkane index
i	of component *i*
iso	isomerization/isomers
j	alkene index
k	carbenium ion index
L	liquid
M	metal site
mo	monobranched
mu	multibranched
n	normal
p	primary
phys	physisorption / physical interactions
prot	protonation
q	product alkane index
q	quaternary
r	‘reduced’ property value, i.e., divided by the critical value
r	reverse
r	product carbenium ion index
reac	reactions
ref	reference
regres	regression
S	solid
sat	saturation
secondary	secondary
stab	stabilization
surf	surface, i.e., without distinction between the different H atom additions
t	tertiary
t	total
tol	toluene
tot	total

u	product alkane index
v	product alkene index
vpr	vapour pressure
zeo	zeolite

Nederlandstalige Samenvatting

1. Hydrokraken: Geschiedenis en Perspectieven van een Conversieproces

Ruwe aardolie en afgeleide producten kunnen moeilijk weggedacht worden uit de wereld zoals we die vandaag kennen. Dergelijke producten worden voornamelijk gebruikt als energiebron voor transport, namelijk LPG, benzine, diesel, kerosine of voor verwarming, namelijk huisbrandolie en zwaardere oliën, zie Figuur 1 [1.1][1]. Daarnaast zijn ook vele petrochemische grondstoffen, zoals ethyleen, propyleen, benzeen, tolueen,… uit aardolie afgeleide producten. Nog andere toepassingen zijn onder meer de asfaltproductie en de smeeroliën.

1.1. De Rol van de Raffinaderij

De omzetting van een ruwe aardolie naar de gewenste afgeleide producten gebeurt in een raffinaderij. Via destillatie wordt de aardolie in verschillende fracties gescheiden. Sommige van die fracties, zoals de benzine- en de dieselfractie, hebben de gewenste eigenschappen qua kookpunt en ondergaan enkel nog processen zoals katalytische reforming of

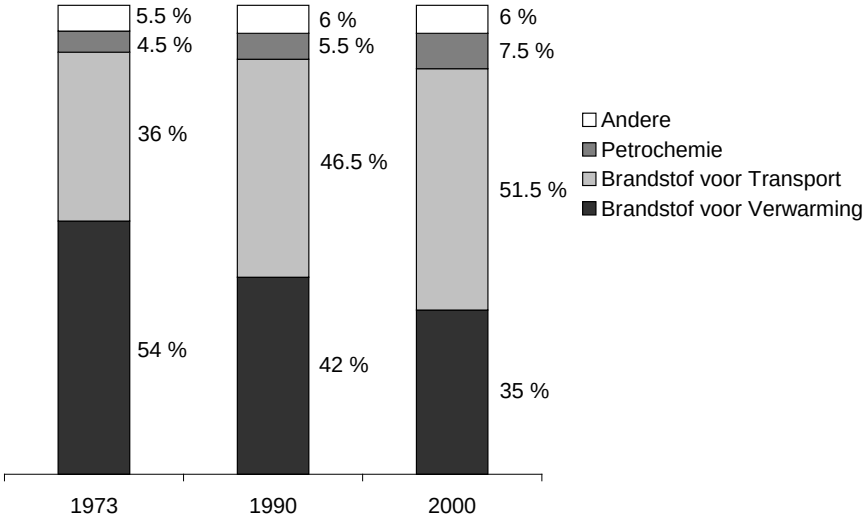

Figuur 1 Evolutie van de oliemarkt [1.1]

[1] In deze manier van refereren verwijst het eerste getal naar het hoofdstuknummer en het tweede naar de corresponderende referentie uit dat hoofdstuk

waterstofbehandeling. Dergelijke processen verhogen het octaangetal van een benzine, het cetaangetal van een diesel of verlagen het gehalte aan b.v. aromatische, zwavel- en stikstofhoudende componenten. Andere fracties hebben een te hoog kookpunttraject om als dusdanig aangewend te worden en worden gevaloriseerd door ze naar lichtere fracties om te zetten. Enkele typische processen daartoe zijn “visbreaking” (reductie van de viscositeit door een thermische behandeling), katalytisch kraken en hydrokraken. Bij “visbreaking” en katalytisch kraken wordt het koolstofgetal van de componenten gereduceerd door zogenaamde ‘koolstofverwijdering’. In katalytisch kraken bijvoorbeeld wordt koolstof uit de voedingscomponenten gehaald onder de vorm van koolstofafzetting op de katalysator (cokesvorming). Dit leidt tot de vorming van een niet onbelangrijke hoeveelheid onverzadigde koolwaterstoffen, hetgeen de verbrandingskwaliteit (octaangetal) van een benzine ten goede komt. Bij hydrokraken wordt het koolstofgetal van de voedingscomponenten teruggebracht door de toevoeging van waterstof. De aanwezigheid van waterstof leidt op zijn beurt tot de vorming van hoofdzakelijk verzadigde producten via hydrogenering van aromaten wat de dieselkwaliteit bevordert. Bovendien zijn hydrokrakingskatalysatoren tot op zekere hoogte verwant met de katalysatoren aangewend bij waterstofbehandelingsprocessen en treedt bij hydrokraken dus ook een zekere ontzwaveling en ontstikstoffing van de voeding op. In het licht van huidige en toekomstige specificaties betreffende de samenstelling van brandstoffen vormt dit laatste aspect een belangrijk voordeel van hydrokraken ten opzichte van andere conversieprocessen [1.3].

1.2. Hydrokraken

Hydrokraken in zijn huidige vorm, werd een economisch belangrijk proces rond 1960 [1.5]. De beschikbaarheid van waterstof geproduceerd bij een ander toen opkomend raffinaderijproces, namelijk katalytische reforming was hierbij een bepalende factor. De huidige interesse voor hydrokraken is onder meer gebaseerd op de steeds strenger worden milieunormen en de zwaardere ruwen oliën die geraffineerd worden [1.3]. Een belangrijk aspect daarbij is de hydrogenering van aromaten die optreedt bij hydrokraken.

Er zijn verschillende configuraties mogelijk voor hydrokraken: een één-stap-configuratie, zie Figuur 2, of een twee-stap-configuratie, zie Figuur 3. Daarnaast komen ook nog andere vormen zoals mild hydrokraken, katalytisch ontwassen en “slurry” hydrokraken voor. Meerdere katalysatoren, zelfs meerdere reactoren zijn mogelijk in de één-stap-configuratie. Eén-stap betekent immers dat er geen scheiding van de te behandelen stroom plaatsvindt tussen de verschillende reactoren in het proces, in tegenstelling tot de twee-stap-configuratie

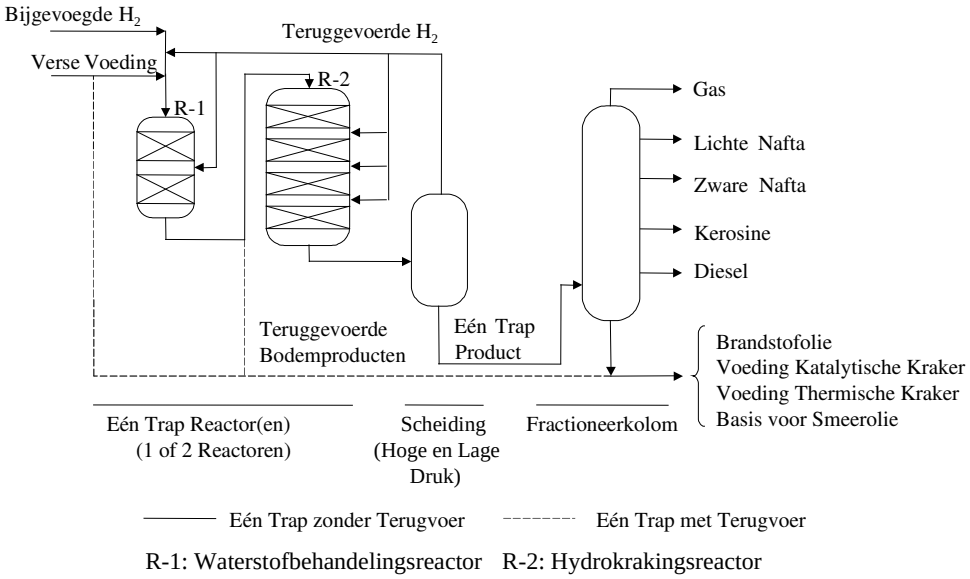

Figuur 2 Vereenvoudigd stroomdiagramma van één-stap-hydrokraken

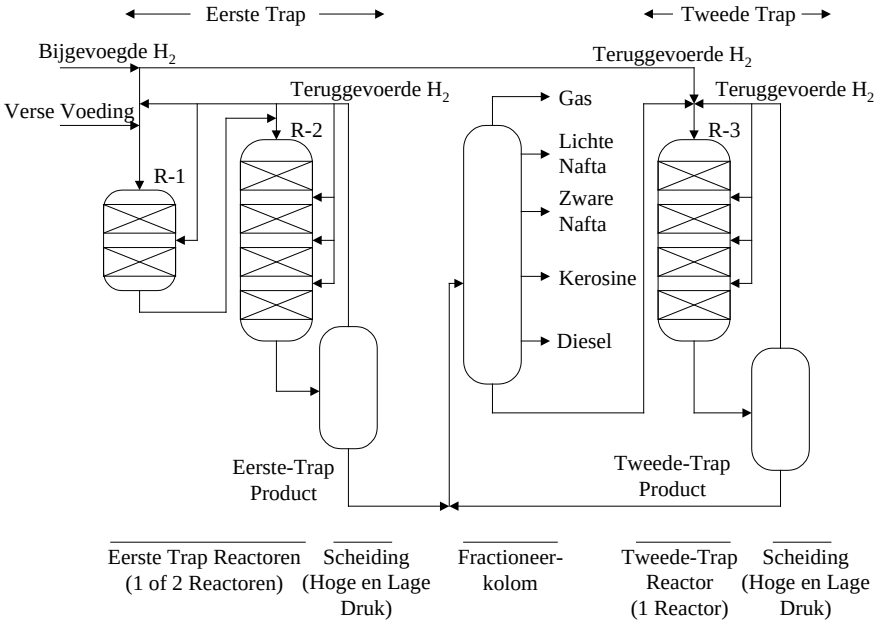

Figuur 3 Vereenvoudigd stroomdiagramma van twee-stap-hydrokraken

waar een dergelijke intermediaire scheiding wel gebeurt. Het voordeel van de twee-stap-configuratie ligt in de flexibiliteit van de productenopbrengst. Hogere werkings- en investeringskosten in de twee-stap-configuratie zijn het onvermijdelijke gevolg. Bij mild hydrokraken wordt slechts één katalysator in één reactor gebruikt. In feite is mild hydrokraken equivalent met een doorgedreven ontzwaveling en ontstikstoffing, zodat ook hydrokraking in niet geringe mate optreedt. De term katalytisch ontwassen is van toepassing als het proces vooral de verbetering van eigenschappen zoals de viscositeit, stolpunt,…

beoogt. Het zijn immers de lineaire alkanen, de wassen, die de minder goede eigenschappen van de voeding veroorzaken.

1.3. Kinetische Modellering

Simulatiemodellen zijn noodzakelijke middelen in reactorontwerp en -optimalisatie Een dergelijk model bevat een reactor- en een reactiemodel. Het reactormodel houdt rekening met het type reactor en het inwendige stromingspatroon. Het volgt uit het opstellen van balansen over de reactor zoals een materiaal, energie- en impulsbalans. In deze balansen komen reactiesnelheden voor die berekend worden aan de hand van een reactiemodel. Een dergelijk reactiemodel vormt over het algemeen een compromis tussen nauwkeurigheid en vereiste rekentijd. Algemeen gesproken neemt met de nauwkeurigheid van het model ook de vereiste rekentijd toe. De uitdaging bestaat er dus in om een zo nauwkeurig mogelijk model te ontwikkelen dat van aanvaardbare rekentijden gebruikt maakt. De reactiemodellen kunnen onderverdeeld worden in twee grote klassen, namelijk die van de gegroepeerde en die van de fundamentele modellen

Het basiskenmerk van een gegroepeerd model is dat het het gedrag van meerdere componenten als dat van één pseudocomponent beschrijft. Het aantal pseudocomponenten dat gebruikt wordt, varieert en analoog aan de eerder geformuleerde stelling geldt voor de gegroepeerde modellen dat de nauwkeurigheid van het model toeneemt met het aantal pseudocomponenten evenals de vereiste rekentijd. Het eenvoudigste model beschouwt slechts 2 pseudocomponenten, namelijk de voedingspseudocomponent, gedefinieerd als de fractie van het materiaal in de voedingsstroom kokend boven het gewenste eindkookpunt van het product, en de productpseudocomponent, waarvan de definitie onmiddellijk volgt uit de voorgaande [1.2]. Modellen met meer pseudocomponenten, bijvoorbeeld het tien-pseudocomponent model van Weekman [1.19,1.20], werden eveneens ontwikkeld. Verdere inspanningen waren gericht op het inbrengen van enig fundamenteel karakter in het gegroepeerd model. Het leggen van verbanden tussen de reactiviteit en de structuur van de reagerende componenten stond hierbij centraal [1.23-1.28]. Enige vorm van uitmiddeling van eigenschappen van meerdere componenten tot die van één pseudocomponent blijft in deze modellen echter steeds behouden. Een andere, meer recent ontwikkelde, techniek is de continue groeperingsmethode en is gebaseerd op de beschrijving van aardoliefracties als mengsels van een oneindig aantal componenten met eigenschappen die een continu verloop vertonen als functie van variabelen zoals bijvoorbeeld de kooktemperatuur [1.29,1.30]. De samenstelling wordt dan bijvoorbeeld uitgedrukt als een waarschijnlijkheidsdichtheid van de

kooktemperatuur. Ook een verband tussen kooktemperatuur en reactiviteit kan gelegd worden. Een laatste vereiste is een tweede waarschijnlijkheidsdichtheid, als functie van opnieuw bijvoorbeeld de kooktemperatuur, die de productendistributie beschrijft van een component met een bepaalde kooktemperatuur.

Zowel voor thermisch kraken, katalytisch kraken als hydrokraken werden fundamentele modellen ontwikkeld, gebaseerd op de elementaire stappen die optreden bij deze processen [1.31-1.37]. De meer dan proportionele toename van de omvang van de reactienetwerken in dergelijke processen met het koolstofgetal van de reagerende componenten heeft geleid tot de ontwikkeling van algoritmes voor de generering van deze netwerken. Zonder verdere veronderstellingen omtrent de kinetische coëfficiënten, zou een fundamentele aanpak tot een onhandelbaar groot aantal te bepalen parameters leiden. Vandaar dat tussen snelheidscoëfficiënten van verwante reacties, behorend tot zogenaamde reactiefamilies, bepaalde verbanden vooropgesteld worden. Lineaire-vrije-energie-relaties, zoals bijvoorbeeld de Polanyi-relatie waarin een lineair verband wordt vooropgesteld tussen de activeringsenergie en de gekende of berekenbare reactie-enthalpie, worden in deze context vaak gebruikt. Simulatie van het gedrag van een industriële voeding met het detail van een fundamenteel model is quasi onmogelijk gezien de vereiste rekentijd, maar is anderzijds ook overbodig omdat de beschikbare analysemethoden niet toelaten samenstellingen zo gedetailleerd te bepalen. Om die reden werd dan ook een hergroeperingsmethode ontwikkeld waarin, hoewel met pseudocomponenten gewerkt wordt, het fundamentele karakter bewaard blijft. De enige vereiste veronderstelling in dit gehergroepeerde model is dat thermodynamisch evenwicht heerst binnen de gebruikte pseudocomponenten. Een weloverwogen definitie van de pseudocomponenten in het gehergroepeerde model voor hydrokraken maakt dit tot een aanvaardbare veronderstelling.

1.4. Raffinage in de toekomst

De huidige milieunormen zijn reeds streng en zullen in de toekomst nog verstrengen. Tabel 1 geeft een overzicht van de specificaties voor *zuivere brandstoffen*. Beperkingen op het gehalte aan zwavel en aan aromaten dwingen de raffinaderijen tot een doorgedreven waterstofbehandeling van de corresponderende fracties. Bovendien zijn olievoorraden niet oneindig groot en zullen steeds zwaardere oliën, met een over het algemeen hoger gehalte aan zwavel en aromaten, moeten behandeld worden. Deze twee redenen, samen met een verhoogde vraag naar middendestillaten eerder dan naar benzine, zullen ertoe leiden dat hydrokraken steeds belangrijker zal worden voor de conversie van zware aardoliefracties.

Tabel 1 Diesel specificaties [1.40]

	Californië	Zweden Urban 1	Zweden Urban 2	Europa 2005
Zwavelgehalte (wt%-max)	500	10	50	30-50
Aromaten (vol%-max)	10	5	20	-
Polyaromaten ([a]wt%, [b]vol%-max)	1.4[a]	0.02[b]	0.1[b]	5-11[a]
Cetaangetal (min)	48	50	47	52-56

Verscheidene recente patentaanvragen [1.41-1.46] weerspiegelen de huidige interesse in hydrokraken. Ook in nieuw gebouwen raffinaderijen, zoals de MIDOR-raffinaderij in Egypte [1.47] neemt (hydro)-conversie een belangrijke plaats in.

2. Procedures

Het werk in het kader van dit proefschrift bestaat uit twee grote delen, een experimenteel deel aan de ene kant en een modelleringgedeelte aan de andere kant. Via de experimentele resultaten wordt inzicht verworven in het reactiemechanisme. Door regressie van de experimentele gegevens aan modellen, opgesteld gebaseerd op mogelijke reactiemechanismen, kunnen de modelparameters geschat worden. Daarnaast zijn ook kwantumchemische methoden gebruikt om inzicht in reactiemechanismen te verwerven.

2.1. Experimenteel

Verschillende katalysatoren zijn gebruikt in verschillende experimentele opstellingen. In de hydrokrakingsexperimenten werden drie met platina beladen (ultrastabiele) Y-zeolieten aangewend. Deze reeks van zeolieten verschilt van elkaar door een dealuminerende behandeling die tot verschillen leidt in zure eigenschappen van de betrokken zeolieten. De atomaire roostersiliciumaluminiumverhouding van deze zeolieten varieert van 2.6 tot 60. Met platina beladen ZSM-22 is gebruikt in de hydrogeneringsexperimenten vanwege de vormselectieve eigenschappen. Omwille van de vormselectiviteit wordt verwacht dat reacties gekatalyseerd door zuren zoals isomerisatie en kraking onderdrukt worden en aldus de hydrogeneringskinetiek niet beïnvloed wordt. Dit onderzoek richt zich voornamelijk op de tweede stap in twee-stap hydrokraken. Daar kunnen immers met edelmetaal beladen zeolitische dragers als katalysatoren gebruikt worden.

Drie verschillende experimentele opstellingen zijn gebruikt in het kader van dit proefschrift, waarvan er zich twee aan het Laboratorium voor Petrochemische Techniek aan de Universiteit Gent bevinden. De derde opstelling behoort tot het Centrum voor Oppervlakchemie en Katalyse aan de Katholieke Universiteit Leuven. Alle drie de opstellingen zijn continu doorstroomd en worden stationair bedreven. De opstellingen aan de Universiteit Gent omvatten een volkomen vermengde reactor, de ene een gasfasereactor van het Berty-type, de andere een driefasereactor van het Robinson-Mahoney-type en werden gebruikt in de hydrogeneringsexperimenten. De opstelling in Leuven is opgebouwd rond een gasfase-propstroomreactor en werd gebruikt in de hydrokrakingsexperimenten.

De schematische opbouw van de gebruikte opstellingen is sterk analoog. Alle drie omvatten ze een voedings-, reactie-, uitlaat- en analysesectie. In de drie gevallen worden zowel vloeibare als gasvormige reagentia gebruikt. Terwijl de vloeibare reagentia met behulp van een HPLC-pomp gevoed worden, worden de gasvormige reagentia vanuit gascilinders gevoed, al dan niet via een lokaal distributienetwerk. De reagentia zijn aan een zodanige zuiverheid aangekocht dat verdere zuivering overbodig is. Uiteraard bevindt zich in de voedingssectie van de opstellingen met een gasfasereactor een verdamper om de onder omgevingsomstandigheden vloeibare reagentia te verdampen. De reactiesecties bevatten de hierboven reeds kort beschreven reactoren. Volkomen vermenging in de reactoren van de opstellingen aan de Universiteit Gent wordt verwezenlijkt aan de hand vaan een magnetisch aangedreven roerder. Een magnetische aandrijving voorkomt problemen met de afdichtingen ter hoogte van de lagers van de roerder. In alle gevallen wordt de temperatuurregeling van de reactor uitgevoerd met behulp van een PID-regelaar en een thermokoppel dat zich in de reactor bevindt ter hoogte van het katalysatorbed. Afzonderlijke thermokoppels zijn steeds aanwezig om ook een onafhankelijke meting van de reactortemperatuur te kunnen uitvoeren.

De uitlaat- en analysesectie van de twee gasfaseopstellingen is sterk analoog, bestaande uit een zeswegkraan waarmee “on-line” een monster kan genomen worden om te analyseren op een gaschromatograaf uitgerust met een vlamionisatiedetector (FID). De uitlaat- en analysesectie van de driefaseopstelling bevat echter extra elementen ten opzichte van de overige twee opstellingen vanwege de aanwezigheid van een extra fase, namelijk een vloeibare fase, in de uitlaatstroom. Het reactoreffluent wordt gescheiden in een vloeibare en een gasstroom in een cycloon en een mistvanger alvorens monsters van de stromen genomen worden. Voor de monstername wordt de vloeistofstroom ontspannen van de werkvoorwaarden naar omgevingsomstandigheden, waarbij nog een deel van de opgeloste gassen ontsnapt. De analyse van de stroom die vloeibaar is onder de werkvoorwaarden bestaat

aldus uit een analyse van een gas- en een vloeistofmonster onder omgevingsomstandigheden. De analyse van de vloeistofstroom gebeurt “off-line”. De analyse van de gasstroom gebeurt “on-line”. Bovendien is de gaschromatograaf, verbonden aan de driefaseopstelling, naast een vlamionisatiedetector ook uitgerust met een thermischeconductiviteitsdetector (TCD), zodat ook de waterstoffractie in de verschillende effluentstromen kan bepaald worden. Het gebruik van een interne standaard laat toe de atomaire koolstof- en waterstofbalans alsook de totale massabalans over de reactor te controleren.

2.2. Modellering

Parameterschattingen worden uitgevoerd via een minimalisatie van de kwadratensom van de residuelen tussen de experimentele en de aan de hand van het model berekende responsen. De minimalisatie gebeurt door de waarden van de modelparameters aan te passen. Deze waarden worden verondersteld de echte parameterwaarden te benaderen in het optimum. Bij de minimalisatie van de residuele kwadratensom worden de responsen gewogen om responsen met hoge en lage numerieke waarden eenzelfde relatief belang toe te kennen. Parameterschattingen werden uitgevoerd aan de hand van een combinatie van een Rosenbrock- en een Marquardt-algoritme. De methode van Rosenbrock heeft minder de neiging tot divergentie wanneer de parameterwaarden nog ver van het optimum verwijderd zijn, terwijl de methode van Marquardt superieur is in het bepalen van het ‘exacte’ optimum. Daarom wordt bij parameterschattingen initieel een eigen geschreven Rosenbrock-routine gebruikt en wordt nadien overgeschakeld op het Marquardt-algoritme via de ‘gewone kleinste kwadraten’-optie in het vrij beschikbare pakket ODRPACK [2.18,2.19]. Enige aanvullende code werd aan het pakket toegevoegd om extra statistische informatie te verkrijgen. De gebruikte statistische toetsen omvatten de zogenaamde *F*-toets voor de significantie van de regressie en de *t*-toets voor de individuele betrouwbaarheid van de parameters. Bij deze toetsen worden steeds 95 % betrouwbaarheidsintervallen gebruikt. Daarnaast worden ook de binaire correlatiecoëfficiënten tussen de modelparameters gebruikt. Een absolute waarde van een dergelijke coëfficiënt die 1 benadert, wijst op een uitgesproken lineair of invers linear verband tussen beide parameters en is ongewenst.

De modelvergelijkingen voor de reactor volgen uit massabalansen voor de componenten over de reactor. In het geval van een volkomen vermengde reactor leiden dergelijke balansen tot een stelsel algebraïsche vergelijkingen, terwijl voor een propstroomreactor een stelsel gewone differentiaalvergelijkingen verkregen wordt. In beide gevallen komen reactiesnelheden voor in de vergelijkingen. De vereiste uitdrukkingen voor de reactiesnelheden zijn het onderwerp

van meerdere van de volgende hoofdstukken van dit proefschrift en worden afgeleid met de temperatuur, de totaaldruk, en de samenstelling van de voedingsstroom als onafhankelijke variabelen. De oplossing van het stelsel algebraïsche vergelijkingen of de integratie van het stelsel differentiaalvergelijkingen gebeurt met vrij beschikbare routines als DNSQE [2.21,2.22] voor het stelsel algebraïsche vergelijkingen en LSODA [2.23,2.24] voor het stelsel differentiaalvergelijkingen.

Kwantumchemische berekingen werden uitgevoerd gebruik makend van Densiteit Functionaal Theorie (DFT) [2.25]. Het platina-oppervlak werd gemodelleerd als een dubbel gelaagd Pt_{22}-cluster, waarbij de interatomaire afstand werd vastgehouden op de bulkwaarde van 277 pm. De reacties werden bestudeerd op de centrale atomen van deze platina-cluster.

3. Effect van Werkvoorwaarden op Hydrokraken

Hydrokraken verloopt volgens een bifunctioneel reactiemechanisme [3.4], zie Figuur 4. Verzadigde reagentia worden gedehydrogeneerd op metallische actieve centra. De resulterende onverzadigde producten migreren van de metallische naar de zure centra van de katalysator waar ze geprotoneerd worden tot carbeniumionen. Rechtstreekse protonering van verzadigde reagentia op de zure centra verloopt uiterst traag en kan in de aanwezigheid van bovenstaand, sneller alternatief verwaarloosd worden. De gevormde carbeniumionen ondergaan isomerisatie- en krakingsreacties die leiden tot geïsomeriseerde en gekraakte carbeniumionen en onverzadigde producten. Via de terugwaartse stappen van de reeds beschreven protonering en dehydrogenering worden de producten opnieuw verzadigd.

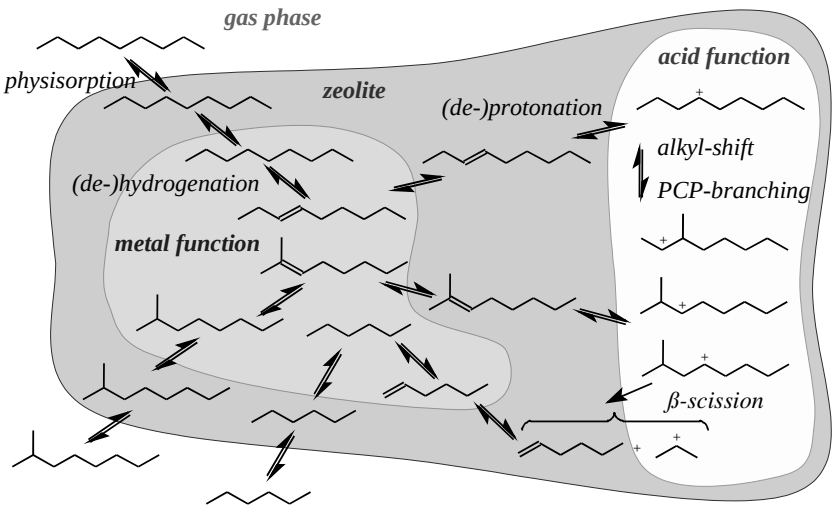

Figuur 4 Bifunctioneel reactieschema bij hydrokraken

Voorafgaand aan deze chemische stappen uit het reactiemechanisme treedt fysisorptie op van de reagentia in de katalysatorporiën.

3.1. *Ideaal* Versus *Niet-Ideaal* Hydrokraken

De wisselwerking tussen beide types actieve centra op een hydrokrakingskatalysator is bepalend voor de waargenomen activiteiten en de selectiviteiten [3.7-3.11]. Wanneer bijvoorbeeld de (de)-hydrogeneringsreacties gekatalyseerd door de metallische centra potentieel snel zijn en bij quasi-evenwicht kunnen verondersteld worden, daalt de activiteit voor hydrokraken met stijgende totaaldruk en is de selectiviteit voor isomerisatie maximaal. Bovendien kan deze isomerisatieconversie uitgedrukt worden als een unieke functie van de totale conversie, onafhankelijk van werkvoorwaarden zoals temperatuur, totaaldruk en molaire waterstof-op-koolwaterstofverhouding. Als de (de)-hydrogeneringsreacties bij quasi-evenwicht zijn wordt van *ideaal* hydrokraken gesproken, omdat onder dergelijke omstandigheden een maximum aan informatie over de reactiestappen gekatalyseerd door zure centra kan verkregen worden [3.12]. Wanneer echter de isomerisatie- en krakingsreacties gekatalyseerd door de zure centra potentieel snel zijn, stijgt de activiteit voor hydrokraken met stijgende totaaldruk en wijkt de isomerisatieconversie meestal sterk af van deze waargenomen wanneer de (de)-hydrogeneringsreacties bij quasi-evenwicht zijn. Daarnaast verdwijnt ook het unieke verband tussen de isomerisatieconversie en de totale conversie [3.16,3.17]. Gezien deze niet-verwaarloosbare effecten van de relatieve potentiële snelheden ten opzichte van elkaar van de reacties gekatalyseerd door de metallische en de zure centra is het belangrijk het effect van de werkvoorwaarden op deze relatieve potentiële snelheden te kennen en te kunnen begroten. Voor een gegeven katalysator wordt het effect van de temperatuur, de totaaldruk, de waterstof-op-koolwaterstofverhouding en van de voedingssamenstelling in eerste instantie beschreven en wordt nadien besproken hoe deze effecten tot uiting komen in snelheidsvergelijkingen voor hydrokraken.

3.2. Experimentele Resultaten

Tabel 2 bevat de werkvoorwaarden waarbij hydrokrakingsexperimenten werden uitgevoerd met *n*-dodecaan, onderverdeeld in groepen waarvan het identificatiegetal stijgt naarmate de afwijking van *ideaal* hydrokraken toeneemt [3.16,3.17]. Groep 1 bevat de werkvoorwaarden waaronder *ideaal* hydrokraken werd vastgesteld. Volgende waarnemingen zijn gebaseerd op de resultaten in Tabel 2:

Tabel 2 **Werkvoorwaarden aangewend bij *n*-dodecaan hydrokraken gegroepeerd volgens de afwijking van *ideaal* hydrokraken (hogere indentificatiegetallen corresponderen met sterkere afwijkingen)**

	temperatuur (K)	druk (MPa)	molair waterstof-op-koolwaterstof-verhouding (mol mol^{-1})
groep 1	493	1, 2	50, 100, 200, 300
	513	2, 5	50, 100, 200, 300
groep 2	513	1	200
groep 3	513	1	300
	553	2	100
groep 4	513	0.8	300
	553	2	200
groep 5	553	2	300
groep 6	513	0.5	200, 300
	533	1	200, 300
groep 7	553	1	200, 300

(1) Hogere temperaturen werken *niet-ideaal* hydrokraken in de hand: bij een totaaldruk van 1 MPa en een molaire waterstof-op-koolwaterstofverhouding van 200 wordt *ideaal* hydrokraken waargenomen bij 493 K, terwijl de experimenten bij 513 K, 533 K en 553 K behoren tot de groepen 2, 6 en 7 respectievelijk.

(2) Lagere totaaldrukken werken *niet-ideaal* hydrokraken in de hand: bij een temperatuur van 513 K en een molaire waterstof-op-koolwaterstof verhouding van 300 wordt *ideaal* hydrokraken waargenomen bij 2 MPa, terwijl de experimenten bij 1 MPa, 0.8 MPa en 0.5 MPa behoren tot de groepen 3, 4 en 6 respectievelijk.

(3) Hogere molaire waterstof-op-koolwaterstof verhoudingen werken *niet-ideaal* hydrokraken in de hand: bij een temperatuur van 553 K en een totaaldruk van 2 MPa behoren de experimenten met een molaire waterstof-op-koolwaterstofverhouding van 100, 200 en 300 tot de groepen 3, 4 en 5 respectievelijk.

Uit analoge tabellen als Tabel 2 voor *n*-alkanen met een ander koolstofgetal blijkt dat een toename van het koolstofgetal van het reactant *niet-ideaal* hydrokraken in de hand werkt.

Aan de hand van experimenten met alkaanmengsels en alkaan-cycloalkaanmengsels [3.18] werd vastgesteld dat het mengen van een *n*-alkaan met andere *n*-alkanen geen effect heeft op

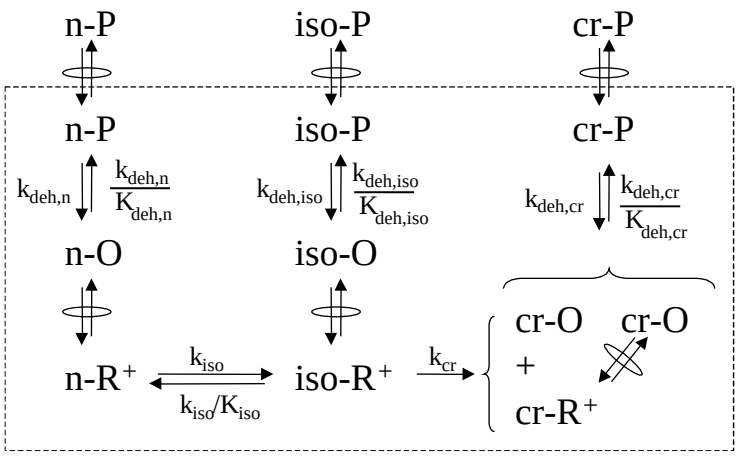

Figuur 5 Gehergroepeerd reactieschema gebruikt bij de bouw van een kinetisch model voor hydrokraken

de selectiviteiten in hydrokraken. Indien hetzelfde *n*-alkaan echter gemengd wordt met een cycloalkaan werd een significante verlaging van de selectiviteit voor isomerisatie van het *n*-alkaan vastgesteld. Aldus blijkt de toevoeging van cycloalkanen *niet-ideaal* hydrokraken in de hand te werken. Dit kan verklaard worden door een sterkere chemisorptie van de cycloalkanen dan de *n*-alkanen op de metallische centra zodat een tekort aan metallische centra ontstaat om het quasi-evenwicht tussen de alkanen en de alkenen in te stellen, zoals dat wel gebeurt bij *ideaal* hydrokraken.

3.3. Snelheidsvergelijkingen: Ontwikkeling en Interpretatie

De snelheidsvergelijkingen afgeleid in deze sectie corresponderen met een reactieschema gebruik makend van pseudocomponenten, zie Figuur 5. Zulk een reactieschema is voldoende om de effecten van de werkvoorwaarden op hydrokraken te bespreken. De uiteindelijke snelheidsvergelijking houdt rekening met de fysisorptie van de pseudocomponenten in de katalysatorporiën [3.5,3.6] en beschouwt zowel de reacties gekatalyseerd door de metallische als de zure centra als potentieel snelheidsbepalend. De concentratie aan carbeniumionen kan onder de gebruikte omstandigheden verwaarloosd worden ten opzichte van de totale concentratie aan zure centra en de concentratie van de onverzadigde componenten op de metallische centra kan verwaarloosd worden ten opzichte van de concentratie van de verzadigde componenten. Dit alles leidt tot de volgende uitdrukking voor de initiële verdwijnsnelheid van een *n*-alkaan door hydrokraken:

$$R_{n-P} = \frac{-\dfrac{C_{sat} K_{L,n-P} (1+\gamma)}{1+\gamma+\sum_i K_{L,i} y_i p_t} \left(\dfrac{k^*_{deh,iso}}{K_{deh,iso}} \gamma p_t + (1+\gamma) k^*_{cr} \right) k^*_{iso} k^*_{deh,n} y_{n-P} p_t}{\dfrac{k^*_{deh,n}}{K_{deh,n}} \dfrac{k^*_{deh,iso}}{K_{deh,iso}} \gamma^2 p_t^2 + \left(\dfrac{k^*_{deh,n}}{K_{deh,n}} \left(\dfrac{k^*_{iso}}{K_{iso}} + k^*_{cr} \right) + \dfrac{k^*_{deh,iso}}{K_{deh,iso}} k^*_{iso} \right) (1+\gamma) \gamma p_t + k^*_{iso} k^*_{cr} (1+\gamma)^2} \quad (1)$$

waarin

$$k^*_{deh,f} = \frac{k_{deh,f} C_t^M}{\left(1 + \dfrac{\sum_j C_{sat} K_j^M K_{L,j} y_j \; p_t / (1+\gamma)}{1+\sum_i K_{L,i} y_i \; p_t / (1+\gamma)} \right)} \quad (2)$$

en

$$k^*_f = k_f C_t^A \quad (3)$$

waarbij *f* staat voor *n* of *iso* en voor *iso* of *cr*, respectievelijk. Bovenstaande vergelijking (1) bevat verschillende termen waarvan er zijn die corresponderen met *ideaal* hydrokraken en andere met *niet-ideaal* hydrokraken. Indien bijvoorbeeld de (de)-hydrogeneringsreacties potentieel snel zijn en dus de corresponderende snelheidscoëfficiënten veel groter zijn dan die corresponderend met de reacties gekatalyseerd door de zure centra, dan zal de waarde van de eerste term in de teller, $\gamma p_t \, k^*_{deh,iso} / K_{deh,iso}$, en in de noemer, $\gamma^2 p_t^2 \, k^*_{deh,n} k^*_{deh,iso} / K_{deh,n} K_{deh,iso}$, de waarden van de teller respectievelijk de noemer domineren. Andersom, als de isomerisatie- en de krakingsreacties potentieel snel zijn, dan zijn het de waarden van de laatste term in de teller, $(1+\gamma) k^*_{cr}$, en de noemer, $k^*_{iso} k^*_{cr} (1+\gamma)^2$, die de waarde ervan domineert. De werkvoorwaarden die de relatieve waarde van de eerste ten opzichte van de laatste term beïnvloeden, zijn belangrijk met betrekking tot het *(niet)-ideale* karakter van hydrokraken bij deze werkvoorwaarden.

Het effect van de totaaldruk op de idealiteit van hydrokraken blijkt rechtstreeks uit de uitdrukkingen voor de hoger vermelde termen. De termen die de waarde van de teller en de noemer domineren bij *ideaal* hydrokraken nemen toe met de totaaldruk, terwijl de termen die de waarde van de teller en de noemer domineren bij *niet-ideaal* hydrokraken deze niet bevatten. Aldus is het evident dat hogere totaaldrukken *ideaal* hydrokraken in de hand werken.

Het effect van de temperatuur op de idealiteit bij hydrokraken zit eveneens vervat in de reeds besproken termen, meer bepaald via de temperatuurafhankelijkheid van de snelheidscoëfficiënten die erin voorkomen. De activeringsenergieën voor

hydrogeneringsreacties zijn lager dan die voor isomerisatie- en krakingsreacties. De snelheidscoëfficiënten voor isomerisatie en kraking op de zure katalytische functie stijgen aldus meer met de temperatuur. Bij voldoend lage temperatuur domineren de eerste termen van teller en noemer de waarden ervan, maar door de snellere toename met de temperatuur van de isomerisatie- en krakingssnelheidscoëfficiënten dan de (de)-hydrogeneringssnelheidscoëfficiënten, gaan bij voldoend hoge temperaturen de laatste termen van de teller en de noemer de waarde ervan domineren. Op die manier kunnen hogere temperaturen *niet-ideaal* hydrokraken in de hand werken.

De molaire waterstof-op-koolwaterstofverhouding heeft een quasi identiek effect op de termen die de waarde van de teller en de noemer domineren in geval van *(niet)-ideaal* hydrokraken. Zoals echter experimenteel vastgesteld kan hier echter niet de conclusie aan gekoppeld worden dat de molaire waterstof-op-koolwaterstofverhouding geen effect op de idealiteit van hydrokraken zou hebben. Het effect van de molaire waterstof-op-koolwaterstofverhouding houdt verband met de gedetailleerde uitdrukking voor de samengestelde snelheidscoëfficiënt voor dehydrogenering. Indien $\sum_j C_{sat} K_j^M K_{L,j} y_j \; p_t \,/\left(1+\gamma\right) >> 1$, terwijl $\sum_i K_{L,i} y_i \; p_t \,/\left(1+\gamma\right) << 1$, hetgeen correspondeert met hoge koolwaterstofconcentraties op de metallische centra terwijl de katalysator helemaal niet verzadigd is door fysisorptie, dan heeft de molaire waterstof-op-koolwaterstofverhouding een extra verhogend effect op de termen die de waarde van de teller en de noemer domineren in het geval van *ideaal* hydrokraken. Indien een dergelijk effect ook optreedt en meer uitgesproken is voor de termen die de waarden van de teller en de noemer domineren bij *niet-ideaal* hydrokraken, verklaart dit het effect van de molaire waterstof-op-koolwaterstofverhouding op de idealiteit van hydrokraken. Dit laatste lijkt echter in tegenspraak met de aanname dat de concentratie aan carbeniumionen veel kleiner is dan de totale concentratie aan zure centra. Verder, quantitatief onderzoek kan hierin duidelijkheid brengen en dan vooral met betrekking tot de vereiste koolwaterstofconcentraties op de zure en de metallische centra om het effect van de molaire waterstof-op-koolwaterstofverhouding te verklaren.

Het effect van het koolstofgetal op de idealiteit van hydrokraken is tweeledig. Voor alkanen met koolstofgetal lager dan 10 neemt het aantal reacties gekatalyseerd door de zure centra sneller toe dan het aantal reacties gekatalyseerd door metallische centra. De gegroepeerde snelheidscoëfficiënten voor isomerisatie en kraking zullen aldus sneller stijgen met het koolstofgetal dan die voor (de)-hydrogenering, hetgeen een verschuiving in relatieve

belangrijkheid van de termen in de teller en de noemer van de snelheidsvergelijking kan veroorzaken. Als tweede effect zijn er de hogere koolwaterstofconcentraties op de metallische centra voor zwaardere koolwaterstoffen. Dit effect is analoog aan dat van het voeden van een alkaan-cycloalkaan mengsel.

Het effect van de hogere koolwaterstofconcentraties op de metallische centra op de idealiteit bij hydrokraken wordt uitgelegd aan de hand van Verg. (2). Bij een lage waarde van de laatste term in de noemer, $\sum_h C_{sat} K^M_{L_{h-P}} K_{L,h-P} p_t$, hetgeen overeenkomt met verwaarloosbare concentraties van de op de metallische centra gechemisorbeerde componenten in vergelijking met het totaal aantal metallische centra, wordt Verg. (2) gereduceerd tot $k^*_{deh} = k_{deh} C^M_t$. Wanneer de concentratie van de op de metallische centra gechemisorbeerde componenten echter niet verwaarloosbaar is, heeft de laatste term in de noemer van Verg. (2), corresponderend met deze chemisorptie, een verkleinend effect op de waarde van de termen in Verg. (1) die belangrijk zijn bij *ideaal* hydrokraken. Aldus zullen voedingscomponenten die sterk chemisorberen op de metallische centra *niet-ideaal* hydrokraken in de hand werken.

4. Kinetische Modellering van Hydrokraken van Modelcomponenten en van Complexe Voedingen Gebaseerd op Enkelvoudige Gebeurtenissen

Omwille van de complexiteit van reële voedingen wordt in experimenteel werk frequent gebruik gemaakt van welgekozen modelcomponenten om een maximum aan informatie uit deze experimenten te kunnen halen. In een later stadium worden dan meestal ook een aantal experimenten met een reële voeding uitgevoerd ter bevestiging van de besluiten volgend uit de modelcomponentexperimenten. Modelvergelijkingen worden dan ook initieel afgeleid voor de beschrijving van modelcomponentgedrag en nadien voor het gedrag van een reële voeding.

4.1. Elementaire Snelheidvergelijkingen

De snelheidsbepalende elementaire stappen in hydrokraken behoren tot een beperkt aantal reactiefamilies, namelijk alkylverschuivingen (AS), geprotoneerdcyclopropaanvertakkings-reacties (PCP) en β-scissies. Binnen een reactiefamilie wordt verondersteld dat de snelheidscoëfficiënt voor een enkelvoudige stap enkel afhangt van de aard van het reactant en product carbenium ion, namelijk secundair of tertiair. De uitdrukking voor de reactiesnelheid

van een elementaire stap in het geval van zogenaamd *ideaal hydrokraken,* wordt gegeven door:

$$r^{AS/PCP/\beta}\left(m_{i,k};n_{q,r}\right)= \frac{C_t \frac{\sigma_{O_{i,j}}}{\sigma_{\neq ikqr}} \tilde{k}^{AS/PCP/\beta}\left(m_{i,k};n_{q,r}\right)\tilde{K}_{prot}\left(O_{ref};m\right)\tilde{K}_{iso}\left(O_{i,j};O_{ref}\right)K_{deh}\left(P_i;O_{i,j}\right)C_{sat,P_i}K_{L,P_i}\frac{p_{P_i}}{p_{H_2}}}{1+\sum_j K_{L,P_j}p_{P_j}} \quad (4)$$

Waarbij $\tilde{k}^{AS/PCP/\beta}$ correspondeert met de snelheidscoëfficiënt waarbij geen rekening gehouden wordt met symmetrie-effectten. Aangezien enkel *ideale* hydrokrakings-experimenten gemodelleerd worden in dit proefschrift voldoet bovenstaande vergelijking. Een belangrijke veronderstelling in de afleiding van bovenstaande snelheidsvergelijking is dat de concentratie aan carbeniumionen veel kleiner is dan de totale concentratie aan zure centra zodat de adsorptieterm in de noemer van de uitdrukking voor de chemisorptie van de onverzadigde componenten op de zure centra, kan verwaarloosd worden. Deze veronderstelling wordt verrechtvaardigd in Appendix D. De netto-vormingssnelheden van de verschillende verzadigde producten worden verkregen via sommatie van de elementaire reactiesnelheden waarin carbeniumionen of onverzadigde componenten met dezelfde skeletstructuur als het verzadigde product geproduceerd of verbruikt worden:

$$R_{P_i}=\sum_k R^{AS/PCP/\beta}_{R^+_{i,k}}+\sum_j R^{\beta}_{O_{i,j}} \quad (5)$$

Het merendeel van de parameters in de uitdrukking voor de reactiesnelheid van de elementaire stappen is gekend uit onafhankelijke experimenten, zoals de fysisorptie parameters C_{sat,P_i} en K_{L,P_i}, of kan berekend worden gebaseerd op thermodynamische gegevens, zoals de evenwichtscoëfficiënten voor (de)-hydrogenering en isomerisatie. De parameters waarvoor geen berekende of vooraf bepaalde waarden beschikbaar zijn, zijn de protoneringsevenwichtscoëfficiënt gebaseerd op enkelvoudige gebeurtenissen, $\tilde{K}_{prot}$, en de snelheidscoëfficiënt gebaseerd op enkelvoudige gebeurtenissen, $\tilde{k}^{AS/PCP/\beta}$. Aangezien in de uitdrukking voor de reactiesnelheid enkel het product van de beide coëfficiënten voorkomt, kunnen deze niet afzonderlijk bepaald worden, zodat parameterschattingen leiden tot samengestelde snelheidscoëfficiënten en samengestelde activeringsenergieën. Via een berekening van de samengestelde preëxponentiële factoren op basis van transitiestoestandstheorie wordt het totaal aantal te schatten parameters herleid tot 10. De

samengestelde activeringsenergie bevat de som van de eigenlijke activeringsenergie en de standaardprotoneringsenthalpie:

$$E_A^{AS/PCP/\beta-comp} = E_A^{AS/PCP/\beta} + \Delta H_{prot}^0 \tag{6}$$

4.2. Hergroepering

Voor zwaardere koolwaterstoffen met een uitgebreid netwerk aan reacties gekatalyseerd door zure centra kan de sommatie in Verg. (5) heel tijdrovend worden. Bovendien kunnen huidige analytische technieken de samenstelling van aardoliefracties niet in zulk detail weergeven. Daarom werd de techniek van het hergroeperen toegepast waarbij voor elk koolstofgetal 8 pseudocomponenten gebruikt worden: *n*-alkaan, mono-, di- en trivertakte alkanen, mono-, di-, tri- en tetraring cycloalkanen [4.11]. De reactiesnelheden tussen de verschillende pseudocomponenten worden echter op een zodanige manier uitgerekend, dat deze rekening houden met alle elementaire stappen tussen deze pseudocomponenten. Om de reactiesnelheden op deze manier te kunnen berekenen, is de kennis van de interne moleculaire samenstelling van de pseudocomponent vereist. De pseudocomponenten zijn op een dusdanige manier gedefinieerd dat thermodynamisch evenwicht kan worden aangenomen bij hydrokraken op Pt/H-(US)Y-zeolieten, wat toelaat de interne samenstelling van deze pseudocomponenten op moleculair niveau te berekenen.

De reactiesnelheid tussen twee pseudocomponenten in het gehergroepeerd model correspondeert met de sommatie van de snelheden van alle snelheidsbepalende elementaire stappen tussen deze twee pseudocomponenten en kan uitgedrukt worden als:

$$r^{PCP}(g;h) = \frac{k_{lump}^{PCP}(g;h) H_g \dfrac{p_g}{p_{H_2}}}{1 + \sum_f K_{L,f}\, p_f} \tag{7}$$

waarbij de gegroepeerde snelheidscoëfficiënt als volgt functie is van de op enkelvoudige gebeurtenissen gebaseerde snelheidscoëfficiënten van de snelheidsbepalende stappen [4.11]:

$$\begin{aligned} k_{lump}^{PCP}(g;h) = \Big[& LC_{s;s}^{PCP}(g;h) \tilde{K}_{prot}(s) \tilde{k}^{PCP}(s;s) + LC_{s;t}^{PCP}(g;h) \tilde{K}_{prot}(s) \tilde{k}^{PCP}(s;t) \\ & + LC_{t;s}^{PCP}(g;h) \tilde{K}_{prot}(t) \tilde{k}^{PCP}(t;s) + LC_{t;t}^{PCP}(g;h) \tilde{K}_{prot}(t) \tilde{k}^{PCP}(t;t) \Big] C_t \end{aligned} \tag{8}$$

De groeperingscoëfficiënten in deze uitdrukking bevatten de sommatietermen die het gevolg zijn van de sommatie over alle elementaire stappen tussen de betrokken pseudocomponenten en zijn onafhankelijk van de op enkelvoudige gebeurtenissen gebaseerde snelheidscoëfficiënten:

$$LC_{m;n}^{PCP}(g;h)=\sum_{i\in g}\sum_{k\in g}\sum_{q\in h}\sum_{r\in h}\frac{\sigma_{O_{i,j}}}{\sigma_{\neq_{ikqr}}}K_{iso}(O_{i,j};O_{ref})K_{deh}(P_i;O_{i,j})y_{i,g} \tag{9}$$

De sommatie over alle elementaire stappen die bij het originele model bij elke berekening van de reactiesnelheden moet herhaald worden, hoeft in het geval van het gehergroepeerde model slechts eenmaal te gebeuren, namelijk vooraf bij de berekening van de groeperingscoëfficiënten. Inderdaad, uit Verg. (9) blijkt dat deze groeperingscoëfficiënten enkel afhankelijk zijn van de samenstelling van de gekozen pseudocomponenten en van het reactienetwerk van elementaire stappen, maar onafhankelijk van de op enkelvoudige gebeurtenissen gebaseerde snelheidscoëfficiënten.

Hoewel deze manier van hergroeperen het mogelijk maakt het hydrokraken van componenten uit het bereik van de middendestillaten te beschrijven, is ze niet geschikt voor zware koolwaterstoffen zoals, deze uit een vacuümgasolie, omdat in dat bereik ook de gehergroepeerde techniek zoals hoger uitgelegd heel tijdrovend wordt. Het is echter mogelijk de expliciete sommatie over alle elementaire stappen te vermijden zonder het fundamentele karakter van het gehergroepeerde model te verliezen [4.3,4.4,4.13]. Daartoe wordt de uitdrukking voor de groeperingscoëfficiënt als volgt opgesplitst in drie factoren:

$$LC_{m;n}^{PCP}(g;h)=\frac{N_{m;n}^{PCP}(g;h)K_{ref,g}^{*}(n;T)}{K_{g}^{*}(n;T)} \tag{10}$$

waarbij $K_{ref,g}^{*}(n;T)$ de evenwichtscoëfficiënt voorstelt voor de vorming van het referentie-alkeen en waterstof uit de elementen:

$$K_{ref,g}^{*}(n;T)=\exp\left(-\frac{\Delta\tilde{G}_{f}^{0}(O_r)+\Delta\tilde{G}_{f}^{0}(H_2)}{RT}\right) \tag{11}$$

en $K_{g}^{*}(n;T)$ de som van de evenwichtscoëfficiënten voor de vorming van alle (cyclo)-alkanen uit pseudocomponent *g*:

$$K_{g}^{*}(n;T)=\sum_{i\in g}\frac{\exp\left(-\frac{\Delta\tilde{G}_{f}^{0}(P_i)}{RT}\right)}{\sigma_{P_i}} \tag{12}$$

en $N_{m_1;m_2}^{PCP}$ ten slotte rekening houdt met symmetrie-effecten in de snelheidsbepalende elementaire stappen.

$$N_{m_1;m_2}^{PCP}=\sum_{i\in g}\sum_{j\in g}\sum_{q\in h}\sum_{r\in h}\frac{1}{\sigma_{\neq_{ikqr}}\sigma_{H_2}} \tag{13}$$

De berekening van $K^*_{ref,g}(n;T)$ omvat enkel eigenschappen van waterstof en het referentie-alkeen. De CPU-tijd is aldus onafhankelijk van het koolstofgetal van de pseudocomponent waarvoor deze factor berekend wordt. De berekening van de twee overige factoren omvat echter wel een sommatie over componenten of reacties in het netwerk en wordt dus meer tijdrovend naarmate het koolstofgetal van de pseudocomponent waarvoor deze factoren uitgerekend worden, toeneemt. Indien echter de waarde van $K^*_g(n;T)$ berekend wordt gebruik makend van de methode van Benson [4.14], kan de sommatie over alle componenten in de pseudocomponent omgevormd worden tot een sommatie over een beperkt aantal klassen van componenten in de pseudocomponent. Deze klassen zijn gedefinieerd door gemeenschappelijke waarden voor het globale symmetriegetal, standaard vormingsenthalpie, de op enkelvoudige gebeurtenissen gebaseerde standaard entropie en specifieke warmtecapaciteit. Gebruik makend van de methode van Benson om deze eigenschappen uit te rekenen wordt elke klasse gekenmerkt door het aantal primaire, secundaire, tertiaire en quaternaire koolstofatomen, alsook het aantal vijf- en zesringen, het globale symmetriegetal en het minimum aantal gauche interacties. Terwijl het aantal componenten toeneemt met het koolstofgetal, zijn de klassen zodanig gedefinieerd dat hun aantal onafhankelijk is van het koolstofgetal. Voor elke klasse is een minimum aantal koolstofatomen vereist, echter, voor voldoend hoge koolstofgetallen neemt het aantal mogelijke klassen niet meer toe met het koolstofgetal. Op een analoge manier kunnen de carbeniumionen betrokken in de reacties waarover in $N^{PCP}_{m_1;m_2}$ gesommeerd wordt, ingedeeld worden in klassen met een gemeenschappelijke waarde voor het globale symmetriegetal in de corresponderende transitietoestand. De ontwikkeling van deze methode om de groeperingscoëfficiënten te berekenen gebaseerd op structurele klassen, maakt de toepassing van het gehergroepeerde model voor hydrokraken mogelijk voor componenten met om het even welk koolstofgetal.

5. Dubbelebindingprotoneringsenthalpie als Maatstaf voor Zuursterkte

Een veel gebruikte methode om de zure eigenschappen van zeolieten in het algemeen en van (US)Y-zeolieten in het bijzonder, te wijzigen is via de verwijdering van aluminium uit het zeolietrooster [5.1,5.2]. De katalysatoractiviteit als functie van het roostergehalte aan aluminium vertoont typisch een ‘vulkaan’ verloop [5.3-5.9]. Een dergelijk verloop wordt vaak gerelateerd met een toename van de sterkte van de zure centra met dealuminering enerzijds en

een afname van het totale aantal centra anderzijds. In geval van beperkte dealuminering neemt de sterkte van de centra in belangrijke mate toe en overcompenseert het verlies aan zure centra zodat globaal een verhoging van de activiteit wordt waargenomen bij dealuminering. Bij hoge dealumineringsgraden echter neemt de sterkte van de centra nog nauwelijks toe, zodat het verlies aan zure centra niet gecompenseerd wordt en dat globaal een verlies aan activiteit optreedt [5.10,5.11]. Dit beeld is echter te sterk vereenvoudigd omdat de coördinatie van aluminium in het rooster afhangt van de precieze omstandigheden in de dealumineringsprocedure [5.12,5.13].

In de homologe reeks van de alkanen neemt de reactiviteit voor hydrokraken toe met het koolstofgetal [5.17-5.19]. Deze vaststelling werd in de literatuur reeds in verband gebracht met sterkere fysisorptie van en een meer uitgebreid reactienetwerk voor zwaardere koolwaterstoffen. In dit deel van dit proefschrift wordt het effect van de zuursterkte van (US)Y-zeolieten, met atomaire Si/Al_F-verhoudingen van 2.6, 18, en 60, op het gedrag onder hydrokrakingsomstandigheden van alkanen met verschillend koolstofgetal in het bereik van vijf tot twaalf behandeld.

5.1. *n*-Octaan Hydrokraken op een Referentiezeoliet

In het reactienetwerk van alkanen met acht koolstofatomen of meer komen alle mogelijke isomerisatie- en krakingsmechanismen voor. Wegens analytische redenen werd voor octaan gekozen als referentiecomponent. Als referentiekatalysator werd deze genomen met Si/Al_F-verhouding 60. Deze Pt/USY-zeoliet vertoont een activiteit intermediair aan die van de twee andere zeolieten en het grootste conversie bereik werd behaald met deze katalysator. Uit de productendistributies blijkt dat bij *n*-alkaan hydrokraken het evenwicht zich snel instelt binnen de groep van de monovertakten, zie Tabel 3 en Figuur 6a. Dit wijst erop dat de

Tabel 3 Evenwichtssamenstelling in de groep van octaan isomeren bij 506 K

isomeergroep / individueel isomeer		groepfractie / individuele fractie	
normaal		0.09	
monovertakt	2-methylheptaan	0.44	0.38
	3-methylheptaan		0.39
	4-methylheptaan		0.13
	3-ethylhexaan		0.10
divertakt		0.44	
trivertakt		0.03	

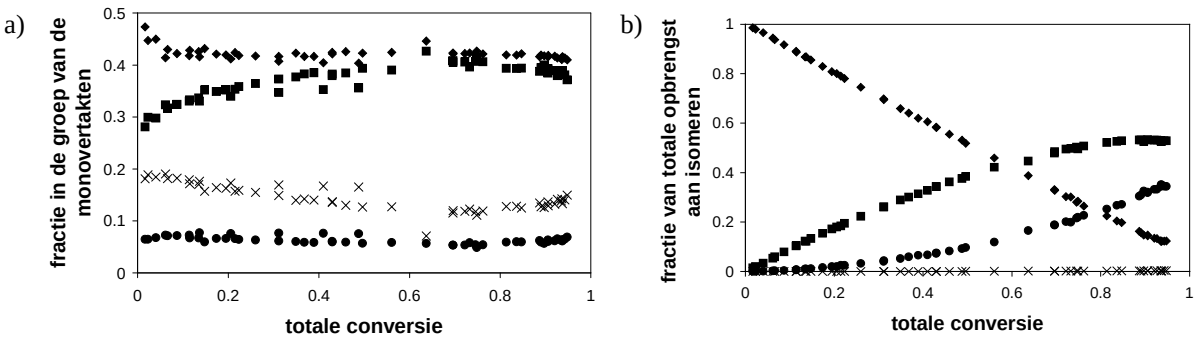

Figuur 6 **Experimentele distributie a) in de groep van de monovertakte isomeren (♦: 3-methylheptaan, ■: 2-methylheptaan, ●: 3-ethylhexaan, ×: 4-methylheptaan) b) voor alle isomeren gegroepeerd volgens hun vertakkingsgraad (♦: normaal, ■: monovertakt, ●: divertakt, ×: trivertakt)**

Tabel 4 **Samengestelde activeringsenergieën (en bijhorende 95% betrouwbaarheidsintervallen) geschat door middel van regressie gebruik makend van de experimentele data van *n*-octaan op Pt/CBV-760**

	Alkylverschuiving	PCP-vertakking	β-scissie
		(kJ mol^{-1})	
(s;s)	16.7 (±0.1)	45.6 (±0.1)	79.2 (±0.6)
(s;t)	13.7 (±2.4)	38.8 (±5.5)	63.7 (±4.5)
(t;s)			55.1 (±0.6)
(t;t)	7.7 (±2.9)	31.5 (±2.3)	33.9 (±1.7)

alkylverschuivingen tussen de monovertakten onderling sneller zijn dan zowel de PCP-vertakkingreacties waarbij de vertakkingsgraad van de monovertakten wijzigt als dan de β-scissies waarbij de monovertakten in twee worden gesplitst. Hetzelfde geldt voor de divertakten, maar niet voor de trivertakten, waar de snelle (t;t)-β-scissies de evenwichtsinstelling verhindert. Tussen isomeren met een verschillende vertakkingsgraad wordt geen evenwicht bereikt, tenzij tussen de mono- en de divertakten bij hoge totale conversies, zie Tabel 3 en Figuur 6b. Waarden voor de samengestelde activeringsenergieën in het op enkelvoudige gebeurtenissen gebaseerde model voor hydrokraken, verkregen via parameterschattingen, zijn in overeenstemming met waarden uit eerder werk en met de kwalitatieve analyse van de experimentele resultaten [5.18,5.20], zie Tabel 4.

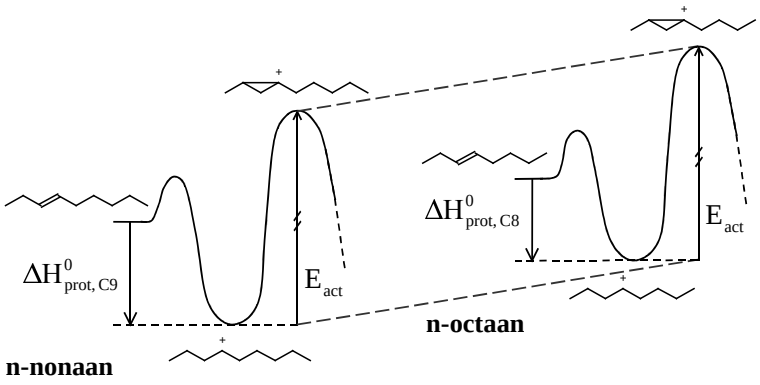

Figuur 7 Energieniveaus bij een elementaire stap gekatalyzeerd door een zuur centrum

5.2. Effect van het Koolstofgetal op de Alkeenprotoneringsenthalpie

De hogere reactiviteit met toenemend koolstofgetal in het bereik van pentaan tot nonaan wordt in verband gebracht met de sterkere fysisorptie en de uitbreiding van het reactienetwerk. De lagere reactiviteit van dodecaan ten opzichte van nonaan wordt veroorzaakt door saturatie-effecten. Ondanks de hogere Langmuir-coëfficiënt voor fysisorptie van dodecaan is de concentratie aan dodecaan in de katalysator lager dan die aan nonaan onder gelijke omstandigheden wegens de lagere saturatieconcentratie van dodecaan dan nonaan.

In het model gebaseerd op enkelvoudige gebeurtenissen worden bovenstaande waarnemingen volledig toegeschreven aan fysisorptie en reactienetwerkeffecten. De stabiliteit van het carbeniumion wordt in het model enkel afhankelijk verondersteld van zijn aard, namelijk secundair of tertiair. Het oct-3-yl ion heeft in het model dezelfde stabiliteit als het 2,2,4-trimethylpent-3-yl ion:

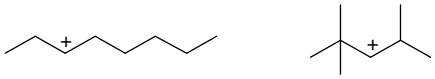

terwijl een verschil in stabiliteit van enkele *kJ mol*$^{-1}$ kan verwacht worden tussen dergelijke ionen. Het verwaarlozen van dergelijke verschillen heeft als gevolg dat de geschatte waarden voor de samengestelde activeringsenergieën in het model corresponderen met een gemiddeld stabiliteitsniveau van de carbeniumionen. De veronderstelde onafhankelijkheid van de samengestelde activeringsenergieën impliceert dat dit gemiddeld niveau onafhankelijk is van het koolstofgetal.

Aangezien in het model gebaseerd op enkelvoudige gebeurtenissen zowel het intermediair als het geactiveerde complex een ionair karakter hebben, kan hetzelfde effect van het koolstofgetal op de stabiliteit van het intermediair en het geactiveerde complex verwacht

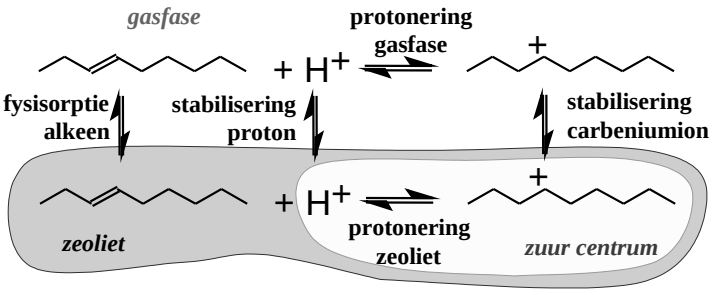

Figuur 8 **Verband tussen de standaardprotoneringsenthalpie in de gasfase en op de katalysator via een Born-Haber cyclus**

worden, zie Figuur 7. Een eventueel effect van het koolstofgetal op de samengestelde activeringsenergie kan aldus toegewezen worden aan een effect op de protoneringsenthalpie:

$$\Delta_{CN_j-CN_i}\left(E_A^{comp}\right)=\Delta_{CN_j-CN_i}\left(\Delta H^0_{prot}\right) \tag{14}$$

Verschillen in standaardprotoneringsenthalpie op de zeoliet kunnen als volgt in verband gebracht worden met de gasfasestandaardprotoneringsenthalpie van het corresponderend alkeen, *O*, via een Born-Haber cyclus, zie Figuur 8:

$$\Delta H^0_{prot,zeo}=\Delta H^0_{stab,R^+}+\Delta H^0_{prot,gas}-\Delta H^0_{stab,H^+}-\Delta H^0_{phys,O} \tag{15}$$

waarin $\Delta H^0_{stab,H^+}$ uiteraard onafhankelijk is van het koolstofgetal. $\Delta H^0_{phys,O}$ correspondeert met de alkeen fysisorptie. De stabilisatie van het corresponderend carbeniumion door de zeoliet, $\Delta H^0_{stab,R^+}$, bestaat uit twee bijdragen die op hun beurt aanleiding kunnen geven tot een afhankelijkheid van het koolstofgetal:

$$\Delta_{CN_j-CN_i}\left(\Delta H^0_{stab,R^+}\right)=\Delta_{CN_j-CN_i}\left(\Delta H^0_{phys,R^+}\right)+\Delta_{CN_j-CN_i}\left(\Delta H^0_{chem,R^+}\right) \tag{16}$$

Verg. (16) drukt uit dat de stabilisatie van het carbeniumion door de zeoliet bestaat uit een bijdrage ten gevolge van fysische interacties tussen het ion en het zeolietrooster en een bijdrage ten gevolge van de ionaire binding tussen het ion en het gedeprotoneerd zuur centrum. Het effect van het koolstofgetal op de bijdrage ten gevolge van de fysische interacties wordt gelijkaardig verondersteld aan het effect op de alkeenfysisorptieenthalpie, zodat het effect van het koolstofgetal op de standaardprotoneringsenthalpie op de zeoliet kan geschreven worden als:

$$\Delta_{CN_i-CN_j}\left(\Delta H^0_{prot,zeo}\right)=\Delta_{CN_i-CN_j}\left(\Delta H^0_{prot,gas}\right)+\Delta_{CN_i-CN_j}\left(\Delta H^0_{chem,R^+}\right) \tag{17}$$

namelijk bestaande uit een bijdrage ten gevolge van verschillen in gasfasestandaard-protoneringsenthalpie en een tweede bijdrage ten gevolge van verschillen in ionaire binding

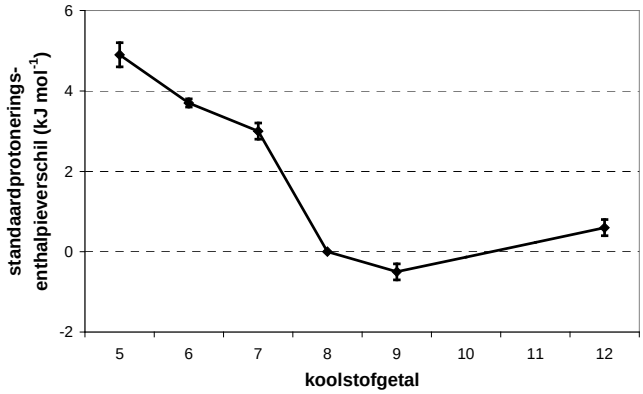

Figuur 9 Verschillen in standaardprotoneringsenthalpie op CBV-760 als functie van het koolstofgetal (referentie: *n*-octaan)

van het carbeniumion met het gedeprotoneerd zuur centrum. Een analoge uitdrukking kan afgeleid worden gebruik makend van het concept van de 'protontransferenergie' Q_p zoals gebruikt door van Santen en Kramer [5.11] voor de protonering van een gasfasealkeen op een zuur centrum:

$$Q_p = -PA_{gas}^{base} + PA_{solid}^{acid} + E_{zi} \tag{18}$$

Hierin staat PA_{gas}^{base} voor de protonaffiniteit van het gasfasecarbeniumion, corresponderend met $\Delta H^0_{prot,gas}$. PA_{solid}^{acid} staat voor de protonaffiniteit van een hydroxylgroep en E_{zi} is de Zwitter-ionstabiliseringsenergie tussen de geprotoneerde base, namelijk het carbeniumion, en de negatief geladen zeolietwand, namelijk het gedeprotoneerd zuur centrum. Deze beide laatste termen kunnen geïdentificeerd worden met $\Delta H^0_{stab,H^+}$ en $\Delta H^0_{chem,R^+}$.

De verschillen in standaardprotoneringsenthalpie ten opzichte van die van octeen zijn geschat gebruik makend van de experimentele gegevens voor hydrokraken van alkanen van pentaan tot dodecaan op de Pt/USY-zeoliet met een atomaire Si/Al_F-verhouding 60. De effecten van het koolstofgetal op de fysisorptie en op de omvang van het reactienetwerk worden expliciet in rekening gebracht via de gebruikte fysisorptieparameters en via de sommaties in Verg. (5). Het effect van het koolstofgetal op standaardprotoneringsenthalpie, zie Verg. (17), komt tot uiting in de reactiesnelheid van de elementaire stappen, zie Verg. (4), waarover in Verg. (5) gesommeerd wordt. De geschatte waarden voor de verschillen in standaardprotoneringsenthalpie nemen aanvankelijk af en vlakken nadien uit met het koolstofgetal, zie Figuur 9. De grootteorde van de verschillen valt in het bereik verwacht wanneer koolstof-koolstof bindingen in β-positie ten opzichte van het geladen koolstofatoom worden aangehaald ter verklaring van deze verschillen. De significante verschillen in standaardprotoneringsenthalpie

in het bereik pentaan - octaan zijn gerelateerd met de significante toename van het aantal mogelijke koolstof-koolstof bindingen in β-positie ten opzichte van het geladen koolstofatoom. Dit leidt tot een significant verschil in gemiddeld stabiliteitsniveau van de carbeniumionen in het bereik van pentaan tot octaan, terwijl dit gemiddeld niveau voor zwaardere koolwaterstoffen niet significant meer wijzigt omdat er geen belangrijke toename van het mogelijke aantal koolstof-koolstofbindingen in β-positie van het geladen atoom mogelijk is. Deze laatste vaststelling is in overeenkomst met de in eerder werk vastgestelde onafhankelijkheid van het koolstofgetal van de op enkelvoudige gebeurtenissen gebaseerde snelheidscoëfficiënten [5.20].

5.3. Effect van de Gemiddelde Zuursterkte op de Alkeenprotoneringsenthalpie

Experimenteel worden enkel verschillen in activiteit en niet in selectiviteit vastgesteld bij het hydrokraken van eenzelfde alkaan over Pt/(US)Y-zeolieten met verschillende atomaire Si/Al_F-verhoudingen. De identieke selectiviteiten op de verschillende zeolieten wijzen erop dat de snelheidsbepalende stappen in dezelfde mate beïnvloed worden door verschillen in zuursterkte.

Analoog aan het effect van het koolstofgetal, kan het effect van een verschil in zuursterkte van het zuur centrum op het intermediair en het geactiveerd complex hetzelfde verondersteld worden, omwille van het ionair karakter van beide speciës. Het effect van een verschillende zuursterkte uit zich aldus in een verschil in standaardprotoneringsenthalpie op de zeoliet. In Verg. (15), zie ook Figuur 8, moeten in dit geval enkel de parameters afhankelijk van de zuursterkte behouden worden om de fysische betekenis van het verschil in standaard protoneringsenthalpie voor verschillende zuursterkte te verduidelijken. De gasfasestandaard-protoneringsenthalpie, $\Delta H^0_{prot,gas}$, is uiteraard onafhankelijk van de zuursterkte. $\Delta H^0_{stab,R^+}$ kan op dezelfde manier als eerder opgesplitst worden in een fysische en een chemische bijdrage, zie Verg. (16). Het effect van de zuursterkte op de fysische bijdrage in de stabiliseringsenthalpie van het carbeniumion door de zeoliet en op de fysisorptie-enthalpie van het alkeen worden gelijkaardig verondersteld:

$$\Delta_{zeo_{II}-zeo_I}\left(\Delta H^0_{phys,R^+}\right) \cong \Delta_{zeo_{II}-zeo_I}\left(\Delta H^0_{phys,O}\right) \tag{19}$$

zodat het effect van de zuursterkte op de standaardprotoneringsenthalpie door de zeoliet kan geschreven worden als volgt:

$$\Delta_{zeo_{II}-zeo_I}\left(\Delta H^0_{prot,zeo}\right) = \Delta_{zeo_{II}-zeo_I}\left(\Delta H^0_{chem,R^+}\right) - \Delta_{zeo_{II}-zeo_I}\left(\Delta H^0_{stab,H^+}\right) \tag{20}$$

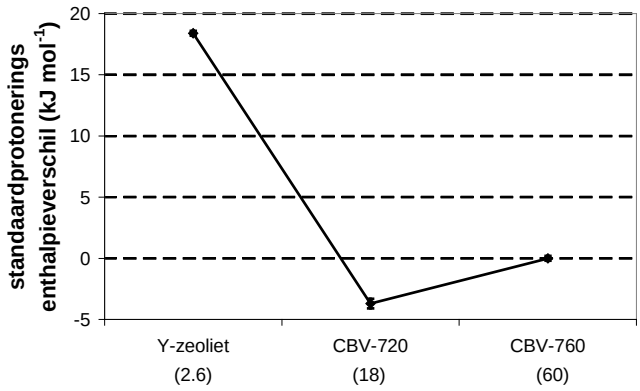

Figuur 10 **Verschillen in standaardprotoneringsenthalpie voor nonaan op drie Pt/H-(US)Y-zeolieten (referentie: Pt/CBV-760; tussen haakjes: atomaire roostersilicium-aluminiumverhouding)**

en is dus een gevolg van het verschil in stabiliseringsenthalpie van het carbeniumion door de zeoliet via de ionaire binding met het gedeprotoneerd zuur centrum en van het verschil in stabiliseringsenthalpie van het proton door de zeoliet. Dezelfde vergelijking met het concept van de 'protontransferenergie' als eerder aangehaald kan ook hier gemaakt worden. De analogie kan nog verder doorgetrokken worden naar werk van Dumesic en van Klein [5.33]. Deze auteurs introduceerden met ΔH^+ een katalysatorafhankelijke parameter die de stabiliseringsenthalpie van het carbeniumion door de zeoliet voorstelt, relatief ten opzichte van de stabiliseringsenthalpie van het proton door de zeoliet. Het zonet gedefinieerde verschil in standaardprotoneringsenthalpie ten gevolge van verschillen in zuursterkte komt overeen met het verschil tussen de twee ΔH^+–waarden voor de betrokken katalysatoren:

$$\Delta_{zeo_{II}-zeo_I}\left(\Delta H^0_{prot,zeo}\right) = \Delta H^+_{zeo_{II}} - \Delta H^+_{zeo_I} \qquad (21)$$

De verschillen in standaardprotoneringsenthalpie op (US)Y-zeolieten met variabele atomaire Si/Al_F-verhoudingen ten opzichte van de USY-zeoliet met atomaire Si/Al_F-verhouding 60 zijn geschat gebruik makend van de experimentele gegevens voor nonaan hydrokraken. Verschillen in fysisorptie worden in rekening gebracht via de gebruikte fysisorptieparameters. Uit de geschatte waarden blijkt dat de standaardprotoneringsenthalpie op de Y-zeoliet veel minder negatief is dan op de referentiezeoliet met atomaire Si/Al_F-verhouding 60, corresponderend met een uitgesproken lagere gemiddelde zuursterkte van de Y-zeoliet ten opzichte van de referentiezeoliet. De standaardprotoneringsenthalpie op de zeoliet met intermediaire graad aan dealuminatie, met atomaire Si/Al_F-verhouding 18, is iets sterker negatief dan die op de referentiezeoliet. De hogere sterkte van de zure centra op de USY-

zeoliet met intermediaire dealuminatiegraad is in overeenstemming met de eerder besproken trends, cfr. de 'vulkaan' curven.

5.4. Gecombineerd Effect van het Koolstofgetal en de Gemiddelde Zuursterkte

Een reeks experimenten met alkanen in het bereik van pentaan tot dodecaan werd eveneens uitgevoerd op de Pt/Y-zeoliet zodat het effect van het koolstofgetal en van de gemiddelde zuursterkte simultaan kon onderzocht worden. De relatieve activiteit van de alkanen op de Pt/Y-zeoliet was dezelfde als op de referentiezeoliet, maar de absolute activiteit was vele keren lager op de Pt/Y-zeoliet. Het verschil in standaardprotoneringsenthalpie voor de alkenen op Pt/Y met die voor octeen op de referentiezeoliet werd geschat. Een vergelijking van de aldus verkregen waarden met de waarden verkregen door het optellen van de waarden van beide afzonderlijke effecten laat toe de additiviteit van de effecten van het koolstofgetal en de gemiddelde zuursterkte te onderzoeken. Binnen statistische grenzen blijkt aan deze additiviteit voldaan te zijn. De hoge waarde voor de standaardprotoneringsenthalpie op de Pt/Y-zeoliet weerspiegelt hoe moeilijk koolwaterstofconversie gekatalyseerd door zuren doorgaat op deze katalysator. Andere, nevenreacties zoals hydrogenolyse gekatalyseerd door metallische centra kunnen dan belangrijk worden. In de experimenten behandeld in dit proefschrift was dit het meest uitgesproken voor pentaan, waar hydrogenolyse verantwoordelijk was voor ongeveer de helft van de totale pentaan conversie. De gemiddelde zuursterkte van de Pt/Y-zeoliet is te zwak voor de protonering van penteen.

6. Modellering van de Hydrogenering van Aromaten Gebaseerd op Enkelvoudige Gebeurtenissen

De methodologie gebaseerd op enkelvoudige stappen werd tot op heden vooral toegepast voor reactiestappen gekatalyseerd door zuren [6.1-6.7]. Een analoge methode voor reacties gekatalyseerd door metalen en hydrogenering in het bijzonder werd reeds ontwikkeld [6.8,6.9], maar niet als dusdanig toegepast.

6.1. (De)-Hydrogeneringscoëfficiënten Gebaseerd Op Enkelvoudige Gebeurtenissen

In tegenstelling tot de reacties gekatalyseerd door zuren bestaat in de literatuur geen overeenkomst voor het mechanisme van reacties gekatalyseerd door metalen. Voor de hydrogenering van aromaten bijvoorbeeld bestaan modellen met atomaire [6.11-6.15] en met

moleculaire [6.16,6.17] watersstofadditie. In sommige modellen wordt een snelheidsbepalende stap aangenomen [6.14-6.17], terwijl dat in andere modellen dan weer niet gedaan wordt [6.11-6.13]. Om die reden is het model gebaseerd op enkelvoudige gebeurtenissen voor hydrogenering gerelateerd met de globale (de)-hydrogeneringsreactie [6.9] en dus niet rechtstreeks met de elementaire oppervlakreactiestappen wat in wezen in tegenstrijd is met de filosofie die aan de basis ligt van het model gebaseerd op enkelvoudige gebeurtenissen, namelijk dat elementaire stappen beschouwd worden. De oppervlakreactiestappen worden wel, zij het impliciet, verondersteld snelheidsbepalend te zijn in het reactiemechanisme voor (de)-hydrogenering. Aangezien het globale mechanisme beschouwd wordt en dus ook geen specifieke structuur voor het geactiveerde complex wordt aangenomen, wordt de originele definitie van het aantal enkelvoudige gebeurtenissen, n_e, zijnde de verhouding van het globale symmetriegetal van het reactant tot dat van het geactiveerd complex, vervangen door de definitie van het aantal identische transformaties, n_s, zijnde de verhouding van de statistische factoren van het reactant en het product.

De snelheidscoëfficiënten voor dehydrogenering worden verondersteld enkel afhankelijk te zijn van de koolstofatomen aanwezig in de gevormde dubbele binding, namelijk primaire, secundaire of tertiaire koolstofatomen. Een grotere sterische hindering en een verhoogde stabiliteit van de gevormde dubbele binding met de substitutiegraad van de betrokken koolstofatomen vormen de basis voor deze aanname. Aldus worden zes op enkelvoudige gebeurtenissen gebaseerde snelheidscoëfficiënten voor dehydrogenering gedefinieerd: $\tilde{k}_{deh}(p;p)$, $\tilde{k}_{deh}(p;s)$, $\tilde{k}_{deh}(p;t)$, $\tilde{k}_{deh}(s;s)$, $\tilde{k}_{deh}(s;t)$ en $\tilde{k}_{deh}(t;t)$. Bij de dehydrogenering van alkenen tot dienen kunnen de pas gedefinieerde coëfficiënten gebruikt worden indien het om niet geconjugeerde dubbele bindingen gaat. Preferentieel worden echter geconjugeerde dubbele bindingen gevormd en omwille van niet verwaarloosbare effecten van deze conjugatie op de stabiliteit van het gevormde dieen, kan ook verwacht worden dat het effect op de stabiliteit van het geactiveerd complex en dus de activeringsenergie van deze conjugatie niet verwaarloosbaar is. Dit leidt tot zes additionele parameters: $\tilde{k}_{deh}(p;as)$, $\tilde{k}_{deh}(p;at)$, $\tilde{k}_{deh}(s;as)$, $\tilde{k}_{deh}(s;at)$, $\tilde{k}_{deh}(t;as)$, en $\tilde{k}_{deh}(t;at)$, waarbij *a* staat voor allyllisch. De dehydrogenering van cyclische dienen tot aromaten vereist nog drie extra parameters: $\tilde{k}_{deh}(as;as)$, $\tilde{k}_{deh}(as;at)$ en $\tilde{k}_{deh}(at;at)$. omdat in dit geval beide koolstofatomen in de te vormen dubbele bindingen zich in allyllische positie bevinden en omwille van de resonantie-energie gepaard met aromatenvorming.

De definitie van de snelheidscoëfficiënten voor hydrogenering hangt af van deze van de snelheidscoëfficiënten voor dehydrogenering via:

$$K_{(de)-hydrogenering} = \frac{k_{dehydrogenering}}{k_{hydrogenering}} \tag{22}$$

Aangezien de waarde van de evenwichtscoëfficiënt afhankelijk is van het reagens en product zal, indien de snelheidscoëfficiënt voor dehydrogenering onafhankelijk verondersteld wordt van het gevormde alkeen, de snelheidscoëfficiënt voor hydrogenering er zeker van afhangen. Daarom worden de op enkelvoudige gebeurtenissen gebaseerde hydrogeneringscoëfficiënten als volgt geschreven, $\tilde{k}_{hyd}\left(O_{i,j};m;n\right)$ waarbij $O_{i,j}$ het alkeen j voorstelt dat gehydrogeneerd wordt tot het corresponderend alkaan i.

Aldus bevat het model evenveel snelheidscoëfficiënten voor hydrogenering als onverzadigde componenten. Dit aantal kan echter gereduceerd worden aan de hand van bovenstaande evenwichtsbetrekking. Deze laat toe een verband te leggen tussen de op enkelvoudige gebeurtenissen gebaseerde snelheidscoëfficiënten voor hydrogenering en dehydrogenering:

$$\tilde{k}_{hyd}\left(O_{i,j};m;n\right) = \tilde{k}_{deh}\left(m;n\right)\frac{n_{s,deh_{i,j}}}{n_{s,hyd_{i,j}}}\frac{K_{P_i-M}}{K_{O_{i,j}-M}\,K_{deh}\left(P_i;O_{i,j}\right)} \tag{23}$$

Dit verband introduceert geen nieuwe parameters, het bevat enkel reeds aanwezige model parameters die kunnen berekend worden of die bepaald moeten worden door regressie. Gebruik makend van dit verband wordt het aantal op enkelvoudige gebeurtenissen gebaseerde snelheidscoëfficiënten gereduceerd van de som van vijftien en het aantal onverzadigde componenten tot enkel vijftien.

6.2. Gebruik van (De)-Hydrogeneringscoëfficiënten voor de Hydrogenering van Aromaten

Het gebruik van de op enkelvoudige gebeurtenissen gebaseerde snelheidscoëfficiënten zoals hierboven gedefinieerd stuit op enkele praktische en fundamentele bezwaren. Deze zijn een mogelijke verklaring waarom de modellering gebaseerd enkelvoudige gebeurtenissen totnogtoe niet als dusdanig is toegepast voor (de)-hydrogeneringsreacties. Ook in dit proefschrift wordt voor de kinetische modellering van de hydrogenering van tolueen geen beroep gedaan op snelheidscoëfficiënten gebaseerd op enkelvoudige gebeurtenissen.

De definitie van de op enkelvoudige gebeurtenissen gebaseerde snelheidscoëfficiënten voor (de)-hydrogenering impliceert dat de hydrogenering van een aromaat tot het corresponderend cycloalkaan verloopt via een 1,3-cyclodieen en een cycloalkeen intermediair.

Kwantumchemische berekeningen door Saeys over de hydrogenering van benzeen geven echter aan dat de additie van het tweede waterstofatoom aan de aromatische ring bij voorkeur in β-positie gebeurt van het koolstofatoom waaraan het eerste waterstofatoom is geaddeerd. De intermediairen bij de hydrogenering van aromaten corresponderen dus niet noodzakelijk met het 1,3-cyclodieen, noch met het 1,4-cyclodieen. Uit de resultaten van deze berekeningen volgt dat de definitie van een snelheidscoëfficiënt voor (de)-hydrogenering beter kan gerelateerd worden aan de additie van slechts één waterstofatoom in plaats van aan twee zoals in de huidige definitie. Het secundaire of tertiaire karakter van het betrokken koolstofatoom evenals het feit of het deel uitmaakt van één enkele of een geconjugeerde dubbele binding zijn mogelijke factoren om in rekening te brengen bij de definitie van de snelheidscoëfficiënten.
Het reactienetwerk dat correspondeert met de tot op heden gebruikte definitie van de op enkelvoudige gebeurtenissen gebaseerde snelheidscoëfficiënten voor (de)-hydrogenering bevat niet-onderscheidbare parallelle routes tussen het aromaat en het gehydrogeneerde product en leidt aldus tot volledig gecorreleerde parameters. Voor de hydrogenering van tolueen tot methylcyclohexaan in het werk van Verstraete [6.9] is de situatie zelfs zodanig dat slechts één onafhankelijke parameter overblijft om het hydrogeneringsgedrag te beschrijven. Een nauwgezette definitie van de op enkelvoudige gebeurtenissen gebaseerde snelheids-coëfficiënten voor (de)-hydrogenering en de selectie van geschikte modelcomponenten zijn vereist om tot betrouwbare op enkelvoudige gebeurtenissen gebaseerde snelheidscoëfficiënten voor (de)-hydrogenering te komen.

7. Gasfasehydrogeneringskinetiek van Tolueen op Pt/ZSM22

In de literatuur is reeds heel wat voorgaand onderzoek aanwezig naar de hydrogenering van aromaten [7.6-7.36]. Verschillende modelcomponenten en verschillende katalysatoren werden gebruikt. Een groot aantal kinetische modellen werd reeds voorgesteld voor de hydrogenering van aromaten. De belangrijkste verschilpunten in deze modellen zijn het al of niet aannemen van een snelheidsbepalende stap en de veronderstelling of de additie van waterstof aan de aromatische ring moleculair dan wel atomair gebeurt. Andere mogelijke verschilpunten zijn de al dan niet competitieve chemisorptie van waterstof en het aromaat en de eventuele aanwezigheid van een gedehydrogeneerd oppervlakspeciës.
Behalve uit de experimentele resultaten en eerder modelleringswerk werd voor de kinetische modellering in dit werk ook relevante informatie gehaald uit fysicochemische studies over de

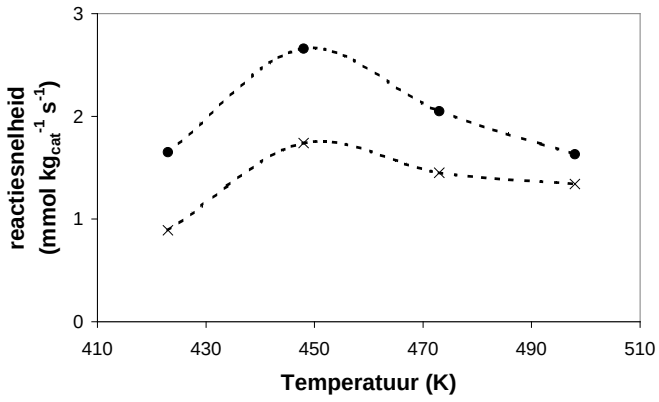

Figuur 11 **Reactiesnelheid als functie van de temperatuur ($p_{H2,0}$ = 100 kPa, W/F_0 = 82 kg s mol^{-1}), • : $p_{tol,0}$ = 10 kPa; × : $p_{tol,0}$ = 20 kPa**

interactie tussen aromatische componenten en de corresponderende gehydrogeneerde producten met metaaloppervlakken [7.39-7.47] of uit kwantumchemische berekeningen [7.48].

7.1. Effect van de Werkvoorwaarden op de Hydrogeneringssnelheid

Een maximum als functie van de temperatuur werd waargenomen voor de tolueen hydrogeneringssnelheid, zie Figuur 11. Een dergelijk maximum werd reeds eerder waargenomen voor tolueen en eveneens voor andere aromaten op typische hydrogeneringsmetalen zoals platina, palladium, nikkel,… [7.16,7.19,7.22-7.24,7.30,7.31, 7.34] Algemeen wordt aangenomen dat oppervlakconcentratie-effecten aan de basis liggen van dit effect. Vanaf een bepaalde temperatuur wordt de toename van de snelheidscoëfficiënt overgecompenseerd door de afname van de oppervlakconcentratie van de reagerende speciës. Massatransportlimitaties kunnen als oorzaak uitgesloten worden omdat het intrinsieke karakter van de experimenten geverifieerd werd. Nog andere oorzaken zoals chemisch evenwicht, katalysatorvergiftiging of sintering kunnen uitgesloten worden.

Een verhoging van de waterstofinlaatpartieeldruk terwijl alle andere werkvoorwaarden worden vastgehouden, leidt tot een verhoging van de reactiesnelheid bij alle temperaturen. Een verhoging van de tolueen inlaatpartieeldruk terwijl alle andere werkvoorwaarden worden vastgehouden leidt dan weer tot een daling van de hydrogeneringssnelheid bij alle temperaturen. De partiële reactieordes, bepaald door een regressie van alle beschikbare data zijn dan ook positief voor waterstof en negatief voor tolueen. Voor de partiële reactieorde in waterstof wordt bovendien een stijgende trend met de temperatuur waargenomen, hetgeen in overeenstemming is met waarnemingen uit de literatuur. De lagere hydrogeneringssnelheden

bij hogere inlaatpartieeldrukken voor tolueen en de bijhorende negatieve partiële reactieorde voor tolueen kan verklaard worden als de toename van de tolueen concentratie op het oppervlak leidt tot en overgecompenseerd wordt door een afname van de waterstofconcentratie op het oppervlak. Impliciet wordt hier dus verondersteld dat de chemisorptie tussen het aromaat en waterstof competitief verloopt en dat de oppervlakreactie snelheidsbepalend is. Zowel competitieve als niet-competitieve chemisorptie worden in de literatuur vermeld. Het al dan niet waarnemen van competitieve chemisorptie lijkt af te hangen van de werkvoorwaarden. Bij temperaturen lager dan deze onderzocht in dit werk is het metaaloppervlak quasi volledig verzadigd aan aromaatmoleculen. Tussen de gechemisorbeerde aromaatmoleculen is echter een quasi constant aantal centra beschikbaar voor de chemisorptie van waterstof. Als bij hogere temperaturen het oppervlak niet meer verzadigd is aan aromaatmoleculen neemt de waterstofchemisorptiecapaciteit gevoelig toe, hetgeen het competitieve karakter van de waterstof- en aromaatchemisorptie waargenomen in dit werk verklaart. Bij nog hogere temperaturen zijn de oppervlakconcentraties zodanig laag dat opnieuw geen competitie meer wordt waargenomen.

7.2. Modelveronderstellingen en Snelheidsvergelijking

In een kinetische modellering gebaseerd op stationaire toestand gegevens zonder in situ karakterisatie van het katalysatoroppervlak is er geen directe informatie over de oppervlakintermediairen beschikbaar. Dit heeft geleid tot een variëteit aan kinetische modellen zoals eerder beschreven. In dit proefschrift wordt de kinetische modelbouw en -discriminatie mede gebaseerd op inzicht verworven via kwantumchemische berekeningen en onafhankelijke oppervlakstudies. Deze laatste worden doorgaans op uitgevoerd op een specifiek kristaloppervlak, zoals Pt(111).

In vele modellen voor de hydrogenering van aromaten wordt de additie van het eerste waterstofatoom als snelheidsbepalend verondersteld. Naar analogie met homogene gasfase-hydrogenatie wordt het verbreken van de resonantiestabilisatie van de ring als snelheidsbepalend verondersteld. Er zijn echter twee belangrijke argumenten om te veronderstellen dat het snelheidsbepalende karakter van de resonantiestabilisatie op de hydrogenering verdwijnt bij chemisorptie van het aromaat op een hydrogeneringsmetaal zoals platina. Ten eerste liggen de kwantumchemisch bepaalde activeringsenergieën voor de additie van het eerste en van het tweede waterstofatoom zo dicht bij elkaar, respectievelijk 75 en 73 kJ mol^{-1}, dat de snelheidscoëfficiënten voor de additie van het eerste en van het tweede

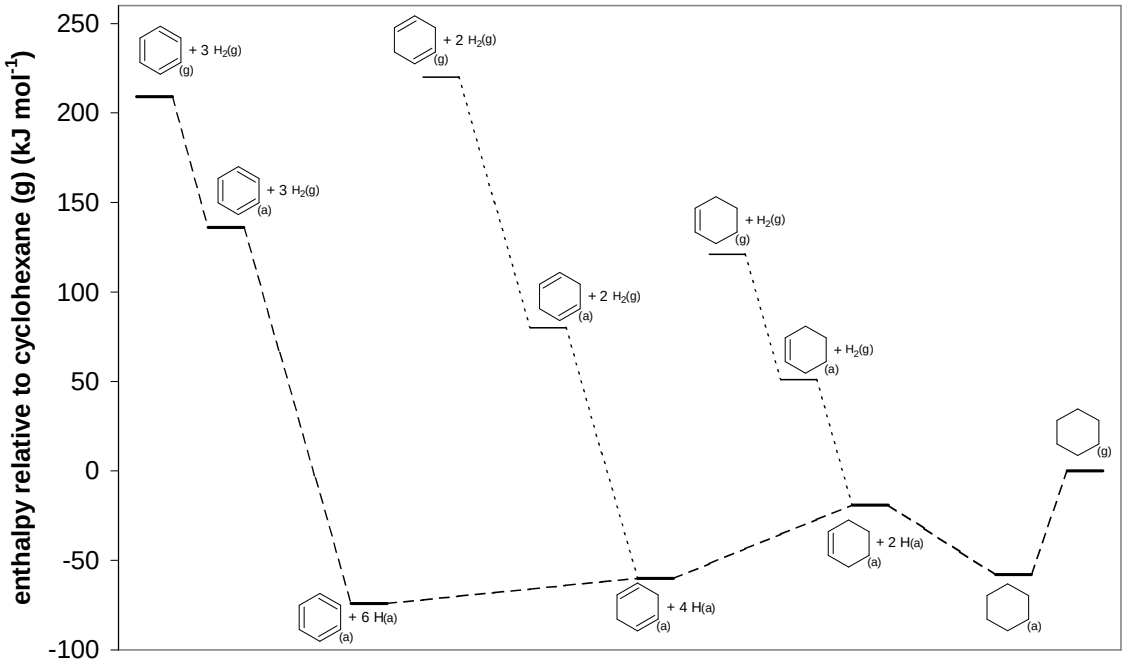

Figuur 12 Enthalpieniveaus voor de componenten betrokken bij benzeenhydrogenering

waterstofatoom niet significant van elkaar verschillen. Indien de additie van het eerste waterstofatoom de resonantiestabilisatie zou breken, dan wordt een significant hogere activeringsenergie voor de additie van het eerste waterstofatoom verwacht dan voor de additie van het tweede waterstofatoom. Het tweede argument wordt gehaald uit een thermodynamische analyse van de reactiepaden voor hydrogenering van benzeen in de gasfase en op een Pt(111)-oppervlak, zie Figuur 12. In de gasfase bevindt cyclohexadieen samen met 2 waterstofmoleculen zich op het hoogste enthalpieniveau van de hydrogeneringssequentie. Door de exothermiciteit van hydrogeneringsreacties liggen de enthalpieniveaus van cyclohexeen samen met 1 waterstofmolecule en van cyclohexaan veel lager dan dat van cyclohexadieen samen met 2 waterstofmoleculen. Vanwege de resonantiestabilisatie ligt het enthalpieniveau van benzeen samen met 3 waterstofmoleculen niet significant hoger, maar zelfs iets lager dan dat van cyclohexadieen samen met 2 waterstofmoleculen. Hieruit volgt de conclusie dat het verbreken van deze resonantiestabilisatie de snelheidsbepalende stap is in de gasfasehydrogeneringssequentie. Door verschillen in chemisorptieenthalpieën van de verschillende koolwaterstoffen is dit beeld echter niet meer geldig op een platina oppervlak. Cyclohexadieen chemisorbeert heel sterk, veel sterker dan benzeen, zodat het effect van de resonantiestabilisatie zoals het optreedt tussen benzeen en cyclohexadieen in de gasfase niet langer optreedt tussen deze beide componenten op een platina oppervlak Bovendien chemisorbeert cyclohexeen relatief zwak,

hetgeen resulteert in het hoogste enthalpieniveau voor cyclohexeen samen met 2 gechemisorbeerde waterstofatomen in de hydrogenerings-sequentie op een platina oppervlak. Gebruik makend van een Evans-Polanyi relatie voor de activeringsenergieën voor de verschillende stappen in deze hydrogeneringssequentie wordt een eventuele snelheidsbepalende stap gesitueerd bij de derde of de vierde waterstofadditie, eerder dan bij de eerste of de tweede. Andere voorgestelde reactiemechanismen nemen geen snelheidsbepalende stap aan, maar beschouwen twee of meer waterstofadditiestappen als niet in quasi-evenwicht. De enthalpieniveaus in de hydrogeneringssequentie op het platina oppervlak zijn in overeenstemming met een dergelijk mechanisme waarbij de eerste vier waterstofadditiestappen niet in quasi-evenwicht zijn. De exothermiciteit van de hydrogenering van cyclohexeen tot cyclohexaan op het katalysatoroppervlak leidt dan weer tot de veronderstelling dat deze stappen wel potentieel sneller en dus bij quasi-evenwicht zijn.

De vorming van gedehydrogeneerde speciës op het katalysatoroppervlak is een ander punt waarover in verschillende modellen andere veronderstellingen gemaakt worden. Recent werden deze speciës in evenwicht verondersteld met het aromatisch reactant door Vannice. Bovendien werd verondersteld dat de concentratie van één van deze gedehydrogeneerde speciës op het oppervlak groot was ten opzichte van de concentraties van de andere speciës op het oppervlak, zowel van de gedehydrogeneerde als van het aromatisch reactant en de partieel gehydrogeneerde intermediairen. Uit parameterschattingen bleek het dominante speciës dit te zijn corresponderend met het aromatisch reactant waarvan één of twee waterstofmoleculen van afgesplitst zijn. In een thermochemische studie van de hydrogenering van benzeen berekenden Koel et al. de energieniveaus van onder meer de speciës betrokken in een dergelijke dehydrogenering. Onzekerheden over de aard van deze speciës hebben ertoe geleid dat voor de gedehydrogeneerde speciës twee energieniveaus werden voorgesteld. Terwijl het stabielste niveau nauwelijks stabieler is dan dat van benzeen, ligt het minst stabiele meer dan 100 kJ mol^{-1} hoger dan dat van benzeen. Indien quasi-evenwicht heerst tussen deze speciës en benzeen, lijkt het dus onwaarschijnlijk dat de concentraties van de gedehydrogeneerde speciës significant groter zouden zijn dan die van benzeen. De resultaten van kwantumchemische berekeningen door Saeys zijn het meest in overeenstemming met de minst stabiele niveaus uit bovenstaande thermochemische studie. De endothermiciteit van gechemisorbeerd benzeen tot gechemisorbeerd fenyl wordt tussen 76 en 102 kJ mol^{-1} berekend, terwijl die van gechemisorbeerd benzeen tot gechemisorbeerd benzyn tussen 13 en 66 kJ mol^{-1} berekend wordt. Uit deze waarden blijkt dat voor de dehydrogenering van benzeen op het katalysatoroppervlak een activeringsenergie verwacht kan worden die minstens even groot is

als de activeringsenergie voor hydrogenering. Bovenstaande argumenten hebben ertoe geleid de vorming van gedehydrogeneerde speciës niet in de kinetische modellering op te nemen.

Zoals eerder uitgelegd, werden de experimentele resultaten geïnterpreteerd steunend op competitieve chemisorptie tussen waterstof en het aromaat. Net zoals in de andere kinetische modellen in de literatuur worden de chemisorptiestappen in quasi-evenwicht verondersteld. De desorptie van methylcyclohexaan wordt potentieel snel en irreversibel verondersteld, zodat de methylcyclohexaanconcentratie op het oppervlak steeds verwaarloosbaar is.

Steunend op de hierboven uitgelegde modelveronderstellingen, kan volgend reactieschema voorgesteld worden:

$$H_2(g)+2* \rightleftharpoons 2H* \qquad K_{chem,H_2} \qquad (24)$$

$$A(g)+* \rightleftharpoons A* \qquad K_{chem,A} \qquad (25)$$

$$A*+H* \overset{k_1}{\rightleftharpoons} AH*+* \qquad K_1 \qquad (26)$$

$$AH*+H* \overset{k_2}{\rightleftharpoons} AH_2*+* \qquad K_2 \qquad (27)$$

$$AH_2*+H* \overset{k_3}{\rightleftharpoons} AH_3*+* \qquad K_3 \qquad (28)$$

$$AH_3*+H* \overset{k_4}{\longrightarrow} AH_4*+* \qquad K_4 \qquad (29)$$

$$AH_4*+H* \rightleftharpoons AH_5*+* \qquad K_5 \qquad (30)$$

$$AH_5*+H* \rightleftharpoons AH_6*+* \qquad K_6 \qquad (31)$$

$$AH_6* \longrightarrow AH_6(g)+* \qquad (32)$$

Voor eindige waarden van K_5 en K_6 leidt de veronderstelling van potentieel snelle en irreversibele methylcyclohexaandesorptie tot een verschuiving van het quasi-evenwicht naar rechts zodat ook de concentraties op het oppervlak van de partieel gehydrogeneerde speciës waaraan 4 of 5 waterstofatomen toegevoegd zijn, verwaarloosbaar zijn. De netto-vormingssnelheid van gasfasemethylcyclohexaan kan dan als volgt geschreven worden:

$$R_{AH_6(g)} = C_t k_4 \theta_{AH_3*} \theta_{H*} \qquad (33)$$

Toepassing van de hypothese van de quasi-stationaire toestand voor de partieel gehydrogeneerde speciës waaraan 1, 2 of 3 waterstofatomen toegevoegd zijn leidt tot de volgende massabalansen voor de speciës met 1 of 2 waterstofatomen toegevoegd:

$$0 = k_i \, \theta_{AH_{i\ 1}*} \, \theta_{H*} + \frac{k_{i+1}}{K_{i+1}} \theta_{AH_{i+1}*} \, \theta_* - k_{i+1} \, \theta_{AH_i*} \, \theta_{H*} - \frac{k_i}{K_i} \theta_{AH_i*} \, \theta_* \qquad i = 1,2 \qquad (34)$$

en voor de speciës met 3 waterstofatomen toegevoegd:

$$0 = k_3 \, \theta_{AH_2*} \, \theta_{H*} - k_4 \, \theta_{AH_3*} \, \theta_{H*} - \frac{k_3}{K_3} \theta_{AH_3*} \, \theta_* \qquad (35)$$

Uitdrukkingen voor de chemisorptie-evenwichten voor waterstof en tolueen en voor een balans over de actieve centra vervolledigen het stelsel van algebraïsche vergelijkingen die de hydrogeneringskinetiek uitdrukken als functie van waarneembare grootheden zijnde de partieeldrukken van waterstof en tolueen.

7.3. Modelleringsresultaten

In het kinetisch model voor de hydrogenering van tolueen zoals het tot hiertoe werd ontwikkeld, treden negen verschillende coëfficiënten op: vier voorwaartse snelheidscoëfficiënten, drie oppervlakreactie-evenwichtscoëfficiënten en twee chemisorptiecoëfficiënten. Om de hydrogenering van tolueen onder niet-isotherme omstandigheden te beschrijven zijn dus achttien parameters vereist, hetgeen een te groot aantal is om te schatten gebaseerd op slechts één onafhankelijke respons. Daarom werden de preëxponentiële factoren van de verschillende coëfficiënten berekend gebaseerd op transitietoestandstheorie. Eén waarde werd gebruikt voor de preëxponentiële factoren van de vier snelheidscoëfficiënten Ook voor de preëxponentiële factoren van de drie oppervlakreactie-evenwichtscoëfficiënten wordt slechts één waarde berekend. Afhankelijk van de veronderstellingen in verband met de mobiliteit van de betrokken speciës worden voor de preëxponentiëlen het volgende bereik van waarden gevonden: van 10^{-10} Pa^{-1} tot 10^{-13} Pa^{-1} en van 10^{-8} Pa^{-1} tot 10^{-13} Pa^{-1} voor de preëxponentiële factoren van de tolueen respectievelijk de waterstofchemisorptiecoëfficiënt. De preëxponentiële factoren van de snelheidscoëfficiënten en van de oppervlakreactie-evenwichtscoëfficiënten hebben als bereik respectievelijk 10^8 s^{-1} tot 10^{13} s^{-1} en van 10^{-5} tot 1, hoewel het bereik van de preëxponentiële factor van de snelheidscoëfficiënt hoger dan 10^{13} s^{-1} kan zijn indien de mobiliteit van het geactiveerd complex hoger is dan van de reagentia.

Het aantal overblijvende, te schatten parameters, namelijk negen, blijft aan de hoge kant om via regressie te bepalen. De veronderstelde gelijkaardigheid tussen de verschillende additiestappen die geleid heeft tot het gelijkstellen van de bijhorende preëxponentiële factoren kan opnieuw ingeroepen worden om zowel de activeringsenergieën als de oppervlakreactie-enthalpieën aan elkaar gelijk te stellen. Op die manier wordt een model met gelijke

snelheidscoëfficiënten verkregen voor de eerste vier additiestappen samen met quasi-evenwicht voor de vijfde en de zesde waterstofadditiestap. Een andere mogelijkheid om het aantal parameters te reduceren is de aanname van één snelheidsbepalende stap. Op basis van de verschillen in enthalpieniveaus kan een eventuele snelheidsbepalende stap verwacht worden ter hoogte van de derde of de vierde waterstofadditiestap. In wat volgt worden parameters geschat voor de verschillende voorgestelde mogelijkheden en worden de resultaten ten opzichte van elkaar afgewogen.

Verdere uitwerking van de snelheidsvergelijking voor het model met gelijke snelheidscoëfficiënten leidt tot de volgende uitdrukking voor de hydrogeneringssnelheid van tolueen:

$$R_{AH_6(g)} = \frac{C_t k_{surf}}{\left(B^3+B^2+B+1\right)} \frac{B^3 K_{chem,A} p_A \sqrt{K_{chem,H_2} p_{H_2}}}{\left(1+\sqrt{K_{chem,H_2} p_{H_2}} + K_{chem,A} p_A \frac{\left(4B^3+3B^2+2B+1\right)}{\left(B^3+B^2+B+1\right)}\right)^2} \tag{36}$$

waarin B staat voor:

$$B = K_{surf} \sqrt{K_{chem,H_2} p_{H_2}} \tag{37}$$

Uit initiële parameterschattingen bleek dat de temperatuursafhankelijkheid van de factor B gering is en dus niet significant kon geschat worden. Verdere parameterschattingen voor het model met gelijke snelheidscoëfficiënten werden uitgevoerd gebruik makend van bovenstaand verband. Verschillende combinaties van waarden voor de preëxponentiële factoren werden uitgetest. De combinatie die aanleiding gaf tot de beste resultaten was deze corresponderend met een lage mobiliteit voor de koolwaterstoffen op het oppervlak, een hogere mobiliteit voor de oppervlak waterstofatomen en een hogere mobiliteit van het koolwaterstof in de transitietoestand dan de koolwaterstof intermediairen. Dit laatste kan in verband worden gebracht met een in de transitietoestand bewaard gebleven translationele vrijheidsgraad van het waterstofatoom dat geaddeerd wordt. De corresponderende waarden voor de preëxponentiële factoren zijn vermeld in Tabel 5. De geschatte parameterwaarden en bijhorende betrouwbaarheidsintervallen zijn vermeld in Tabel 6. Het betrouwbaarheids-interval van de waterstofchemisorptieënthalpie is groter dan dat van de tolueenchemisorptie-enthalpie. Dit is een gevolg van de relatieve concentraties van beide componenten op het katalysatoroppervlak. Het model is gevoeliger aan de adsorptietermen van componenten met een hoge oppervlakconcentratie dan aan de adsorptietermen van componenten met een lage oppervlakconcentratie. De waarde van de chemisorptie-enthalpie van tolueen, -70 kJ mol^{-1}, is

Tabel 5 **Waarden voor de preëxponentiële factoren berekend gebaseerd op transitietoestandstheorie**

k^0_{surf} (s^{-1})	K^0_{surf}	$K^0_{chem,A}$ (Pa^{-1})	K^0_{chem,H_2} (Pa^{-1})
10^{15}	10^{-2}	10^{-12}	10^{-10}

Tabel 6 **Parameterschattingen en bijhorende betrouwbaarheidsintervallen verkregen via regressie van de drie gerbuikte kinetische modellen**

	$E^{comp}_{A,surf}$ (kJ mol^{-1})	$\Delta H^0_{chem,H_2}$ (kJ mol^{-1})	$\Delta H^0_{chem,A}$ (kJ mol^{-1})
model met gelijke oppervlaksnelheidscoëfficiënten	-53[a] (± 5)	-42 (± 12)	-70 (± 2)
model met de additie van het derde H-atoom als snelheidsbepalende stap	-51[b] (± 1)	N.S.[d]	-68 (± 1)
model met de additie van het vierde H-atoom als snelheidsbepalende stap	-59[c] (± 7)	-42 (± 12)	-70 (± 2)

[a] $E^{comp}_{A,surf} = E_{A,surf} + \Delta H^0_{chem,A} + 0.5\,\Delta H^0_{chem,H_2}$, [b] $E^{comp}_{A,surf} = E_A + \Delta H^0_{chem,A} + 1.5\,\Delta H^0_{chem,H_2} + \Delta H^0_1 + \Delta H^0_2$, [c] $E^{comp}_{A,surf} = E_A + \Delta H^0_{chem,A} + 2\,\Delta H^0_{chem,H_2} + \Delta H^0_1 + \Delta H^0_2 + \Delta H^0_3$, [d] Niet Significant

iets minder negatief dan de kwantumchemisch berekende waarde voor de chemisorptie-enthalpie van benzeen, hetgeen een verklaring kan zijn voor de in de literatuur vermelde lagere hydrogeneringssnelheid van tolueen ten opzichte van benzeen [7.19,7.23]. De chemisorptie-enthalpie van waterstof wordt minder negatief geschat dan kwantumchemisch berekend, -42 kJ mol^{-1} ten opzichte van –70 kJ mol^{-1}. Het corresponderende betrouwbaarheidsinterval is echter relatief ruim en doorsnijdt het bereik van in de literatuur vermelde waarden voor de waterstofchemisorptieënthalpie [7.56]. Van de waarde voor de samengestelde activeringsenergie wordt een waarde van 38 kJ mol^{-1} voor de werkelijke activeringsenergie verkregen. Deze is lager dan de kwantumchemisch berekende waarden, maar dit wordt mede veroorzaakt door de relatief beperkte geschatte exothermiciteit van de waterstofchemisorptie. Een pariteitsdiagramma is voorgesteld in Figuur 13.

De verdere uitwerking van de modelvergelijkingen indien de derde of de vierde waterstof additiestap als snelheidsbepalend wordt verondersteld leidt tot volgende uitdrukking voor de hydrogeneringssnelheid:

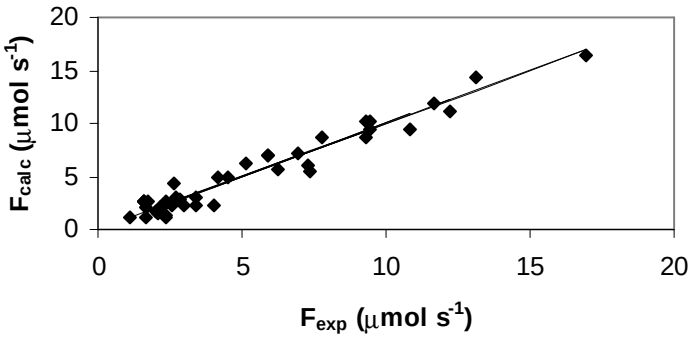

Figuur 13 **Pariteitsdiagramma voor het methylcyclohexaanuitlaatdebiet; lijn: experimenteel, symbolen: berekend gebruik makend van het model met gelijke snelheidscoëfficiënten, Verg. 36 met de preëxponentiële factoren uit Tabel 5 en de samengestelde activeringsenergie en chemisorptie-enthalpieën uit Tabel 6**

$$R_{AH_6(g)} = \frac{C_t k_i \left(\prod_{j=1}^{i} K_j \right) K_{chem,A} \, K_{chem,H_2}^{i/2} \, p_A \, p_{H_2}^{i/2}}{\left(1 + K_{chem,A} \, p_A + \sqrt{K_{chem,H_2} \, p_{H_2}}\right)^2} \tag{38}$$

waarbij *i* het nummer van de snelheidsbepalend veronderstelde waterstofadditiestap is, namelijk 3 of 4. Voor *i=3* kon de waterstofchemisorptie-enthalpie niet significant geschat worden. Voor de chemisorptie-enthalpie van tolueen wordt in beide gevallen een gelijkaardige waarde gevonden als in het model met gelijke snelheidscoëfficiënten. Voor *i=4* wordt voor de waterstofchemisorptieënthalpie dezelfde waarde gevonden als in het model met gelijke snelheidscoëfficiënten. Waarden voor de werkelijke activeringsenergie verkregen uit de geschatte waarden voor de samengestelde activeringsenergie en liggen in het bereik 80 tot 109 kJ mol^{-1} voor *i=3* en in het bereik 35 tot 65 kJ mol^{-1} voor *i=4*.

Van de drie geteste modellen hebben het model met gelijke snelheidscoëfficiënten en het model met de vierde additie als de snelheidsbepalende stap de hoogste *F*-waarde voor de significantie van de regressie, namelijk 10^4. De vergelijkbare waarden verkregen voor de parameters in beide modellen zijn met name het gevolg van het feit dat het model met de vierde waterstofadditie als snelheidsbepalende stap een limietgeval is van het meer algemene model met gelijke snelheidscoëfficiënten. Indien de concentraties van de oppervlak-intermediairen sterk van elkaar verschillen, dan kan in het model met gelijke snelheidscoëfficiënten de stap waarin het intermediair met de laagste concentratie verbruikt wordt, inderdaad snelheidsbepalend worden. Indien dit het geval is voor het intermediair

waaraan reeds drie waterstofatomen geaddeerd zijn, dan wordt het model met gelijke snelheidscoëfficiënten mathematisch gelijk aan het model met de vierde waterstofadditie als snelheidsbepalende stap. Omwille van het meer algemene karakter van het model met gelijke snelheidscoëfficiënten, wordt dit model verkozen boven dat waarin de vierde waterstofadditie snelheidsbepalend verondersteld wordt.

8. Vloeistoffasehydrogeneringskinetiek van Tolueen op Pt/ZSM22

Ondanks het feit dat raffinageprocessen zoals hydrokraken typisch onder driefaseomstandigheden uitgevoerd worden [8.1,8.2], wordt in laboratoriumonderzoek aan dergelijke processen vaak in de gasfase gewerkt. Werken onder gasfasecondities maakt de kinetiek van het proces toegankelijker omdat gas-vloeistof aspecten niet hoeven beschreven te worden. Anderzijds, moet de bruikbaarheid onder driefasecondities van een kinetisch model ontwikkeld gebaseerd op gasfase-experimenten uiteraard geverifieerd worden. Naast het aspect van verificatie, gaat dit deel van dit proefschrift ook dieper in op de methodologie toegepast bij de beschrijving van vloeistoffasekinetiek.

8.1. Experimentele Resultaten

Zowel de temperatuur als de totaaldruk hebben een positief effect op de hydrogeneringssnelheid. Toch werd bij de gasfase-experimenten een maximum in de hydrogeneringssnelheid als functie van de temperatuur waargenomen. Dit maximum werd veroorzaakt door een significante daling van de concentratie van tolueen op het metaaloppervlak vanaf 448 K. Een dergelijk maximum wordt onder driefasecondities slechts verwacht bij hogere temperaturen vanwege de hogere tolueen concentraties aan de vloeistof–katalysatorfasegrens onder driefasecondities dan onder gasfasecondities. Daarnaast kan ook een licht toegenomen waterstofoplosbaarheid bij hogere temperaturen bijdragen tot het achterwege blijven van een maximum in hydrogeneringssnelheid als functie van de temperatuur. Het effect van de totaaldruk is het gevolg van een grotere oplosbaarheid van waterstof bij hogere totaaldrukken. Aangezien de hydrogeneringssnelheid een positieve partiële reactieorde in waterstof vertoont, verhoogt met de waterstofconcentratie in de vloeistoffase ook de hydrogeneringssnelheid.

8.2. Thermodynamische Niet-Idealiteit

Thermodynamische niet-idealiteit in een binair mengsel met moleculen van type A en van type B wordt veroorzaakt door verschillen in interacties tussen moleculen van hetzelfde type en moleculen van een verschillend type [8.5]. Indien moleculen van type A en B van dezelfde aard zijn en niet te sterk verschillen wat betreft molair volume, kan verwacht worden dat A-B interacties sterk gelijken op A-A en B-B interacties en dat een dergelijk binair mengsel zich ideaal gedraagt. Wanneer de vloeistoffasekinetiek van een mengsel van alifatische koolwaterstoffen met een beperkt koolstofgetalbereik beschreven wordt, kan het mengsel als een ideale vloeistof beschreven worden. Voor een uitgebreider koolstofgetalbereik zoals onder industriële omstandigheden, kunnen afwijkingen van ideaal vloeistofgedrag verwacht worden, zeker indien het voedingsmengsel aromatische componenten bevat.

De niet-idealiteit van een thermodynamisch systeem wordt steeds uitgedrukt ten opzichte van een, vrij te kiezen, standaardtoestand. De berekening van een chemische potentiaal via:

$$\mu_i = \mu_i^{standaard} + RT \ln a_i \tag{39}$$

is immers onafhankelijk van de gebruikte standaardtoestand. De selectie van een standaardtoestand bepaalt immers enkel de interpretatie, en dus ook de waarde, van de veralgemeende activiteit a_i in Verg. (39). Drie veel voorkomende standaardtoestanden zijn [8.5]:

(1) De ideale gastoestand bij 1 bar, in het geval van niet-ideale gassen.

(2) In het geval van een vloeibaar mengsel dat vergelijkbare hoeveelheden van de verschillende componenten in het mengsel bevat of voor het solvent in een oplossing: de zuivere component in de vloeistoffase.

(3) In het geval van een stof opgelost A in een vloeistof B: de hypothetische toestand van zuivere vloeibaar A waarin A-A interacties zich gedragen als A-B interacties.

De bovenvermelde standaardtoestanden en de situatie waarin ze gebruikt worden, zijn echter niet onlosmakelijk met elkaar verbonden. Zo kan het bijvoorbeeld bepaalde voordelen opleveren, cfr. infra, om een vloeistof te beschrijven als afwijkend ten opzichte van een ideaal gas bij 1 bar. De enige voorwaarde waaraan daartoe moet voldaan zijn, is de beschikbaarheid van een accurate berekeningsmethode voor de corresponderende veralgemeende activiteit, in dit geval een fugaciteit. Voor een systeem dat waterstof en koolwaterstoffen bevat, voldoet een kubische toestandsvergelijking zoals die van Peng-Robinson aan de gestelde voorwaarde. Bij de berekening van het gas-vloeistofevenwicht in een dergelijk systeem wordt de gelijkheid van de chemische potentialen als voorwaarde voor chemisch evenwicht gereduceerd tot de

gelijkheid van de fugaciteiten van de verschillende componenten in de gas- en de vloeistoffase. Voor de beschrijving van de chemisorptiestappen in de vloeistoffasekinetiek levert het werken met de idealegastoestand bij 1 bar als standaardtoestand het voordeel op van een eenvoudige vergelijking met de resultaten voor de chemisorptiestappen in de gasfasekinetiek waarin dezelfde standaardtoestand gebruikt werd.

De reagentia op het katalysatoroppervlak bevinden zich in een gechemisorbeerde toestand waarin interacties met de katalysator veel sterker zijn dan met niet-gechemisorbeerde fluïdum moleculen. Volgens Madon en Iglesia [8.15] kunnen als gevolg hiervan de interacties tussen de gechemisorbeerde reactanten en niet gechemisorbeerde fluïdummoleculen verwaarloosd worden. Singh en Vannice [8.16] verwaarlozen dergelijke interacties niet, maar veronderstellen daarentegen dat de interacties tussen gechemisorbeerde reagentia en fluïdummoleculen de som zijn van de interacties tussen niet gechemisorbeerde reagentia en fluïdummoleculen enerzijds en van de interacties tussen een vrij actief centrum en fluïdummoleculen anderzijds. Gezien de significante veranderingen in de omgeving van zowel reactant moleculen als vrije centra door fluïdummoleculen bij chemisorptie lijkt deze laatste veronderstelling vrij onwaarschijnlijk. Daarom wordt in eerste instantie gewerkt met de veronderstelling dat de interacties tussen gechemisorbeerde reagentia en niet gechemisorbeerde fluïdum moleculen verwaarloosbaar zijn. De gechemisorbeerde reagentia en vrije actieve centra worden beschouwd als een ideale vloeistof en dus kunnen oppervlakfracties gebruikt worden als maat voor de activiteit van de gechemisorbeerde reagentia en de vrije centra.

8.3. Vloeistoffase Kinetisch Model

Voor de chemisorptiestappen bij kinetische modelbouw in de gasfase werd impliciet aangenomen dat gasfase als ideaal kon beschouwd worden. Om het model uit te breiden zodat het ook toepasbaar is voor vloeistoffasekinetiek, moet de niet-idealiteit van de vloeistoffase ten opzichte van de idealegastoestand bij 1 bar in rekening gebracht worden bij de beschrijving van de chemisorptiestappen. Aangezien de interacties tussen gechemisorbeerde reagentia en niet-gechemisorbeerde fluïdummoleculen verwaarloosd werden [8.14,8.15] is de beschrijving van de kinetiek op het katalysatoroppervlak onafhankelijk van de aggregatietoestand van de niet-gechemisorbeerde reagentia. Het verschil in de beschrijving van de kinetiek in de gas- of de vloeistoffase bevindt zich aldus exclusief in de chemisorptiestappen.

Voor een chemisorptiestap zoals in Verg. (25) geldt volgende evenwichtsrelatie:

$$K_A^f = \frac{\theta_{A*}}{f_A^F \theta_*} \tag{40}$$

waarbij de bovenindex F staat voor de aggregatietoestand van de chemisorberende component.

$$1 = \theta_* + \theta_{A*} \tag{41}$$

Gebruik makend van deze balans kan de fractie aan vrije centra uit Verg. (40) geëlimineerd worden, hetgeen leidt tot volgende uitdrukking:

$$\theta_{A*} = \frac{K_A^f f_A^F}{\left(1 + K_A^f f_A^F\right)} \tag{42}$$

Voor chemisorptie vanuit de ideale gasfase herleidt Verg. (42) zich dan tot:

$$\theta_{A*} = \frac{K_A^f p_A}{\left(1 + K_A^f p_A\right)} \tag{43}$$

corresponderend met de eerder gebruikte uitdrukking in de beschrijving van de gasfase kinetiek. Om bij chemisorptie vanuit de vloeistoffase de vloeistoffaseconcentratie van de chemisorberende reagentia in de chemisorptieuitdrukking te brengen wordt volgend verband tussen de fugaciteit en de vloeistoffaseconcentratie gebruikt:

$$f_A^L = \Phi_A^L p_t V_m^L C_A^L \tag{44}$$

Zodat Verg. (42) voor het chemisorptie-evenwicht herleid wordt tot:

$$\theta_{A*} = \frac{K_A^f \Phi_A^L p_t V_m^L C_A^L}{\left(1 + K_A^f \Phi_A^L p_t V_m^L C_A^L\right)} \tag{45}$$

Indien dus concentraties gebruikt worden bij de beschrijving van de chemisorptie vanuit de vloeibare fase, bestaat de globale chemisorptiecoëfficiënt uit twee bijdragen: een bijdrage, K_A^f, corresponderend met de chemisorptiecoëffciënt gebaseerd op fugaciteiten enerzijds en een bijdrage, $\Phi_A^L p_t V_m^L$, rekening houdend met de afwijking van de vloeistof van de standaardtoestand, namelijk de ideale gas toestand bij 1 bar [8.3,8.4].

8.4. Modelsimulaties en Regressie

Bij de beschrijving van de vloeistoffasekinetiek van de tolueenhydrogenering werd gebruik gemaakt van bovenstaande methodologie. De gebruikte snelheidsvergelijking was deze met gelijke snelheidscoëfficiënten voor de oppervlakreactiestappen, afgeleid gebaseerd op de kinetische modelbouw voor de tolueenhydrogenering in de gasfase. Aanpassing van de chemisorptiecoëfficiënten aan de vloeistoffaseomstandigheden leidt tot de volgende uitdrukking voor de reactiesnelheid van de tolueenhydrogenering in de vloeistoffase:

Tabel 7 **Parameterwaarden en bijhorende betrouwbaarheidsintervallen voor het model met gelijke snelheidscoëfficiënten gebruikt bij de kinetische modellering van de tolueen hydrogenering in de vloeistoffase**

$E^{comp}_{A,surf}$ (kJ mol^{-1})	$\Delta H^{0}_{chem,H_2}$ (kJ mol^{-1})	$\Delta H^{0}_{chem,A}$ (kJ mol^{-1})
-40[a] ± 8	-40 ± 21	-72 ± 4

[a] $E^{comp}_{A,surf} = E_{A,surf} + \Delta H^{0}_{chem,A} + 0.5\,\Delta H^{0}_{chem,H_2}$

$$R_{AH_6(g)} = \frac{C_t k_{surf}}{\left(B^3 + B^2 + B + 1\right)} \frac{B^3 K^f_A \Phi^L_A p_t V^L_m C^L_A \sqrt{K^f_{H_2} \Phi^L_{H_2} p_t V^L_m C^L_{H_2}}}{\left(1 + \sqrt{K^f_{H_2} \Phi^L_{H_2} p_t V^L_m C^L_{H_2}} + K^f_A \Phi^L_A p_t V^L_m C^L_A \frac{\left(4B^3 + 3B^2 + 2B + 1\right)}{\left(B^3 + B^2 + B + 1\right)}\right)^2} \quad (46)$$

Gebruik makend van de waarden voor de preëxponentiële factoren in Tabel 5 en van de parameterwaarden vermeld in Tabel 6 in bovenstaande snelheidsvergelijking, worden hogere hydrogeneringssnelheden berekend voor de tolueenhydrogenering in de vloeistoffase dan experimenteel waargenomen. Om tot een betere overeenstemming te komen tussen de modelvoorspellingen en de experimentele resultaten werden de gebruikte parameterwaarden herschat. Dit heeft geleid tot de waarden vermeld in Tabel 7. Uit deze waarden blijkt een goede overeenkomst tussen de chemisorptie-enthalpieën voor waterstof en tolueen geschat op basis van de vloeistoffasekinetiek en deze geschat op basis van de gasfasekinetiek. De verkregen waarden zijn statistisch niet verschillend van elkaar. Dit resultaat ondersteunt de gebruikte werkwijze voor de beschrijving van chemisorptie op een katalysatoroppervlak vanuit een fluïdum, gas of vloeistof.

Op basis van de geschatte samengestelde activeringsenergie en de chemisorptie-enthalpieën wordt een eigenlijke activeringsenergie van 52 kJ mol^{-1} verkregen op basis van de vloeistoffasekinetiek. Dit is beduidend hoger dan en bovendien statistisch significant verschillend van de waarde van de eigenlijke activeringsenergie geschat gebaseerd op de gasfasekinetiek, namelijk 38 kJ mol^{-1}. De verwaarlozing van de interactie van gechemisorbeerde reagentia met niet-gechemisorbeerde fluïdummoleculen lijkt een voor de hand liggende verklaring voor dit verschil. Gasfasemoleculen hebben een hogere kinetische energie ten opzichte van vloeistoffasemoleculen. Aldus kan verwacht worden dat botsingen tussen een gasfasemolecule en een gechemisorbeerd reagens het gechemisorbeerd reagens in een hoger energetische toestand brengen dan botsingen tussen een vloeistoffasemolecule en

een gechemisorbeerd reagens, met een lagere activeringsenergie in de gasfase dan in de vloeistoffase tot gevolg, overeenkomstig de geschatte waarden.

9. Simulatie van het Hydrokraken van een Aromaten Bevattende Vacuümgasolie in een Industriële Reactor

Simulatiemodellen zijn nuttige middelen bij het ontwerp en het bedrijven van chemische reactoren. De gebruiksvriendelijkheid van dergelijke modellen is een bepalende factor voor de industriële relevantie ervan. Vanwege hun eenvoud worden vaak gegroepeerde modellen gebruikt, maar dergelijke modellen hebben als nadeel dat de parameterwaarden voedingsafhankelijk zijn. Fundamentele modellen hebben dit nadeel dan weer niet, echter, hun complexiteit en de vereiste gedetailleerde analyse van de voeding beperken hun gebruiksvriendelijkheid. Met het gehergroepeerde model gebaseerd op structurele klassen (cfr. supra) werd een compromis ontworpen tussen beide types van modellen. De hydrogenering van aromaten tot cycloalkanen werd aan dit model toegevoegd. De effecten hiervan op de simulatie van een industriële hydrokrakingsreactor worden besproken.

9.1. Simulatieprocedures

Een partieel gehydrogeneerde vacuümgasolie (VGO) wordt gebruikt als voeding in de simulaties. Per koolstofgetal wordt de gewichtsfractie aan *n*-alkanen, mono-, di- en trivertakte alkanen, mono-, di-, tri- en tetraring cycloalkanen en mono-, di- en triring aromaten opgegeven. Het gehalte aan aromaten in de voeding bedraagt 17.7 gewichtsprocent. Bij simulaties met variërend totaal aromaatgehalte in de voeding werd via het gebruik van gepaste schalingsfactoren de interne samenstelling van de verzadigde en de aromatische fractie behouden. Indien mogelijk werd voor de fysische eigenschappen van de componenten een beroep gedaan op literatuurwaarden, zoniet werd gebruik gemaakt van groepadditiviteitmethoden zoals die van Benson voor bijvoorbeeld de standaard vormingsenthalpie.

Industrieel wordt hydrokraken uitgevoerd in driefasereactoren die een gas-, vloeistof- en een vaste fase omvatten. De vaste fase bestaat over het algemeen uit een vast katalysatorbed, terwijl de gas- en de vloeistoffase in gelijkstroom neerwaarts door de reactor bewegen. De katalysator kan verondersteld worden volledig bevochtigd te zijn. Het gebruikte reactormodel is een 1-dimensionaal heterogeen model waarbij de gas- en de vloeistoffase in propstroom door de reactor bewegen. De weerstanden tegen massa- en energieoverdracht tussen de gas-

en de vloeistoffase worden expliciet in rekening gebracht, terwijl deze ter hoogte van het vloeistof-vast grensvlak verwaarloosd worden. Interne temperatuurgradiënten worden eveneens verwaarloosd, maar de weerstand tegen interne massaoverdracht wordt wel in rekening gebracht.

Het reactienetwerk werd uitgebreid met de hydrogenering van mono-, di-, tri- en tetraring aromaten tot respectievelijk mono-, di-, tri- en tetraring cycloalkanen. Tetra-ring aromaten waren dan wel niet aanwezig in de gebruikte voeding, maar werden voor de volledigheid van het reactienetwerk toch opgenomen. Gezien de hoge hydrogeneringssnelheden ten opzichte van isomerisatie- en krakingssnelheden, werden behalve de hydrogeneringsreacties geen andere reacties voor de aromaten in het netwerk opgenomen. De snelheidsvergelijking voor hydrogenering is deze afgeleid voor de hydrogenering van tolueen in de gasfase aangepast aan vloeistoffasecondities, cfr. supra. Dezelfde parameterwaarden werden gebruikt voor alle aromaten. Mogelijke substituent- en multiringeffecten zijn het onderwerp van lopend onderzoek en zullen in een later stadium in rekening gebracht worden. Het reactienetwerk en de snelheidsvergelijkingen voor isomerisatie en kraking van (cyclo)-alkanen is identiek aan die gebruikt door Martens en Marin [9.2,9.3].

Voor de integratie van de concentratie-, temperatuur- en drukprofielen in axiale richting wordt gebruik gemaakt van de methode van Gear [9.23]. De integratie van de interne concentratieprofielen in de katalysator bij de berekening van de benuttingsgraden van de katalysator voor de verschillende reacties wordt uitgevoerd aan de hand van een collocatiemethode [9.24]. De vereiste rekentijd voor een simulatie bedraagt 10 tot 90 CPU minuten op een gewone PC met een Pentium IV 1GHz processor. Het grootste deel daarvan wordt besteed aan de berekening van de benuttingsgraden

9.2. Simulatieresultaten en Bespreking

De hydrogenering van aromaten is een sterk exotherme reactie. Als gevolg hiervan worden belangrijke temperatuureffecten verwacht indien de voeding een beduidende aromatische fractie bevat. Een quasi onmiddellijke temperatuurstijging wordt waargenomen. Een zogenaamde “hot spot” wordt ontwikkeld in de eerste twee decimeter van de reactor, zie Figuur 14a. Gezien het snelle verbruik van de reagentia voor hydrogenering, zowel waterstof als aromaten, zie Figuur 14b, daalt de hydrogeneringssnelheid. Als gevolg hiervan daalt het ontwikkeld thermisch vermogen en wordt dit vermogen ter hoogte van de “hot spot” kleiner dan het vermogen overgedragen van de vloeistof- naar de gasfase. In het gebied van dalende vloeistoffasetemperatuur wordt de residuele aromatische fractie gehydrogeneerd en stijgt de

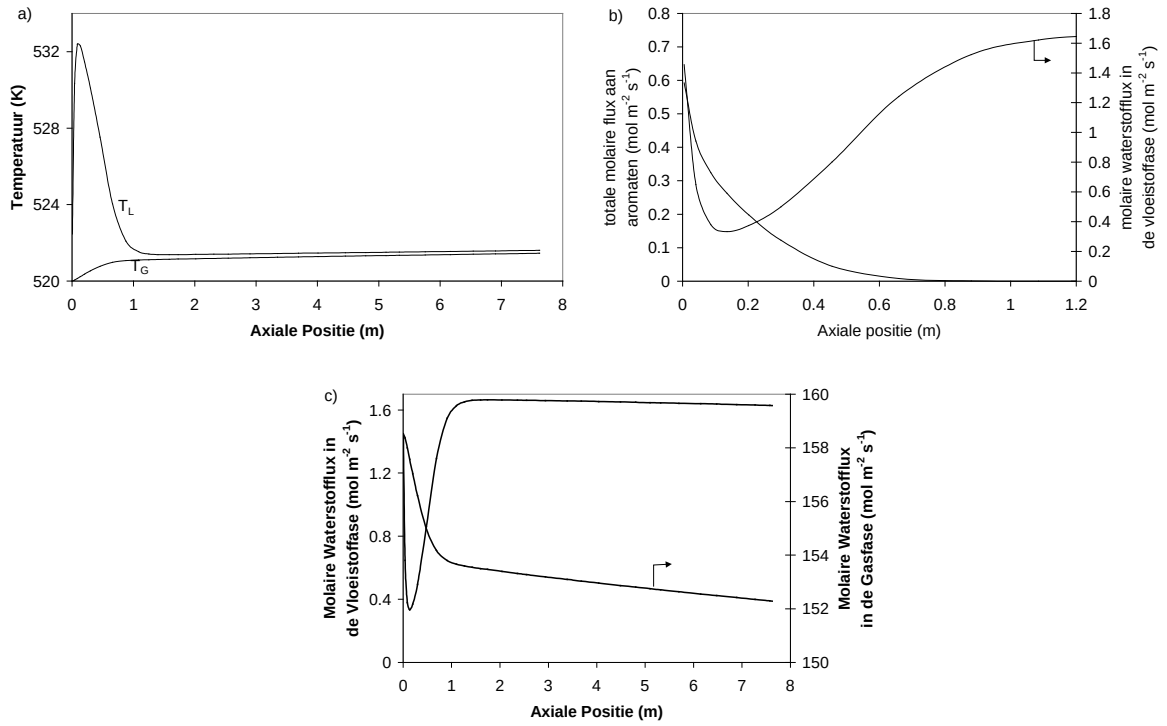

Figuur 14 **Profielen voor a) de vloeistof- ,T_L, en de gasfase, T_G, temperatuur; b) de totale flux aan aromaten en de molaire waterstofflux in de vloeistoffase en c) molaire waterstofflux in de gas- en vloeistoffase als functie van de axiale positie in de reactor bij 520 K, 12 MPa en een molaire waterstof-op-koolwaterstofverhouding van 25 voor een gehalte aan aromaten in de voeding van 10 gewichtsprocent**

gasfasetemperatuur. Na 0.6 tot 0.8 meter is de volledige aromatische fractie gehydrogeneerd en een quasi constant temperatuurverschil van 0.2 K stelt zich in tussen de vloeistof- en de gasfasetemperatuur. In het tweede deel van de reactor, waar alle aromaten reeds gehydrogeneerd zijn, treedt een beperkte temperatuurstijging op als gevolg van de exothermiciteit van het eigenlijke hydrokraken.

De molaire waterstofflux in de gasfase daalt over de volledige lengte van de reactor, zie Figuur 14c. De daling gaat snel in de eerste meter van de reactor waar de hydrogenering van de aromatische fractie plaatsvindt. Een meer gematigde daling vindt plaats in het tweede deel van de reactor, corresponderend met het waterstofverbruik bij het eigenlijke hydrokraken. De molaire waterstofflux in de vloeistoffase daalt aanvankelijk snel door de snelle, initiële hydrogenering en dit veel meer uitgesproken dan in de gasfase door de optredende overdrachtslimitering voor waterstof tussen de gas- en de vloeistoffase (cfr. infra). Wanneer het grootste deel van de aromaten gehydrogeneerd is, herstelt de molaire waterstofflux in de vloeistoffase zich en bereikt waarden corresponderend met verzadiging van de vloeistof aan waterstof vanaf 1 tot 2 meter.

Uit simulaties van het hydrokraken van voedingen met een variërend gehalte aan aromaten blijkt dat zich vanaf een voldoend hoog gehalte aan aromaten een bijzonder effect voordoet, namelijk de ontwikkeling van een schouder in het temperatuurprofiel van de vloeistoffase. Bij lagere gehalten aan aromaten is steeds een stoechiometrische overmaat aan waterstof in de vloeistof aanwezig. Wanneer de hydrogeneringssnelheid vertraagt omwille de verlaagde concentraties aan reagentia, neigt de hydrogeneringssnelheid naar *nul* en herstelt de molaire waterstofflux zich van het snelle, initiële verbruik. Bij hogere gehalten aan aromaten in de voeding wordt waterstof in de vloeistoffase echter het stoechiometrisch limiterend reagens. Zolang een niet-verwaarloosbaar gehalte aan aromaten in de vloeistof aanwezig is, wordt de overdracht van waterstof van de gas- naar de vloeistoffase snelheidsbepalend in de hydrogenering. Wanneer de hydrogeneringssnelheid daalt, neigt de hydrogeneringssnelheid niet onmiddellijk naar *nul* maar naar een snelheid die overeenkomt met die van de aanvoer van waterstof uit de gas- naar de vloeistoffase. Ook het ontwikkeld thermisch vermogen neigt niet naar *nul* maar naar een waarde corresponderend met de snelheid van de waterstofoverdracht, hetgeen leidt tot de schouder zoals waargenomen in Figuur 15a.

De ontwikkeling van een regime waarin de overdracht van waterstof van de gas- naar de vloeistoffase snelheidsbepalend wordt voor de hydrogenering blijkt ook uit Figuur 15b en c.

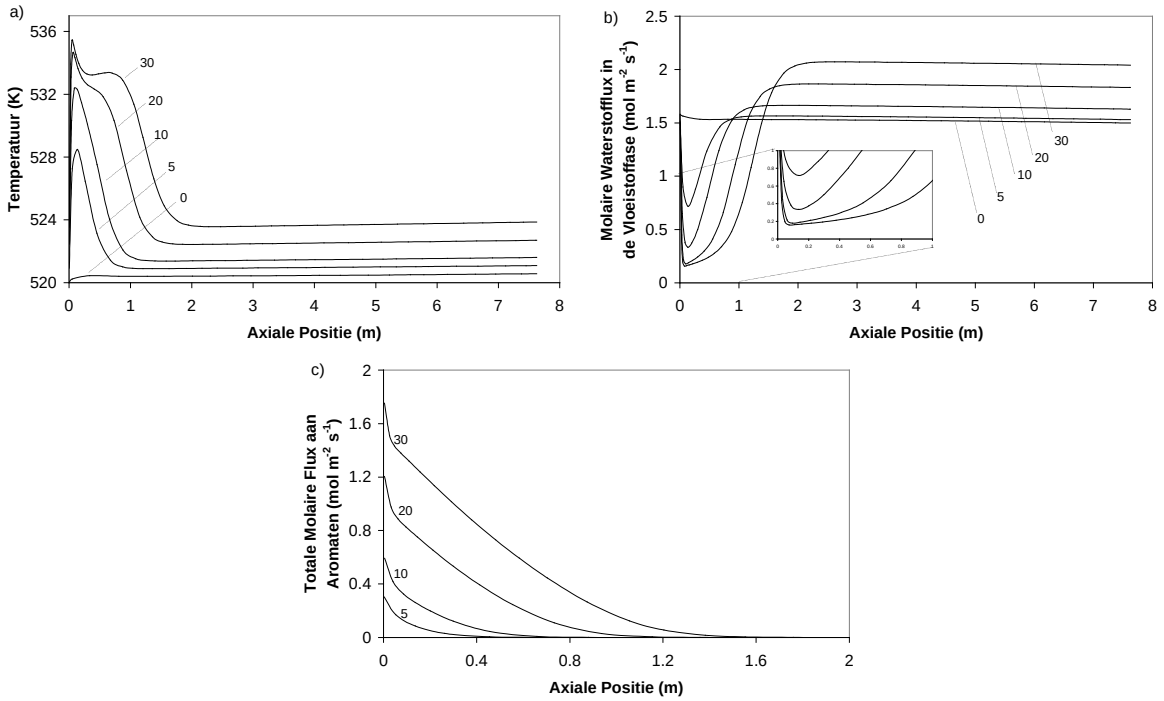

Figuur 15 **Effect van het gehalte aan aromaten in de voeding op a) de vloeistoffase-temperatuur, b) de molaire waterstofflux in de vloeistoffase en c) de totale molaire flux aan aromaten als functie van de axiale positie in de reactor bij 520 K, 12 MPa en een molaire waterstof-op-koolwaterstofverhouding van 25**

Na het snelle initiële verbruik van waterstof vertoont de molaire waterstofflux in de vloeistoffase bij hogere gehalten aan aromaten in de voeding aanvankelijk een trager herstel dan bij lagere gehalten aan aromaten in de voeding, zie Figuur 15b. In deze zone van trager herstel is nog steeds een aanzienlijke fractie aan aromaten aanwezig in de voeding en wordt de hydrogeneringssnelheid bepaald door de snelheid van de aanvoer van waterstof vanuit de gasfase naar de vloeistoffase.
Hetzelfde blijkt uit het verloop van de profielen van de totale molaire flux aan aromaten als functie van de afstand in de reactor, zie Figuur 15c. Voor lage gehalten aan aromaten in de voeding wordt een exponentiele daling waargenomen corresponderend met het verdwijnen van een component via een eerste orde kinetiek. Bij hogere gehalten aan aromaten in de voeding ontwikkelt zich na de snelle, initiële daling een minder snel dalend linear deel dat uiteindelijk overgaat in een exponentiële daling tot *nul*. Een lineaire daling is te verwachten wanneer de betreffende component via een nulde orde kinetiek verdwijnt, namelijk wanneer de aanvoer van een ander reagens zoals in dit geval waterstof, snelheidsbepalend wordt. Uiteindelijk worden de aromaten het limiterend reagens en wordt een exponentiële daling van de corresponderende flux waargenomen zoals eerder beschreven.

10. Conclusies

Het werk in het kader van dit proefschrift maakt deel uit van het continue onderzoek aan hydrokraken aan het Laboratorium voor Petrochemische Techniek aan de Universiteit Gent. Nieuwe onderwerpen zoals de hydrogenering van aromaten en de afhankelijkheid van het koolstofgetal van de op enkelvoudige gebeurtenissen gebaseerde kinetische parameters zijn behandeld. Daarnaast werd het onderzoek aan reeds bestaande onderwerpen zoals niet-ideaal hydrokraken en de katalysatorafhankelijkheid van de op enkelvoudige gebeurtenissen gebaseerde kinetische parameters verdergezet en meer in detail behandeld.
Het effect van de werkvoorwaarden op de idealiteit van het hydrokrakingsgedrag wordt verklaard aan de hand van snelheidsvergelijkingen die rekening houden met potentieel snelheidsbepalende stappen op zowel de zure als de metallische centra. De katalysator- en koolstofgetalafhankelijkheid van de op enkelvoudige gebeurtenissen gebaseerde kinetische parameters wordt bepaald door de standaardprotoneringsenthalpie van de betrokken alkenen.
In tegenstelling tot de hydrogenering van aromaten onder homogene gasfaseomstandigheden, leidt de resonantiestabilisatie niet tot het snelheidsbepalend zijn van de additie van het eerste waterstofatoom aan de aromatische ring op een platina oppervlak. Op een dergelijk oppervlak gaat de hydrogenering van aromaten door volgens een mechanisme met gelijke

snelheidscoëfficiënten voor de eerste vier waterstofatoomadditiestappen en quasi-evenwicht voor de laatste twee waterstofatoomadditiestappen. Vergelijking van gasfase- met vloeistoffasekinetiek gebaseerd op fugaciteiten voor de uitdrukking van het chemisorptie-evenwicht wijst erop dat interacties tussen gechemisorbeerde speciës en niet gechemisorbeerde moleculen niet kunnen verwaarloosd worden.

De hydrogenering van aromaten moet in rekening gebracht worden om een industriële hydrokrakingsreactor adequaat te kunnen beschrijven. De exotherme effecten leiden tot de ontwikkeling van een zogenaamde “hot spot” in de eerste decimeters van de reactor. Een dergelijk model is een krachtig instrument voor het ontwerp en de optimalizatie voor waterstofbehandelingsprocessen aangewend bij de productie van brandstoffen die voldoen aan de steeds strenger wordende milieunormen

Verder onderzoek is uiteraard wenselijk. De modellering van *niet-ideaal* hydrokraken is een echte uitdaging, zeker wanneer het gaat om complexe voedingen. Voor wat betreft de hydrogenering van aromaten is de kennis van substituent- en meerringeffecten op de hydrogeneringssnelheid een noodzakelijke voorwaarde voor een adequate, quantitatieve beschrijving van de conversie van het volledige spectrum aan aromaten.

Chapter 1

Hydrocracking: History and Perspectives of a Refinery Conversion Process

It is difficult to imagine the world of today without crude oil derived products. The most prominent use of such products is as transportation fuel (LPG, gasoline, kerosene, diesel), heating gas (methane) or heating oil (diesel oil and heavier oils), vide Figure 1-1 [1]. Apart from that also many petrochemical feedstocks, such as ethylene, propylene, benzene, toluene, etc… are crude oil derivatives. Typical applications of these products can be found in the polymer industry (plastics, insulation material, synthetic rubber). Other products obtained from crude oils are, e.g., asphaltenes and lube oils.

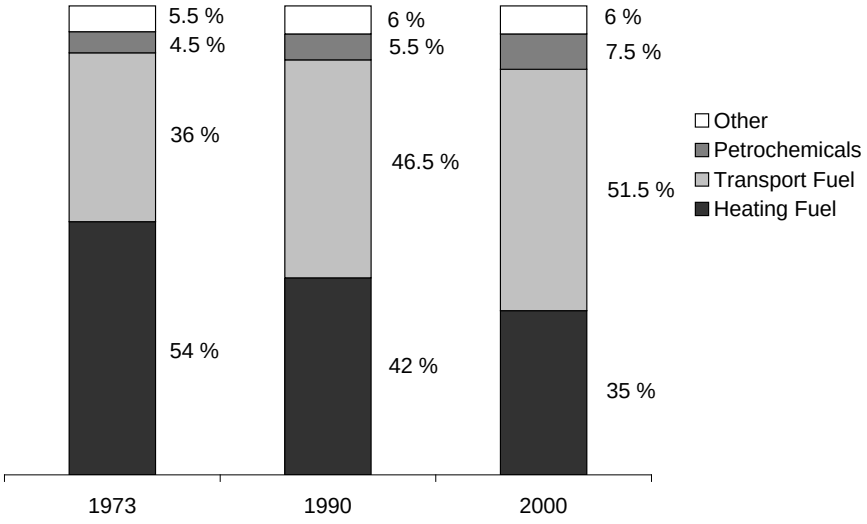

Figure 1-1 Evolution of the oil market [1]

1.1 Role of the Refinery

Refineries are used to 'refine' the crude oil into the valuable fractions required by the oil market. In the simplest possible refinery scheme, representing a so-called 'hydroskimming' refinery, the crude oil is only subject to a distillation into the different oil fractions. Some units for quality improvement, such as catalytic reforming or hydrotreating, may also be incorporated in the scheme, however, no conversion units are present. As a result 'hydroskimming' refineries can only be used when the composition of the crude oil processed meets the oil market demands. This condition may be fulfilled for relatively light crude oils if heavy fuel oil consumption is high and private car use is limited or if the heavy fractions can be processed at other refineries.

However, in general important differences exist between the market demands and crude oil composition, with the latter containing (much) more heavier fractions than required, vide Figure 1-1 and Table 1-1 [1]. Hence, conversion of the heavier fractions into the more valuable lighter fractions such as gasoline and middle distillates is desirable. The typical units used in this respect are delayed coking, visbreaking, FCC (Fluid Catalytic Cracking), and

Table 1-1 Composition (wt%) of various crude oils [1]

Crude	Brent (England)	Sahara (Algeria)	Arabian light (S. Arabia)	Safaniyah (S. Arabia)	Boscan (Venezuela)
Gas (C_1-C_4)	2	4	2	3	-
Gasoline	29	35	27	17	-
Middle Distillate	33	35	21	28	22
Heavy Products	36	26	40	52	78

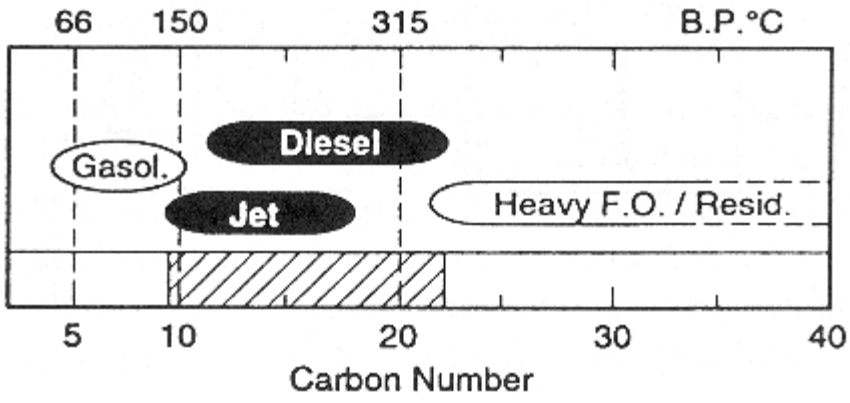

Figure 1-2 Carbon number and boiling point range of several key petroleum refining products (diesel & jet ~ middle distillate) [2]

hydrocracking, depending on the feedstock characteristics and the desired product fractions. Delayed coking and visbreaking are non-catalytic processes. Visbreaking is generally applied when the feedstock is too viscous to be handled by one of the catalytic alternatives.

FCC is a typical gasoline producing process. It increases the H/C ratio of the product by removing carbon from the feedstock. Together with delayed coking and visbreaking, FCC is a so-called 'carbon rejection' process. In FCC the carbon is removed under the form of coke deposition on the catalyst. This leads to a rapid catalyst deactivation and requires continuous regeneration of the latter. Fluidized bed or riser configurations are built to enable a continuous transport of catalyst from the reactor to the regenerator and vice versa. Due to the absence of H_2 and a hydrogenation function in the system, FCC products are generally rich in alkenes and aromatics. To a certain extent this is beneficial for the quality of the gasoline produced, however, current and future environmental legislation seriously limit the content of unsaturated components, and of aromatics in particular, in gasolines. Another issue in FCC is the sulfur and nitrogen content of the feed. Because such components are generally good coke precursors, they will be concentrated on the coked catalyst leading to SO_x and NO_x in the flue gases of the regenerator. If the feed content of sulfur and nitrogen containing compounds is too high, appropriate measures have to be taken to remove them a priori, e.g., by feedstock hydrotreatment, or a posteriori, e.g., by product hydrotreatment and SO_x/NO_x absorption or adsorption from catalyst regenerator flue gases by, e.g., SNAP processes.

Hydrocracking units usually yield more middle distillates than gasoline. The H/C ratio of the feedstock is increased by 'hydrogen addition' instead of 'carbon rejection'. This is achieved by hydrogenation of unsaturated feedstock components and cracking products. The low aromatic content in the product results in a superior diesel quality, i.e., a high cetane index. By the appropriate choice of the hydrocracking catalyst, severe deactivation by sulfur and nitrogen containing components can be avoided. Moreover, these components can be converted yielding H_2S and NH_3. The former can be sent to a Claus unit for production of

Table 1-2 Typical FCC and hydrocracking product flow composition

	FCC	Hydrocracking
Gas (C_1-C_4)	19	6
Gasoline	50	28
Middle Distillate	25	56
Heavy Products	6	10

elementary sulfur. The main advantage of the hydrocracking process is its flexibility. A wide variety of feedstocks can be used. Straight run vacuum gas oils as well as mixed feedstocks consisting of straight run fractions, delayed coking gas oil, deasphalted gas oil,… are used for hydrocracking treatment. Also a Fischer Tropsch effluent can be sent to a hydrocracker for quality improvement. The hydrocracking severity is a useful tool in determining the selectivity to the various product fractions. The main drawback of the process are the huge investment and operating costs. High pressure equipment is needed and substantial amounts of hydrogen are consumed in the process. Despite the high costs associated with hydrocracking, it is an efficient technology because of the 'clean' character of its products, which is required to meet the current and future environmental legislation concerning transportation and heating fuels, vide the 'Clean Air Act' [3].

1.2 Hydrocracking

1.2.1 History

The origin of hydrocracking dates back to the 1920's when a technology was developed in Germany to convert domestic coal deposits into liquid fuels. In the same period IG Farben also developed a hydrocracking technology to convert heavy gas oils to lighter fuels [4]. Later on, during World War II, hydrocracking was applied in the production of aviation turbine fuel. However, after World War II, the incentive to produce liquid fuels from coal disappeared with the availability of the Middle Eastern crude oil. Moreover another more economical process to convert heavy petroleum fractions to gasoline emerged, i.e., catalytic cracking. Hence, in general the interest in the hydrocracking technology disappeared [2].

Table 1-3 Selected hydrocracking processes [2]

Process	Company
Unicracking	UOP
Isocracking	Chevron
Ultracracking	Amoco
Shell	Shell Development Co.
BASF-IFP Hydrocracking	Badische Anilin und Soda Fabrik, and Institut Français du Pétrole
MAK	Mobil – Akzo Chem. – Kellog

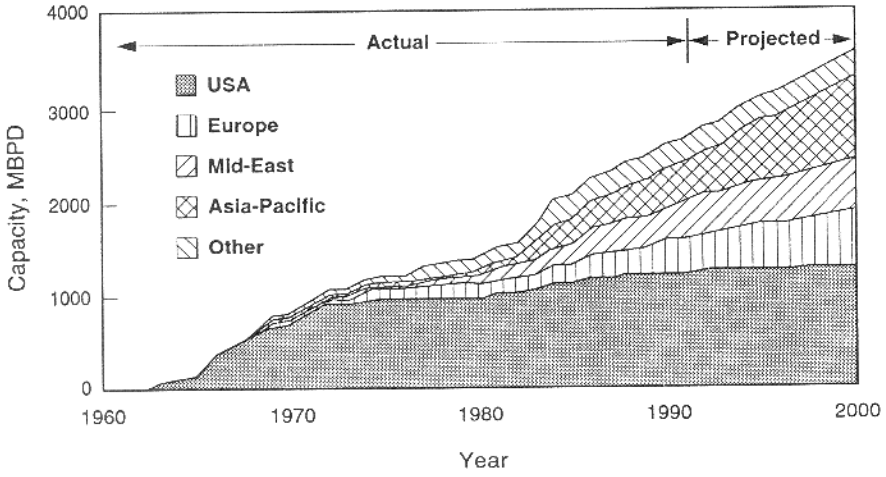

Figure 1-3 Actual (1993) and projected worldwide hydrocracking capacity [2]

Around 1960 the commercial development of modern oil-feedstock-based hydrocracking started [5]. It was Chevron, which started with its 'Isocracking' process [6]. Some example hydrocracking processes are reported in Table 1-3. Multiple factors caused the renewed interest in hydrocracking. The availability of hydrogen formed as a by-product in catalytic reforming was an important pricing factor. The increased gasoline production via FCC also generated large quantities of refractory cycle stock. This refractory cycle stock was an effluent difficult to be converted into gasoline and lighter products via FCC, but easier converted to those products via hydrocracking. In addition, the oil market requirements shifted partly from gasoline to middle distillates by the switch of railroads from steam to diesel engines and by the introduction of commercial jet aircraft. The worldwide hydrocracking capacity shows a continuous increase since the first commercial units were built in the early 1960's. The hydrocracking capacity increased primarily in the USA in the late 1960's and early 1970's. The capacity increased ever since, however at a more moderate pace. The rest of the world followed in the late 1970's and the 1980's. An important share in hydrocracking capacity is projected for the Asia-Pacific region. Currently, reinforced interest in hydrocracking technology originates from the more stringent environmental legislation (cfr. supra) and the decline in crude oil quality.

1.2.2 Process Configurations

The flexibility of the hydrocracking process is reflected in several possible process configurations. Moreover, a strong relation between hydrotreating and hydrocracking exists. The catalysts used in both processes have similar properties, which make the coupling or even the integration of both processes possible, as will be discussed in this paragraph. Depending

on feedstock composition and on the required product specifications, combined hydrotreating and hydrocracking can be performed in a single- or a two-stage configuration with or without recycle of the unconverted feed. General hydrocracking process operating conditions are a reactor temperature between 573 – 723 K, reactor total pressure between 8.5 – 20 MPa, liquid hourly space velocity of 0.5 to 2.5 h^{-1}, hydrogen-to-oil-ratio between 500 – 1700 Nm^3 m^{-3}, corresponding to a molar hydrogen to oil ratio of about 8 to 30, and a hydrogen consumption between 200 – 600 Nm^3 m^{-3}, corresponding to a molar hydrogen consumption of about 4 to 10 per mole of oil fed.

a Single-Stage Hydrocracking

The single-stage hydrocracking configuration typically employing an amorphous catalyst is generally used to maximize diesel production. A simplified flow diagram for this configuration is shown in Figure 1-4. The fresh feed, eventually combined with the recycled unconverted fraction, is passed downward through the reactor in the presence of hydrogen. Because hydrogen is consumed during hydrocracking make-up hydrogen has to be added to the recycle hydrogen. The effluent of the hydrocracking reactor is passed through high- and low-pressure separators where the hydrogen is recovered and recycled. The liquid product, denoted in Figure 1-4 as 'Single-Stage Product' is sent to a fractionator where the final products are separated from the unconverted fraction. Typically 40 to 80 vol% of the feed is

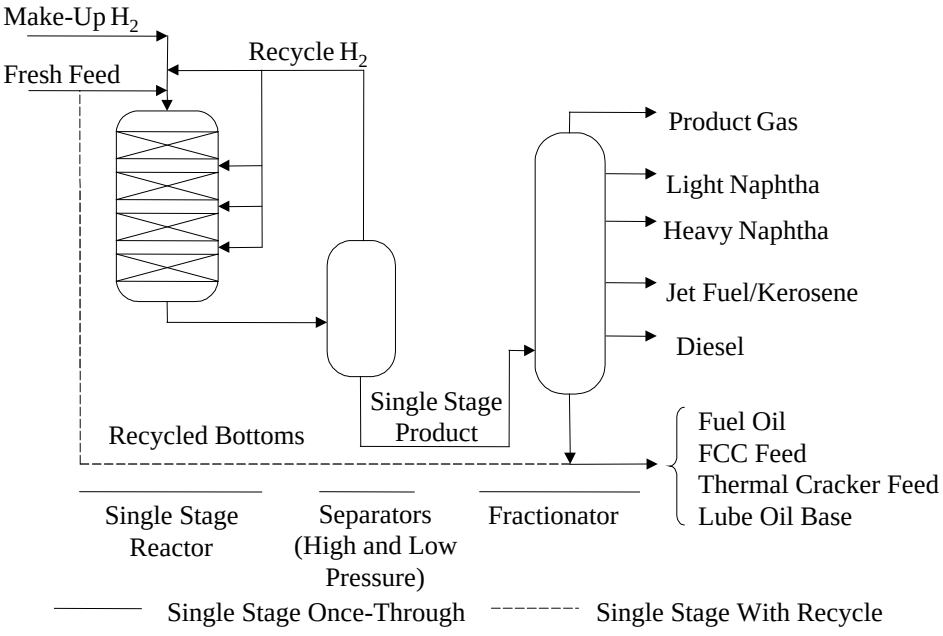

Figure 1-4 Simplified flow diagram of single-stage, single-catalyst hydrocracking, with and without (i.e., once-through) recycle

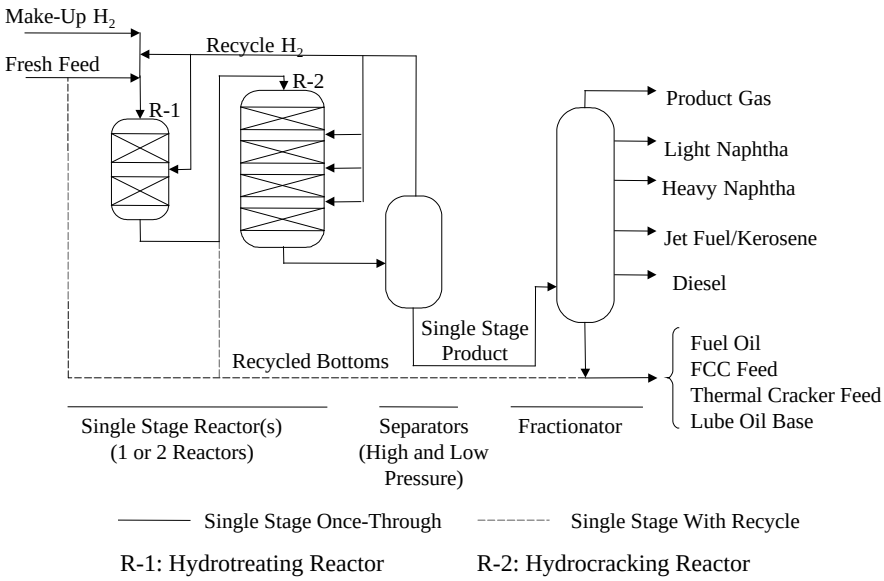

Figure 1-5 Simplified flow diagram of single-stage, dual-catalyst hydrocracking, with and without (i.e., once-through) recycle

converted per pass in a hydrocracking reactor. A recycle of the unconverted fraction to the hydrocracking reactor can be used. If an overall conversion of 100% is aimed at, a total recycle, so-called 'recycle-to-extinction', has to be used. Other options are to use the unconverted fraction as fuel oil, FCC feed, thermal cracker feed or as lube oil base.

The reactor contains several catalyst beds with intermediate hydrogen injection. This hydrogen injection serves as a quench to temper the heat effects in hydrocracking. Indeed, because of the hydrogenation of the unsaturated fractions and products during hydrocracking, it becomes an overall exothermic process in contrast to, e.g., FCC and thermal cracking. For process optimization the catalyst beds can be loaded with different catalysts so that optimal catalyst selection can be performed for hydrotreating and hydrocracking separately. To enable even further optimization a separate reactor for hydrotreating may be added, vide Figure 1-5. Employing such a separate reactor for hydrotreating enables independent optimization of reaction conditions for hydrotreating and –cracking. Such a configuration is still denoted as a single-stage process because the effluent of the first reactor, i.e., R-1, is not subject to any separation process before entering the second, R-2.

Typically for single-stage processes, hydrocracking occurs in the presence of heavy aromatic molecules, and sulfur- and nitrogen-containing components. In order to saturate these aromatic molecules and to remove the hetero atoms, a catalyst with a high hydrogenation-to-cracking activity, such as amorphous γ-alumina with a CoMo, NiMo or NiW metal phase, is used.

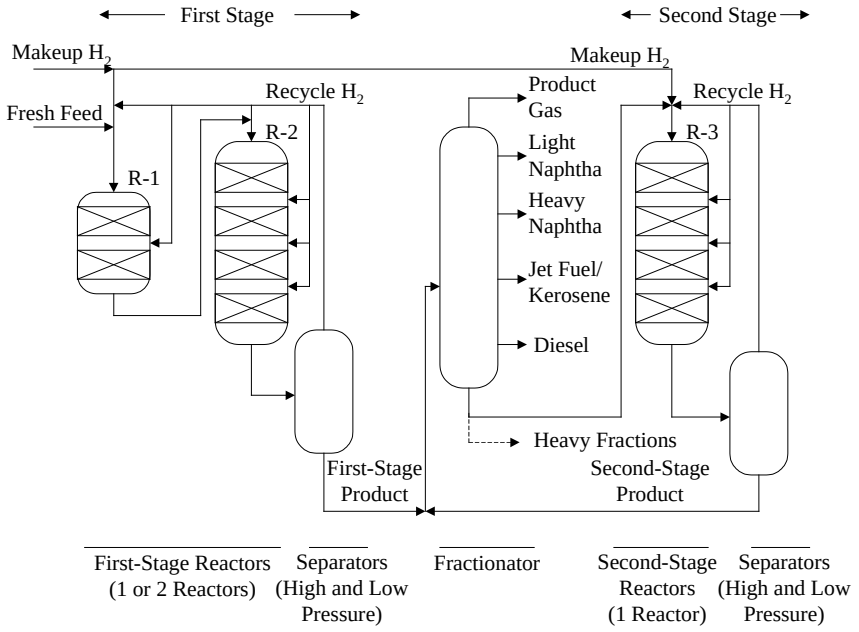

Figure 1-6 Simplified flow diagram of two-stage Unicracking process

b Two-Stage Hydrocracking

The two-stage configuration provides the hydrocracking process with an even higher flexibility than the single-stage configuration. A simplified schematic representation of UOP's two-stage Unicracking process is given in Figure 1-6. The reactors R-1 and R-2 constitute the first stage, the effluent of which is first separated and then fractionated, similar to the single-stage hydrocracking. However, instead of recycling the fractionator bottoms to R-1 or R-2, they are (partly) sent to a third reactor R-3, constituting the second stage. The second-stage product is generally recycled to the same fractionator as the first-stage product. Hence, when the fractionator bottoms are entirely sent to the second-stage reactor, this two-stage configuration works with a recycle-to-extinction. The catalyst and the operating conditions in reactors R-1 and R-2 are generally similar to those applied in single-stage hydrocracking but may be somewhat milder because of the presence of the second-stage reactor in the process. Because of the much lower hetero atom concentrations in the second-stage compared to the first-stage reactor, noble metals can be used in the second-stage reactor as hydrogenation function when deep hydrogenation of the product is required. Lower temperatures, i.e., 543 to 643 K, can be used in the second-stage reactor leading to higher feed isomer yields.

c Mild Hydrocracking

Whereas in the single- and two-stage configuration hydrotreating and –cracking are typically performed in several reactors using different catalysts, mild hydrocracking is the result of the integration of hydrotreating and –cracking into one reactor and using one catalyst. It's a configuration which only became important the last two decades. Generally speaking, a mild hydrocracker is a VGO desulfurization unit operated at more severe conditions and, hence, apart from the hydrotreating reactions, c.q., desulfurization, also hydrocracking occurs to an appreciable extent. A comparison of typical process conditions in mild hydrocracking with conventional hydrocracking, vide Table 1-4, shows the less severe character of the mild hydrocracking process conditions. It is most evident from the hydrogen partial pressure applied in the reactor and the hydrogen-to-oil ratio, since the temperatures applied are very similar. In addition, while conventional hydrocrackers commonly use recycles, mild hydrocrackers operate on a once-through basis explaining the lower conversion levels for the latter. Therefore product quality levels in mild hydrocracking are inferior to those obtained by conventional hydrocracking. Mild hydrocracking is mainly applied in combination with FCC to produce the entire slate of crude oil based products.

d Catalytic Dewaxing

Hydrocracking technology is not only applied to convert heavier fractions into more valuable and useful lighter fractions, it can also serve to improve the properties of several cuts. The process denoted as *'catalytic dewaxing'* is used for pour point lowering and viscosity improvement of middle distillates and lubricants and for cloud point and freeze point lowering of diesel and jet fuel respectively. Especially at low temperatures these properties are becoming important.

Because the *n*-alkanes are responsible for the waxy behaviour of the various cuts, dewaxing is a synonym for removal of *n*-alkanes. The less a branched alkane resembles its linear isomer, the lower its waxy character, e.g., in the C_{20} range a 5-methylbranched isomer has a melting point 20 – 25 K and 40 – 45 K lower than the corresponding 2-methylbranched isomer and *n*-alkane respectively [7]. The removal of the *n*-alkanes is not accomplished by separation, but by selectively converting them into other products. These can be cracked products which are easily removed from the desired cut, but these can also be its isomers, resulting in higher yields of the original cut. In the latter case the process is denoted as *iso*-dewaxing. The process configuration is generally similar to the once-through single-stage hydrocracking flow diagram presented in Figure 1-4. Typical operating conditions in catalytic dewaxing are

Table 1-4 Typical process and operating conditions in hydrocracking processes

	mild hydrocracking	conventional hydrocracking	catalytic dewaxing	slurry	ebullated bed
Stages	single	single - two	single	single	single
Operating Conditions					
Conversion, wt%	20 – 70	70 – 100	-	55 – 90	-
Temperature, K	573 – 713	573 – 723	533 – 703	> 723	623 – 773
H_2-pressure, MPa	3 – 7	8.5 – 20	2 – 5	3.2 – 24	6 – 20
Liquid Hourly Space Velocity, h^{-1}	0.3 – 1.5	0.5 – 2.5	-	0.3 – 1	0.15 – 5
H_2/oil, $Nm^3\ m^{-3}$	300 – 1000	500 – 1700	250 – 450	< 750	300 – 500

reported in Table 1-4.

Catalysts frequently used in catalytic dewaxing are based on zeolites with a medium pore size such as ZSM-5 and erionite. The restricted pore size results in a reduced accessibility of the active sites for components with a higher kinetic diameter, i.e., the iso-alkanes, compared to the unwanted *n*-alkanes. Nevertheless, also large pore zeolites such as mordenite can be used. Other possible zeolites for dewaxing reported in patent literature are H-ferrierite[8], ZSM-22[9], ZSM-23 [10], zeolite β [11], SAPO-11 [12] or zeolite L [13].

e Slurry and Ebullated Bed Hydrocracking

In the above described process configurations fixed bed hydrocracking reactors are used. However, hydrocracking can also be performed as a slurry [14,15] or an ebullated bed [16,17] process. Operating conditions for both processes are mentioned in Table 1-4 while schematic representations are shown in Figure 1-7.

The slurry processes described by Sears et al. [14] and Benham et al. [15] are thermal hydrocracking processes. Typically 0.01 to 4 wt% of iron sulphate additive particles are added to the feedstock in order to inhibit coke formation. The slurry is passed upwards through the hydrocracking reactor R-1 after which it is sent to a hot separator S-1. In this separator a liquid phase containing heavy hydrocarbons and the coke inhibiting additive is removed from the mixed reactor effluent. The liquid phase is further fractionated in S-2 to obtain a heavy oil boiling above 723 K which also contains the additive particles. This heavy oil is then recycled to the hydrocracking reactor. The lighter products from the fractionator and the gas phase from the hot separator are fed to a cold separator S-3. This cold separator

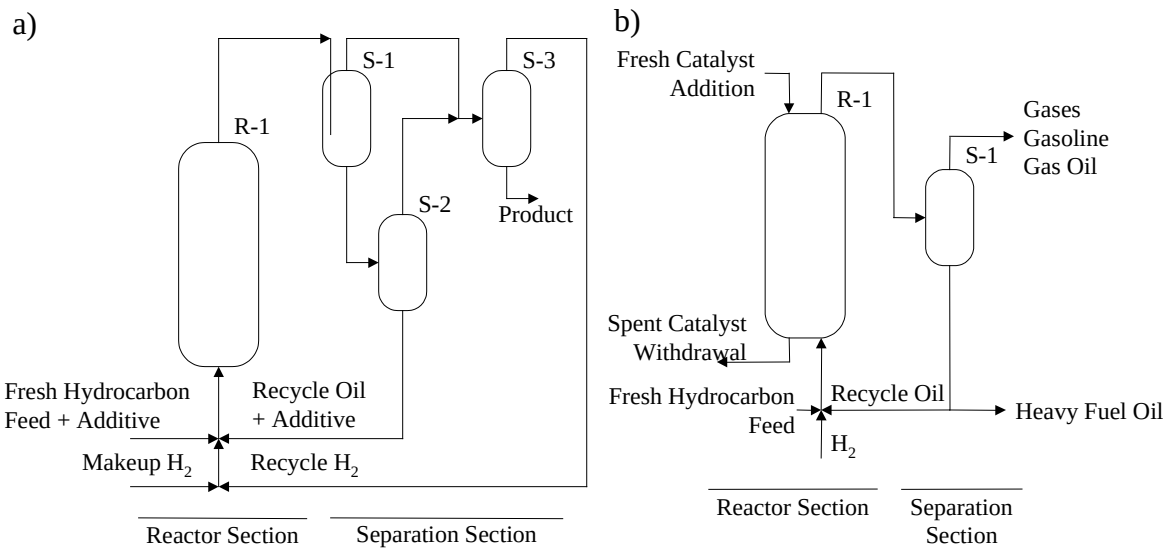

Figure 1-7 Simplified flow diagram for a) slurry and b) ebullated bed hydrocracking

condenses the product hydrocarbons and separates them from the hydrogen which is recycled to the hydrocracking reactor.

The ebullated bed processes discussed here are catalytic processes, e.g., the H-Oil process [16,17]. The gas liquid mixture flows upwards through the ebullated bed reactor where it is contacted with a NiMo or CoMo on Al_2O_3 catalyst. Fresh catalyst is added at the top of the reactor while the spent catalyst is withdrawn from the bottom. The construction of the reactor is such that it enables continuous hydrocracking operation even when catalyst replacement occurs discontinuously. The reactor effluent is sent to an atmospheric distillation unit. If the gasoline/gas oil composition of the distillate meets the market requirements it is sent to a final fractionator to obtain the gasoline and gas oil fractions from this distillate, if not, it will undergo appropriate further treatment. The residue can be used as heavy fuel oil, however, in most cases it will be be recycled to the ebullated bed hydrocracking reactor or it will be subjected to other treatment such as catalytic cracking.

1.2.3 Kinetic Models

Simulation models are essential tools for reactor design and optimization. A general simulation model consists of a reactor and a reaction model. The reactor model accounts for the type of the reactor used and for the flow pattern in the reactor, while the reaction or kinetic model describes the kinetics of the chemical reactions occurring. This paragraph will focus on different kinetic models proposed for complex feedstock conversion in general and hydrocracking in particular.

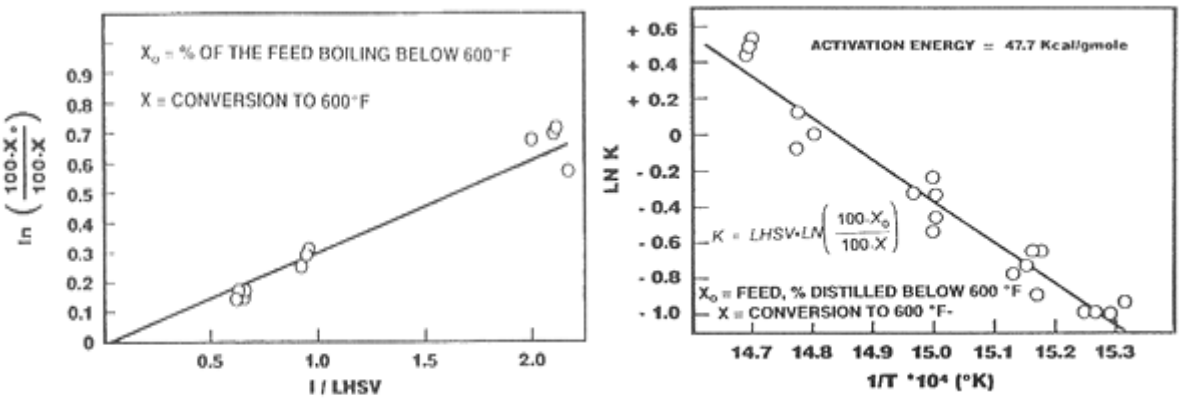

Figure 1-8 Hydrocracking first order kinetics (left) and Arrhenius diagram [2]

Describing the kinetics of complex feedstock processing requires a compromise between accuracy and time consumption. Generally stated, the more explicitly a kinetic model accounts for the individual reactions which are occurring, the better it is in describing the simulated process but the more time consuming it becomes. The better describing capabilities include, e.g., the feed invariance of the kinetic parameters and a high accuracy over an extended range of operating conditions. Less explicit models consider various components as one reacting pool of components, a so-called lump, the properties of which are an average over the components included in that lump.

a Lumped Kinetic Models

Scherzer and Gruia [2] discuss a model for VGO hydrocracking considering only 2 lumps based on the desired endpoint or final boiling point (FBP). The reactant lump, denoted as EP^{+}_{feed}, is defined as the fraction of material in the feed boiling above the desired endpoint and can be expressed both in wt% and vol%. The conversion is defined as:

$$\%\,conversion = \left(\frac{EP^{+}_{feed} - EP^{+}_{product}}{EP^{+}_{feed}} \right) \times 100 \tag{1.1}$$

And the rate expression is as follows:

$$Rate = k_0 \; exp\left[\frac{-E_A}{RT} \right] \left(EP^{+}_{feed} \right)^n \tag{1.2}$$

From Figure 1-8 a first order relationship for the rate equation is evident with an activation energy of 47.7 kcal mol^{-1} or 200 kJ mol^{-1}. Another lumped model, developed for catalytic cracking by Weekman and Nace [18] takes into account one extra lump for the inevitable coke formation during catalytic cracking. However, the broad definition of the lumps containing many components with different reactivities leads to a strong feed dependence of

the kinetic parameters in such kinetic models. Therefore, new models were developed with an increased number of lumps accounting into more detail for the feedstock composition. A 10 lump model for catalytic cracking was developed by Mobil [19,20]. Similar models for hydrocracking were developed by Quader et al. [21] and Stangeland and Kitrell [22]. Improving the predicting capabilities with an increasing number of lumps considered is however limited since the number of reactions and, hence, the number of parameters to be determined, increases more than proportionally with the number of lumps considered.

Further modelling efforts to account for the detailed chemistry occurring, while maintaining a manageable set of kinetic parameters, are focussed on dealing with the structural similarities of the components involved. For catalytic cracking Liguras and Allen [23-25] grouped all components in classes whereby each class was represented by a pseudo-component. Selection of the pseudo-components and determination of their concentrations was performed based a on molecular analysis, i.e., gas chromatography in combination with mass spectrometry, as well as on a structural analysis, i.e., NMR spectra. Since the reaction rate expressions are based on the structural building blocks in the pseudo-components, only a limited set of about 25 parameters needed to be estimated using experimental data on model components [23]. The approach developed by Quann and Jaffe [26,27] was called structured oriented lumping. These authors represented the occurring components by a hydrocarbon structure vector, based on the structural building blocks, as structural increments. Structural isomers have the same structural vector and, hence, are considered as one pseudo-component with equal physical and chemical properties, vide Chapter 4. Similar to Liguras and Allen [23-25] the reaction rate expressions are now related to the structural increments leading to a limited set of parameters to be determined. The main difference in the two above presented approaches lies in the determination of the pseudo-components. In the approach by Quann and Jaffe [26,27] the selection of the structural increments determines the pseudo-components used in the model, while in the method of Liguras and Allen [23-25] the number and amount of pseudo-components is not a priori determined. A more or less related approach was developed by Klein et al. [28] for the pyrolysis of asphaltenes. However, these authors developed probability density functions for the several possible building blocks in an asphaltene and generated the feedstock components in a stochastic way.

Another possibility to decrease the number of parameters required while increasing the detailed character of the model is using continuous lumping methods [29,30]. This approach is based on the approximation of petroleum fractions as mixtures with an infinite number of components with properties that are continuous functions of one or more variables such as

boiling points. Considering a physical property *x*, the composition of a petroleum fraction can be described using a density function *n(x)* defined in such a way that the number of components for which *x* lies between x_1 and x_2 is given by:

$$N(x_1,x_2)=\int_{x_1}^{x_2} n(x)dx \tag{1.3}$$

One particular chemical property is the reactivity of the components considered. Since rate coefficients for hydrocracking increase in a monotonic way as a function of the carbon number, the following power law dependence could be proposed:

$$k = k_{\max}\theta^{1/\alpha} \tag{1.4}$$

with k_{max} the rate coefficient for the heaviest species and α a model parameter. θ represents the normalized true boiling point:

$$\theta = \frac{TBP - TBP(l)}{TBP(h) - TBP(l)} \tag{1.5}$$

with *TBP(h)* and *TBP(l)* being the highest and lowest possible boiling point of the reaction mixture. The last important aspect related to the continuous lumping approach is the introduction of a yield distribution function. This function, a density function $p_X(x)$ describes the product composition from a species with a value of *X* for that property *x*.

b Fundamental Kinetic Models

Fundamental kinetic models have been developed for thermal cracking [31,32], catalytic cracking [33,34] and hydrocracking [35-37]. Such models are developed based upon the elementary steps occurring during the reaction. The size of the reaction networks involved increases rapidly with the carbon number. Therefore, the generation of reaction networks requires a computerized algorithm, certainly for heavier components. In such an algorithm the components are manipulated in a vector or in a matrix representation. The reactions occurring in the network are represented by some specific matrix manipulations causing the reactant matrix to be transformed into the product matrix. Figure 1-9 shows the reaction matrix for a methyl shift in the approach developed by Watson et al. [33]. Adding the reaction matrix to

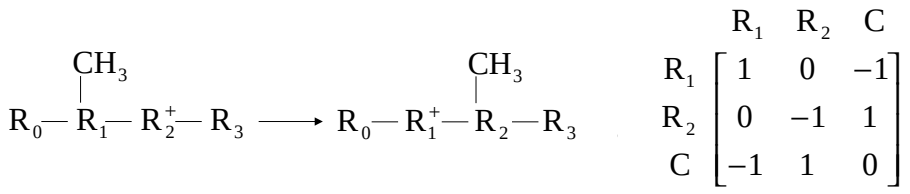

Figure 1-9 Reaction matrix for methyl shift [33]

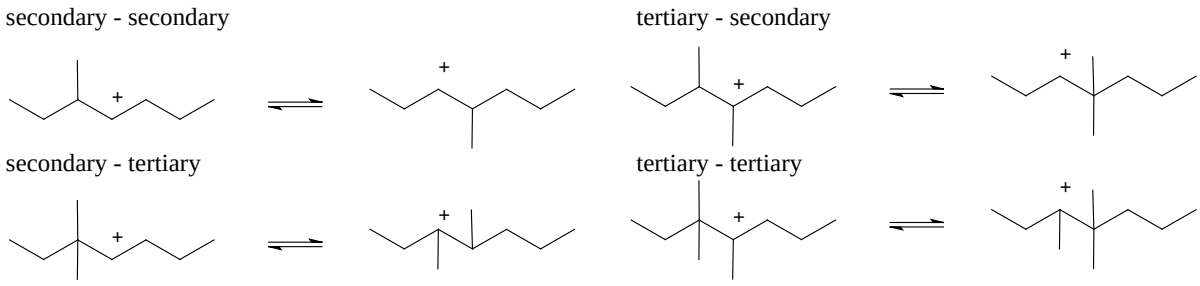

Figure 1-10 Reaction family of methyl shifts in the single-event model

the reactant matrix, the bond between R_1 and *C (methyl group)* is broken, i.e., *1* is subtracted and a bond between R_2 and *C* is formed, i.e., *1* is added, resulting in the product matrix. Deriving the kinetic equations corresponding with the generated networks without further assumptions on the kinetic coefficients involved would lead to an insurmountable number of parameters to be determined. Therefore, parameters corresponding with structurally related reactions are taken together in one reaction family, e.g., the reaction family of the methyl shifts. Within such a reaction family Watson et al. [33] used a linear free energy relationship for the activation energy. This allows the kinetic coefficient to be expressed as follows:

$$k_{i,j} = k_{0,i} \exp\left[\frac{-\left(E_{0,i} + \alpha_i \, \Delta_r H_j^0\right)}{RT}\right] \tag{1.6}$$

relating the kinetic coefficient for reaction *j* of reaction family *i* to 3 reaction family specific parameters, i.e., A_i, $E_{0,i}$ and α_i, and 1 reaction specific parameter $\Delta_r H_j^0$ which these authors obtained via calculations. In the single-event approach [31,34-37] it is assumed that, within a reaction family, the single-event kinetic coefficient only depends on the type of the radical or carbenium ion involved as reactant and product in the corresponding elementary step. Applying this to the reaction family of the methyl shifts in hydro- or catalytic cracking, 4 parameters have to be considered, vide Figure 1-10, because only secondary and tertiary carbenium ions are assumed to occur.

Although the fundamental character of such models is no doubt valuable and although they can be applied in a straightforward way for model component reactions, they become very time consuming when the conversion of realistic feedstocks, such as a vacuum gasoil is simulated. Moreover, present day analytical techniques do not allow analyses in such detail. Hence, in the case of the single-event model a relumping strategy has been developed for that purpose, retaining the fundamental character of the original model. The lumps in the model consist per carbon number of the isomers with the same branching degree. The only assumption required in the development of the relumped single event model is that within a

lump the thermodynamic equilibrium is established. Regarding the experimental observations that this equilibrium is easily established among the monobranched isomers, that it is approached among the dibranched isomers and that tribranched isomers only occur in minor amounts, this assumption is thought to be valid. Kinetic modelling of alkane and cycloalkane hydroconversion [37,38] shows the qualities of this relumped single event model for hydrocracking. Moreover, simulations of hydrotreated vacuum gasoil hydroconversion using the relumped single event model demonstrated that CPU time is not an issue [39].

1.3 Future Trends in Refining

Fuel specifications have become stringent and will even become more stringent in the future [40]. An overview of *clean fuel* specifications is given for diesels in Table 1-5. Limits on sulfur and aromatic content force the refiner to a severe hydrotreatment of the corresponding fractions. Moreover, oil reserves are not infinite and therefore the conversion of heavier, more sulfur and aromatics containing crude oil fractions will only become more important than it is already now. Typical units for conversion are delayed coking, FCC and hydrocracking, vide Section 1.1.

Because of the above presented issues, together with an increased market demand for middle distillates rather than gasoline [5], hydrocracking will inevitably increase its share in heavy oil fraction conversion. The current interest in hydrocracking technology is reflected by the various recent patent applications by UOP [41,42], Chevron [43,44] and others [45,46]. The trend for more (hydro)-conversion is evident from the Egyptian MIDOR-refinery built in 2001 [47]. The conversion capacity, i.e., 1.7 Mt yr^{-1} hydrocracking and 1.1 Mt yr^{-1} delayed coking, amounts to about 56% of the refinery's distillation capacity. Processing a wide spectrum of Arabian crude, ranging from 100% Arabian Light to 50% Arabian Light/50% Arabian heavy crude, the refinery will meet the 2005 European standards for unleaded high octane gasoline and low sulfur diesel.

Table 1-5 Diesel fuel specifications [40]

	California	Sweden Urban 1	Sweden Urban 2	Europe 2005
Sulfur content (wt%-max)	500	10	50	30-50
Aromatics (vol%-max)	10	5	20	-
Polyaromatics ([a]wt%, [b]vol%-max)	1.4[a]	0.02[b]	0.1[b]	5-11[a]
Cetane number (min)	48	50	47	52-56

1.4 References

[1] Martino, G., Courty, P., and Marcilly, C., *Handbook of heterogenous Catalysis, Chapter 3.1, Perspectives in Oil Refining* (Eds. Knözinger, Ertl, and Weitkamp) **Wiley – VCH** 1801-1818 (1997).

[2] Scherzer, J., and Gruia, A. J., *Hydrocracking Science and Technology, Chapter 1, 2 & 10, Introduction, Historical Aspects & Hydrocracking Processes* **Marcel Dekker Inc.** *New York*, 1-8, 9-12, 174-199 (1996).

[3] Environmental Protection Agency, U.S. Government, http://www.epa.gov/.

[4] Heinemann, *Catalysis: Science and Technology, Vol.1* (Eds. Anderson, J. R., and Boudart, M.) **Springer-Verlag** *New York*, 1 (1981).

[5] Maxwell, I. E., Minderhoud, J. K., Stork, W. H. J., and van Veen, J. A. R., *Handbook of heterogenous Catalysis, Chapter 3.13, Hydrocracking and Catalytic Dewaxing* (Eds. Knözinger, Ertl, and Weitkamp) **Wiley – VCH** 1801-1818 (1997).

[6] Stormont, D. H., **Oil Gas J.** *57* 48-49 (1959).

[7] Chen, N. Y., Garwood, W. E., and Dwyer, F. G., *Shape Selective Catalysis in Industrial Applications* **Marcel Dekker** *New York* (1989).

[8] Bowes, E., and Pelrine, B. P., **U.S. Patent** No. 4,388,177 (1983).

[9] Chester, A. W., Garwood, W. E., and Vartuli, J. C., **U.S. Patent** No. 4,574,043 (1986).

[10] Garwood, W. E., LeQuang, N., and Wong, S. S., **U.S. Patent** No. 5,037,528 (1991).

[11] LaPierre, R. B., and Partridge, R. D., **U.S. Patent** No. 5,284,573 (1994).

[12] Miller, S. J., **U.S. Patent** No. 4,921,594 (1990).

[13] Olavesen, C., **U.S. Patent** No. 4,421,634 (1983).

[14] Sears, P. L., de Bruijn, T. J. W., Dawson, W. H., Pruden, B. B., and Jain, A. K., **U.S. Patent** No. 5,374,348 (1994).

[15] Benham, N. K., Pruden, B. B., and Roy, M., **U.S. Patent** No. 6,004,453 (1999).

[16] Morel, F., Duplan, J. L., Billon, A, and Kressmann S., **FR. Patent** No. 2 776 297 (1998); **U.S. Patent**. No. 6,277,270 B1 (2001).

[17] Morel, F., Duplan, J. L., Billon, A, and Kressmann S., **FR. Patent** No. 2 776 298 (1998).

[18] Weekman, V. W., and Nace, D. M., *Kinetics of catalytic cracking selectivity in fixed, moving, and fluid be reactors* **AIChE J.** *16* 397-404 (1970).

[19] Jacob, S. M., Gross, B., Voltz, S.R., and Weekman, V. W., *A lumping and reaction scheme for catalytic cracking* **AIChE J.** *22* 701-713 (1976).

[20] Weekman, V. W. Jr., *Lumps, Models, and Kinetics in Practice* **AIChE J. Monogr. Ser.** *75* 3-29 (1979).

[21] Quader, S. A., Singh, S., Wiser, W. H., and Hill, G. R., *Hydrocracking of Petroleum Oils* **J Inst. Petrol.** *56* 187 (1970).

[22] Stangeland, B. E., and Kittrel, J. R., *Jet fuel selectivity in hydrocracking* **Ind. Eng. Chem. process. Des. Dev.** *11* 16 (1972).

[23] Liguras, D. K., and Allen, D. T., *Structural Models for Catalytic Cracking: 1. Model compound Reactions* **Ind. Eng. Chem. Res.** *28* 665-673 (1989).

[24] Liguras, D. K., and Allen, D. T., *Structural Models for Catalytic Cracking: 2. Reactions of Simulated Oil Mixtures* **Ind. Eng. Chem. Res.** *28* 674-683 (1989).

[25] Allen, D. T., and Liguras, D. K., *Chemical Reactions in Complex Mixtures, Structural Models of Catalytic Cracking Chemistry: a Case Study of a Group Contribution Approach to Lumped Kinetic Modelling* (Eds. Sapre A. V., and Krambeck, F. J.) **Elsevier Science Publ.** 101 – 125 (1991).

[26] Quann, R. J., and Jaffe, S. B., *Structure Oriented Lumping: Describing the chemistry of Complex Hydrocarbon Mixtures* **Ind. Eng. Chem. Res.** *31* 2483-2497 (1992).

[27] Quann, R. J., and Jaffe, S. B., *Building useful Models of Complex Reaction Systems in Petroleum Refining* **Chem. Eng. Sci.** *51* 1615-1635 (1995).

[28] Klein, M. T., Neurock, M., Nigam, A., and Libanati, C., *Chemical Reactions in complex Mixtures, Monte Carlo Modelling of Complex Reaction Systems: An Asphaltene example* (Eds. Sapre A. V., and Krambeck, F. J.) **Elsevier Science publ.** 126-142 (1991).

[29] Cicarelli, P., Astarita, G., and Gallifuoco, A., *Continuous Kinetic Lumping of Catalytic Cracking Processes* **AIChE J.** *38* 1038-1044 (1992).

[30] Laxminarasimhan, C. S., Verna, R. P., and Ramachandran, P.A., *Continuous Lumping Model for Simulation of Hydrocracking* **AIChE J.** *42* 2645-2653 (1996).

[31] Clymans, P. J., and Froment, G. F., *Computer Generation of Reaction Paths and Rate Equations in the Thermal Cracking of Normal and Branched Paraffins* **Comp. & Chem. Eng.** *8,* 137 (1984).

[32] Broadbelt, L. J., Stark, S. M., and Klein, M. T., *Computer Generated Pyrolysis Modelling: on-the-fly Generation of Species, Reactions, and Rates* **Ind. Eng. Chem. Res.** *33* 790-799 (1994).

[33] Watson, B. A., Klein, M. T., and Harding, R. H., *Mechanistic Modelling of n-heptane cracking on H-ZSM-5* **Ind. Eng. Chem. Res.** *35* 1506-1516 (1996).

[34] Dewachtere, N. V., Froment, G. F., Vasalos, I., Markatos, N., and Skandalis, N, *Advanced modelling of Riser-Type Catalytic Cracking Reactors* **Appl. Thermal. Eng.** *17* 837-844 (1997).

[35] Svoboda, G. D., Vynckier, E., Debrabandere, B., and Froment, G. F., *Single-event rate parameters for paraffin hydrocracking on a Pt/US-Y Zeolite* **Ind. Eng. Chem. Res.** *34* 3793-3800 (1995).

[36] Martens, G. G., and Froment, G. F., *Kinetic Modelling of Paraffins Hydrocracking Based Upon Elementary Steps and the Single Event Concept* **Stud. Surf. Sci. Catal.** *122* 333-340 (1999).

[37] Martens, G. G., Marin, G. B., Martens, J. A., Jacobs, P. A., and Baron, G. V., *A Fundamental Model for Hydrocracking of C_8 to C_{12} Alkanes on Pt/US-Y Zeolites* **J. Catal.** *195* 253-267 (2000).

[38] Martens, G. G., Thybaut, J. W., and Marin, G. B., *Single-Event Rate Parameters for the Hydrocracking of Cycloalkanes on Pt/US-Y Zeolites* **Ind. Eng. Chem. Res.** *40* 1832-1844 (2001).

[39] Martens, G. G., and Marin, G. B., *Kinetics for Hydrocracking Based on Structural Classes: Model Development and Application* **AIChE J.** *47* 1607-1622 (2001).

[40] Cooper, B. H., and Donnis, B. B. L., *Aromatic saturation of distillates: an overview* **Appl. Catal. A Gen.** *137* 203-223 (1996).

[41] Hoehn, R. K., and Bjorklund, B. L., **E.P. Patent** No. 1 149 886 (2001).

[42] Kalnes, T., **U.S. Patent** No. 6,328,879 (2001).

[43] Habib, M. M., **U.S. Patent** No. 5,925,235 (1999).

[44] Cash, D. R., and Dahlberg, A. J., **U.S. Patent** No. 6,224,747 (2001).

[45] Tsao, Y.-Y. P., Huang, T. J., and Angevine, P. J., **U.S. Patent** No. 6,210,563 (2001).

[46] Ishida, K., Kobayashi, M., Koyama, H., Togawa, S., and Sakaguchi, F., **U.S. Patent** No. 2002/0008051 (2002).

[47] Chang, H., *Egypt builds high-conversion refinery* **Oil Gas J.** *99* 66-68 (2001).

Chapter 2

Procedures

The work performed in the framework of this thesis can be divided into two major parts, an experimental and a modelling part. The experimental work provides, among others, insight in the effect of the operating conditions on the reaction rates and selectivities. The interpretation of the experimental results leads to guidelines for the construction of kinetic models. Via regression of those models to the experimental data, values for the kinetic parameters in these models can be estimated. Apart from the experimental work, also computational tools have been applied in the kinetic model construction [1].

2.1 Experimental

Several catalysts have been used in several experimental set-ups. A series of three Pt loaded H-(US)Y zeolites with varying aluminum content have been used to investigate average acid strength effects in alkane hydrocracking. The variation in aluminum content expressed based on the atomic silicon to framework aluminum ratio, denoted as Si/Al_F, for the catalysts used ranged from 2.6 to 60. The hydrocracking experiments on these catalysts, vide Chapter 3 and Chapter 5, have been performed at the Centrum voor Oppervlakchemie en Katalyse at Leuven University. Other hydrocracking experiments discussed in Chapter 3 have been performed at the Laboratorium voor Petrochemische Techniek at Ghent University. The hydrogenation experiments in vapour and liquid phase, vide Chapter 7 and Chapter 8 respectively, have been performed at two set-ups also at Ghent University. Pt/H-ZSM-22 was used in these experiments as hydrogenation catalyst.

2.1.1 Catalysts

Typical hydrocracking catalysts consist of a metal function deposited on an acidic support. In this work platinum was selected as metal component because of its excellent (de)-hydrogenation performance. The choice for such a hydrogenation metal implies that second stage hydrocracking is focussed on.

Four commercially available H(US)-Y zeolites were used in the hydrocracking experiments, vide Table 2-1. The acidity of most of these samples was previously characterized using ^{27}Al MAS-NMR [2,3], ammonium cation exchange capacity determination and ammonia TPD [2,3] following the method explained by Niwa et al. [4]. Platinum was deposited on these catalysts by cation exchange with $Pt(NH_3)_4Cl_2$ in aqueous solution to obtain a typical Pt content of 0.5 wt%. Activation was performed in flowing oxygen, by increasing the temperature from room temperature to 673 K at 6 K/min, and keeping this temperature for 1 h. After a purge with nitrogen, the platinum was reduced in a flow of hydrogen for 1 h at 673 K.

For the hydrogenation experiments H-ZSM-22 was selected as the acidic support because of its shape selective properties. The ZSM-22 zeolite was synthesized according to a recipe described elsewhere [5], calcined, exchanged with ammonium cations, and impregnated with an aqueous solution of $Pt(NH_3)_4Cl_2$ to obtain a Pt loading of 0.5 wt% [6]. The Pt dispersion of such a sample is 30% [7]. This low value indicates that most of the Pt metal is present as particles with a diameter of 3 nm and is located on the external surface of the zeolite crystallites since the crystal pores have only a cross section of 0.45×0.55 nm [6]. Hence, the hydrogenation occurs in the intercrystalline pores of the zeolite and no significant interaction

Table 2-1 Zeolite properties

	Provider	Si/Al [a]	Si/Al_F	C_t [b]	C_t [c]	C_t [d]	C_{strong} [d]	C_{weak}
				(mol kg_{cat}^{-1})				
H-Y-zeolite	Zeocat	2.6	2.6	4.6	-	-	-	-
CBV-720	PQ	14	18	0.600	0.604	0.620	0.560	0.060
CBV-760	PQ	30	60	0.217	0.365	0.235	0.189	0.046
LZ-Y20	Mobil	2.6	29	-	-	0.237	-	-
ZSM-22	KUL	30	30	0.36	-	0.36	-	-

[a] from ICP-AES measurements [b] Al(IV) from quantitative ^{27}Al MAS-NMR [2,3], [c] determined by cation exchange with ammonium and chemical analysis (MicroKjeldahl); [d] determined with ammonia TPD, weak sites: ΔH = 90-95 kJ mol^{-1}; strong sites: ΔH = 115-127 kJ mol^{-1}. The method was explained in [4], some of these data were published in [3]

between the Pt and the acid sites is expected. As a consequence, the hydrogenation behaviour on Pt/H-ZSM-22 is expected to be similar to that on a Pt/silica catalyst. However, because the ultimate goal of the research on hydrocracking at the 'Laboratorium voor Petrochemische Techniek' is the development of simulation models for industrial hydrocracking units, a hydrocracking catalyst, c.q., Pt/H-ZSM-22, is selected rather than a pure hydrogenation catalyst such as Pt/silica. The total concentration of active sites on Pt/H-ZSM-22, C_t, is calculated based on the accessible number of Pt atoms and amounts to 7.7 10^{-3} mol kg_{cat}^{-1}. Acid catalyzed conversion of hydrocarbons is limited by the shape selective character of the intracrystalline pores of the ZSM-22 zeolite [8]. The rest of the activation procedure is similar to that of the H(US)Y-zeolites described above.

2.1.2 Vapour-Phase Continuous Stirred Tank Reactor Set-Up

A schematic representation of the set-up is given in Figure 2-1, with the symbols used explained in Figure 2-2. Four different sections can be distinguished, i.e., (i) the feed section, (ii) the reaction section, (iii) the effluent section and (iv) the analysis section. Each of these sections will be discussed in detail below.

a Feed Section

The liquid hydrocarbon feed (1) is pumped to the reaction section using an HPLC pump (High Pressure Liquid Chromatography) (2). Liquid flow rates can be adjusted between 10 μmol s^{-1} and 500 μmol s^{-1}. The viscosity of the feed determines the upper flow rate. In order to avoid too low maximum flow rates for heavy components, the feed line can be heated to reduce the viscosity of the feed. The purities of hydrogen (99.99 vol%, L'Air Liquide) and nitrogen (99.8 vol%, L'Air Liquide) were selected so that further purification was unnecessary [9]. The hydrogen and nitrogen flow rates are controlled using Brooks thermal mass flow controllers in the range of 5 to 100 μmol s^{-1} for hydrogen (3) and of 50 μmol s^{-1} to 1 mmol s^{-1} for nitrogen (4). Both gas flows are mixed and the majority of the mixture is sent to the reaction section via a mixer/evapourator/preheater (6) where it is mixed with the evapourating hydrocarbons and preheated to a typical temperature of 473 K. The remaining part of the hydrogen/nitrogen mixture enters the reaction section via the shaft of the magnetic drive assembly to cool it and to prevent hydrocarbon condensation in that shaft.

b Reaction Section

The high pressure reactor (8) is of the Berty type constructed by Autoclave Engineers. A magnetic driven impeller (11) induces an internal recycle flow pattern in the reactor going

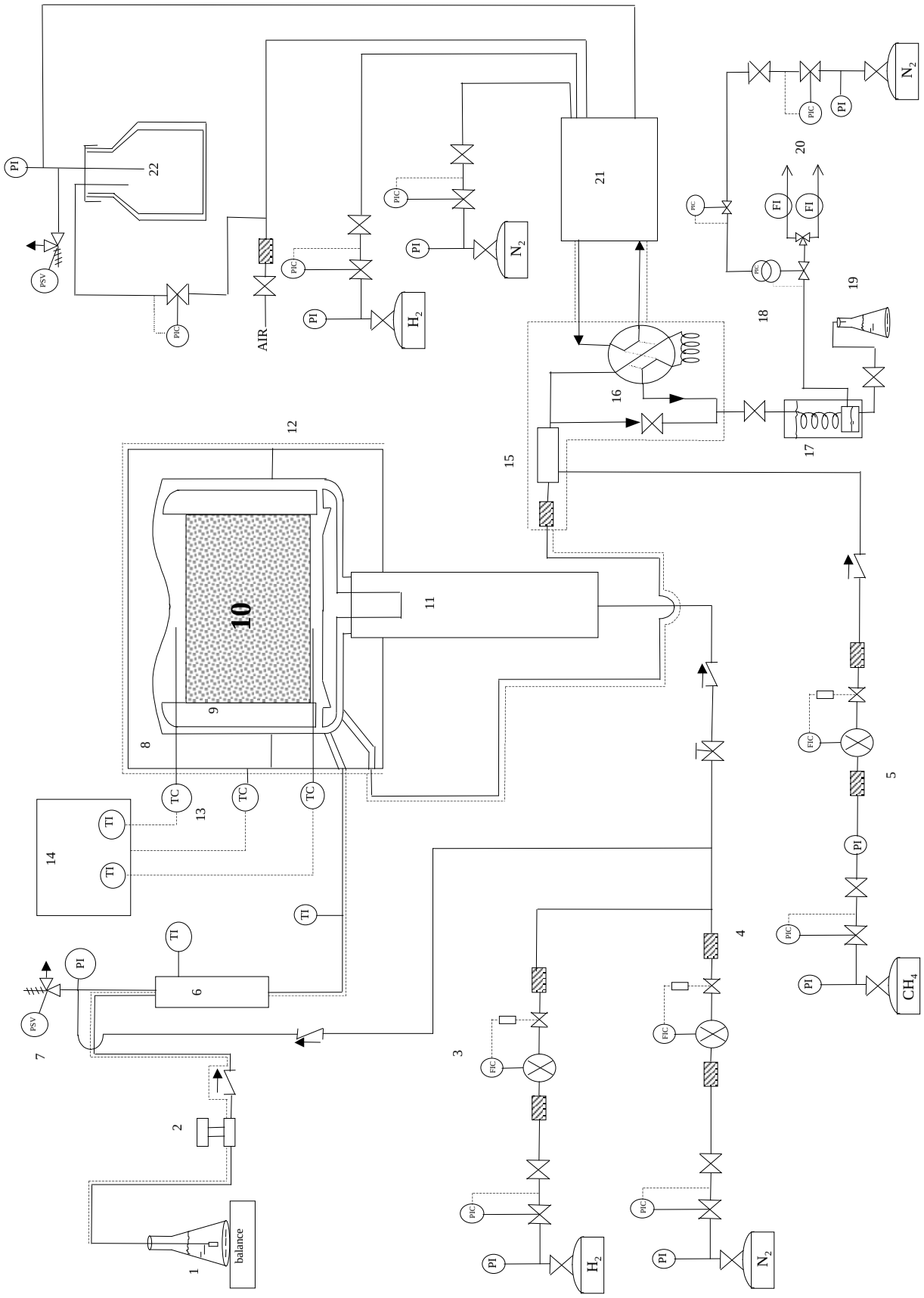

Figure 2-1 Schematic representation of the vapour-phase CSTR set-up

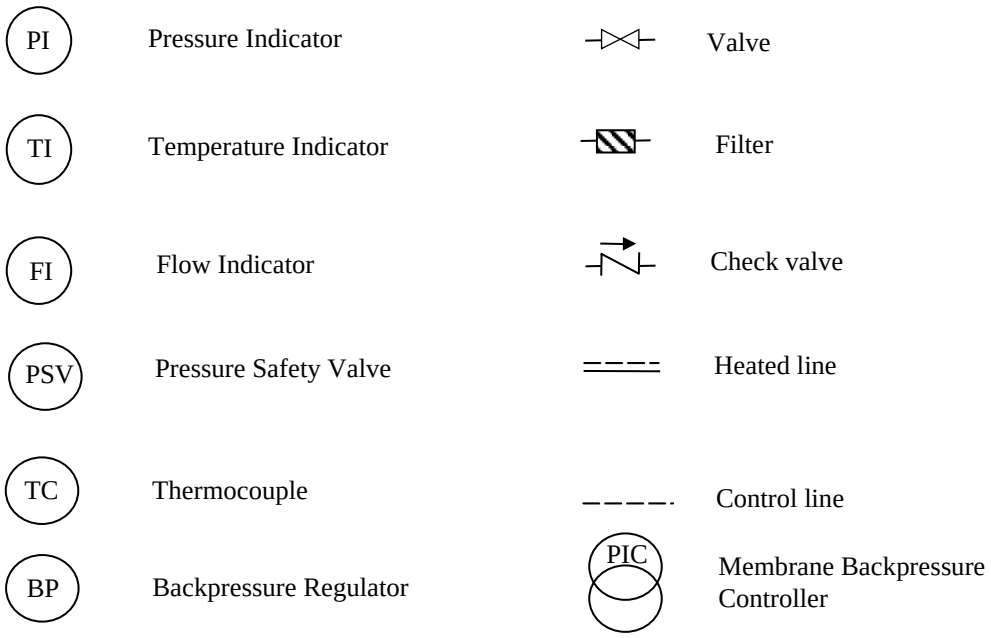

Figure 2-2 Symbols used in the schematic representations of the various experimental set-ups

upward between the catalyst basket (9) and the reactor wall and going down through the catalyst basket (10). The gaseous hydrogen/nitrogen/hydrocarbon mixture enters the reactor just above the blades of the impeller, while the effluent leaves the reactor at the bottom under the impeller. If a uniform flow through the catalyst bed is established and a recycle ratio of at least 20 is obtained, the Berty reactor can be modeled as a continuous stirred tank or a mixed flow reactor [10]. Typically the impeller is set to revolve at a speed of 1500 rpm. The temperature in the reactor is maintained by a heating cap (12) containing three heating elements of 500 W each controlled by two PID controllers (13) and (14) connected to two thermocouples measuring the temperature just on top of and below the catalyst basket. A third thermocouple is used as a safety control to measure the external wall temperature of the reactor. It is connected to an on-off switch ensuring that the temperature will not rise above a certain safety level. The sealing between the reactor body and cover is ensured by the use of a ductile aluminum gasket. Due to its high ductility, the gasket needs to be replaced after tightening the reactor screws a few times.

c Effluent and Analysis Section

The reactor effluent passes through a filter (15) before being mixed with the internal standard methane. The molar methane (99,95 vol% L'Air Liquide) flow rate is controlled with a Brooks thermal mass flow controller (5) in the range 5 to 100 μmol s^{-1} and is taken equal to the molar hydrocarbon feed flow rate. The mixture of the reactor effluent and the internal

standard is split into two flows. The major flow is directly sent to a condenser (17), while a minor flow passes through a six-way sampling valve (16) before being sent to the condenser. In the condenser the major part of the hydrocarbons condenses and is kept in a collector. The uncondensed part of the reactor effluent flows through the back pressure regulator (18) which is used to keep the installation under the desired pressure and is sent to the vent afterwards (20).

A 20 µl sample of the reactor effluent is sent on-line to a gas chromatograph (GC Hewlett Packard 5890 series II) (21) by changing the position of the six-way valve. A capillary column of 60 m and internal diameter 0.25 mm with a 1 µm thick polydimethylsiloxane film is used to separate the various hydrocarbons in the mixture. With a cryogenic cooling equipment (22) it is possible to work at temperatures lower than room temperature improving the separation of light components. An FID-detector is used in the GC-analysis. The signal generated by the detector is sent to a local PC where the XChrom package performs the integration of the chromatogram.

2.1.3 Vapour-Phase Plug Flow Reactor Set-Up

A schematic representation of the vapour-phase plug flow reactor set-up at Leuven University is given in Figure 2-3 with the symbols used explained in Figure 2-2. Similar to the previously described vapour-phase CSTR set-up, four sections can be distinguished, i.e., the feed, the reaction, the effluent and the analysis section.

a Feed Section

The liquid hydrocarbons are pumped by an HPLC pump (2) from a feed recipient (1) to a flash vessel (3) where they are mixed with hydrogen. Typical hydrocarbon feed flow rates are in the range 5 to 50 µmol s^{-1}. The hydrogen (99.99 vol% L'Air Liquide) flow rate is controlled using a Brooks thermal mass flow controller (4) in the range 5 to 150 µmol s^{-1}. Separate gas feed lines for catalyst pretreatment are also available: an oxygen and nitrogen feed line (5) for calcination and one for hydrogen (6) to reduce the catalyst. A six-way valve (7) is used to select the flow, which is sent to the reactor.

b Reaction Section

The reactor (8) consists of a 0.18 m long round inox tube with an internal diameter of 10^{-2} m. Quartz wool is used to maintain the catalyst in its position. Catalyst weights between 0.3 10^{-3} and 4.5 10^{-3} kg can be loaded into the reactor. The reactor is located in an oven, the

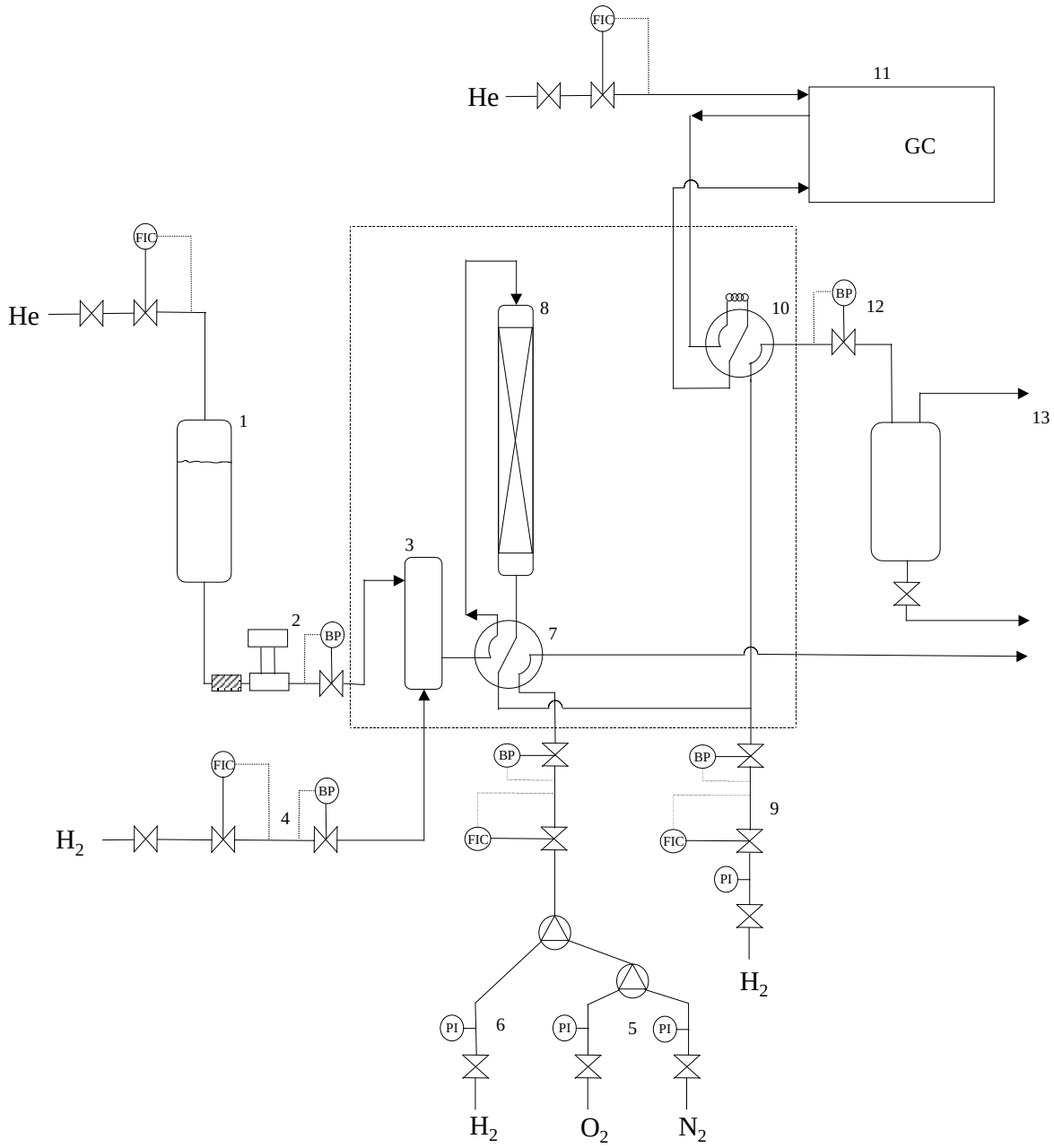

Figure 2-3 Schematic representation of the vapour-phase plug flow set-up

temperature of which is controlled by a PID-regulator. A thermocouple is also present inside the reactor to know the exact temperature of the catalyst bed.

c Effluent and Analysis Section

Downstream of the reactor the reactor effluent is diluted with hydrogen (9) before being sent to a second six-way valve (10) with which an effluent sample is sent on-line to the GC (11). The extra dilution with hydrogen is required not to saturate the column of the GC. After the six-way valve the effluent flow is sent to a condenser via the back-pressure regulator (12). In

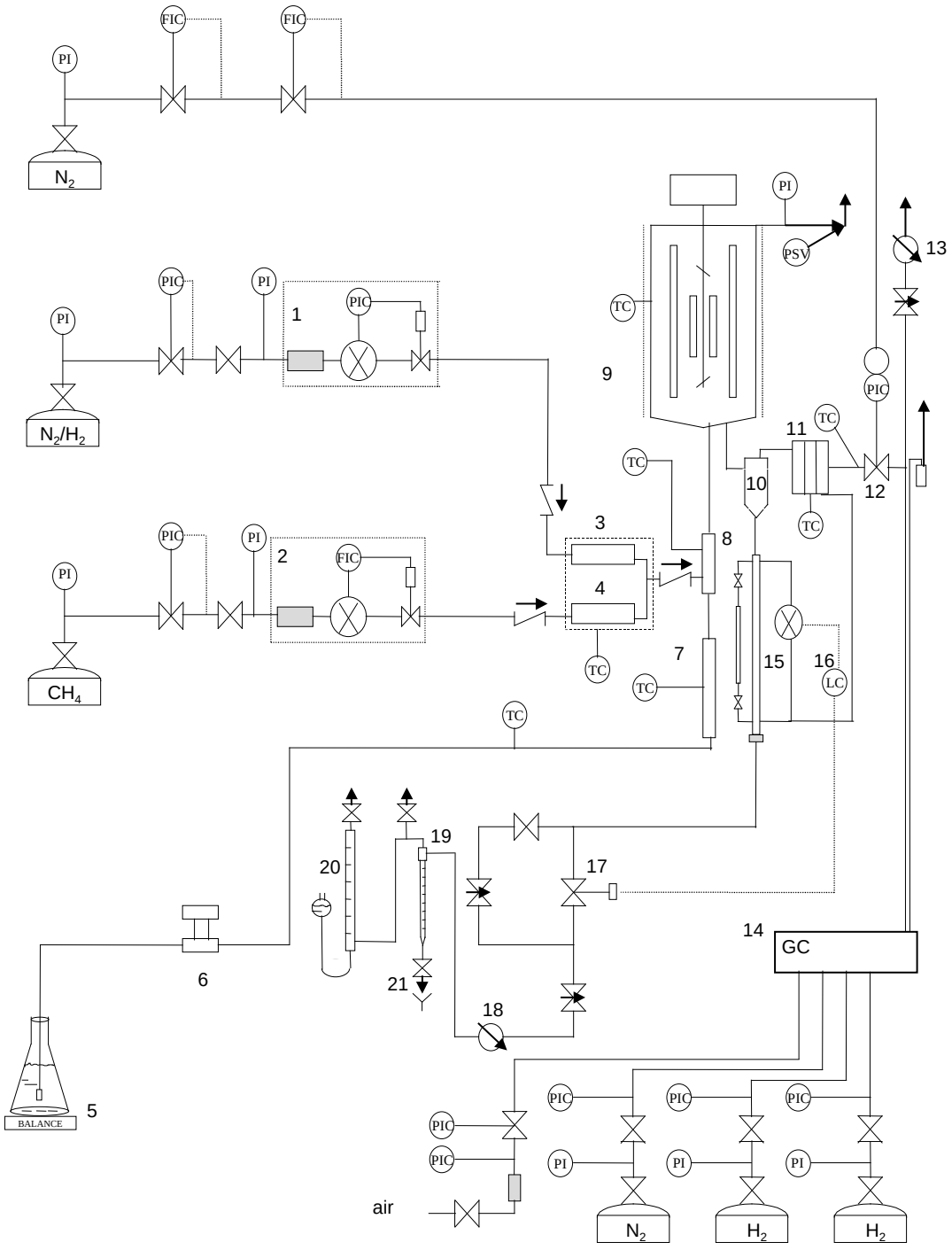

Figure 2-4 Schematic representation of the liquid-phase CSTR set-up

the condenser, the hydrocarbons are collected and the non condensable gases are sent to the vent (13). The GC is equipped with a 50 m CP-SIL 5 CB a-polar capillary column to separate the hydrocarbons in the sample. The separated components are detected by an FID, the signal of which is sent to a local PC for further treatment.

2.1.4 Three-Phase Continuous Stirred Tank Reactor Set-Up

A schematic representation of the liquid-phase CSTR set-up is given in Figure 2-4 with the symbols used explained in Figure 2-2. Similar to the previously described set-ups, four sections can be distinguished, i.e., the feed, the reaction, the effluent and the analysis section.

a Feed Section

Two gas feed lines are available for a hydrogen/nitrogen mixture (10 vol% H_2/90 vol% N_2, L'Air Liquide) and for methane as internal standard (99.95 vol%, L'Air Liquide). The purities of the gases are selected so that no further purification is required. The flow rates are controlled by two Brooks thermal mass flow controllers in the range 10 to 700 μmol s^{-1} for the hydrogen/nitrogen mixture (1) and in the range 1 to 70 μmol s^{-1} for methane (2). The two gas flows are preheated separately, (3) and (4), before they are mixed (8) and sent to the reaction section. The liquid hydrocarbon feedstock (5) is fed by an HPLC pump (6), identical to the one used in the vapour-phase CSTR set-up. The liquid feed line can be heated to reduce the viscosity of the feed and, hence, to allow higher liquid flow rates through the feed line. Before entering the reaction section, the liquid feed is preheated (7) and mixed with the gas flows (8). In this mixer, the gases are dispersed in the liquid phase by means of a sintered stainless steel filter.

b Reaction Section

The Robinson Mahoney reactor, vide Figure 2-5, is a multiphase (gas/liquid/solid) reactor equipped with a cylindrical catalyst basket. The catalyst, mixed with inert material, is located at mid-height of the basket, where the flow through the basket is most uniform. More inert material is present in the catalyst basket directly above and under the catalyst/inert mixture, while at the top and the bottom the basket is filled with glass wool. A magnetically driven impeller induces a flow pattern directed to the reactor wall through the catalyst basket and with recirculation above and under the basket. Typically the impeller is set to revolve at a speed of 1500 rpm, ensuring a good mixing of the reaction mixture inside the Robinson Mahoney reactor.

c Effluent Section

The gas liquid mixture leaves the Robinson Mahoney reactor via a down-comer and is separated in a cyclone (10). Because some small droplets may still be entrained with the gas flow, it is passed through a demister (11). The droplets are retained there in a gauze and collected in a tube connected to the liquid effluent outlet of the cyclone. The 'dry' gas leaves

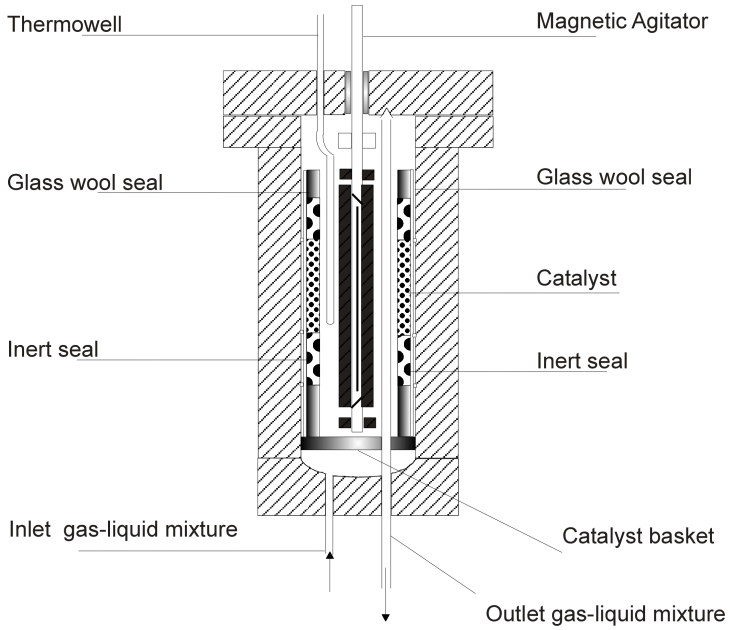

Figure 2-5 Schematic representation of the Robinson Mahoney reactor.

the demister at the top and flows to a back pressure regulator (12) with which the set-up is kept under the working pressure. After the back pressure regulator the gas flow is split into a main stream which is sent directly to a condenser (13) and into a smaller stream which is sent to a GC (14) for on-line analysis.

The liquid effluent of the cyclone enters a tubular reservoir (15). The liquid level in this tube is governed by an automatic level controller (16), which discharges periodically the liquid from the reservoir by means of an automatic valve (17). Downstream of the level control system the liquid flow is cooled (18) and flashed (19). Upon flashing the gas dissolved in the liquid is liberated and captured in a gas burette (20) connected with a vessel open to the air. This allows to measure the flow rate of the gas that was dissolved in the liquid under reaction conditions, further denoted as 'flashed gas'. The 'flashed liquid' falls down by gravity and is collected in a liquid burette (21) where the flashed liquid flow rate can be measured. Off-line samples can be taken from the flashed liquid and flashed gas for analysis on the GC (14).

d Analysis Section

The analyses of the effluent streams were performed with a CP 9000 GC. Two systems are installed in this GC, one using a thermal conductivity detector (TCD) for the determination of the hydrogen content in the effluent streams and a second using a flame ionization detector (FID) for the determination of the hydrocarbons in the effluent streams.

For the on-line analysis of the gas effluent two heated six way sampling valves (4) and (5) are used, vide Figure 2-6. The effluent gas continuously flows through the valves in short-circuit.

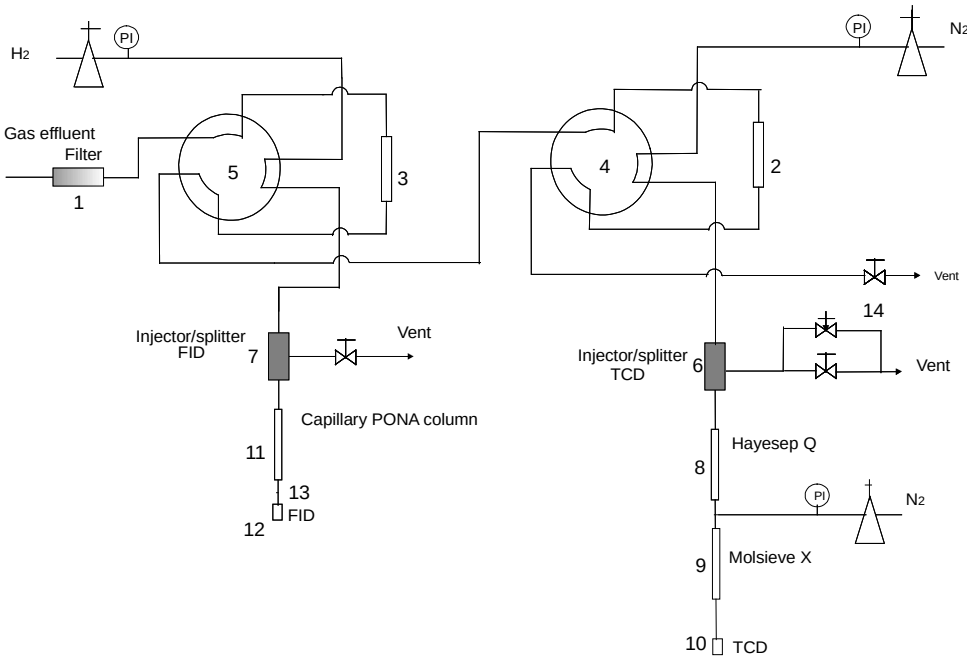

Figure 2-6 Detailed schematic representation of the analysis section used in the liquid-phase CSTR set-up

Actuators driven by compressed air perform manipulation of the valves. By changing the position of the valves once, the sample loops (2) and (3) are filled with effluent and by restoring the original position of the sampling valves, the actual injection occurs. The off-line analysis of the flashed liquid and the flashed gas is performed by injection of the samples by syringe via the injection ports.

On the TCD system hydrogen and methane are separated on a 1m packed Molsieve CP5A column with a 3.175 mm diameter. The separation of both components can be easily performed under isothermal conditions at 308 K. Nitrogen is used as carrier gas. A Hayesep-Q pre-column combined with a back-flush system prevents the heavier components in the sample from reaching the molsieve column and disturbing its performance. On the FID system the hydrocarbons are separated on a 100m capillary HP-PONA column with a 0.25 mm diameter. The film thickness in the column is 0.5 μm and hydrogen is used as carrier gas.

2.1.5 Conversion, Yields and Selectivities

The conversion of a feedstock component *i* is defined by:

$$X_i = \frac{F_i^0 - F_i}{F_i^0} \times 100\% \tag{2.1}$$

while the total feedstock conversion is defined as a weighted average of the individual components' conversions:

$$X_{tot} = \sum_{i=1}^{n_{feed}} z_i^0 X_i \tag{2.2}$$

Due to *cracking*, the total conversion X_{tot} can amount to 100%. This calculation of the conversion is dependent on the method used in the calculation of the outlet flow rates [11]. The outlet flow rates are calculated using an internal standard, vide paragraph 2.1.6, to enable the verification of mass and element balances over the set-up. However, to obtain reliable values for the conversion, yields and selectivities, the values of the individual outlet flow rates used in the calculation of these values are scaled in order to match a 100% carbon balance.

For the hydrocracking experiments isomer and cracking yields are defined on weight basis:

$$Y_{iso} = \sum_{j=1}^{n_{iso}} \frac{MW_j F_j}{MW_i F_i^0} \tag{2.3}$$

$$Y_{cr} = \sum_{j=1}^{n_{cr}} \frac{MW_j F_j}{MW_i F_i^0} \tag{2.4}$$

with n_{iso} and n_{cr} being the number of isomers and cracked products respectively. The selectivities to isomers and cracked products are expressed as isomerization and cracking conversion and are obtained from:

$$X_{iso} = \frac{\sum_{j=1}^{n_{iso}} F_j}{F_i^0} \times 100\% \tag{2.5}$$

$$X_{cr} = \frac{\sum_{j=1}^{n_{cr}} F_j}{F_i^0} \times 100\% \tag{2.6}$$

Because only isomers and cracked products are formed, the isomerization and cracking conversion are related to each other via:

$$X_{tot} = X_{iso} + X_{cr} \tag{2.7}$$

2.1.6 Calculation of the Outlet Flow Rates

a Vapour-Phase Set-Ups

In both vapour-phase set-ups the effluent analysis is only performed with an FID detector. Because an FID detector is insensitive to hydrogen and nitrogen, the effluent composition is determined only in terms of hydrocarbons. The corresponding mole fraction y_i of the hydrocarbon *i* is calculated from:

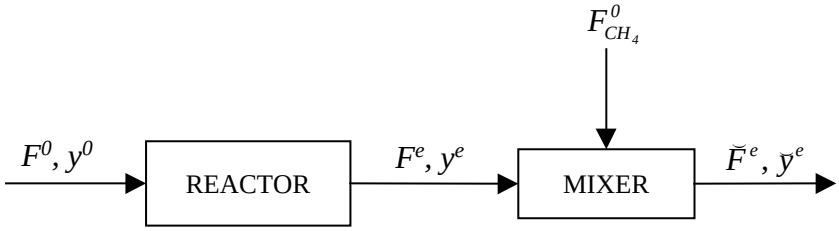

Figure 2-7 Hydrocarbon flow diagram with use of an internal standard

$$y_i = \frac{A_i \, CF_i^{FID} / MW_i}{\sum_j A_j \, CF_j^{FID} / MW_j} \tag{2.8}$$

with A_i the integrated surface area for hydrocarbon i and with CF_i and MW_i its calibration factor and molecular weight respectively. The calibration factors can be determined according to the method proposed by Dierickx et al. [12], however, this method results in calibration factor which are essentially the same as those reported by Dietz [13]. If the outlet flow rate of one of the components is known, the outlet flow rates of all other hydrocarbons in the effluent can be derived and, hence, a mass balance over the reactor can be calculated. Therefore a controlled flow rate of methane is added to the reactor effluent, vide Figure 2-7. Methane is chosen for several reasons, the most important one being the availability of methane in high pressure cylinders, higher than the pressures typically used in hydrocracking experiments. Minor amounts of methane and ethane can, however, be produced during reaction due to hydrogenolysis. The occurrence of hydrogenolysis is verified via experiments without internal standard fed. If so, the methane outlet flow rate in the corresponding experiment with internal standard has to be corrected for the amount of methane that has been produced by hydrogenolysis. From the experiment without internal standard, the ratio of the molar outlet flow rates of methane and ethane can be determined:

$$C_{1/2} = \frac{F^e_{CH_4}}{F^e_{C_2H_6}} = \frac{y^e_{CH_4}}{y^e_{C_2H_6}} \tag{2.9}$$

However, since the peak resolution between methane and ethane is often insufficient when methane is fed as internal standard, the ratio of the molar outlet flow rates of ethane and propane has to be determined as well:

$$C_{2/3} = \frac{F^e_{C_2H_6}}{F^e_{C_3H_8}} = \frac{\breve{F}^e_{C_2H_6}}{\breve{F}^e_{C_3H_8}} = \frac{\breve{y}^e_{C_2H_6}}{\breve{y}^e_{C_3H_8}} \tag{2.10}$$

Eq. (2.9) and Eq. (2.10), together with a methane balance over the mixer:

$$\breve{F}^e_{CH_4} = F^e_{CH_4} + F^0_{CH_4} \tag{2.11}$$

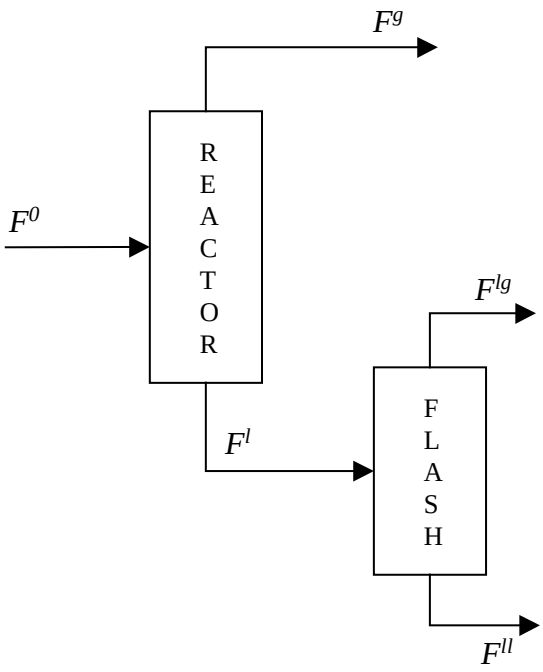

Figure 2-8 Scheme of in- and outlet flows of the liquid-phase set-up

lead to the following expression for the total molar hydrocarbon outlet flow rate in an experiment with internal standard:

$$\breve{F}^e_{HC} = \frac{F^0_{CH_4}}{\breve{y}^e_{CH_4} - C_{1/2}\, C_{2/3}\, \breve{y}^e_{C_3H_8}} \tag{2.12}$$

With the effluent mole fractions from Eq. (2.8) and the total molar outlet flow rate from Eq. (2.12) all individual hydrocarbon molar outlet flow rates can be calculated and can be used in the verification of the carbon balance:

$$BAL_C = 100\% \frac{\breve{F}^e_{HC} \sum_i C_i \breve{y}^e_i - F^0_{CH_4}}{F^0_{HC} \sum_i C_i y^0_i} \tag{2.13}$$

Only those experiments with values for BAL_C between 95 and 105 % are retained. As explained in paragraph 2.1.5 the use of the internal standard is limited to the verification of the performance of the set-up.

b Liquid-Phase Set-Up

The in- and outlet streams of the liquid-phase set-up are schematically represented in Figure 2-8. The set-up has three effluent streams: (1) the gas-phase effluent, denoted as F^g, (2) the flashed gas effluent, F^{lg}, and (3) the flashed liquid effluent, F^{ll}. Samples of all effluent streams can be analyzed on an FID as well as on a TCD detector, the analysis of the gas effluent being on-line and the analyses of the flashed gas and flashed liquid effluent being off-line.

Hydrogen and nitrogen are the most abundant gases in the *flashed gas* effluent, together with some small amounts of light hydrocarbons. The composition of the flashed gas effluent is determined on the FID as well as on the TCD detector. The FID analysis of the flashed gas effluent leads to the mole fractions of the hydrocarbons without hydrogen and nitrogen:

$$x_i^{*,lg} = \frac{A_i \; CF_i^{FID} / MW_i}{\sum_j A_j \; CF_j^{FID} / MW_j} \tag{2.14}$$

From the TCD-analysis the molar hydrogen to methane fraction is determined:

$$x_{H_2}^{*,lg} = \frac{CF_{H_2}^{TCD} \; A_{H_2} \; x_{CH_4}^{*,lg}}{A_{CH_4}} \tag{2.15}$$

The molar hydrogen to nitrogen ratio $x_{H_2}^{*,lg} / x_{N_2}^{*,lg}$ is determined by ASPEN [14] simulations of the reactor mixture, vide Appendix A. Normalization of the mole fractions without hydrogen and nitrogen, $x^{*,lg}$, leads to the mole fractions x^{lg} covering all components in the flashed gas effluent.

The total volumetric flow rate of the flashed gas effluent is measured and applying the ideal gas law, the total molar flow rate can be obtained:

$$F^{lg} = \frac{Q^{lg} \, p}{RT} \tag{2.16}$$

The *flashed liquid* effluent is a mixture consisting of mainly hydrocarbons. The amount of light gases dissolved in the flashed liquid is very low, e.g., the amount of hydrogen is lower than the TCD detection limit. Hence, only an FID analysis of the flashed liquid is required to determine the overall composition of the flashed liquid.

$$x_i^{ll} = x_i^{*,ll} = \frac{A_i \; CF_i^{FID} / MW_i}{\sum_j A_j \; CF_j^{FID} / MW_j} \tag{2.17}$$

The total volumetric flow rate of the flashed liquid is measured. Using the molar volume of the flashed liquid, calculated based on the Hankinson-Brobst-Thomson method [15], the total molar flow rate of the flashed liquid is obtained:

$$F^{ll} = \frac{Q^{ll}}{V_m^{ll}} \tag{2.18}$$

The *gas effluent* is a mixture consisting of nitrogen, hydrogen and hydrocarbons and is, therefore, analyzed on the FID as well as on the TCD detector. Similar to the determination of

the flashed gas effluent composition the mole fractions of the hydrocarbons without hydrogen and nitrogen are obtained via an FID analysis:

$$y_i^{*,g} = \frac{A_i \; CF_i^{FID} / MW_i}{\sum_j A_j \; CF_j^{FID} / MW_j} \tag{2.19}$$

and the molar hydrogen to methane ratio from a TCD analysis:

$$y_{H_2}^{*,g} = \frac{CF_{H_2}^{TCD} \; A_{H_2} \; y_{CH_4}^{*,g}}{A_{CH_4}} \tag{2.20}$$

The molar hydrogen to nitrogen ratio $y_{H_2}^{*,lg} / y_{N_2}^{*,lg}$ is determined by ASPEN simulations of the reactor mixture. Normalization of the mole fractions without hydrogen and nitrogen, $y^{*,g}$, leads to the mole fractions y^g covering all components in the flashed gas effluent.

The total gas effluent flow rate is determined using an internal standard. Methane is used as internal standard for similar reasons as in the vapour-phase set-up. Assuming that no methane is formed or consumed during reaction, the total gas effluent flow rate is determined from:

$$F^g = \frac{F_{CH_4}^g}{y_{CH_4}^g} = \frac{F_{CH_4}^0 - F_{CH_4}^{lg} - F_{CH_4}^{ll}}{y_{CH_4}^g} \tag{2.21}$$

It was verified with ASPEN simulations that the methane gas effluent flow rate approaches the methane inlet flow rate and, hence, Eq. (2.21) can be simplified into:

$$F^g = \frac{F_{CH_4}^g}{y_{CH_4}^g} \approx \frac{F_{CH_4}^0}{y_{CH_4}^g} \tag{2.22}$$

The individual flow rates of the components in the reactor effluent are then calculated as the sum of the individual flow rates in the three effluent streams:

$$F_i = F_i^g + F_i^{lg} + F_i^{ll} \tag{2.23}$$

The verification of the calculated individual outlet flow rates is performed by calculating the hydrogen and the carbon balance over the reactor. These balances are based on the individual molar in- and outlet flow rates:

$$BAL_C = 100\% \frac{\sum_j CN_j \; F_j^g + \sum_j CN_j \; F_j^{lg} + \sum_j CN_j \; F_j^{ll}}{\sum_j CN_j \; F_j^0} \tag{2.24}$$

$$BAL_H = 100\% \frac{\sum_j HN_j \; F_j^g + \sum_j HN_j \; F_j^{lg} + \sum_j HN_j \; F_j^{ll}}{\sum_j HN_j \; F_j^0} \tag{2.25}$$

Only experiments with values for BAL_C and BAL_H between 95% and 105% are retained.

2.2 Modelling

2.2.1 Parameter Estimation Method

Parameter estimation occurs by minimization of the weighted sum of squares of the residuals between the experimental and model calculated outlet flow rates. The minimization occurs by adjusting the model parameter vector ***b***, which is expected to approach the real parameter vector β when the optimum is reached:

$$SSQ = \sum_{k=1}^{nob} \sum_{j=1}^{nresp} w_i \left(F_{i,k} - \hat{F}_{i,k}\right)^2 \xrightarrow{\boldsymbol{b}} Min \tag{2.26}$$

in which $F_{i,j}$ stands for the experimentally observed outlet flow rate of response j in experiment i and where the ^ represents model calculated values. The outlet flow rates are used as responses and not the net production rates in order to eliminate correlation between the independent variables and the responses. Such a correlation is encountered when the net production rates are used as responses because the outlet flow rates are then used to calculate both the experimentally observed net production rates and the partial pressures used in the model calculated net production rates. In case of a normal distribution with zero mean of the experimental errors the weighting factors w_j are obtained as the diagonal elements of the inverse of the covariance matrix of the experimental errors. In general this matrix is not readily available and has to be estimated. This is possible when at r different inlet conditions n_{k_r} replicate experiments are available. The weighting factors can then be obtained from:

$$w_j = \left[\frac{1}{\left(\sum_{k=1}^{r} n_k \right) - r} \sum_{k=1}^{r} \sum_{i=1}^{n_k} \left(F_{j,i}^k - \overline{F}_j^k\right)^2 \right]^{-1} \tag{2.27}$$

with $F_{j,i}^k$ the experimental value of response j in experiment i under conditions k and with $\overline{F}_{j,i}^k$ the mean value for response j under conditions k. If no replicate experiments are available the weighting factors can be calculated from:

$$w_j = \frac{\left(\sum_{k=1}^{nob} F_{j,k} \right)^{-m}}{\sum_{j=1}^{nresp} \left(\sum_{k=1}^{nob} F_{j,k} \right)^{-m}} \tag{2.28}$$

For *m=0* all responses are equally weighted while for *m=1* the weighting factors express the relative importance of the responses.

Parameter estimations were performed using a combination of a Rosenbrock [16] and a Marquardt [17] algorithm. Because the Rosenbrock method has a smaller chance to diverge when the parameter values are far from the optimum, this method is applied first to find an appropriate direction leading to a possible optimum. Only afterwards the Marquardt algorithm takes over to arrive at the optimum. In order to prevent the combined Rosenbrock Marquardt search from arriving in a local optimum a cycle of a few Rosenbrock Marquardt searches is performed until the residual sum of squares obtained from both methods is identical and does not improve significantly with variations in the parameters. An in-house written code was used for the Rosenbrock method, while for the Marquardt algorithm the 'ordinary least squares' (OLS) option of the ODRPACK-package version 2.01 [18,19] was used. Some additional source code was added to ODRPACK in order to retrieve additional statistical information.

Several statistical tests are performed to evaluate the parameter estimation results. These tests include the *F*-test on the significance of the regression and the Student's *t*-test on the significance of the individual parameters. The values tabulated for the 95% confidence level are typically used when performing these tests.

The *F*-value to test the significance of the regression is calculated as the ratio of the regression sum of squares and the residual sum of squares divided by their respective degrees of freedom:

$$F_{regres} = \frac{\dfrac{\sum_{i=1}^{nob}\sum_{j=1}^{nresp} w_j \hat{F}_{i,j}^2}{npar}}{\dfrac{\sum_{i=1}^{nob}\sum_{j=1}^{nresp} w_j \left(F_{i,j} - \hat{F}_{i,j}\right)^2}{nob\ nresp - npar}} \tag{2.29}$$

with the regression being significant when the calculate F_{regres}-value is higher than the tabulated $F_{npar,\ nob\ nresp\ -\ npar}(0.95)$-value.

The 95% approximate individual confidence interval for the parameters are calculated as:

$$b_i - t_{nob\,nresp-npar}(0.95)\sqrt{V(b)_{i,i}} < b_i < b_i + t_{nob\,nresp-npar}(0.95)\sqrt{V(b)_{i,i}} \tag{2.30}$$

with $t_{nob\ nresp\ -\ npar}(0.95)$ the tabulated *t*-value and $V(b)_{i,i}$ the diagonal element on row *i* of the covariance matrix $V(b)$ of the parameter values b_i:

$$V(b) = \left[\sum_{i=1}^{nresp} w_i J_i{}^T J_i \right]^{-1} \tag{2.31}$$

with J_i the Jacobian matrix of response i:

$$J_i = \left[\frac{\partial F_i(b)}{\partial b} \right] \tag{2.32}$$

The element on row j and column k of J_i represents the partial derivative of response i, F_i, with respect to parameter b_k for the reaction conditions of experiment j at the final parameter values.

The correlation between the estimated parameter values is investigated based upon the binary linear correlation coefficients:

$$\rho_{i,j} = \frac{V(b)_{i,j}}{\sqrt{V(b)_{i,i} V(b)_{j,j}}} \tag{2.33}$$

Absolute values for $\rho_{i,j}$ close to *1* indicate a strong linear relationship between the estimated values of the corresponding parameters i and j. The value of parameter i determines the value of parameter j to a proportional, $\rho_{i,j} \sim 1$, or inverse proportional, $\rho_{i,j} \sim -1$, extent without changing the calculated responses and, hence, the residual sum of squares in a significant way.

2.2.2 Reactor Model Equations

The calculated responses used in the determination of the residual sum of squares are obtained from a mass balance over the reactor. Pseudohomogeneous models are used in the reactor modelling [20]. In case of a CSTR (Berty, Robinson Mahoney reactor) the molar outlet flow rate of a component j in experiment i is obtained from the solution of the set of *nresp* algebraic equations in the *nresp* unknown molar outlet flow rates $F_{i,j}$:

$$F_{i,j} - F_{i,j}^0 - R_{i,j} W_i = 0 \tag{2.34}$$

W_i being the catalyst mass used in experiment i and $R_{i,j}$ being the net rate of formation of component j at the reaction conditions of experiment i. In case of a plug flow reactor a one-dimensional model is used to obtain the axial flow rate profiles through the reactor and, hence, the outlet flow rates by integration of the set of differential equations for each individual response:

$$\frac{dF_{i,j}}{dW_i} = R_{i,j} \tag{2.35}$$

or in integrated form:

$$F_{i,j} - F_{i,j}^{0} = \int_{0}^{W_i} R_{i,j}\, dW \tag{2.36}$$

Only *nresp – 2* of the outlet flow rates are independent one from another since the outlet flow rate for *2* of the components are calculated using the hydrogen and the carbon balance. It was chosen to calculate the hydrogen flow rate from the hydrogen balance and the feed component flow rate from the carbon balance. For a given set of kinetic parameters the net rates of formation for the components *j* under the conditions corresponding with experiment *i* are a function of the reaction temperature, T_i, the reaction total pressure, p_t, and the composition of the reaction mixture, $z_{i,j}$:

$$R_{i,j} = f\left(T_i; p_t; z_{i,1}; z_{i,2}; \ldots; z_{i,nresp}\right) \tag{2.37}$$

and is calculated using the appropriat rate equations developed further in this thesis. The mole fractions $z_{i,j}$ of the components are calculated from:

$$z_{i,j} = \frac{F_{i,j}}{\sum_{j=1}^{nresp} F_{i,j}} \tag{2.38}$$

These mole fractions represent the global composition of the reaction mixture. In case of multiphase operation, such as in a Robinson Mahoney reactor, the vapour and liquid phase composition is calculated from this global composition, temperature and total pressure via equilibrium calculations using the Peng-Robinson equation of state, vide Appendix A. Because it is assumed that the catalyst is completely wetted in the Robinson-Mahoney reactor, ultimately, the liquid composition is used to obtain the net production rates of the components in the reaction mixture.

Solving the set of algebraic equations (2.34) is performed using the routine DNSQE obtained from the NETLIB software library [18]. It is an implementation of a hybrid Powell method which is a modification of the method originally developed by Powell [21,22] for minimization of a function in *n* dimensions but with computation of the function's gradient in the calculation of the search directions. The function being minimized is the Euclidian norm of the vector containing the *nresp-2* values of equations (2.34).

Integration of the set of ordinary differential equations (ODE's) (2.35) was performed with the LSODA-subroutine also available at NETLIB [18]. It is a powerful integration routine that can handle both non-stiff and stiff sets of equations based on linear multi step methods. LSODA itself has the built-in ability to decide on the stiffness of the problem and selects the

appropriate method, i.e., Adams and Backward Differentiation Formulas (Gear's method) methods for non-stiff and stiff problems, respectively, to integrate the set of ODE's [23,24].

2.2.3 Quantumchemical Methods

Quantumchemical calculations were performed using density functional theory [1]. Calculations were done with the Amsterdam Density Functional package [25] using self-consistent Becke Perdew (BP86) [26,27] generalized gradient (GGA) corrections to the Vosko-Wilk-Nusair [28] LDA exchange-correlation energy. Scalar relativistic effects were included through the Zero-Order Regular Approximation (ZORA, [29]) Hamiltonian. Basis sets were of double zeta quality and constructed with Slater Type Orbitals. The innermost atomic shells were kept frozen and replaced by an effective core potential. The extent of these frozen cores was up to and including the Pt 4f and the C 1s shell. Unrestricted DFT calculations were done and in all the computations the spin multiplicity was optimized for the lowest energy spin state. Standard SCF- and geometry-convergence criteria were applied. The Pt(111) surface was modeled using a two-layered Pt_{22} cluster. The Pt-Pt distance was kept fixed at the bulk value of 277 pm [30]. Reactions were studied on the central atoms of this cluster. This approach was shown to yield adsorption enthalpies consistent with fully periodic slab calculations as well as experimental results for benzene [31] and 1,4-cyclohexadiene [32] on Pt(111) and for various C_2H_x intermediates on Pd [33].

2.3 References

[1] Parr, R. G., and Yang, W., *Density-Functional Theory of Atoms and Molecules* **Oxford University Press** *New York* (1989).

[2] Remy, M. J., Stanica, D., Poncelet, G., Feijen, E. J. P., Grobet, P. J., Martens, J. A. and Jacobs, P. A., *Dealuminated H-Y zeolites: Relation between Physicochemical Properties and catalytic Activity in Heptane and Decane Isomerization* **J. Phys. Chem.** *100* 12440-12447 (1996).

[3] Collignon, F., Mariani, M., Moreno, S., Remy, M., and Poncelet, G., *Gas Phase Synthesis of MTBE from Methanol and Isobutene over Dealuminated Zeolites* **J. Catal.** *166* 53-66 (1997).

[4] Niwa, M., Katada, N., Sawa, M., and Murakami, Y., *Temperature-Programmed Desorption of Ammonia with Readsorption Based on the Derived Theoretical Equation* **J. Phys. Chem.** *99* 8812-8816 (1995).

[5] Ernst, S., Weitkamp, J., Martens, J. A., and Jacobs, P. A., *Synthesis and Shape-Selective Properties of ZSM-22* **Appl. Catal. A: Gen.** *48* 137-148 (1989).

[6] Martens, J. A., Parton, R., Uytterhoeven, L., Jacobs, P. A., and Froment, G. F., *Selective Conversion of Decane into branched Isomers. A Comparison of Pt/ZSM-22, Pt/ZSM-5 and Pt/USY zeolite catalysts* **Appl. Catal.** *76* 95-116 (1991).

[7] Parton, R., Uytterhoeven, L., Martens, J. A., and Jacobs, P. A., *Synergism of ZSM-22 and Y zeolites in the bifunctional conversion of n-alkanes* **Appl. Catal.** *76* 131-142 (1991).

[8] Martens, J. A., Vanbutsele, G., Jacobs, P. A., Denayer, J., Ocakoglu, R., Baron, G., Muñoz Arroyo, J. A., Thybaut, J., and Marin, G. B., *Evidences for Pore Mouth and Key-lock Catalysis in Hydroisomerization of long n-Alkanes over 10-Ring Tubular Pore Bifunctional Zeolites* **Catal. Today** *65* 111-116 (2001).

[9] Steijns, M., Froment, G., Jacobs, P., Uytterhoeven, J., and Weitkamp, J., *Hydroisomerization and hydrocracking. 2. Product distributions from* n*-decane and n-dodecane* **Ind. Eng. Chem. Prod. Res. Dev.** *20* 660-668 (1981).

[10] Berty, J. M., *Reactor for vapour-phase catalytic studies* **Chem. Eng. Progr.** *70* 78-84 (1974).

[11] Chen, Q., *The implementations of Definitions and Quantities* **Eindhoven University of Technology** (1993).

[12] Dierickx, J. L., Plehiers, P. M., and Froment, G. F., *On-line gas chromatographic analysis of hydrocarbon effluents. Calibration factors and their correlation* **J. Chromat.** *362* 155-174 (1986).

[13] Dietz, W. A., *Response Factors for Gas Chromatographic Analyses* **J. of G.C.** *Feb.* 68-71 (1967).

[14] Aspen Technology, Inc. *ASPEN PLUS User Guide* **Aspen Technology, Inc.** (2001).

[15] Poling, B. E., Prausnitz, J. M., and O'Connell, J. P., *The Properties of Gases and Liquids 5th ed.* **McGraw-Hill** *New York* (2000).

[16] Rosenbrock, H. H., *An automatic method for finding the greatest or least value of a function* **Comput. J.** *3* 175-184 (1960).

[17] Marquardt, D. W., *An algorithm for least squares estimation of nonlinear parameters* **Ind. Appl. Math.** *11* 431-441 (1963).

[18] NETLIB, http://www.netlib.org.

[19] Boggs, P. T., Byrd, R. H., Rogers, J. E., and Schnabel, R. B., *NISTIR* **92-**4834 (1992).

[20] Froment, G. F., and Bischoff, K. B., *Chemical Reactor Analysis and Design 2nd ed.* **J. Wiley,** New York, 1990.

[21] Powell, M. J. D., *An Efficient Method for Finding the Minimum of a Function of Several Variables Without Calculating Derivatives* **Comput. J.** *7* 155-162 (1964).

[22] Powell, M. J. D., *A Hybrid Method for Nonlinear Equations* in *Numerical Methods for Nonlinear Algebraic Equations* (Ed. P Rabinowitz, Gordon and Breach) (1988).

[23] Byrne, G. D., and Hindmarsch, A. C., *Stiff ODE Solvers – A Review of Current and Coming Attractions* **J. Comp. Phys.** *70* 1-62 (1987).

[24] Petzold, L., *Automatic Selection of Methods for Solving Stiff and Nonstiff Systems of Ordinary Differential Equations* **Siam. J. Sci. Stat. Comput.** *4* 136-148 (1983).

[25] Te Velde, G., Bickelhaupt, F. M., Baerends, E. J., Fonseca Guerra, C., Van Gisbergen, S. J. A., Snijders, J. G., and Ziegler, T. *Chemistry with ADF* **J. Comp. Chem.** *22* 931-967 (2001).

[26] Becke, A. D., *Density-Functional Exchange-Energy Approximation with Correct Asymptotic Behaviour* **Phys. Rev. A** *38* 3098-3100 (1988).

[27] Perdew, J. P., *Density-Functional Approximation for the Correlation-Energy of the Inhomogeneous Electron-Gas* **Phys. Rev. B** *33* 8822-8824 (1986).

[28] Vosko, S. H., Wilk, L., and Nusair, M., *Accurate Spin-Dependent Electron Liquid Correlation Energies for Local Spin Density Calculations – A Critical Analysis* **Can. J. Phys.** *58* 1200-1211 (1980).

[29] van Lenthe, E., Baerends, E. J., and Snijders, J. G., *Relativistic Regular 2-Component Hamiltonians* **Chem. Phys.** *99* 4597-4610 (1993).

[30] Somorjai, G. A., *Introduction to Surface Chemistry and Catalysis* **Wiley & *Sons*** *New York* (1994).

[31] Saeys, M., Reyniers, M.-F., Marin, G. B., and Neurock, M., *Density Functional study of Benzene adsorption on Pt(111)* **J. Phys. Chem. B** *106* 7489-7498 (2002).

[32] Saeys, M., Reyniers, M.-F., Marin, G. B., and Neurock, M., *Density Functional study of the adsorption of 1,4-cyclohexadiene on Pt(111): Origin of the CH stretch red-shift* **Surf. Sci.** *513* 315-327 (2002).

[33] Neurock, M., and van Santen, R. A., *A First Principles Analysis of C-H Bond Formation in Ethylene Hydrogenation* **J. Phys. Chem B** *104* 11127-11145 (2000).

Chapter 3

Effect of Operating Conditions on Hydrocracking

Model component hydrocracking has been performed in a continuous stirred tank reactor and a plug flow reactor at the 'Laboratorium voor Petrochemische Techniek' at Ghent University and at the 'Centrum voor Oppervlakchemie en Katalyse' at Leuven University respectively. Given a catalyst with a well-defined ratio of metal to acid sites, five important factors were identified affecting the *ideal* character, i.e., the quasi equilibration of the (de)-hydrogenation reactions, in the hydrocracking experiments. In the range of operating conditions applied (1) a decreasing total pressure, (2) an increasing temperature, (3) an increasing molar hydrogen to hydrocarbon ratio (4) a higher reactant carbon number and (5) the addition of a component strongly chemisorbing on the metal sites favor *non ideal* hydrocracking. A rate equation for *non ideal* hydrocracking was developed based on a lumped reaction scheme. More detailed reaction schemes lead to the same qualitative interpretation as the lumped reaction scheme used. A qualitative analysis of these equations demonstrates that these equations are capable to describe the observed effects of the operating conditions on the *non ideal* hydrocracking behaviour. Moreover, the variations in selectivity pattern between *ideal* and *non ideal* hydrocracking, i.e., the high isomerization yield in *ideal* and the high cracking yield in *non ideal* hydrocracking, can also be explained based on this equation.

3.1 Introduction

Among others, one of the attractive features of the hydrocracking process is its capability of transforming *n*-alkanes into *iso*-alkanes to a high extent before the cracking reactions become important [1,2], vide Chapter 1. Processes focussing on this isomerization rather than on

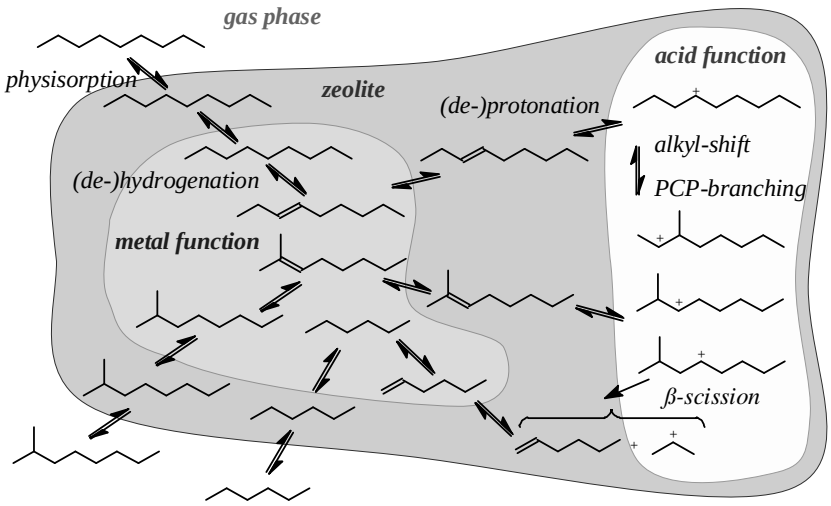

Figure 3-1 Bifunctional reaction scheme in hydrocracking

cracking are referred to as hydroisomerization processes. Isodewaxing is an example of such a process and has the advantage over dewaxing in general that the waxy *n*-alkanes are isomerized into the desired lube oil molecules instead of being cracked into lighter products [1-3].

3.1.1 Reaction Mechanism

Hydrocracking occurs via a bifunctional mechanism requiring a metal and an acid function. This mechanism can be interpreted based on the classical theory of bifunctional catalysis advanced by Weisz [4], vide Figure 3-1. Saturated reactants are dehydrogenated on the metal function. The unsaturated species migrate to the acid function to be protonated into carbenium ions. These carbenium ions are susceptible to hydride shifts, alkyl shifts, PCP branchings and β-scissions. Other well-known acid catalyzed reactions, such as hydride transfer and oligomerization do not have to be accounted for in hydrocracking under the applied experimental conditions, vide Appendix B. Isomers and cracked products leave the acid site as unsaturated species and migrate back to the metal function to be hydrogenated. Prior to these chemical steps, the reactants are physisorbed in the micropores of the catalyst [5,6].

3.1.2 (Non)-Ideality in Hydrocracking

The balance between the number and the activity of the metal and the acid sites plays a key role in the product selectivities observed in hydrocracking [7-11]. On hydrocracking catalysts with sufficient metal sites with a high hydrogenation activity and a weak acid function the (de)-hydrogenation reactions are easily quasi-equilibrated and, hence, the unsaturated products are hydrogenated rather than being subject to further acid catalyzed

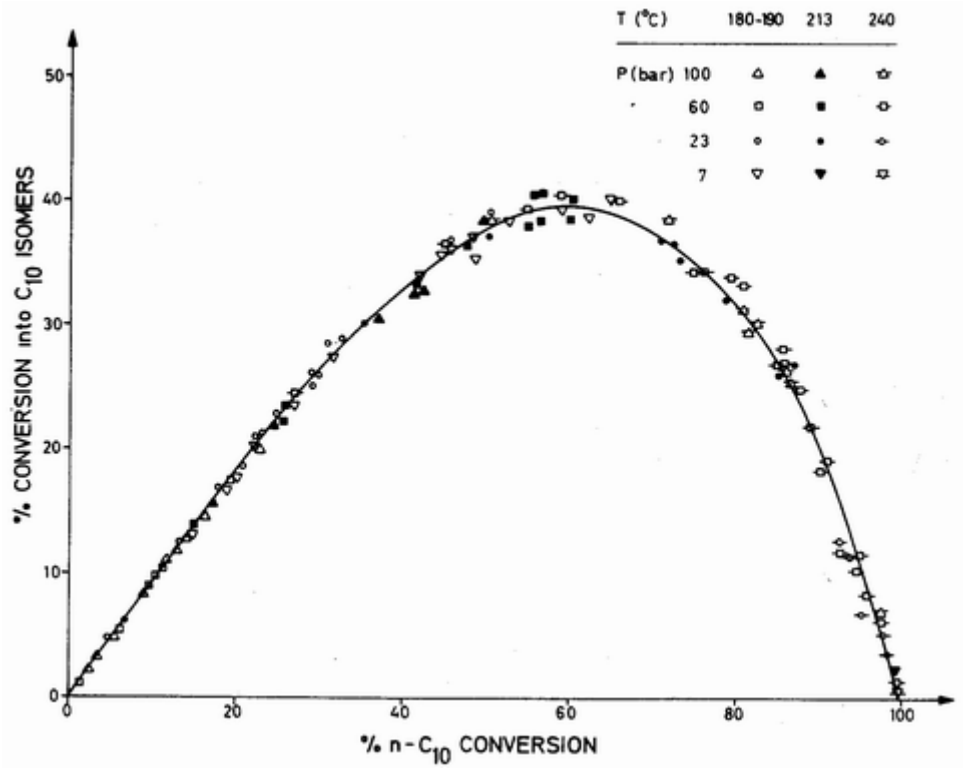

Figure 3-2 ***n*-Decane isomerization conversion on Pt/USY (obtained by steaming, no Si/Al_F ratio reported) as a function of the total *n*-decane conversion [15]**

rearrangement or cracking reactions. Weitkamp [12] introduced the term *ideal* hydrocracking because considerable insight in the acid catalyzed reaction mechanisms can be obtained under such conditions. On catalysts with metal sites with a lower hydrogenation activity and/or more active acid sites, the quasi equilibration of the (de)-hydrogenation reactions might no longer be established, leading to so-called *non ideal* hydrocracking. On a given catalyst, the metal acid site balance is fixed and, hence, the occurrence of *(non) ideal* hydrocracking depends on the operating conditions, such as temperature, total pressure and feedstock composition.

Under *ideal* hydrocracking conditions an apparently unique relationship between product yields and total conversion is obtained on a NiMo/Al_2O_3 [13] and on a Pt/USY zeolite [14-18], vide Figure 3-2. Hence, it could be concluded that the effects of operating conditions on the isomerization and cracking rates are identical, or at least similar. In particular for the temperature effect on the reaction rates, this leads to the conclusion that the activation energies of the acid catalyzed steps are similar [15]. From Table 5-3 it is clear that differences up to 71.5 kJ mol^{-1} exist between the estimated composite activation energies. However, the composite activation energies along the major reaction pathways, i.e., branching isomerisation and cracking involving tertiary carbenium ions, are closer to each other. This, together with a

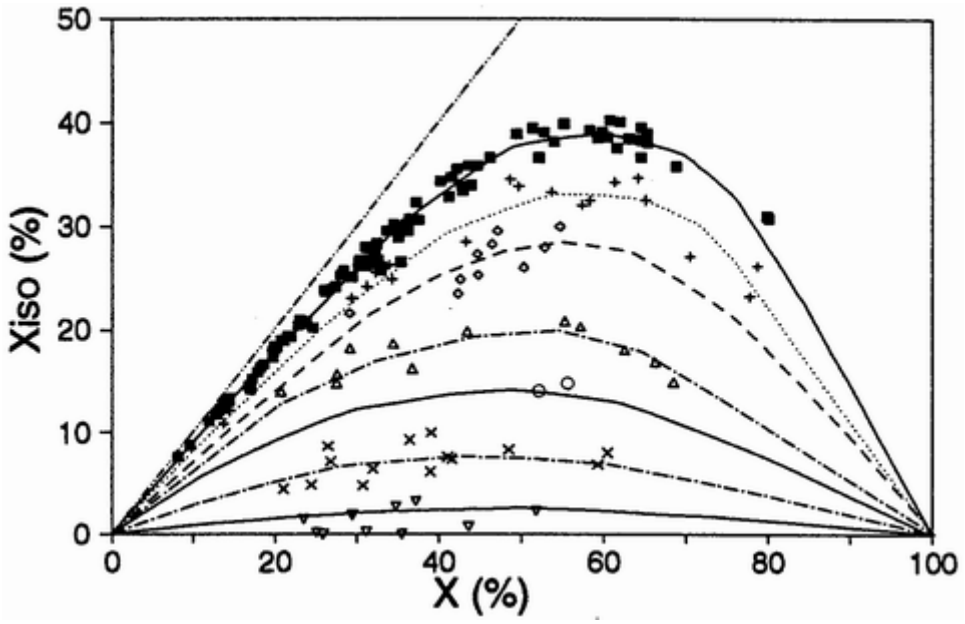

Figure 3-3 Isomerization conversion versus total conversion for *n*-dodecane vapour phase hydrocracking on MC-389 (containing 65 wt% USY zeolite, vide Section 3.2 and Table 3-1) in a CSTR-reactor [16]

not too broad investigated temperature range, explains the apparently unique relationship between the isomerization and total conversion in Figure 3-2. Under the same *ideal* hydrocracking conditions the feed isomer yield is maximum.

When entering *non ideal* hydrocracking conditions the unsaturated products may undergo a second acid catalyzed step prior to being hydrogenated. As a result, under *non ideal* hydrocracking conditions the isomer yield is lower than under *ideal* hydrocracking conditions. The lower the maximum isomerization yield, the stronger the deviation from the *ideal* hydrocracking yield pattern, vide Figure 3-3 [16,17].

This Chapter reports on how hydrocracking rate equations can reflect the transition from *ideal* to *non ideal* hydrocracking and vice versa. Degnan and Kennedy [9] have performed considerable modelling work on this, however, these authors focussed on the catalyst properties as synthesized, while in this work the focus lies on the effect of the operating conditions, including the effect of feeding alkane – cycloalkane mixtures.

3.2 Experimental Procedures

Two catalysts, denoted as MC-389 and Pt/CBV-720, containing Pt deposited on USY zeolitic material have been used. The CBV-720 is a pure USY-zeolite with a framework silicon to aluminum ratio of 18. MC-389 is a commercial catalyst containing 65 wt% LZ-Y20 as USY zeolitic component and 35 wt% alumina binder. Some important properties of these zeolites

Table 3-1 Catalysts, model components and range of the experimental conditions [16-18] (see Section 2.1.1 and Table 2-1 for catalyst properties)

	Feeds	W/F_0 (kg s mol^{-1})	X (%)	T (K)	P (MPa)	H_2/HC
MC-389	*n*-C_8, *n*-C_{10}, *n*-C_{12}, *n*-C_{14}, *n*-C_{16}	100 – 800	0.1 – 80	473 – 553	0.5 - 5	50 - 300
Pt/CBV-720	C_8, C_{10}, MecC_6	20 - 800	15 – 95	506 – 563	0.45	13.13

are listed in Table 2-1. Hydrocracking experiments on MC-389 [16,17] were performed in the Berty-type packed bed reactor described in detail in Section 2.1.2, while the experiments on CBV-720 [18] were performed in a plug flow packed bed reactor described in Section 2.1.3. The reaction conditions and model components used are reported in Table 3-1. Because methane and ethane were only formed in trace quantities, hydrogenolysis could be neglected. During the experiments no catalyst deactivation was observed. In the catalyst pellets of a Y-zeolite the most important mass transport resistance is located in the macropores [19]. Given the similarity of particle size and porosity [20] it was assumed that the same holds for other faujasite type zeolites such as CBV-720 and LZ-Y20 samples considered in this work. The Weisz modulus for macropore diffusion for the Y-zeolite pellet is of the order of 10^{-3} [6].

3.3 Experimental Results

The effect of the operating conditions on the ideality of the hydrocracking behaviour was extensively investigated by Debrabandere [16,17] and Huybrechts [18]. While Debrabandere [16,17] has focussed on the effect of temperature, total pressure and hydrogen to hydrocarbon ratio for pure alkanes and alkane mixtures, Huybrechts [18] investigated the effect of feeding alkane – cycloalkane mixtures. This section highlights their most important results, which are relevant for the qualitative analysis of hydrocracking rate equations accounting for both *ideal* as well as *non ideal* hydrocracking.

Debrabandere [16,17] has used various *n*-alkanes and *n*-alkane mixtures. The results reported here are those for *n*-dodecane and *n*-tetradecane hydrocracking on MC-389. Figure 3-3 represents the *n*-dodecane isomerization conversion as a function of the total *n*-dodecane conversion. The upper curve corresponds to the isomerization conversion observed in *ideal* hydrocracking. The lower the maximum in the other curves, the stronger the deviation from *ideal* hydrocracking. The operating conditions are grouped in Table 3-2 according to the deviation from *ideal* hydrocracking observed under those conditions, i.e., according to the

Table 3-2 Experimental conditions used in *n*-dodecane hydrocracking grouped according to the deviation from *ideal* hydrocracking (higher group numbers correspond to stronger deviations)

	temperatures (K)	pressures (MPa)	molar hydrogen to hydrocarbon ratios
group 1	493	1, 2	50, 100, 200, 300
		0.5	100
	513	1	50, 100
		2, 5	50, 100, 200, 300
	533	2	100
		3, 4	50, 100, 200, 300
group 2	493	0.5	200
	513	0.8	100
		1	200
	533	1	50
		2	200
group 3	513	0.8	200
		1	300
	533	2	300
	553	2	100
group 4	493	0.5	300
	513	0.8	300
	533	1	100
	553	2	200
group 5	553	2	300
group 6	513	0.5	200, 300
	533	1	200, 300
	553	1	100
group 7	533	0.5	100, 200
	553	0.5	50, 100
		1	200, 300

deviation of the maximum isomer yield under those conditions compared to the maximum isomer yield under *ideal* hydrocracking conditions. This grouping is catalyst dependent.

Depending on the catalyst's metal acid site balance the same operating conditions can belong to a different group. In the extreme case, operating conditions leading to *ideal* hydrocracking on one catalyst may lead to *non ideal* hydrocracking on another catalyst which is less active for hydrogenation. The higher the group number, the stronger the deviation from *ideal* hydrocracking, with group 1 containing the *ideal* hydrocracking conditions. From Table 3-2 it can be observed that:

(1) increasing temperatures favor *non ideal* hydrocracking: for a total pressure of 1 MPa and a molar hydrogen to hydrocarbon ratio of 200 *ideal* hydrocracking is observed at 493 K, while the experiments at 513 K, 533 K and 553 K belong to the groups 2, 6 and 7 respectively.

(2) lower total pressures favor *non ideal* hydrocracking: for a temperature of 513 K and a molar hydrogen to hydrocarbon ratio of 300 *ideal* hydrocracking is observed at 2 MPa, while the experiments at 1 MPa, 0.8 MPa and 0.5 MPa belong to the groups 3, 4 and 6 respectively.

(3) higher molar hydrogen to hydrocarbon ratios favor *non ideal* hydrocracking: for a temperature of 553 K and a total pressure of 2 MPa the experiments with molar hydrogen to hydrocarbon ratios from 100, 200 and 300 belong to the groups 3, 4 and 5 respectively.

While the effect of temperature and total pressure are easily explainable from the rate equation developed in Section 3.4, the effect of the molar hydrogen to hydrocarbon ratio is less evident and may even seem contra intuitive because one could expect the hydrogenation reactions to proceed at higher rates when more hydrogen is present. However, because of the range of molar hydrogen to hydrocarbon ratios used in the experiments, i.e., from 50 to 300, an increase in molar hydrogen to hydrocarbon ratio at the same total pressure hardly affects the hydrogen partial pressure. E.g., for a total pressure of 2 MPa, when the molar hydrogen to hydrocarbon ratio varies from 50 to 300, the corresponding hydrogen partial pressure ranges from 1.96 to 1.99 MPa. The hydrocarbon partial pressure is, however, strongly affected and this partial pressure effect is invoked to explain the observed effect of the molar hydrogen to hydrocarbon ratio on the *(non) ideal* character of the hydrocracking experiments, vide Section 3.4.2c.

Table 3-3 contains the information for *n*-tetradecane analogous to that of Table 3-2 for *n*-dodecane. From a comparison of the reported temperatures, total pressures and molar hydrogen to hydrocarbon ratios grouped according to the deviation from *ideal* hydrocracking, it is clear that for identical operating conditions the deviations from *ideal* hydrocracking are somewhat more pronounced for *n*-tetradecane than for *n*-dodecane. E.g., for a temperature of

Table 3-3 Experimental conditions used in *n*-tetradecane hydrocracking grouped according to the deviation from *ideal* hydrocracking (higher group numbers correspond to stronger deviations)

	temperature (K)	total pressure (MPa)	molar hydrogen to hydrocarbon ratio
group 1	493	0.5	100
		1, 2	50, 100, 200, 300
	513	2	50, 100, 200, 300
	533	2	100
group 2	493	0.5	200
	513	1	100, 200
	533	2	200
group 3	513	1	300
	533	1	50
		2	300
group 4	533	1	100
group 5	513	0.5	50, 100, 200, 300
	533	1	200, 300

513 K, a total pressure of 1 MPa and a molar hydrogen to hydrocarbon ratio of 100, ideality was observed when feeding *n*-dodecane, while the same conditions belong to group 2 for *n*-tetradecane. Similarly the experimental conditions 533 K, 1 MPa and a molar hydrogen to hydrocarbon ratio of 50 are attributed to group 2 for *n*-dodecane and to group 3 for *n*-tetradecane. This effect has been related with the more rapid extension with the carbon number of the reaction network for the acid catalyzed reactions than for the metal catalyzed reactions [16,17], however, from Section 3.4, it may be clear that a higher hydrocarbon concentration on the metal sites may also contribute to the effect.

Huybrechts [18] investigated the effect of feeding *n*-alkane – cycloalkane mixtures on the hydrocracking behaviour on Pt/CBV-720 compared to pure *n*-alkane and *n*-alkane mixture behaviour. Figure 3-4a, b and c represent the isomerization conversion of *n*-octane as a function of total *n*-octane conversion for pure *n*-octane, for *n*-octane mixed with other *n*-alkanes and for *n*-octane mixed with methylcyclohexane respectively. The pure *n*-octane and the *n*-octane mixed with other *n*-alkanes lead to the same pattern for the isomerization conversion, whereas the *n*-octane mixed with methylcyclohexane leads to a significantly

Table 3-4 Chemisorption enthalpies of various components on Pt(111)

Component	*n*-butane	*n*-pentane	cyclohexane	cyclohexene
ΔH^{0}_{chem} (kJ mol^{-1})	-34.3[a]	-42.7[a]	-58[b]	-71[b]

[a] from [21], [b] from [22] and [23]

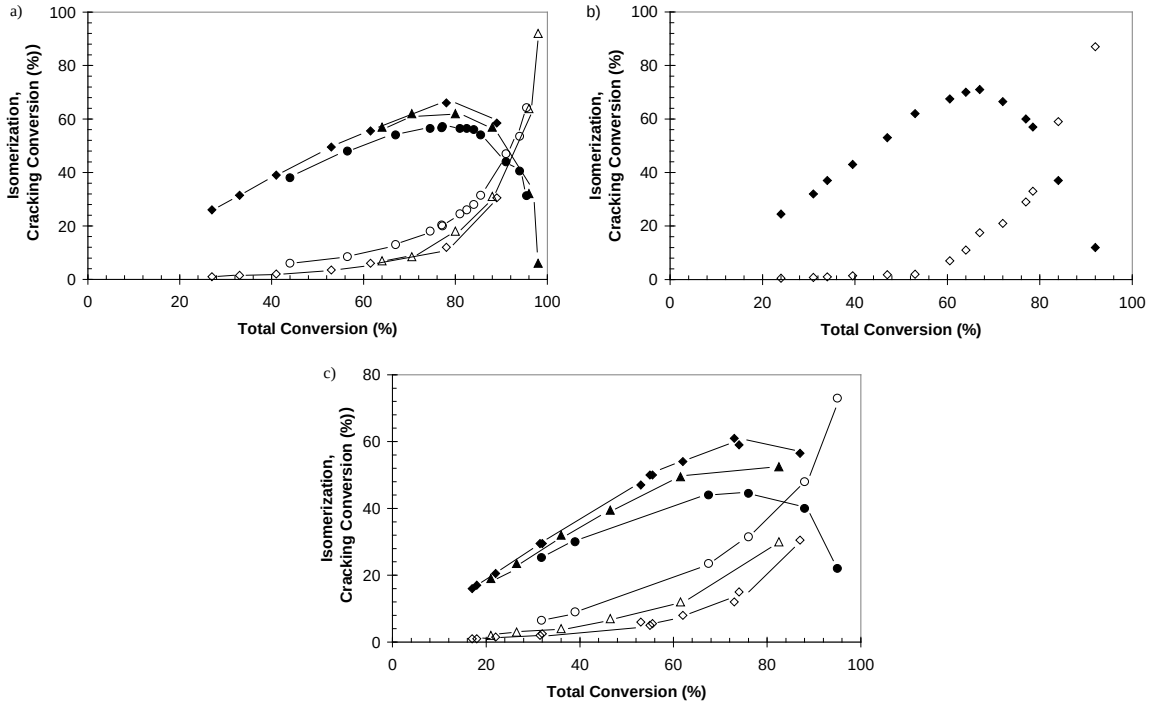

Figure 3-4 Isomerization (closed symbols) and cracking (open symbols) conversion for *n*-octane on Pt/CBV-720 at 503 K (♦), 523 K (▲), 543 K (●) and a molar hydrogen to hydrocarbon ratio of 13.13 as a function of a) the octane conversion when fed as a pure component b) the weighed conversion when feeding a C_6, C_7, C_8 and C_9 mixture and c) the octane conversion when feeding an octane-methylcyclohexane mixture [18]

lower maximum isomerization conversion. From this it can be concluded that the addition of cycloalkanes induces *non ideal* hydrocracking behaviour. The effect can be related with a preferential chemisorption of cyclic hydrocarbons on the metal sites compared to the aliphatic hydrocarbon chemisorption. From the chemisorption enthalpies for *n*-butane and *n*-pentane reported in Table 3-4 a value of 51.1 kJ mol^{-1} is obtained for *n*-hexane using the same increment from *n*-pentane to *n*-hexane as determined from *n*-butane to *n*-pentane. The chemisorption enthalpy for *n*-hexane is clearly less negative than that of cyclohexane. Assuming similar entropy losses for both components upon chemisorption, the surface concentration of the cycloalkane is higher than that of the alkane at equal partial pressures.

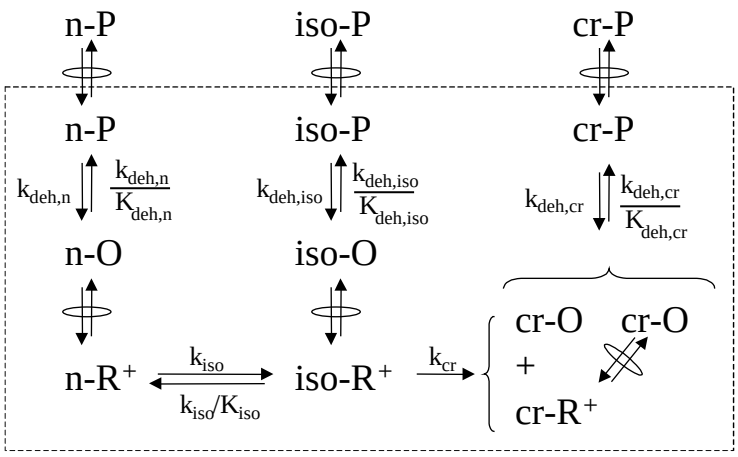

Figure 3-5 Lumped reaction scheme used in the kinetic model construction

This results in an insufficient number of metal sites available for the alkanes to establish quasi equilibrium between the saturated and the unsaturated components.

The same effect was investigated with *n*-decane instead of *n*-octane. Because of the selective physisorption of heavier hydrocarbons compared to lighter, the effect of methylcyclohexane addition was expected to be less pronounced. However, similar or even stronger deviations from *ideal* hydrocracking were observed, which can probably related with the previous observation that *non ideal* effects are more pronounced for components with a higher carbon number, overcompensating the physisorption effects.

3.4 Rate Equations

3.4.1 Development

The hydrocracking reaction mechanism as outlined in Section 3.1.1 comprises several elementary steps, which have to be accounted for in the kinetic modelling. For simplicity, the model equations are developed using the lumped reaction scheme depicted in Figure 3-5. This is sufficient to determine trends as a function of operating conditions and feedstock composition in hydrocracking. The rate equations corresponding to a more detailed reaction scheme are developed in Appendix C and lead to the same qualitative interpretation. Physisorption in the zeolite pores of hydrocarbon molecules belonging to one pseudo-component is taken into account via a Langmuir relationship [5,6]:

$$C_f = \frac{C_{sat,f}\, K_{L,f}\, p_f}{1 + \sum_g K_{L,g}\, p_g} \tag{3.1}$$

in which *f* stands for *n*, *iso* or *cr*, according to the notation used in Figure 3-5. The dehydrogenation of an alkane pseudo-component into an alkene pseudo-component involves the chemisorption of the alkane pseudo-component on a metal site, the surface dehydrogenation step and the alkene pseudo-component desorption from the metal. As illustrated in Appendix C the qualitative interpretation of the rate equations may depend on the assumptions with respect to the (de)-hydrogenation reaction mechanism and with respect to the role of hydrogen in that mechanism in particular, however, an analogous interpretation as made in the subsequent paragraph is always possible. Therefore, an Eley-Rideal mechanism is assumed for the simplicity of the rate equations. The chemisorption steps are considered to be potentially fast and, hence, a quasi-equilibrium relationship exists between the species involved:

$$K_f^M = \frac{C_f^M}{C_f \, C_*^M} \tag{3.2}$$

In Eq. (3.2) *f* represents the alkane or the alkene pseudo-component. The net rate of formation of the alkane pseudo-component then becomes:

$$R_{f-P} = -r_{deh,f} = -k_{deh,f}\left(C_{f-P}^M - \frac{C_{f-O}^M p_{H_2}}{K_{deh,f}^M}\right) \tag{3.3}$$

Accounting for the chemisorption on the metal surface, Eq. (3.3) can be rewritten using the concentrations of physisorbed pseudo-components in the pores

$$R_{f-P} = \frac{-k_{deh,f} K_{f-P}^M C_t^M \left(C_{f-P} - \dfrac{C_{f-O} p_{H_2}}{K_{deh,f}}\right)}{1 + \sum_g K_{g-P}^M C_{g-P}} \tag{3.4}$$

with:

$$K_{deh,f} = K_{deh,f}^M \frac{K_{f-P}^M}{K_{f-O}^M} \tag{3.5}$$

A composite dehydrogenation rate coefficient is defined as follows:

$$k_{deh,f}^* = \frac{k_{deh,f} C_t^M}{1 + \sum_g K_{g-P}^M C_{g-P}} \tag{3.6}$$

In this composite dehydrogenation coefficient the concentration effects in the denominator are neglected in first instance for the ease of the qualitative analysis. Explicitly accounting for such possible variations leads to more nuanciated but similar qualitative conclusions. The

alkene pseudo-component surface concentration on the metal clusters can be assumed to be low compared to the alkane surface concentration under the experimental conditions used in this work. Because of a more favorable interaction with a metal surface, vide Table 3-4, at equal partial pressures, the concentration of unsaturated species on the metal surface is calculated to be a factor 10 to 100 higher than the saturated species surface concentration. However, under typical equilibrium conditions, the ratio between saturated and unsaturated species in the vapour phase amounts to 10^7, and, hence, 10^5 to 10^6 times more saturated than unsaturated species are expected on the metal surface. If the (de)-hydrogenation reactions are not quasi equilibrated and assuming 10^3 times more unsaturated species than under quasi equilibrium conditions, still the ratio of saturated to unsaturated species on the metal surface amounts to 10^2 to 10^3, which is considered enough to neglect the concentration of the unsaturated species on the metal surface. Hence, the denominator only contains terms corresponding to the chemisorption of saturated pseudo-components.

Acid catalyzed isomerization and cracking occurs after protonation of the alkenes produced by dehydrogenation. The (de)-protonation can be assumed to be potentially fast [24] and, hence, a quasi equilibrium relationship is used between the alkene pseudo-component and the carbenium ion pseudo-component concentrations. Moreover, it can be calculated, vide Appendix D, in agreement with [24], that under typical experimental conditions the concentration of free acid sites almost equals the total concentration of acid sites. Hence, the (de)-protonation quasi-equilibrium relationship can be written as:

$$K^{A}_{f-O} = \frac{C_{f-R^+}}{C_{f-O}\, C_t^{A}} \tag{3.7}$$

Applying the steady state hypothesis to the *n*-alkene and the *n*-carbenium ion pseudo-components leads to the following expression for the net rate of formation of physisorbed *n*-alkene pseudo-component:

$$R_{n-O} = k^{*}_{deh,n} K^{M}_{n-P} \left(C_{n-P} - \frac{C_{n-O}\, p_{H_2}}{K_{deh,n}} \right) - k^{*}_{iso} K^{A}_{n-O} \left(C_{n-O} - \frac{C_{iso-O}}{K_{iso}} \right) = 0 \tag{3.8}$$

with:

$$k^{*}_{iso} = k_{iso} C_t^{A} \tag{3.9}$$

The alkene pseudo-component concentrations are the only unknowns in Eq. (3.8). Development of similar equations for the isomer and cracked alkene pseudo-components leads to

$$R_{iso-O} = k^*_{deh,iso} K^M_{iso-P} \left(C_{iso-P} - \frac{C_{iso-O}\, p_{H_2}}{K_{deh,iso}} \right) + k^*_{iso} K^A_{n-O} \left(C_{n-O} - \frac{C_{iso-O}}{K_{iso}} \right) - k^*_{cr} K^A_{iso-O} C_{iso-O} = 0 \quad (3.10)$$

$$R_{cr-O} = k^*_{deh,cr} K^M_{cr-P} \left(C_{cr-P} - \frac{C_{cr-O}\, p_{H_2}}{K_{deh,cr}} \right) + 2k^*_{cr} K^A_{iso-O} C_{iso-O} = 0 \quad (3.11)$$

Eq. (3.8) and Eq. (3.10), i.e., the equations for the normal and isomer alkene pseudo-components, constitute a linear system of two equations and two unknowns which can be solved explicitly. Doing so, the following expressions are obtained for the net rates of formation of the three alkane pseudo-components considered:

$$R_{n-P} = \frac{\dfrac{C_{sat} K_{L,n-P}}{1 + \sum_i K_{L,i}\, p_i} \left(-k^*_{iso} \dfrac{k^*_{deh,iso}}{K_{deh,iso}} k^*_{deh,n}\, p_{H_2} \left(p_{n-P} - \dfrac{K_{L,iso-P}\, p_{iso-P}}{K_{iso} K_{L,n-P}} \right) - k^*_{iso} k^*_{cr} k^*_{deh,n}\, p_{n-P} \right)}{\dfrac{k^*_{deh,n}}{K_{deh,n}} \dfrac{k^*_{deh,iso}}{K_{deh,iso}} p^2_{H_2} + \left(\dfrac{k^*_{deh,n}}{K_{deh,n}} \left(\dfrac{k^*_{iso}}{K_{iso}} + k^*_{cr} \right) + \dfrac{k^*_{deh,iso}}{K_{deh,iso}} k^*_{iso} \right) p_{H_2} + k^*_{iso} k^*_{cr}} \quad (3.12)$$

$$R_{iso-P} = \frac{\dfrac{C_{sat}}{1 + \sum_i K_{L,i}\, p_i} \left(\begin{array}{l} k^*_{iso} \dfrac{k^*_{deh,iso}}{K_{deh,iso}} k^*_{deh,n} K_{L,n-P}\, p_{H_2} \left(p_{n-P} - \dfrac{K_{L,iso-P}\, p_{iso-P}}{K_{iso} K_{L,n-P}} \right) \\ \quad - \left(\dfrac{k^*_{deh,n}}{K_{deh,n}} k^*_{cr} k^*_{deh,iso}\, p_{H_2} + k^*_{iso} k^*_{cr} k^*_{deh,iso} \right) K_{L,iso-P}\, p_{iso-P} \end{array} \right)}{\dfrac{k^*_{deh,n}}{K_{deh,n}} \dfrac{k^*_{deh,iso}}{K_{deh,iso}} p^2_{H_2} + \left(\dfrac{k^*_{deh,n}}{K_{deh,n}} \left(\dfrac{k^*_{iso}}{K_{iso}} + k^*_{cr} \right) + \dfrac{k^*_{deh,iso}}{K_{deh,iso}} k^*_{iso} \right) p_{H_2} + k^*_{iso} k^*_{cr}} \quad (3.13)$$

$$R_{cr-P} = \frac{2\dfrac{C_{sat}}{1 + \sum_i K_{L,i}\, p_i} \left(\begin{array}{l} k^*_{iso} k^*_{cr} k^*_{deh,n} K_{L,n-P}\, p_{n-P} \\ \quad + \left(\dfrac{k^*_{deh,n}}{K_{deh,n}} k^*_{cr} k^*_{deh,iso}\, p_{H_2} + k^*_{iso} k^*_{cr} k^*_{deh,iso} \right) K_{L,iso-P}\, p_{iso-P} \end{array} \right)}{\dfrac{k^*_{deh,n}}{K_{deh,n}} \dfrac{k^*_{deh,iso}}{K_{deh,iso}} p^2_{H_2} + \left(\dfrac{k^*_{deh,n}}{K_{deh,n}} \left(\dfrac{k^*_{iso}}{K_{iso}} + k^*_{cr} \right) + \dfrac{k^*_{deh,iso}}{K_{deh,iso}} k^*_{iso} \right) p_{H_2} + k^*_{iso} k^*_{cr}} \quad (3.14)$$

The expressions for the initial net rate of formation for the three alkane pseudo-components can easily be derived from the above equations, Eq. (3.12) to Eq. (3.14), taking $p_{iso\text{-}P}=0$:

$$R_{n-P} = \frac{-\dfrac{C_{sat} K_{L,n-P}}{1 + \sum_i K_{L,i}\, p_i} \left(\dfrac{k^*_{deh,iso}}{K_{deh,iso}} p_{H_2} + k^*_{cr} \right) k^*_{iso} k^*_{deh,n}\, p_{n-P}}{\dfrac{k^*_{deh,n}}{K_{deh,n}} \dfrac{k^*_{deh,iso}}{K_{deh,iso}} p^2_{H_2} + \left(\dfrac{k^*_{deh,n}}{K_{deh,n}} \left(\dfrac{k^*_{iso}}{K_{iso}} + k^*_{cr} \right) + \dfrac{k^*_{deh,iso}}{K_{deh,iso}} k^*_{iso} \right) p_{H_2} + k^*_{iso} k^*_{cr}} \quad (3.15)$$

$$R_{iso-P} = \frac{\dfrac{C_{sat}}{1+\sum_i K_{L,i}\,p_i}\,k^*_{iso}\,\dfrac{k^*_{deh,iso}}{K_{deh,iso}}\,k^*_{deh,n}\,K_{L,n-P}\,p_{H_2}\,p_{n-P}}{\dfrac{k^*_{deh,n}}{K_{deh,n}}\,\dfrac{k^*_{deh,iso}}{K_{deh,iso}}\,p^2_{H_2} + \left(\dfrac{k^*_{deh,n}}{K_{deh,n}}\left(\dfrac{k^*_{iso}}{K_{iso}}+k^*_{cr}\right)+\dfrac{k^*_{deh,iso}}{K_{deh,iso}}\,k^*_{iso}\right)p_{H_2} + k^*_{iso}\,k^*_{cr}} \tag{3.16}$$

$$R_{cr-P} = \frac{2\,\dfrac{C_{sat}}{1+\sum_i K_{L,i}\,p_i}\,k^*_{iso}\,k^*_{cr}\,k^*_{deh,n}\,K_{L,n-P}\,p_{n-P}}{\dfrac{k^*_{deh,n}}{K_{deh,n}}\,\dfrac{k^*_{deh,iso}}{K_{deh,iso}}\,p^2_{H_2} + \left(\dfrac{k^*_{deh,n}}{K_{deh,n}}\left(\dfrac{k^*_{iso}}{K_{iso}}+k^*_{cr}\right)+\dfrac{k^*_{deh,iso}}{K_{deh,iso}}\,k^*_{iso}\right)p_{H_2} + k^*_{iso}\,k^*_{cr}} \tag{3.17}$$

Written as a function of total pressure, p_t, and hydrogen to hydrocarbon ratio, γ, the Eq. (3.15) to Eq. (3.17) are transformed into:

$$R_{n-P} = \frac{-\dfrac{C_{sat}\,K_{L,n-P}\,(1+\gamma)}{1+\gamma+\sum_i K_{L,i}\,y_i\,p_t}\left(\dfrac{k^*_{deh,iso}}{K_{deh,iso}}\,\gamma\,p_t + (1+\gamma)\,k^*_{cr}\right)k^*_{iso}\,k^*_{deh,n}\,y_{n-P}\,p_t}{\dfrac{k^*_{deh,n}}{K_{deh,n}}\,\dfrac{k^*_{deh,iso}}{K_{deh,iso}}\,\gamma^2\,p_t^2 + \left(\dfrac{k^*_{deh,n}}{K_{deh,n}}\left(\dfrac{k^*_{iso}}{K_{iso}}+k^*_{cr}\right)+\dfrac{k^*_{deh,iso}}{K_{deh,iso}}\,k^*_{iso}\right)(1+\gamma)\,\gamma\,p_t + k^*_{iso}\,k^*_{cr}\,(1+\gamma)^2} \tag{3.18}$$

$$R_{iso-P} = \frac{\dfrac{C_{sat}\,(1+\gamma)}{1+\gamma+\sum_i K_{L,i}\,y_i\,p_t}\,k^*_{iso}\,\dfrac{k^*_{deh,iso}}{K_{deh,iso}}\,k^*_{deh,n}\,K_{L,n-P}\,\gamma\,y_{n-P}\,p_t^2}{\dfrac{k^*_{deh,n}}{K_{deh,n}}\,\dfrac{k^*_{deh,iso}}{K_{deh,iso}}\,\gamma^2\,p_t^2 + \left(\dfrac{k^*_{deh,n}}{K_{deh,n}}\left(\dfrac{k^*_{iso}}{K_{iso}}+k^*_{cr}\right)+\dfrac{k^*_{deh,iso}}{K_{deh,iso}}\,k^*_{iso}\right)(1+\gamma)\,\gamma\,p_t + k^*_{iso}\,k^*_{cr}\,(1+\gamma)^2} \tag{3.19}$$

$$R_{cr-P} = \frac{2\,\dfrac{C_{sat}\,(1+\gamma)}{1+\gamma+\sum_i K_{L,i}\,y_i\,p_i}\,k^*_{iso}\,k^*_{cr}\,k^*_{deh,n}\,K_{L,n-P}\,(1+\gamma)\,y_{n-P}\,p_t}{\dfrac{k^*_{deh,n}}{K_{deh,n}}\,\dfrac{k^*_{deh,iso}}{K_{deh,iso}}\,\gamma^2\,p_t^2 + \left(\dfrac{k^*_{deh,n}}{K_{deh,n}}\left(\dfrac{k^*_{iso}}{K_{iso}}+k^*_{cr}\right)+\dfrac{k^*_{deh,iso}}{K_{deh,iso}}\,k^*_{iso}\right)(1+\gamma)\,\gamma\,p_t + k^*_{iso}\,k^*_{cr}\,(1+\gamma)^2} \tag{3.20}$$

with:

$$p_{n-P} = \frac{y_{n-P}\,p_t}{(1+\gamma)} \tag{3.21}$$

$$p_{H_2} = \frac{\gamma\,p_t}{(1+\gamma)} \tag{3.22}$$

in which $y_{n\text{-}P}$ represents the mole fraction of the *n*-alkane in the hydrocarbon feed and becomes important in the case of mixed feeds, vide Section 3.4.2e.

When the (de)-hydrogenation reactions are potentially fast, the first terms in the numerator and the denominator of Eq. (3.18), i.e., $\gamma\,p_t\,k^*_{deh,iso}/K_{deh,iso}$ and $\gamma^2\,p_t^2\,k^*_{deh,n}\,k^*_{deh,iso}/K_{deh,n}\,K_{deh,iso}$

dominate the value of the numerator and the denominator respectively and, hence, Eq. (3.18) is reduced to:

$$\lim_{k^*_{deh}\to\infty} R_{n-P} = \frac{(1+\gamma)}{\gamma}\frac{C_{sat}\,K_{L,P}}{1+\gamma+\sum_i K_{L,i}\,y_i\,p_t}\,K_{deh,n}\,K^A_{L,n-O}\,k^*_{iso} \tag{3.23}$$

In this case, depending on its value, the total pressure has no or a negative effect on the reaction rate.

When the isomerization and cracking reactions are potentially fast both in the numerator and the denominator of Eq. (3.18) the last term, i.e., $(1+\gamma)k^*_{cr}$ and $k^*_{iso}k^*_{cr}(1+\gamma)^2$ dominate the value of the numerator and the denominator respectively and, hence, Eq. (3.18) is reduced to:

$$\lim_{k^*_{iso},k^*_{cr}\to\infty} R_{n-P} = k^*_{deh,n}\;\; p_t\,\frac{C_{sat}\,K_{L,P}}{1+\gamma+\sum_i K_{L,i}\,y_i\,p_t} \tag{3.24}$$

In this case, also depending on its value, the total pressure has a positive or no effect on the reaction rate.

3.4.2 Qualitative Analysis

a Total Pressure Effect

Eq. (3.18) allows to understand several of the effects observed experimentally. With decreasing pressure a transition from *ideal* to *non ideal* hydrocracking occurs. It is evident from Eq. (3.18) that at high pressures, the first terms of both the numerator and the denominator, i.e., $\gamma\,p_t\,k^*_{deh,iso}/K_{deh,iso}$ and $\gamma^2\,p_t^2\,k^*_{deh,n}k^*_{deh,iso}/K_{deh,n}K_{deh,iso}$ become dominant as it is the case in *ideal* hydrocracking. The pressure dependence of the first terms in the numerator and denominator respectively can however be reduced when the metal site coverage is non negligible, vide 3.4.2e, but a positive total pressure effect will remain in both terms. At lower pressures, however, this term becomes less important while the values of the last terms of the numerator and the denominator, i.e., $(1+\gamma)k^*_{cr}$ and $k^*_{iso}k^*_{cr}(1+\gamma)^2$ are not affected by the total pressure. If the total pressure is sufficiently low, the last terms dominate the value of the numerator and the denominator as it is the case in *non ideal* hydrocracking. Experimentally, this transition can be observed in a plot of the conversion as a function of the total pressure, vide Figure 3-6. At low pressures an increase in the conversion is observed, corresponding to *non ideal* hydrocracking behaviour. At intermediate total pressures a maximum in the conversion is observed and at higher total pressures the conversion is decreasing, indicating that *ideal* hydrocracking occurs.

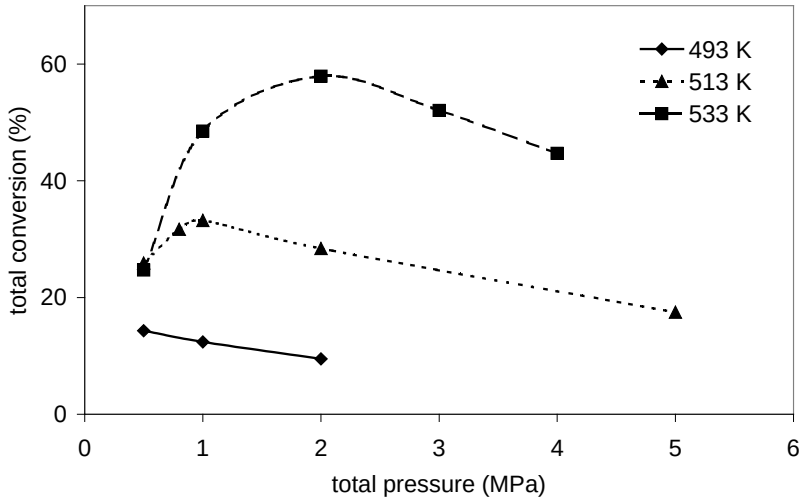

Figure 3-6 **Total *n*-dodecane hydrocracking conversion as a function of the total pressure at a molar hydrogen to hydrocarbon ratio of 200, effect of the temperature (data obtained by De Ketelaere [25])**

b Temperature Effect

Similarly, the effect of temperature on the *(non) ideal* behaviour can be explained. The activation energy of the metal catalyzed (de)-hydrogenation reactions is lower than that of the acid catalyzed reactions [17] which results in a moderate temperature dependence of the (de)-hydrogenation rate coefficients and a more important temperature dependence for the rate coefficients of the acid catalyzed steps. Hence, while at sufficiently low temperatures the first terms in the numerator and the denominator are dominant, with increasing temperature the last terms gain importance and become dominant. As a result, a transition from *ideal* to *non ideal* hydrocracking occurs. This is illustrated in Figure 3-6 by the shift of the maxima in the conversion versus total pressure to higher total pressures as the temperature increases. At higher temperatures higher total pressures are needed for the transition from *non ideal* to *ideal* hydrocracking because of the more moderate increase of the (de)-hydrogenation rate coefficients with the temperature compared to the increase with the temperature of rate coefficients of the acid catalyzed steps.

c Molar Hydrogen to Hydrocarbon Ratio Effect

The third important factor affecting the *(non) ideal* behaviour, i.e., the molar hydrogen to hydrocarbon ratio γ, is not evident from Eq. (3.18) as such. Because the values for the molar hydrogen to hydrocarbon ratio used are high, i.e., $\gamma > 10$, and, hence, $(\gamma + 1) \sim \gamma$, all terms between brackets in the numerator exhibit a linear dependence on γ while all terms in the

denominator exhibit a square dependence on γ. As a result, no difference in relative importance of the terms in the numerator and the denominator is observed. A similar conclusion is drawn when the rate equations are constructed based on other possible (de)-hydrogenation reaction mechanisms, viz, Appendix C. A possible explanation for the effect of the molar hydrogen to hydrocarbon ratio is related to the relative hydrocarbon concentrations on the metal and the acid sites. Substituting the full expression for the composite dehydrogenation rate coefficient, i.e., Eq. (3.6), in the expression for the first term in the numerator, results in:

$$\gamma p_t \frac{k_{deh,iso} C_t^M}{K_{deh,iso}\left(1+\dfrac{\sum_j C_{sat} K_j^M K_{L,j} y_j \; p_t /(1+\gamma)}{1+\sum_i K_{L,i} y_i \; p_t /(1+\gamma)}\right)} \tag{3.25}$$

Performing the same substitution in the first term of the denominator leads to:

$$\gamma^2 p_t^2 \frac{k_{deh,n} k_{deh,iso} \left(C_t^M\right)^2}{K_{deh,n} K_{deh,iso}\left(1+\dfrac{\sum_j C_{sat} K_j^M K_{L,j} y_j \; p_t /(1+\gamma)}{1+\sum_i K_{L,i} y_i \; p_t /(1+\gamma)}\right)^2} \tag{3.26}$$

When the hydrocarbon concentrations on the metal sites are high, i.e., $\sum_j C_{sat} K_j^M K_{L,j} y_j \; p_t /(1+\gamma) >> 1$, while the physisorbed concentrations are not too high, i.e., $\sum_i K_{L,i} y_i \; p_t /(1+\gamma) << 1$, the molar hydrogen to hydrocarbon ratio has an extra enhancing effect on the value of the expressions in Eq. (3.25) and Eq. (3.26) apart from the linear respectively the square effect already present in the numerator of these expressions. If a similar effect exists and is more pronounced for the last terms of the numerator and the denominator of Eq. (3.18), the latter are expected to increase faster with the molar hydrogen to hydrocarbon ratio than the first terms and a transition from *ideal* to *non ideal* hydrocracking may occur. This qualitative explanation for the effect of the molar hydrogen to hydrocarbon ratio on the value of the last terms of the numerator and the denominator of Eq. (3.18) seems, however, in contradiction with the negligible hydrocarbon concentrations on the acid sites. Further investigations using, e.g., a quantitative approach, should clarify how high the fractional surface coverages of the hydrocarbon species on the metal and the acid sites have to be to explain the observed effect of the molar hydrogen to hydrocarbon ratio and

Table 3-5 Ratios between the number of (de)-hydrogenations, alkyl shifts, PCP branchings and β-scissions in the *n*-alkane hydrocracking network and the same *n*-alkane hydrocracking network with one carbon atom less

carbon number	(de)-hydrogenation	alkyl shift	PCP branching	β-scission
8	2.4	3.5	2.9	3.4
9	2.3	2.7	2.3	2.9
10	2.2	2.4	2.2	2.5
11	2	2.1	1.9	2.2
12	1.9	1.9	1.8	2

allow a comparison of these fractional surface coverages with those calculated in Appendix D.

Analogous to the effect of the temperature on *non ideal* hydrocracking, vide Figure 3-6, a shift in the maximum conversion as a function of the total pressure to higher total pressures is expected with increasing molar hydrogen to hydrocarbon ratio. However, in the range of operating conditions investigated, the effect is not pronounced enough to be visualized on the same Figure.

d Carbon Number Effect

The fourth factor identified to affect the *non ideal* hydrocracking behaviour is the feedstock's carbon number. The carbon number effect on the relative importance between the terms in the numerator and denominator of Eq. (3.18) is twofold. The number of elementary acid catalyzed steps increases faster with the carbon number than the number of (de)-hydrogenation reactions, vide Table 3-5, certainly for carbon numbers lower than 10. Hence, the lumped rate coefficients for acid catalyzed reactions are expected to also increase faster with the carbon number than the lumped rate coefficients for the (de)-hydrogenation reactions. As a result, the relative importance of the last with respect to the first terms in both the numerator and the denominator will increase with the carbon number and *non ideal* hydrocracking will be favored for higher feedstock carbon numbers.

This first carbon number effect is reinforced by a second effect related with the hydrocarbon concentration on the metal sites. Higher hydrocarbons have more negative chemisorption enthalpies and, hence, higher concentrations on the catalyst surface. As explained in Section 3.4.2e, higher metal surface concentrations lead to a decrease in the values of the terms in Eq. (3.18) favoring *ideal* hydrocracking.

e Cycloalkane Addition Effect

The final factor observed to have an effect on (non) ideality in hydrocracking can be understood from the detailed pressure dependence of the first terms in both the numerator and the denominator of Eq. (3.18), vide Eq. (3.25) and Eq. (3.26) in Section 3.4.2c. When $\sum_i C_{sat} K_i^M K_{L,i}\, y_i\, p_t/(1+\gamma) << 1$, i.e., when the alkane pseudo-component concentrations on the metal sites are low, the last term in the denominator of Eq. (3.25) and Eq. (3.26) is negligible and the total pressure dependence is reduced to the original dependence discussed in Section 3.4.2a. However, when $\sum_i C_{sat} K_i^M K_{L,i} y_i\, p_t/(1+\gamma) >> 1$, i.e., when the alkane pseudo-component concentrations on the metal sites are high, the last term in the denominator of Eq. (3.25) and Eq. (3.26) becomes non negligible and has a reducing effect on the coefficient of the linear or the square dependence of the value of the term on the total pressure. Moreover, if $\sum_i K_{L,i} y_i\, p_t/(1+\gamma) << 1$ but $\sum_i C_{sat} K_i^M K_{L,i} y_i\, p_t/(1+\gamma) >> 1$, i.e., if, physisorption in the zeolite is far from saturation while chemisorption on the metal sites is closer to saturation, also the linear or the square character of the total pressure dependence is reduced.

When feeding a *n*-alkane/cycloalkane mixture instead of pure *n*-alkane feed, the concentrations of hydrocarbons physisorbed in the catalyst pores and chemisorbed on the metal sites may change because of possible differences in physisorption and/or chemisorption behaviour between n-alkanes and cycloalkanes. In the case of an equimolar *n*-alkane/cycloalkane mixture with the same carbon number for both components the concentration of pseudo-components physisorbed in the catalyst pores will hardly be affected because of the similar physisorption properties between *n*-alkanes and cycloalkanes with the same carbon number. The concentration of pseudo-components chemisorbed on the metal sites, however, will increase because of the stronger chemisorption of cycloalkanes than *n*-alkanes on the metal sites, vide Table 3-4. As a result, the summation in the denominator of Eq. (3.25) and Eq. (3.26) related to the concentrations on the metal sites, $\sum_i C_{sat} K_i^M K_{L,i} y_i\, p_t/1+\gamma$, will be higher in the case of an equimolar *n*-alkane/cycloalkane feed than in the case of a pure *n*-alkane feed. This summation is contained in the denominator of Eq. (3.25) and Eq. (3.26) and, hence, an increase of the value of the summation will have a decreasing effect on the values of the expressions in Eq. (3.25) and Eq. (3.26). Because these expressions correspond to the terms in Eq. (3.18) favoring *ideal* hydrocracking, the decrease

of their value when cycloalkanes are contained in the feed, may lead to a transition from *ideal* to *non ideal* hydrocracking in the presence of cycloalkanes.

f Selectivity

One of the possibilities to identify *ideal* or *non ideal* hydrocracking behaviour is the selectivity observed in the experiments. Under *ideal* hydrocracking conditions, the isomer yield is maximum. The first term in the numerator of Eq. (3.18), i.e., $\gamma p_t k^*_{deh,iso} / K_{deh,iso}$, which dominates its value in *ideal* hydrocracking, is found again in the initial net production rate of the isomer pseudo-component. In the product of rate coefficients in the numerator of the initial net production rate of the isomer pseudo-component, i.e., $k^*_{deh,n} k^*_{iso} k^*_{deh,iso} / K_{deh,iso}$, vide Eq. (3.19), the reaction pathway from the normal alkane to the isomer pseudo-component can be identified: (1) dehydrogenation of the normal alkane to the normal alkenes, $k^*_{deh,n}$, (2) isomerization of the normal alkenes to the isomer alkenes, k^*_{iso}, and (3) hydrogenation of the iso-alkenes to the iso-alkanes, $k^*_{deh,iso} / K_{deh,iso}$.

The second term in the numerator of Eq. (3.18), i.e., $(1+\gamma) k^*_{cr}$, which is negligible in *ideal* hydrocracking corresponds to the formation of cracked products directly from the normal alkane, i.e., via the formation of iso-alkenes which are cracked prior to hydrogenation. The same term is found in the expression for the initial net production rate of cracked products, vide Eq. (3.20). The product of the three rate coefficients, $k^*_{deh,n} k^*_{iso} k^*_{cr}$, in this expression again reflects the reaction pathway: (1) dehydrogenation of the normal alkane to normal alkenes, $k^*_{deh,n}$, (2) isomerization of the normal alkenes to iso-alkenes, k^*_{iso}, and (3) cracking of the iso-alkenes to cracked products, k^*_{cr}. This term, which becomes more important the stronger the deviation from *ideal* hydrocracking is, reflects the shift in selectivities observed between *ideal* and *non ideal* hydrocracking.

3.5 Conclusions

Apart from the catalyst's acid/metal balance also the operating conditions strongly affect the ideality of the hydrocracking behaviour. Increasing total pressures, decreasing temperatures and decreasing molar hydrogen to hydrocarbon ratios were found to favor *ideal* hydrocracking, whereas a higher reactant carbon number and the addition of cycloalkanes to the feedstock were found to cause *non ideal* hydrocracking. The total pressure dependence of

the reaction rate and the isomerization conversion as a function of the total conversion provide two useful means to monitor the ideality of the hydrocracking behaviour.

Rate equations based on a lumped reaction scheme accounting for potentially rate-determining metal and acid catalyzed surface reactions qualitatively accounted for the effects observed experimentally. The qualitative analysis of the rate equations is independent from the exact reaction mechanism for the (de)-hydrogenation reactions. The changes in isomerization conversion according to the deviation from *ideal* hydrocracking are reflected in the model equations.

3.6 References

[1] Ward, J. W., *Hydrocracking processes and catalysts* **Fuel Proc. Tech.** *35* 55-85 (1993).

[2] Scherzer, J., and Gruia, A. J., *Hydrocracking Science and Technology, Chapter 10, Hydrocracking Processes* **Marcel Dekker Inc.** *New York,* 174-199 (1996).

[3] Maxwell, I. E., Minderhoud, J. K., Stork, W. H. J., and van Veen, J. A. R. *Handbook of Heterogeneous Catalysis, Chapter 3.13, Hydrocracking and Catalytic Dewaxing* (Eds. Knözinger, Ertl, and J. Weitkamp) **Wiley – VCH** 2017 – 2038 (1997).

[4] Weisz, P. B., *Polyfunctional Heterogeneous Catalysis* **Adv. Catal.** *13* 137-190 (1962).

[5] Steijns, M., and Froment, G. F., *Hydroisomerization and hydrocracking. 3. Kinetic analysis of rate data for n-decane and n-dodecane* **Ind. Chem. Product Res. Dev.** *20* 660-668 (1981).

[6] Denayer, J. F., Baron, G. V., Souverijns, W., Martens, J. A., and Jacobs, P. A., *Hydrocracking of n-alkane mixtures on Pt/H-Y zeolite: Chain length dependence of the adsorption and kinetic constants* **Ind. Eng. Chem. Res.** *36* 3242-3247 (1997).

[7] Weitkamp, J., *Hydrocracking, Cracking and Isomerization of Hydrocarbons* **Erdöl Kohle Erdgas P.** *31* 13-22 (1978).

[8] Giannetto, G. E., Perot, G. R., and Guisnet, M. R., *Hydroisomerization and hydrocracking of n-alkanes. 1. Ideal hydroisomerization PtHY catalysts* **Ind. Eng. Chem. Prod. Res. Dev.** *25* 481-490 (1986).

[9] Degnan, T. F., and Kennedy, C. R., *Impact of catalyst acid/metal balance in the hydroisomerization of normal paraffins* **AIChE J.** *39* 607-614 (1993).

[10] Alvarez, F., Ribeiro, F. R., Perot, G., Thomazeau, C., and Guisnet, M. *Hydroisomerization and hydrocracking of alkanes : 7. Influence of the balance between acid and hydrogenating functions on the transformation of n-decane on PtHY catalysts* **J. Catal.** *162* 179-189 (1996).

[11] Girgis, M. J., and Tsao, Y. P., *Impact of catalyst metal-acid balance in n-hexadecane hydroisomerization and hydrocracking* **Ind. Eng. Chem. Res.** *35* 386-396 (1996).

[12] Weitkamp, J., *Influence of Chain-Length in Hydrocracking and Hydroisomerization of normal alkanes* **ACS Symp. Ser.** *20* 1-27 (1975).

[13] Goldfarb, Yu. Ya., Katsobashvili, Ya. R., and Rozenthal, A. L., *Kinetics of n-decane Hydrocracking on an Aluminum-Nickel-Molybdenum Oxide Catalyst. I* **Kinet. Catal.** *18* 364-370 (1977).

[14] Weitkamp, J., *Hydrocracking, Cracking and Isomerization of Hydrocarbons* **Erdöl Kohle Erdgas P.** *31* 13-22 (1978).

[15] Steijns, M., Froment, G. F., Jacobs, P., Uytterhoeven, J., and Weitkamp, J., *Hydroisomerization and Hydrocracking. 2. Product Distributions from* n-*Decane and* n-*Dodecane* **Ind. Eng. Chem. Prod. Res. Dev.** *20* (1981) 654-660

[16] Debrabandere, B., and Froment, G. F., *Influence of the hydrocarbon length on the kinetics of the hydroisomerization and hydrocracking of n-paraffins* **Stud. Surf. Sci. Cat.** *106* 379-389 (1997).

[17] Debrabandere, B., *Hydroisomerizatie en Hydrokraking van mengsels koolwaterstoffen op Pt/USY-zeoliten* **PhD Thesis** *Ghent University* (1997).

[18] Huybrechts, W., *Competitieve Adsorptie van Multicomponentenmengsels in Microporeuze Katalysatoren* **Master Thesis** *Leuven University* (2001).

[19] Denayer, J. F. M., and Baron, G. V., *Adsorption of normal and branched paraffins in faujasite zeolites NaY, HY, Pt/NaY and USY* **Adsorption** *3* 1-15 (1997).

[20] Denayer, J. F., Baron, G. V., Vanbutsele, G., Jacobs, P. A., and Martens, J. A., *Evidence for Alkylcarbenium Ion Reaction Intermediates from Intrinsic Reaction kinetics of C6-C9 n-Alkane Hydroisomerization and Hydrocracking on Pt/H-Y and Pt/USY Zeolites* **J. Catal.** *190* 469-473 (2000).

[21] Salmeron, M., and Somorjai, G. A., *Adsorption and Bonding of Butane and Pentane on the Pt(111) Crystal-Surfaces – Effects of Oxygen Treatments and Deuterium Pre-Adsorption* **J. Phys. Chem.** *85* 3835-3840 (1981).

[22] Xu, C., Tsai, Y.-L., and Koel, B. E., *Adsorption of Cyclohexane and Benzene on Ordered Sn/Pt(111) Surface Alloys* **J. Phys. Chem.** *98* 585-593 (1994).

[23] Koel, B. E., Blank, D. A., and Carter, E. A., *Thermochemistry of the selective dehydrogenation of cyclohexane to benzene on pt surfaces* **J. Mol. Catal. A Chem.** *131* 39-53 (1998).

[24] Svoboda, G., Vynckier, E., Debrabandere, B., and Froment, G. F., *Single-Event Rate Parameters for Paraffin Hydrocracking on a Pt/US-Y Zeolite* **Ind. Eng. Chem. Res.** *34* 3793-3800 (1995).

[25] De Ketelaere, I., *Gasfase Hydrokraking in een Reactor met Volkomen Vermenging* **Master Thesis** *Ghent University* (1994).

Chapter 4

Single-Event Kinetic Modelling of Model Component and Complex Feedstock Hydrocracking

Petroleum feedstocks in refinery processes are complex mixtures of various types of hydrocarbon species [1]. Innumerable reactions occur between species of the same or a different nature. A detailed kinetic description accounting for all individual reactions with separate rate parameters is an insurmountable task and, hence, appropriate assumptions have to be made in order to come to a manageable kinetic model [2-4], see also Chapter 1.

A common practice in the investigation of complex feedstocks processing is a study of the behaviour of well-chosen model components because of analytical reasons. Using a fundamental model in describing the model component kinetics allows to obtain fundamental rate parameters, which can then be used in the modelling of the complex feedstock behaviour.

4.1 Elementary Rate Equations

The bifunctional hydrocracking reaction mechanism has been explained in Section 3.1.1 and considers carbenium ions as the reactive intermediates in the acid catalyzed isomerization and cracking reactions. Hydroxyl groups bridging a silicon atom and an aluminum atom in the tetrahedral oxide framework are generally accepted as the active sites in Brönsted acid catalyzed conversions on zeolites. Quantumchemical calculation of the interaction of a light alkene with an acid site of a zeolite framework fragment predicts formation of surface alkoxide species [5-7]. For branched hydrocarbons giving rise to tertiary alkylcarbenium

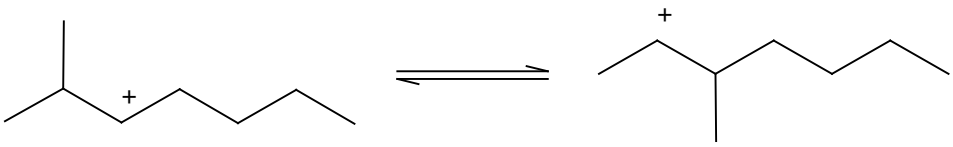

Figure 4-1 Illustration of the single-event concept by secondary-secondary alkyl shift from 2-methylhept-3-yl Ion to 3-methylhept-2-yl Ion

ions, surface alkoxide formation is for sterical reasons rather unlikely [8]. The kinetic model used in this work was based on alkylcarbenium ions as reaction intermediates, although the same rate equations also hold for alkoxide type intermediates. This follows from the derivation of the rate equations [9,10], cfr. infra. In this work elementary rate equations are used for *ideal* hydrocracking only.

The rate-determining acid catalyzed steps in hydrocracking belong to relatively few reaction families, i.e., alkyl shifts (AS), protonated cyclopropane (PCP) branchings and β-scissions (β). Within such a family the single-event rate coefficients are assumed to depend only on the type of carbenium ions involved as reactant and product. The only other structural feature of the reactive moiety, which is accounted for, is the symmetry number. This is illustrated in Figure 4-1 with a (s;s) alkyl shift between the 2-methylhept-3-yl ion and the 3-methylhept-2-yl ion. In the forward reaction 2 methyl groups are candidate to shift from 2 to 3 position, while in the reverse reaction, only 1 candidate methyl group is present. Hence, although both the forward and the reverse reaction are a (s;s) alkyl shift, for symmetry reasons, the forward reaction is expected to proceed at twice the rate of the reverse reaction given the concentrations of both carbenium ions are equal. This symmetry effect can be separated from the rate coefficient as the number of single-events and is calculated as the ratio of the symmetry number of the reactant to that of the transition state [11,12]:

$$k^{AS/PCP/\beta} = n_e \, \tilde{k}^{AS/PCP/\beta} \tag{4.1}$$

$$n_e = \frac{\sigma_{R_{i,k}^+}}{\sigma_{\neq_{ikqr}}} \tag{4.2}$$

The new rate coefficient $\tilde{k}^{AS/PCP/\beta}$ is the so-called single-event rate coefficient, which in the case of an alkyl shift is discussed in Figure 4-1. It corresponds to the shift of strictly one methyl group, independent from the number of candidate shifting methyl groups. The in this manner defined single-event rate coefficient only depends on the reaction family and the carbenium ion types involved as reactant and product. The detailed development of the single

event model and the associated reduction of the number of kinetic parameters is given elsewhere [4,11].

In what follows, the equations will be written with explicit reference to the relevant properties of the transition state rather than the number of single events. The latter approach was also followed by Valéry [13]. Obviously, this does not lead to any change in interpretation of the rate equations but, as clearly appears from the work of Valéry [13] provides several advantages.

Four single-event rate coefficients corresponding to the transformation of secondary and tertiary carbenium ions are to be considered per reaction family when methyl and primary ions are neglected. The rate expression for each type of acid catalyzed step in *ideal* hydrocracking is given by:

$$r^{AS/PCP/\beta}\left(m_{i,k};n_{q,r}\right)= \frac{C_t \frac{\sigma_{O_{i,j}}}{\sigma_{\neq ikqr}} \tilde{k}^{AS/PCP/\beta}\left(m_{i,k};n_{q,r}\right)\tilde{K}_{prot}\left(O_{ref};m\right)\tilde{K}_{iso}\left(O_{i,j};O_{ref}\right)K_{deh}\left(P_i;O_{i,j}\right)C_{sat,P_i}K_{L,P_i}\frac{p_{P_i}}{p_{H_2}}}{1+\sum_j K_{L,P_j}p_{P_j}} \quad (4.3)$$

The symbols used in Eq. (4.3) are explained in the Notation section. Note that the carbon number dependence is limited to the physisorption parameters, K_{L,P_i} and C_{sat,P_i}. The single-event protonation equilibrium coefficient, $\tilde{K}_{prot}\left(O_{ref};m\right)$, which was originally assumed to be carbon number independent [9,11], was found to be carbon number dependent only for carbenium ions with a carbon number of eight or less, vide Chapter 5. The stepwise construction of Eq. (4.3) is explained in the following paragraphs.

4.1.1 Rate-Determining Step

As mentioned above the rate-determining elementary steps in *ideal* hydrocracking are alkyl shifts, PCP branchings and β-scissions. Their rates are expressed as first order in the carbenium ion reactants:

$$r^{AS/PCP/\beta}\left(m_{i,k};n_{q,r}\right)=\frac{\sigma_{R^+_{i,k}}}{\sigma_{\neq ikqr}}\tilde{k}^{AS/PCP/\beta}\left(m_{i,k};n_{q,r}\right)C_{R^+_{i,k}} \quad (4.4)$$

in which $C_{R^+_{i,k}}$ represents the concentration of the reacting carbenium ion *k* stemming from alkane *i*.

4.1.2 Protonation of physisorbed alkene to physisorbed carbenium ion

The carbenium ion concentration is obtained from the alkene concentration through a Langmuir type isotherm expression

$$C_{R^+_{i,k}} = \frac{C_t K_{prot}(O_{i,j};m_{i,k})C_{O_{i,j}}}{1+K_{prot}(O_{i,j};m_{i,k})C_{O_{i,j}}} \tag{4.5}$$

The acid site coverage is calculated to be negligible, vide Appendix D, and, hence, Eq. (4.5) was simplified to

$$C_{R^+_{i,k}} \cong C_t K_{prot}(O_{i,j};m_{i,k})C_{O_{i,j}} \tag{4.6}$$

Similar to the rate coefficient, the symmetry contribution in the (de)-protonation equilibrium coefficient can be accounted for via the symmetry numbers of the alkene and the carbenium ion involved,

$$K_{prot}(O_{i,j};m_{i,k}) = \frac{\sigma_{O_{i,j}}}{\sigma_{R^+_{i,k}}} \tilde{K}_{prot}(O_{i,j};m_{i,k}) \tag{4.7}$$

The number of unknown single event (de)-protonation equilibrium coefficients can be reduced by expressing them as the product of the single-event (de)-protonation equilibrium coefficient of a well chosen reference alkene O_{ref}, $\tilde{K}_{prot}(O_{ref};m)$, leading to a carbenium ion of the same type and the single-event isomerization equilibrium coefficient between the alkene $O_{i,j}$ and this reference alkene O_{ref}, $\tilde{K}_{iso}(O_{i,j};O_{ref})$, [11]

$$\tilde{K}_{prot}(O_{i,j};m_{i,k}) = \tilde{K}_{iso}(O_{i,j};O_{ref})\,\tilde{K}_{prot}(O_{ref};m) \tag{4.8}$$

$\tilde{K}_{prot}(O_{ref};m)$ is considered to be carbon number independent and, hence, can be written as, vide Chapter 5:

$$\tilde{K}_{prot}(O_{ref};m) = \tilde{K}_{prot}(m) \tag{4.9}$$

Hence, the expression for the carbenium ion concentration becomes

$$C_{R^+_{i,k}} = C_t \frac{\sigma_{O_{i,j}}}{\sigma_{R^+_{i,k}}} \tilde{K}_{iso}(O_{i,j};O_{ref})\tilde{K}_{prot}(m)C_{O_{i,j}} \tag{4.10}$$

$\tilde{K}_{iso}(O_{i,j};O_{ref})$ is calculated using thermodynamic data generated with Benson's group contribution method [14,15].

4.1.3 Dehydrogenation of a physisorbed alkane into a physisorbed alkene

(De)-hydrogenation equilibrium expressions provide a relationship between the alkene and the alkane concentration,

Table 4-1a Pre-exponential factors of the Henry coefficients for the alkanes on the H-(US)Y-zeolites used (most of these data are published in [16,17], the other in [18])

	C_5	C_6	C_7	C_8	C_9	C_{12}
	(mol kg_{cat}^{-1} MPa^{-1})					
H-Y-zeolite	$4.2\ 10^{-3}$	$2.4\ 10^{-3}$	$1.6\ 10^{-3}$	$7.9\ 10^{-4}$	$4.5\ 10^{-4}$	$6.8\ 10^{-5}$
CBV-720	-	$1.4\ 10^{-3}$	-	-	$1.9\ 10^{-4}$	-
CBV-760	$9.7\ 10^{-4}$	$4.6\ 10^{-4}$	$1.9\ 10^{-4}$	$9.4\ 10^{-5}$	$4.2\ 10^{-5}$	$6.5\ 10^{-6}$

Table 4-1b Physisorption enthalpies for the alkanes on the H-(US)Y-zeolites used (most of these data are published in [16,17], the other in [18])

	C_5	C_6	C_7	C_8	C_9	C_{12}
	(kJ mol^{-1})					
H-Y-zeolite	-36.1	-44.2	-50.1	-55.9	-62.0	-81.6
CBV-720	-	-41.9	-	-	-60.5	-
CBV-760	-36.7	-43.3	-50.3	-56.5	-63.2	-81.5

Table 4-1c Saturation concentrations for the alkanes on the H-(US)Y-zeolites used (most of these data are published in [16,17], the other in [18])

	C_5	C_6	C_7	C_8	C_9	C_{12}
	(mol kg_{cat}^{-1})					
H-Y-zeolite	1.50	1.29	1.22	1.07	1.02	0.691
CBV-720	-	0.876	-	-	0.623	-
CBV-760	0.800	0.624	0.625	0.620	0.554	0.362

$$C_{O_{i,j}} = \frac{K_{deh} C_{P_i}}{p_{H_2}} \tag{4.11}$$

The equilibrium coefficients for (de)-hydrogenation and isomerization are also calculated using thermodynamic data generated with Benson's group contribution method [14,15].

4.1.4 Physisorption of a vapour phase alkane

The concentration of physisorbed alkanes is calculated via a Langmuir isotherm expression,

$$C_{P_i} = \frac{C_{sat} K_{L,P_i} p_{P_i}}{1 + K_{L,P_i} p_{P_i}} \tag{4.12}$$

The Langmuir physisorption coefficient for an alkane on a zeolite can be determined from its Henry coefficient and saturation concentration

$$K_{L,P_i} = \frac{H_{P_i}}{C_{sat,P_i}} \tag{4.13}$$

Denayer et al. [16] determined physisorption enthalpies and pre-exponential factors for the Henry coefficients using tracer chromatography, vide Table 4-1a and b. The saturation concentrations were taken from [17], vide Table 4-1c. Since the differences in physisorption parameters between the *n*-alkane and its isomers are negligible [19], only one set of Langmuir parameters was considered per carbon number and per Pt/H-(US)Y-zeolite.

4.1.5 Net Rates of Formation

The net rate of formation of an alkane *i*, P_i, is expressed as the sum of all rates of elementary steps in which the carbenium ions *k*, $R^+_{i,k}$, corresponding with alkane *i* are produced minus the rates of all elementary steps in which those carbenium ions *k* are consumed. An extra term is to be incorporated, accounting for the alkenes *j*, $O_{i,j}$, corresponding with alkane *i*, which are directly produced by β-scission, i.e., not via an intermediate product carbenium ion.

$$\begin{aligned} \textit{alkane net production rate} = {} & \textit{corresponding carbenium ions net production rates} \\ & + \textit{corresponding alkenes directly produced via} \\ & \beta - \textit{scission net production rates} \end{aligned} \tag{4.14a}$$

$$R_{P_i} = \sum_k R^{AS/PCP/\beta}_{R^+_{i,k}} + \sum_j R^{\beta}_{O_{i,j}} \tag{4.14b}$$

with

$$\begin{aligned} \textit{carbenium ion net production rate} = {} & \\ & \textit{production by isomerization} - \textit{consumption by isomerization} \\ & + \textit{production by } \beta \textit{ - scission} - \textit{consumption by } \beta \textit{ - scission} \end{aligned} \tag{4.15a}$$

$$\begin{aligned} R^{AS/PCP/\beta}_{R^+_{i,k}} = {} & \sum_l \sum_o r^{AS/PCP}\left(m_{l,o}; m_{i,k}\right) - \sum_l \sum_o r^{AS/PCP}\left(m_{i,k}; m_{l,o}\right) \\ & + \sum_l \sum_o r^{\beta}\left(m_{l,o}; m_{i,k}, O_{u,v}\right) - \sum_l \sum_o r^{\beta}\left(m_{i,k}; m_{l,o}, O_{u,v}\right) \end{aligned} \tag{4.15b}$$

and

$$R^{\beta}_{O_{i,j}} = \sum_l \sum_o r^{\beta}\left(m_{l,o}; m_{q,r}, O_{i,j}\right) \tag{4.16}$$

For clarity the alkenes $O_{u,v}$ and $O_{i,j}$ produced by β-scission are explicitly mentioned in Eq. (4.15) and Eq. (4.16) although their formation is irrelevant with respect to the value of the single event rate coefficient.

4.1.6 Adjustable Parameters

The only unknowns to be estimated in Eq. (4.3) by regression of kinetic data are the single-event rate coefficient and the single-event (de)-protonation equilibrium coefficient. Due to the low acid site coverage, vide Eq. (4.5) and Eq. (4.6) and Appendix D, only the product of the two can be estimated. Hence, parameter estimations based on these equations will result in composite parameters consisting of a protonation part and a contribution from the isomerization or cracking step,

$$\tilde{k}^{AS/PCP/\beta-comp} = \tilde{K}_{prot}\tilde{k}^{AS/PCP/\beta} \tag{4.17}$$

The composite activation energies represent the sum of the standard protonation enthalpy and the real activation energy,

$$E_A^{AS/PCP/\beta-comp} = \Delta H_{prot}^{0} + E_A^{AS/PCP/\beta} \tag{4.18}$$

The composite activation energy compares the energy level of the transition state and the deprotonated acid site with that of the physisorbed alkene and the acid site.

The values for the composite pre-exponential factors are calculated according to the method explained by Martens et al. [10]. Hence, the only parameters to be estimated are the composite activation energies. The number of composite activation energies amounts to 12, i.e., 4 per reaction family. However, due to thermodynamic constraints the value for the (s;t) mode equals that for the (t;s) mode for the reaction family of alkyl-shift and PCP-branching [9]. Hence, the number of parameters to be estimated is reduced to 10.

4.2 Relumping

It is obvious that, especially for heavier hydrocarbons, the summations in Eq. (4.14), Eq. (4.15) and Eq. (4.16) can become very time consuming. Also, the present analytical instrumentation does not allow a specification of feedstocks in full detail. Both above cited reasons have lead to the development of a relumped single-event model [11]. In the relumped model eight lumps are considered per carbon number: *n*-alkane, mono-, di-, and tribranched alkanes, mono-, di-, tri-, and tetraring cycloalkanes. In an alternative relumped single-event model [13] the lumps considered for the alkanes are: *n*-alkane, mono-, and multibranched alkanes, where the lump of the multibranched alkanes also contains eventual isomers with

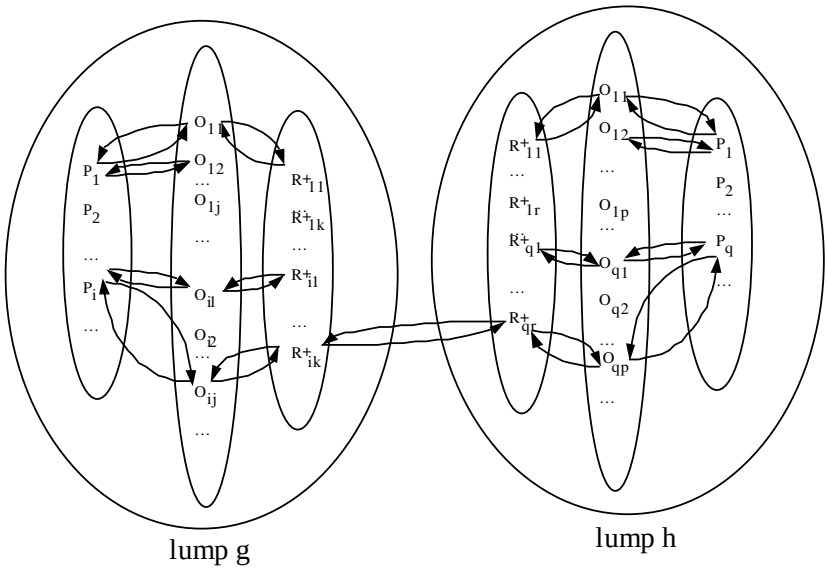

Figure 4-2 Relumping of saturated hydrocarbons and corresponding unsaturated hydrocarbons and carbenium ions

more than three branches. The calculated interconversion rates between the lumps in these relumped models fully account for all possible elementary steps between these lumps. The only assumption required in the relumped single-event model is related to the specification of the internal composition of the lumps. The lumps are defined in such a way that thermodynamic equilibrium can be assumed in hydrocracking on Pt/H-(US)Y-zeolite.

4.2.1 Explicit Network Summation Based Method

The reaction rate between lump *g* and lump *h* corresponds to the summation of the reaction rates of all the elementary steps occurring between species of lumps *g* and *h*. For, e.g., the *PCP*-reactions between two isomer lumps *g* and *h*, vide Figure 4-2, this results in:

$$r^{PCP}(g;h) = \frac{k_{lump}^{PCP}(g;h) H_g \dfrac{p_g}{p_{H_2}}}{1 + \sum_f K_{L,f}\, p_f} \tag{4.19}$$

where the lumped rate coefficient is a function of the fundamental rate coefficients. Hence, the fundamental character of the model is preserved. The lumped rate coefficient also depends on the so-called lumping coefficients [11]:

$$\begin{aligned} k_{lump}^{PCP}(g;h) = \big[& LC_{s;s}^{PCP}(g;h) \tilde{K}_{prot}(s) \tilde{k}^{PCP}(s;s) + LC_{s;t}^{PCP}(g;h) \tilde{K}_{prot}(s) \tilde{k}^{PCP}(s;t) \\ & + LC_{t;s}^{PCP}(g;h) \tilde{K}_{prot}(t) \tilde{k}^{PCP}(t;s) + LC_{t;t}^{PCP}(g;h) \tilde{K}_{prot}(t) \tilde{k}^{PCP}(t;t) \big] C_t \end{aligned} \tag{4.20}$$

The latter are independent of the single-event rate coefficients as is seen from Eq. (4.21):

$$LC_{m;n}^{PCP}(g;h)=\sum_{i\in g}\sum_{k\in g}\sum_{q\in h}\sum_{r\in h}\frac{\sigma_{O_{i,j}}}{\sigma_{\neq_{ikqr}}}K_{iso}(O_{i,j};O_{ref})K_{deh}(P_i;O_{i,j})y_{i,g} \tag{4.21}$$

Each term of the right hand side of Eq. (4.21) consists of values that are known via the reaction network or that can be calculated based on thermodynamic data. The specification of the mole fractions $y_{i,g}$ of the components i in lump g, is the only concession that has to be made to preserve the fundamental character of the relumped model. As mentioned above, a judicious definition of the lumps allows to assume that equilibrium is established within the lumps.

Although the above method proved to be applicable for feedstocks in the middle distillate range [10,20], the calculation of the lumping coefficients becomes a limiting factor for heavy components, such as those present in a vacuum gasoil, because of the more than proportional increase of the size of the reaction network with carbon number. Therefore, a method not requiring the generation of the reaction network was developed to calculate the lumping coefficients [3,4]. The alternative relumped single-event model [13] does also not require the generation of the reaction network.

4.2.2 Structural Class Based Method

The right hand side of Eq. (4.21) can be reorganized into:

$$LC_{m;n}^{PCP}(g;h)=\frac{N_{m;n}^{PCP}(g;h)K_{ref,g}^{*}(n;T)}{K_{g}^{*}(n;T)} \tag{4.22}$$

where $K_{ref,g}^{*}(n;T)$ represents the equilibrium coefficient for formation of the reference alkene and hydrogen from the elements:

$$K_{ref,g}^{*}(n;T)=\exp\left(-\frac{\Delta\tilde{G}_{f}^{0}(O_r)+\Delta\tilde{G}_{f}^{0}(H_2)}{RT}\right) \tag{4.23}$$

and $K_{g}^{*}(n;T)$ accounts for the sum of the equilibrium coefficients for the formation of all (cyclo)-alkanes of lump g:

$$K_{g}^{*}(n;T)=\sum_{i\in g}\frac{\exp\left(-\frac{\Delta\tilde{G}_{f}^{0}(P_i)}{RT}\right)}{\sigma_{P_i}} \tag{4.24}$$

$N_{m_1;m_2}^{PCP}$ accounts for the symmetry effects in the rate-determining elementary steps:

$$N_{m_1;m_2}^{PCP}=\sum_{i\in g}\sum_{j\in g}\sum_{q\in h}\sum_{r\in h}\frac{1}{\sigma_{\neq_{ikqr}}\sigma_{H_2}} \tag{4.25}$$

Table 4-2 Structural classes of dibranched alkanes with a quaternary carbon atom (the numbers of primary, secondary, tertiary and quaternary carbon atoms are identical for the classes listed below and amount to 4, n-5, 0 and 1 respectively)

Alkane Class	global symmetry number σ_i	number of gauche interactions $n_{gch,i}$	number of alkanes, $\#_i$
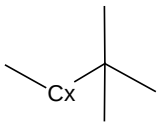	243	2	1
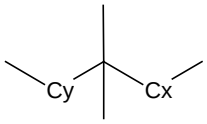 (x ≠y)	81	4	(n-6)/2 for *n* even (n-5)/2 for *n* odd
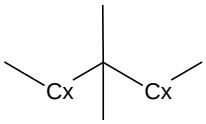	162	4	0 for *n* even 1 for *n* odd
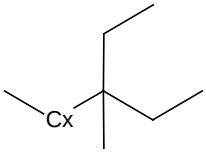	81	6	1
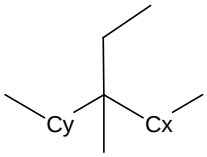 (x ≠y)	81/2	6	(n-10)/2 for *n* even (n-9)/2 for *n* odd
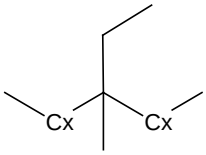	81	6	0 for *n* even 1 for *n* odd
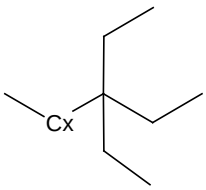	243	8	1
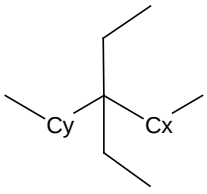 (x ≠y)	81	8	(n-10)/2 for *n* even (n-11)/2 for *n* odd
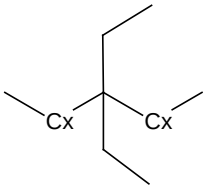	162	8	0 for *n* even 1 for *n* odd

Table 4-3 Structural classes of carbenium ions contributing to $\mathbf{N_{s;t}^{PCP}(diP_n;moP_n)}$

Carbenium ion class R^+_{ik}	transition state global symmetry number $\sigma_{\neq_{ikqr}}$	number of ions, $\#_i$
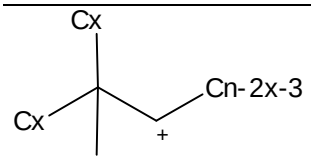 (x = 1, 2)	27/2	2
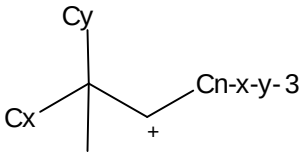 (y = 1, 2; x ≠ y)	27/4	2n-14

The calculation of $K^*_{ref,g}(n;T)$ only involves the properties of hydrogen and those of the reference alkene and, hence, the required CPU-time to obtain the value is independent of the carbon number of the lump for which it is calculated. In contrast to this the calculation of $K^*_g(n;T)$ and $N^{PCP}_{m_1;m_2}$ involves a summation over components or reactions in the network and, hence, the CPU-time required increases with the carbon number when using a network based method. However, for both $K^*_g(n;T)$ and $N^{PCP}_{m_1;m_2}$ a method can be developed not requiring the explicit network summation. For $K^*_g(n;T)$ it suffices to recognize that it can be calculated from group contribution methods such as Benson's [15]. This allows to classify the large number of (cyclo)-alkanes within a lump in a limited number of structural classes. The latter are defined by common values for the global symmetry number, standard enthalpy of formation, single-event standard entropy and specific heat capacity. When applying Benson's group contribution method to calculate the latter, each structural class is characterized by the number of primary, secondary, tertiary, and quaternary carbon atoms, the number of five and six membered rings, the global symmetry number and the minimum number of gauche interactions. Eq. (4.24) can then be rewritten as follows:

$$K^*_g(n;T) = \sum_{i\in g} \frac{\exp\left(-\frac{\Delta\tilde{G}^0_f(P_i)}{RT}\right)}{\sigma_{P_i}} = \sum_{i=1}^{n_{classes}} \frac{\#_i}{\sigma_i} \exp\left(-\frac{n_{p,i}\Delta\tilde{G}^0_{f,p} + n_{s,i}\Delta\tilde{G}^0_{f,s} + n_{t,i}\Delta\tilde{G}^0_{f,t} + n_{q,i}\Delta\tilde{G}^0_{f,q} + n_{gch,i}\Delta\tilde{G}^0_{f,gch}}{RT}\right) \quad (4.26)$$

Similarly for the calculation of $N_{m_1;m_2}^{PCP}$ the involved carbenium ions can be classified into classes defined by a common value for the global symmetry number of the corresponding transition state. If expressions for the number of components belonging to each structural class as a function of the number of carbon atoms are derived, each of the three factors in Eq. (4.22) can be calculated without network generation. All structural classes containing dibranched alkanes with a quaternary carbon atom are listed in Table 4-2. Among all structural classes for alkanes, these classes are characterized by common values for the number of primary, secondary, tertiary and quaternary carbon atoms, i.e., 4, n-5, 0 and 1 respectively. The structural classes of carbenium ions contributing to $N_{s;t}^{PCP}(diP_n;moP_n)$ are listed in Table 4-3. Using the structural class based approach the expression for, e.g., $N_{m_1;m_2}^{PCP}$ is transformed into:

$$N_{m_1;m_2}^{PCP} = \sum_{i\in g}\sum_{j\in g}\sum_{q\in h}\sum_{r\in h}\frac{1}{\sigma_{\neq_{ikqr}}\sigma_{H_2}} = \sum_{i=1}^{nclasses}\frac{\#_i}{\sigma_{\neq_{ikqr}}\sigma_{H_2}} \qquad (4.27)$$

The global symmetry number for H_2, σ_{H_2}, equals 2 and $\#_i$ and $\sigma_{\neq_{ikqr}}$ are listed in Table 4-3. Eq. (4.26) and Eq. (4.27) show the simplification in the calculation of the lumping coefficients with the structural class based method compared to the original network based method.

The alternative relumped single-event model is based on the representation of alkanes and activated complexes as hydrocarbons constituted by side chains and an activated zone [13]. The calculation of the two terms corresponding to those in Eqs. (4.26) and (4.27) is performed using an alternative pathway. It is self-evident that both calculation methods lead to values for the lumping coefficients which are identical to each other and to the values obtained based on the explicit network summation method.

The definition of the structural classes as developed above is analogous to the definition of the lumps in the structure oriented lumping technique proposed by Quann and Jaffe [21,22]. Similar lumps are defined in the relumped single-event model and in the structure oriented lumping technique. However, whereas a lump equals a group of structurally identical hydrocarbons in the structure oriented lumping technique, in the relumped single-event model one lump comprises several structural classes. This is because of the extra properties considered in the definition of the structural classes in the relumped single-event model, i.e., the global symmetry number and the number of gauche interactions, compared to the properties considered in the structure oriented lumping technique. Moreover, the rate

coefficients in the relumped single-event model are calculated in such a way that they account for all elementary steps between the lumps considered, whereas the rate coefficients in the structure oriented lumping technique do not account for the interconversion between the lumps in such detail. This is why the relumped single-event model can be considered as a fundamental model, in contrast to the structure oriented lumping technique by Quann and Jaffe [21,22].

4.3 Conclusions

Describing the kinetics of reactions among several hundreds if not thousands of components at the level of elementary steps involved provides several advantages. The number of elementary reaction families and, hence, of the corresponding kinetic parameters is rather limited. Values for those kinetic parameters can be obtained from model component data and then be applied in the modelling of complex feedstock hydroconversion. The applicability of group additivity to hydrocarbons allows to derive expressions for the rate coefficients without having to generate the full network of elementary steps by classifying the components into a limited number of structural classes.

4.4 References

[1] Scherzer, J., and Gruia, A. J., *Hydrocracking Science and Technology, Chapter 1 & 10, Introduction & Hydrocracking Processes* **Marcel Dekker Inc.** *New York* 1-8, 174-199 (1996).

[2] Martens, G. G., Thybaut, J. W., and Marin, G. B., *Single-Event Rate Parameters for the Hydrocracking of Cycloalkanes on Pt/US-Y Zeolites* **Ind. Eng. Chem. Res.** *40* 1832-1844 (2001).

[3] Martens, G. G., and Marin, G. B., *Kinetics for Hydrocracking Based on Structural Classes: Model Development and Application* **AIChE J.** *47* 1607-1622 (2001).

[4] Martens, G., *Hydrocracking on Pt/US-Y zeolites: fundamental kinetic modelling and industrial reactor simulation* **PhD Thesis** *Ghent University* (2000).

[5] Kazansky, V. B., Frash, M. V., and van Santen, R. A., *Quantumchemical Study of the Isobutane Cracking on Zeolites* **Appl. Catal. A Gen.** *146* 225-247 (1996).

[6] Rigby, A. M., Kramer, G. J., and van Santen, R. A., *Mechanism of Hydrocarbon Conversion in Zeolites: A Quantum Mechanical Study* **J. Catal.** *170* 1-10 (1997).

[7] Natal-Santiago, M. A., Alcala, R., and Dumesic, J. A., *DFT Study of the Isomerization of Hexyl Species Involved in the Acid Catalyzed Conversion of 2-Methyl-Pentene-2* **J. Cat.** *181* 124-144 (1999).

[8] Martens, J. A., and Jacobs, P. A., *Reaction Mechanisms of Acid Catalyzed Hydrocarbon Conversions in Zeolites* in *Handbook of Heterogeneous Catalysis* (Eds. G. Ertl, H. Knözinger and J. Weitkamp) **Wiley-VCH** 1137-1149 (1997).

[9] Svoboda, G. D., Vynckier, E., Debrabandere, B., and Froment, G. F., *Single-event rate parameters for paraffin hydrocracking on a Pt/US-Y Zeolite* **Ind. Eng. Chem. Res.** *34* 3793-3800 (1995).

[10] Martens, G. G., Marin, G. B., Jacobs, P. A., Martens, J. A., and Baron, G. V., *A Fundamental Model for Hydrocracking of C_8 to C_{12} Alkanes on Pt/US-Y Zeolites* **J. Catal.** *195* 253-267 (2000).

[11] Vynckier, E., and Froment, G. F., *Modelling of the kinetics of complex processes based upon elementary steps*, in: *Kinetic and Thermodynamic Lumping of Multicomponent Mixtures* (G. Astarita and S. I. Sandler, Eds.) **Elsevier,** *Amsterdam* 131-161 (1991).

[12] Feng, W., Vynckier, E., and Froment, G. F., *Single-Event Kinetics of Catalytic Cracking* **Ind. Eng. Chem. Res.** *32* 2997-3005 (1993).

[13] Valéry, E., *Application de la Théorie des Evènements Constitutifs à l'Hydrocracquage de Paraffines Lourdes* **PhD Thesis** *Université Claude Bernard – Lyon I* (2002).

[14] Benson, S. W., Cruickshank, F. R., Golden, D. M., Haugen, G. R., O'Neal, H. E., Rodgers, A. S., Shaw, R., and Walsch, R., *Additivity Rules for the Estimation of Thermochemical Properties* **Chem. Rev.** *69* 279-324 (1969).

[15] Benson, S. W., *Thermochemical Kinetics* **Wiley** *New York* 1968.

[16] Denayer, J. F., Baron, G. V., Martens, J. A., and Jacobs, P. A., *Chromatographic study of adsorption of n-alkanes on zeolites at high temperatures* **J. Phys. Chem. B** *102* 3077-3081 (1998).

[17] Denayer, J. F., Baron, G. V., Jacobs, P. A., and Martens, J. A., *Competitive Physisorption Effects in Hydroisomerization of n-Alkane Mixtures on Pt/Y and Pt/USY Zeolite Catalysts* **Phys. Chem. Chem. Phys.** *2* 1007-1014 (2000).

[18] Denayer, J., *Adsorption and Reaction on Zeolites: An Integrated Approach* **PhD Thesis** *Vrije Universiteit Brussel* (1998).

[19] Denayer, J. F. M., and Baron, G. V., *Adsorption of normal and branched paraffins in faujasite zeolites NaY, HY, Pt/NaY and USY* **Adsorption** *3* 1-15 (1997).

[20] Schweitzer, J. M., Galtier, P., and Schweich, D. *A Single-Events Kinetic Model for the Hydrocracking of Paraffins in a Three Phase Reactor* **Chem. Eng. Sci.** *54* 2441-2452 (1999).

[21] Quann, R. J., and Jaffe, S. B., *Structure Oriented Lumping: Describing the chemistry of Complex Hydrocarbon Mixtures* **Ind. Eng. Chem. Res.** *31,* 2483-2497 (1992).

[22] Quann, R. J., and Jaffe, S. B., *Building useful Models of Complex Reaction Systems in Petroleum Refining* **Chem. Eng. Sci.** *51* 1615-1635 (1995).

Chapter 5

Double Bond Protonation Enthalpy as a Measure of Acid Strength

Alkane, c.q., C_5 to C_{12}, hydrocracking was performed on Pt/H(US)-Y-zeolites in a plug flow reactor at the 'Centrum voor Oppervlakchemie en Katalyse' at Leuven University, vide Chapter 2. The catalytic conversion was described with a fundamental molecular model, relying on experimentally determined physisorption equilibria and on a network of elementary reactions according to the bifunctional reaction scheme, vide Chapter 4. The three zeolite samples showed substantial differences in activity, but not in selectivity. The activity differences among the zeolites mainly resulted from differences in both the number of acid sites and the average acid strength, while differences in physisorption effects for these zeolite samples were of minor importance. On each catalyst, the reactivity of alkanes increased with carbon number. This tendency was related to three phenomena: (1) physisorption of heavier molecules was more favorable; (2) the reaction network and the number of parallel reactions became larger with larger molecules and (3) in the range of carbon numbers from pentane to octane the stabilization of alkylcarbenium ions and, hence, their concentration increased with increasing size and electron donating property of alkyl-substituents. The differences in average acid strength between the three catalysts were quantified with alkene standard protonation enthalpy values extracted from the model. The kinetic parameters obtained for a reference alifatic component and a reference Pt/H-(US)-Y-type zeolite are adaptable to any

other alifatic component and any other Pt/H-(US)-Y-type catalyst by adjusting the standard protonation enthalpy.

5.1 Introduction

The acidity of H-Y-type zeolite can be modified by framework dealumination [1,2]. The catalytic activity on catalyst weight basis plotted versus framework aluminum content typically shows a "volcano" curve, with maximum activity at a framework composition that is specific for the feedstock [3-9]. The "volcano" shape has been often explained based on aluminum concentration changes of the tetrahedral oxide framework. When decreasing the Al content, the strength of the residual Brönsted acid sites increases, while the number of sites decreases. At low dealumination levels, the increase in acid strength overcompensates for the loss of acid sites. In strongly dealuminated samples, the acid site strength does not increase any further upon dealumination [10,11]. This picture is, however, oversimplified, since the Al coordination chemistry in dealuminated zeolite samples is very complicated. ^{27}Al NMR has shown that there are several types of Al coordination in the framework [12] and that a significant fraction of the framework Al atoms can change from tetrahedral to octahedral depending on temperature and atmosphere owing to hydrolysis of framework oxo bridges [13]. Catalytic activity is linked with the presence of aluminum defect sites [12]. In USY (Ultra-Stable Y-zeolite) samples, the aluminum concentration in individual crystals shows significant gradients [12]. Several authors reported a synergetic effect of framework and extra-framework Al species in the pores. Extra-framework Al species having Lewis acid properties withdraw electron density from the bridging hydroxyl group and enhance the Brönsted acid strength. For obtaining activity enhancement, the dealumination procedure is critical [4,6,14-16].

In the homologous series of alkanes, the hydrocracking reactivity increases with increasing carbon number, which can be related to a stronger physisorption and the higher number of reaction possibilities [17]. The physisorption equilibrium coefficient increases exponentially with the carbon number, while the reaction network expands rather linearly [18,19].

In this Chapter the effect of the acid strength of the zeolite and of the carbon number of the alkane reactant is quantified. For this purpose, a kinetic model on a molecular level was used instead of previously used lumped or relumped models [17,19,20]. The model was applied to an extended series of alkanes and an as broad as possible variation of acidity in Pt/H-(US)Y-zeolites.

Table 5-1 Catalysts, model components and range of the experimental conditions

	Feeds	W/F_0 (kg s mol^{-1})	X (%)	T (K)	P (MPa)	H_2/HC
Pt/H-Y	$C_5 – C_9, C_{12}$	7-1300	0 - 60	506 - 538	0.45 - 0.7	13.13
Pt/CBV-720	C_6, C_9	1-36	0 - 40	506	0.45	13.13
Pt/CBV-760	$C_5 – C_9, C_{12}$	4-1400	0 - 95	506 - 563	0.45 -1.5	4.23 - 250

5.2 Experimental

Hydrocracking experiments were performed in a tubular flow reactor packed with catalyst pellets under the reaction conditions and with the model components mentioned in Table 5-1. Under these conditions *ideal* hydrocracking occurs and, hence, no differences in selectivity were observed upon altered reaction conditions [17,21]. Methane and ethane formation is indicative of the occurrence of hydrogenolysis, however, the contribution of hydrogenolysis to the observed product distributions was negligible, except for pentane on Pt/H-Y-zeolite. The assessment of transport limitations is analogous to that presented in Chapter 3, i.e., a Weisz modulus of the order 10^{-3} ensures that intrinsic kinetics have been observed.

5.3 Results and Discussion

5.3.1 Hydrocracking of n-octane on a reference zeolite

For alkanes with eight carbon atoms or more, the reaction network comprises all possible isomerization and β-scission pathways. Octane was chosen as the reference component for analytical reasons. All individual skeletal isomers from octane could be separated by gas-chromatography. Pt/CBV-760 was selected as the reference catalyst, since it exhibits an intermediate level of activity between Pt/H-Y and Pt/CBV-720. The largest range of conversion levels was experimentally obtained with this zeolite, vide Table 5-1.

Product distributions obtained from octane hydrocracking show that from a total conversion of 20 to 30 % on equilibrium is established among the group of the monobranched isomers, vide Figure 5-1a and Table 5-2. This indicates that alkyl shifts interconverting monobranched isomers are faster than PCP-branching reactions altering the branching degree of the isomer and than the β-scissions breaking the isomer into 2 hydrocarbon fragments. Generally stated, the same holds for the dibranched isomers. Tribranched isomers were only observed in trace amounts and, hence, no reliable experimental distribution could be obtained. However, the 2,2,4-trimethylpentane isomer, which is the most abundant isomer under equilibrium

Table 5-2 Equilibrium composition of the octane isomers at 506 K

isomer group / individual isomer		group fraction / individual fraction	
normal		0.09	
monobranched	2-methylheptane	0.44	0.38
	3-methylheptane		0.39
	4-methylheptane		0.13
	3-ethylhexane		0.10
dibranched		0.44	
tribranched		0.03	

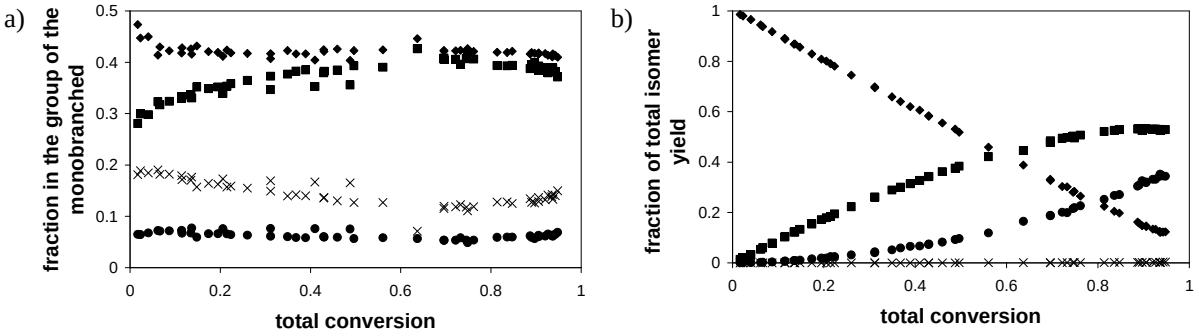

Figure 5-1 Experimental distribution a) for the group of the monobranched isomer (♦: 3-methylheptane, ■: 2-methylheptane, ●: 3-ethylhexane, ×: 4-methylheptane) b) for all isomers classified according to their branching degree (♦: normal, ■: monobranched, ●: dibranched, ×: tribranched)

conditions, is susceptible to fast (t;t)-β-scission and was not observed. This is indicating that no equilibrium is established among the tribranched isomers.

The continuous evolution in distribution between isomers with different branching degree shows that no equilibrium is established between these isomer groups. Nevertheless, at the highest conversions, the distribution between the normal and the monobranched isomers tends to equilibrium, vide Figure 5-1b and Table 5-2. Similar conclusions have been obtained before by Vansina et al. [24] in a Berty reactor.

Estimations of the activation energies in the single-event model for hydrocracking of octane on Pt/CBV-760 with calculated pre-exponential factors as in [20] led to values in agreement with earlier results [18,20], vide Table 5-3. Reactions involving tertiary carbenium ions have a lower composite activation energy than those involving secondary ions. Alkyl shifts have lower composite activation energies than PCP-branching reactions. Since the calculated pre-

Table 5-3 **Composite activation energies ($\Delta H_{prot}+E_{act}$) estimated by a regression on the experimental data with *n*-octane on Pt/CBV-760 and corresponding individual 95% confidence interval**

	Alkylshift	PCP-branching	β-scission
		(kJ mol^{-1})	
(s;s)	16.7 (±0.1)	45.6 (±0.1)	79.2 (±0.6)
(s;t)	13.7 (±2.4)	38.8 (±5.5)	63.7 (±4.5)
(t;s)			55.1 (±0.6)
(t;t)	7.7 (±2.9)	31.5 (±2.3)	33.9 (±1.7)

Table 5-4 **Composite rate coefficients ($K_{prot}(O_r;m)k(m;n)$) obtained with the estimated composite activation energies and the preexponential factors calculated as in [20]**

	Alkylshift	PCP-branching	β-scission
		($kg_{cat}mol^{-1}s^{-1}$)	
(s;s)	$9.9\ 10^6$	$10.3\ 10^3$	$3.9\ 10^3$
(s;t)	$20.2\ 10^6$	$52.0\ 10^3$	$153\ 10^3$
(t;s)			$1.2\ 10^6$
(t;t)	$84.2\ 10^6$	$295\ 10^3$	$183\ 10^6$

exponential factor for both reaction families is the same [20], alkyl shifts are faster than branching rearrangements. β-scissions have the highest composite activation energies, except for the (t;t)-β-scission with a composite activation energy comparable to (t,t)-PCP-branching. However, the higher pre-exponential factor leads to rate coefficients that are similar to those for PCP-branching for the (s;s), (s;t) and (t;s) β-scission and an even higher rate coefficient for (t;t) β-scission than that for (t;t) alkyl-shift, vide Table 5-4.

Modelling the reactor performance with the obtained kinetic parameters resulted in an adequate description of both the conversion and the selectivity ratio of isomerization to cracking (Figure 5-2). The same holds for the outlet flow rates of isomers and cracked products (Figure 5-3).

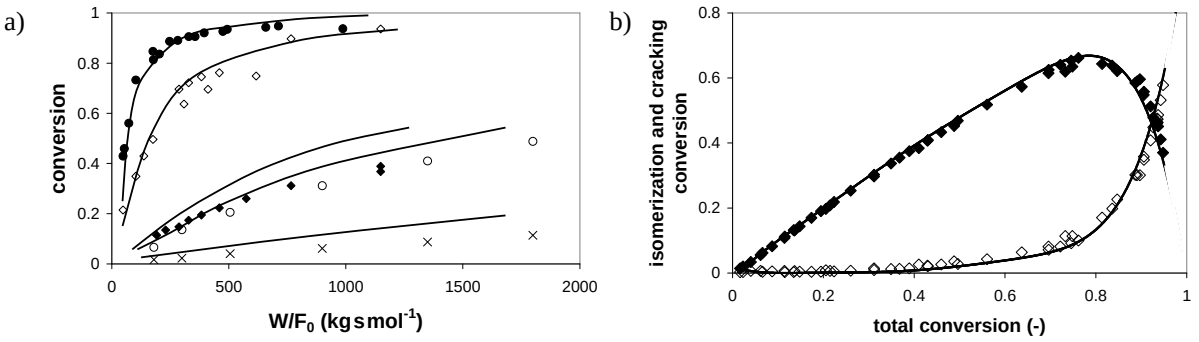

Figure 5-2 **Experimental (symbols) and calculated (lines) results for a) C_8 conversion on Pt/CBV-760 as a function of space time (♦: 506 K - 0.45 MPa - H_2/HC = 13.13, ◊: 539 K - 0.45 MPa - H_2/HC=13.13, ●: 563 K - 0.45 MPa - H_2/HC = 13.13, ○: 539 K - 0.7 MPa - H_2/HC=250, ×: 506 K - 0.7 MPa - H_2/HC=250) and for b) C_8 selectivity on Pt/CBV-760 to isomers (♦) and cracked products (◊). The reaction rates have been calculated using Eq. (4.3) – Eq. (4.16) with the composite rate coefficients from Table 5-4**

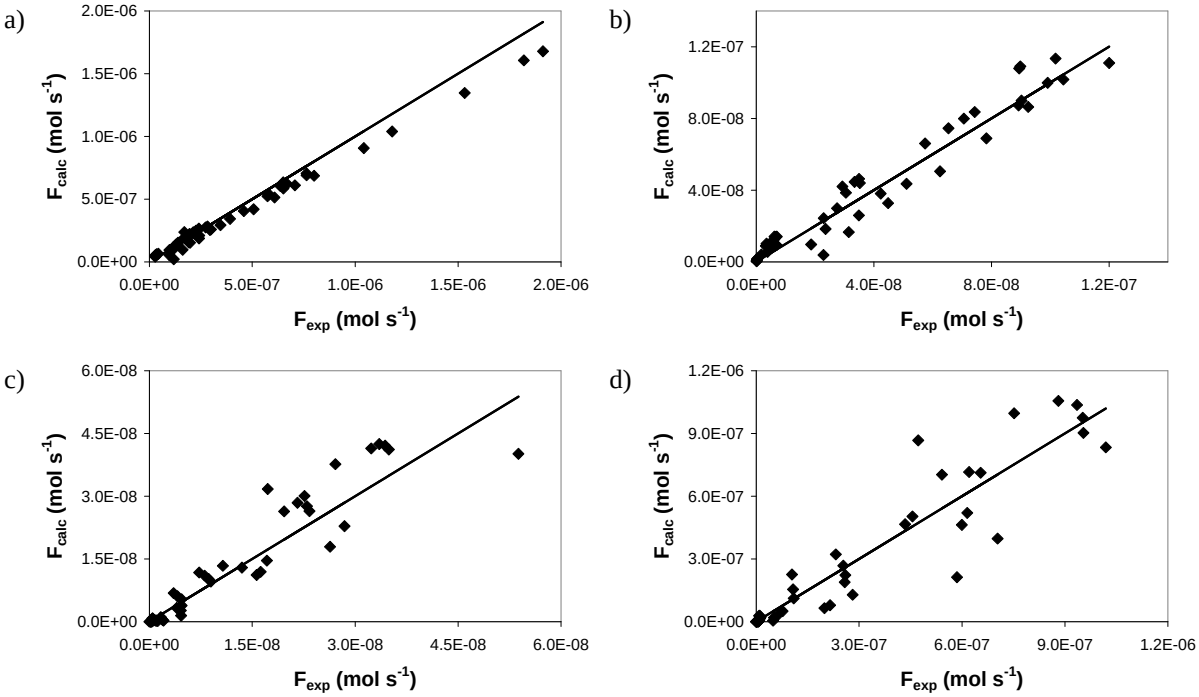

Figure 5-3 **Parity diagrams for the outlet flow rates for some typical hydrocracking products from octane on Pt/CBV-760 a) 3-methyl-heptane, b) 3,3-dimethyl-hexane, c) *n*-pentane and d) isobutane. Range of experimental conversions, vide Table 5-1. The calculated outlet flow rates have been obtained using Eq. (4.3) – Eq. (4.16) with the composite rate coefficients from Table 5-4**

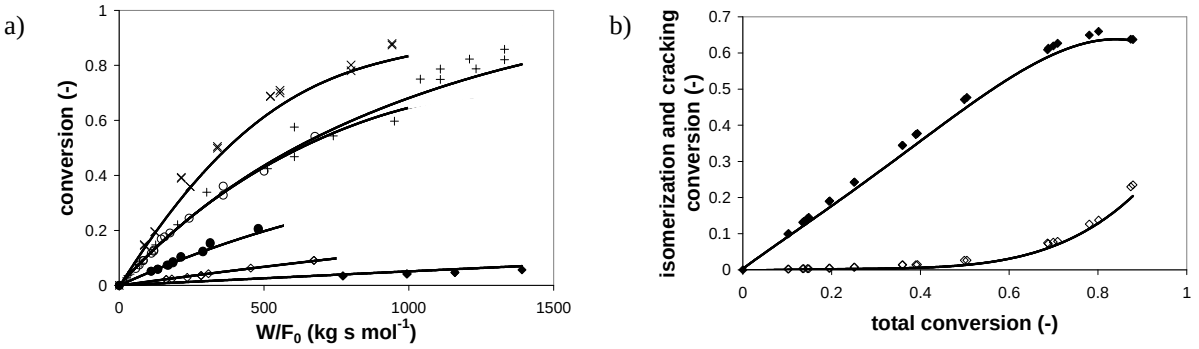

Figure 5-4 **Experimental (symbols) versus calculated (lines) results for a) alkane conversion on Pt/CBV-760 as a function of space time at 506 K - 0.45 MPa - H_2/HC=13.13 (except for pentane at 539 K) (♦: pentane, ◊: hexane, ●: heptane, ○: octane, ×: nonane, +: dodecane) and for b) nonane selectivity to isomers (♦) and cracked products (◊). The calculated outlet flow rates have been obtained using Eq. (4.3) – Eq. (4.16) with the composite rate coefficients from Table 5-4**

5.3.2 Effect of carbon number on alkene protonation enthalpy

An increased reactivity with the carbon number was observed in the range of pentane to nonane, whereas for dodecane a slight decrease in reactivity with respect to nonane was observed (Figure 5-4a). The increased reactivity of heavier alkanes in the range pentane to nonane can be attributed to their stronger physisorption and their more extended set of reaction possibilities. The decrease in reactivity from nonane to dodecane was caused by physisorption saturation effects. Physisorbed nonanes and dodecanes are at relatively 84% and 98% of their saturation concentration. From the saturation concentrations mentioned in Table 4-1c it is clear that the concentration of physisorbed nonanes is higher than that of the physisorbed dodecanes.

According to the single-event model, the carbon number effect on the reaction kinetics is entirely due to physisorption and reaction network effects. In the model, the protonation-deprotonation equilibrium of the reference alkene (2-methylalk-2-ene) is assumed only to depend on the type of alkylcarbenium ion and not on the carbon number, vide Eq. (4.9). The alkylcarbenium ion stability *according to the model* depends on the number of α C-C-bonds [18,20,25]. Methyl and primary alkylcarbenium ions were assumed to be too unstable. Only two types of alkylcarbenium ions were considered, having a different stability, i.e., secondary and tertiary ions. For example, *according to the model* the stability of the oct-3-yl cation is identical to that of the 2,2,4-trimethylpent-3-yl cation.

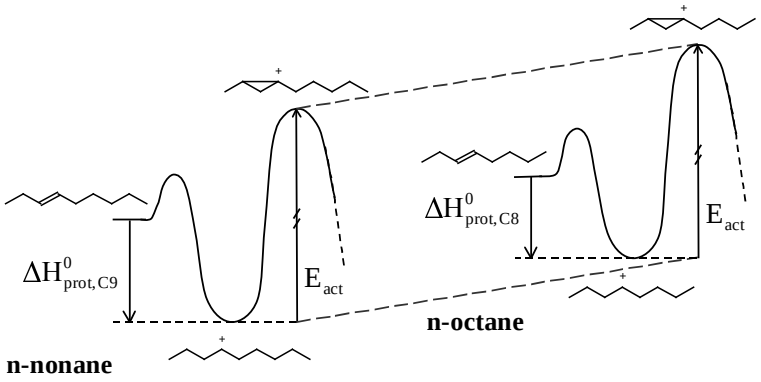

Figure 5-5 Energy levels for the intermediates in an elementary acid catalyzed step, effect of the carbon number of the intermediate

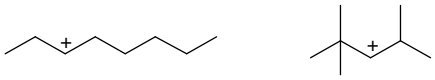

These two cations have 2 α C-C-bonds. However, the 2,2,4-trimethylpent-3-yl cation has 3 β C-C-bonds more than the oct-3-yl cation, resulting in a difference in stability of these two cations in the gas phase of a few *kJ mol*$^{-1}$ [26,27]. The model used considers no differences in stability between these two cations on the catalyst surface. Hence, the estimated composite activation energies, vide Eq. (4.18), are based on an average value of the standard protonation enthalpy. The independence of the single-event rate parameters on the carbon number implies that this average level is independent of the carbon number.

In the model both the intermediate and the activated complex of acid catalyzed steps were considered to have ionic character. The effect of the carbon number on the stability of the intermediate and the activated complex were expected to be the same. Hence, the activation energy is independent of the carbon number, vide Figure 5-5. Consequently, the carbon number effect on the composite activation energy could be entirely attributed to an effect on the standard protonation enthalpy. Hence, from Eq. (4.18) follows that:

$$\Delta_{CN_j - CN_i}\left(E_A^{comp}\right) = \Delta_{CN_j - CN_i}\left(\Delta H^0_{prot}\right) \tag{5.1}$$

Differences in standard protonation enthalpy on the zeolite were related to differences in standard protonation enthalpy in the gas phase by considering the Born-Haber cycle in Figure 5-6,

$$\Delta H^0_{prot,zeo} = \Delta H^0_{stab,R^+} + \Delta H^0_{prot,gas} - \Delta H^0_{stab,H^+} - \Delta H^0_{phys,O} \tag{5.2}$$

In Eq. (5.2) $\Delta H^0_{stab,H^+}$ is carbon number independent. The carbon number dependence of

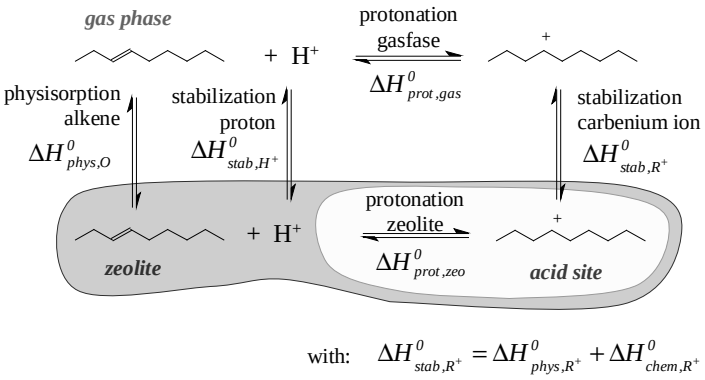

Figure 5-6 Born-Haber cycle relating the standard protonation enthalpy on the zeolite with the gas phase protonation enthalpy

$\Delta H^0_{phys,O}$ is related to differences in alkene physisorption, while that of $\Delta H^0_{stab,R^+}$ consists of two contributions,

$$\Delta_{CN_j-CN_i}\left(\Delta H^0_{stab,R^+}\right)=\Delta_{CN_j-CN_i}\left(\Delta H^0_{phys,R^+}\right)+\Delta_{CN_j-CN_i}\left(\Delta H^0_{chem,R^+}\right) \tag{5.3}$$

In Eq. (5.3) $\Delta H^0_{phys,R^+}$ accounts for physical interactions with the zeolite pores, i.e., physisorption, while $\Delta H^0_{chem,R^+}$ accounts for electrostatic interactions of the carbenium ion with a deprotonated acid site. The effect of the carbon number on $\Delta H^0_{phys,R^+}$ is expected to be similar to the effect of the carbon number on $\Delta H^0_{phys,O}$,

$$\Delta_{CN_j-CN_i}\left(\Delta H^0_{phys,R^+}\right)\cong\Delta_{CN_j-CN_i}\left(\Delta H^0_{phys,O}\right) \tag{5.4}$$

The expression for the standard protonation enthalpy increase for a hydrocarbon with carbon number CN_j with respect to the reference hydrocarbon with carbon number CN_i can then be written as:

$$\Delta_{CN_i-CN_j}\left(\Delta H^0_{prot,zeo}\right)=\Delta_{CN_i-CN_j}\left(\Delta H^0_{prot,gas}\right)+\Delta_{CN_i-CN_j}\left(\Delta H^0_{chem,R^+}\right) \tag{5.5}$$

For two alkenes with different carbon number Eq. (5.5) represents the sum of the difference in gas phase standard protonation enthalpy and the difference in stabilization enthalpy by electrostatic interactions of the alkylcarbenium ion with the deprotonated acid site. A similar equation for the carbon number dependence of the standard protonation enthalpy can be obtained via the concept of the 'proton transfer energy' Q_p as used by van Santen and Kramer [11] to describe the protonation of a gas phase alkene by an acid site,

$$Q_p=-PA^{base}_{gas}+PA^{acid}_{solid}+E_{zi} \tag{5.6}$$

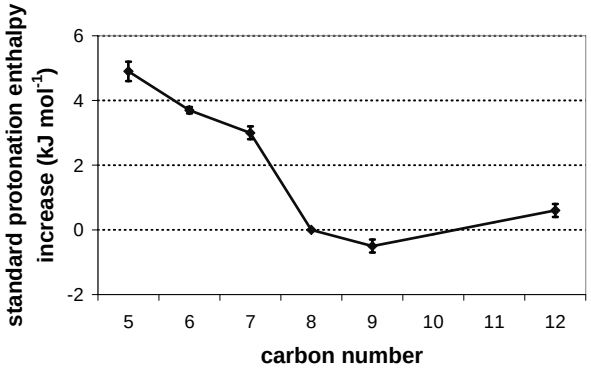

Figure 5-7 Standard protonation enthalpy increases on Pt/CBV-760 as a function of the carbon number (reference: octane)

in which PA_{gas}^{base} stands for the proton affinity of the gas phase carbenium ion, which is equal to $-\Delta H_{prot,gas}^{0}$. PA_{solid}^{acid} is defined as the proton affinity of a surface hydroxyl and E_{zi} is the Zwitterion stabilization energy between the protonated base, i.e., the alkylcarbenium ion, and the negatively charged zeolite wall, i.e., the deprotonated acid site. E_{zi} equals the stabilization enthalpy of the carbenium ion due to electrostatic interactions with the deprotonated acid site, $\Delta H_{chem,R^+}^{0}$. The carbon number dependence of Q_p contains two contributions,

$$\Delta_{CN_i-CN_j}(Q_p) = \Delta_{CN_i-CN_j}(-PA_{gas}^{base}) + \Delta_{CN_i-CN_j}(E_{zi}) \tag{5.7}$$

which can be identified with the two terms in Eq. (5.5).

The values of the standard protonation enthalpy increase for the investigated alkenes with respect to octenes were estimated by regression of experimental hydrocracking data on Pt/CBV-760. This was done keeping the previously determined values of the composite activation energies fixed for alkyl-shift, PCP-branching and β-scission. The effect of the carbon number on the physisorption is taken into account via the physisorption properties (Eq. (4.3), Table 4-1a-c). The extension of the reaction network is apparent from the summations in Eq. (4.14) to Eq. (4.16).

Estimation of the standard protonation enthalpy increase for the various model components resulted, similarly to the reference case, in a satisfactory description of the total conversion and of the selectivity to isomers and cracked products (Figure 5-4). The outlet flow rates of the individual components were adequately described. The estimated values for the standard protonation enthalpy increase first decrease and subsequently level out with increasing carbon number (Figure 5-7). A set of data obtained on one catalyst batch leads to a typical error on the standard protonation enthalpy increase of *0.5 kJ mol^{-1}*. However, a set of data obtained on

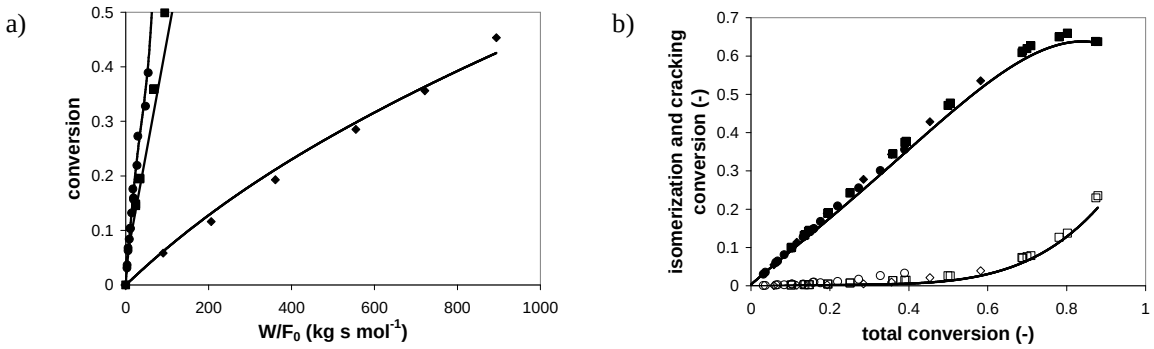

Figure 5-8 **Experimental (symbols) versus calculated (lines) results for a) nonane conversion as a function of space-time at 506 K - 0.45 MPa - H_2/HC=13.13 and for b) nonane selectivity to isomers (closed symbols) and cracked products (open symbols) (♦: Pt/H-Y-zeolite, ●: Pt/CBV-720, ■: Pt/CBV-760). The calculated outlet flow rates have been obtained using Eq. (4.3) – Eq. (4.16) with the composite rate coefficients from Table 5-4**

several catalyst batches has an error of *1* to *1.5 kJ mol*$^{-1}$. The increments with carbon number vary from *-3* to less than *-1 kJ mol*$^{-1}$, which is in the order of magnitude expected when β C-C-bonds are invoked to explain differences in the carbenium ion stability. The significant variations at lower carbon numbers originate from the more pronounced inductive effects of alkyl-substituents in the range pentane to octane compared to heavier components, i.e., octane to dodecane. According to the error obtained on several catalyst batches, no significant variations are observed for the heavier components. The leveling out from carbon numbers of eight on is also in agreement with previous modelling work [20] and supports the carbon number independence of the single-event kinetic parameters for C_8 and heavier hydrocarbons.

5.3.3 Effect of average catalyst acid strength on alkene protonation enthalpy

Experimentally, only differences in activity but not in selectivity were observed when feeding the same alkane over the three Pt/H-(US)Y-zeolites with different average acid strengths. This is illustrated in Figure 5-8 for nonane. Similar results were obtained for hexane on the three zeolites and for the other alkanes on Pt/H-Y and Pt/CBV-760. The absence of selectivity differences indicates that all the rate determining steps were influenced to a same extent upon variation of the average acid strength of the zeolite.

The intermediate and the activated complex in these acid catalyzed reactions were assumed to have ionic character. Hence, the acid strength of an active site will influence the stability of

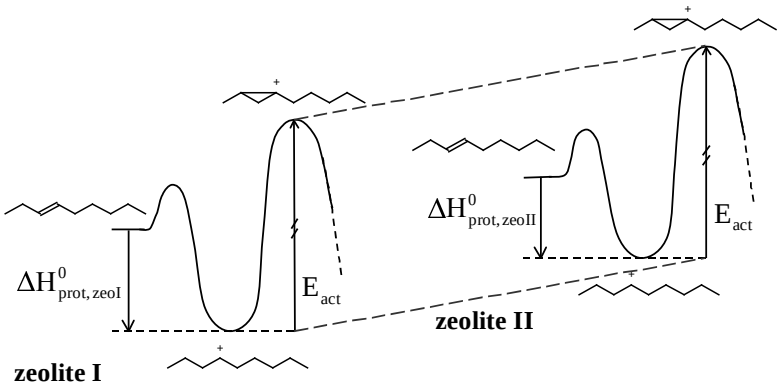

Figure 5-9 Energy levels for the intermediates in an elementary acid catalyzed step, effect of the acid strength of the active site

both species. It can reasonably be assumed that the relative stability of the intermediate and the activated complex is independent of the acid strength and, hence, that the activation energy is not depending on the acid strength. Therefore, the difference in activity can be attributed to a difference in standard protonation enthalpy of the alkenes on the zeolite (Figure 5-9).

The physical meaning of the standard protonation enthalpy of alkenes, Eq. (5.2), is given in Figure 5-6. The acid strength dependence of $\Delta H^0_{stab,R^+}$ can be split up into an electrostatic and a physical contribution, Eq. (5.3). The differences in physisorption of carbenium ions between two zeolite samples were taken as the differences in physisorption between the corresponding alkenes,

$$\Delta_{zeo_{II}-zeo_I}\left(\Delta H^0_{phys,R^+}\right) \cong \Delta_{zeo_{II}-zeo_I}\left(\Delta H^0_{phys,O}\right) \tag{5.8}$$

Following these considerations, the standard protonation enthalpy increase for an alkene on a Pt/H-(US)Y-zeolite with respect to a reference Pt/H-(US)Y-zeolite can be written as:

$$\Delta_{zeo_{II}-zeo_I}\left(\Delta H^0_{prot,zeo}\right) = \Delta_{zeo_{II}-zeo_I}\left(\Delta H^0_{chem,R^+}\right) - \Delta_{zeo_{II}-zeo_I}\left(\Delta H^0_{stab,H^+}\right) \tag{5.9}$$

Similar to the case of the carbon number effect, an analogous equation as Eq. (5.9) can be derived via the so-called proton transfer energy Q_p. The two acid strength dependent contributions in Q_p

$$\Delta_{zeo_{II}-zeo_I}\left(Q_p\right) = \Delta_{zeo_{II}-zeo_I}\left(PA^{acid}_{solid}\right) + \Delta_{zeo_{II}-zeo_I}\left(E_{zi}\right) \tag{5.10}$$

can be identified with the two terms in Eq. (5.9), i.e., PA^{acid}_{solid} with the $-\Delta H^0_{stab,H^+}$ and E_{zi} with $\Delta H^0_{chem,R^+}$. Other groups [9,28-32] made similar considerations on the effect of the acid strength based on the work of Dumesic et al. [33]. Those authors related gas phase reference data to the zeolite considered by the definition of a ΔH^+ which represents the stabilization

enthalpy of the alkylcarbenium ion by the zeolite, relative to the stabilization enthalpy of a proton by the zeolite. The standard protonation enthalpy increase as expressed in Eq. (5.9) is equal to the difference between the two ΔH^{+}-values for the respective zeolites.

$$\Delta_{zeo_{II}-zeo_{I}}\left(\Delta H^{0}_{prot,zeo}\right)=\Delta H^{+}_{zeo_{II}}-\Delta H^{+}_{zeo_{I}} \tag{5.11}$$

The effect of the acid strength on the hydrocracking behaviour was investigated by modelling the hydrocracking experiments with nonane on three Pt/H-(US)Y-zeolites. The standard protonation enthalpy for the nonenes on the Pt/H-(US)Y-zeolites with respect to the nonenes on the reference Pt/H-USY-zeolite, Pt/CBV-760, were estimated, keeping the values of the composite activation energies fixed at the values mentioned in Table 5-3. Differences in physisorption properties of the nonanes on the different catalysts were taken into account via C_{sat} and K_{L,P_i} in Eq. (4.3) (Table 4-1a-c).

The obtained results for each of the Pt/H-(US)Y-zeolites are interpreted in terms of a single acid site strength for each zeolite. In reality, Pt/H-(US)Y-zeolites have an acid strength distribution (Table 2-1), and, hence, the single acid strength reported, represents an average acid strength. Since the acid site coverage is low, vide Appendix D, the average acid strength of only the strongest acid sites is considered. The substitution of the acid strength distribution by a single average acid strength has no effect on the reaction rate of an elementary acid catalyzed step calculated with the single-event model.

The only acid strength dependent parameter in Eq. (4.3) for the rate of an elementary acid catalyzed step is the single-event protonation-deprotonation equilibrium coefficient. Using the standard protonation enthalpy of the alkene on the acid site for the quantification of the acid strength of the site, a normalized acid strength distribution $E_{distr}\left(\Delta H^{0}_{prot}\right)$ can be introduced [34],

$$\int_{\Delta H^{0}_{prot,lower}}^{\Delta H^{0}_{prot,upper}} E_{distr}\left(\Delta H^{0}_{prot}\right) d\left(\Delta H^{0}_{prot}\right)=1 \tag{5.12}$$

The reaction rate on the Pt/H-(US)Y-zeolite of an elementary step equals the sum of the reaction rates on each active site. Considering a continuous distribution, an integration rather than a summation is performed,

$$r^{AS/PCP/\beta}=\int_{\Delta H^{0,lower}_{prot}}^{\Delta H^{0,upper}_{prot}} r^{AS/PCP/\beta}\left(\Delta H^{0}_{prot}\right)E_{distr}\left(\Delta H^{0}_{prot}\right)d\left(\Delta H^{0}_{prot}\right) \tag{5.13}$$

By selection of a reference value for ΔH^{0}_{prot}, the reaction rate on an active site can be written

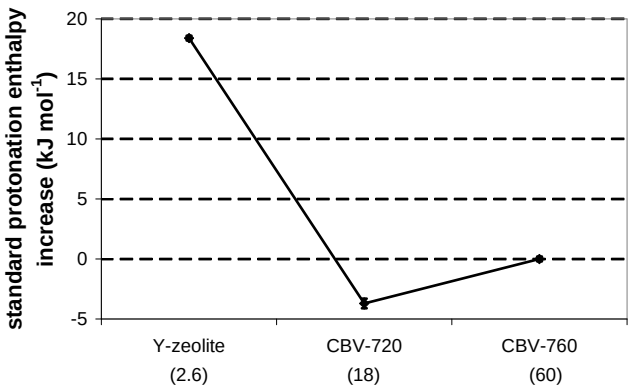

Figure 5-10 Standard protonation enthalpy increase for nonane on three Pt/H-(US)Y-zeolites (reference Pt/CBV-760; between brackets: atomic Si/Al$_F$-ratio)

as,

$$r^{AS/PCP/\beta}\left(\Delta H^{0}_{prot}\right) = r^{AS/PCP/\beta}\left(\Delta H^{0,ref}_{prot}\right)\exp\left(-\frac{\Delta H^{0}_{prot} - \Delta H^{0,ref}_{prot}}{R\,T}\right) \tag{5.14}$$

and, hence, Eq. (5.13) can be transformed into:

$$r^{AS/PCP/\beta} = r^{AS/PCP/\beta}\left(\Delta H^{0,ref}_{prot}\right) exp\left(\frac{\Delta H^{0,ref}_{prot}}{R\,T}\right)\int_{\Delta H^{0,lower}_{prot}}^{\Delta H^{0,upper}_{prot}} exp\left(-\frac{\Delta H^{0}_{prot}}{R\,T}\right) E_{distr}\left(\Delta H^{0}_{prot}\right) d\left(\Delta H^{0}_{prot}\right) \tag{5.15}$$

In Eq. (5.15) the integral equals the mean value of $\exp\left(-\Delta H^{0}_{prot}/R\,T\right)$ from which an average value of ΔH^{0}_{prot} can be determined so that the final equation for the total reaction rate of an acid catalyzed elementary step becomes

$$r^{AS/PCP/\beta} = r^{AS/PCP/\beta}\left(\Delta H^{0,ref}_{prot}\right)\exp\left(-\frac{\Delta H^{0,ave}_{prot} - \Delta H^{0,ref}_{prot}}{R\,T}\right) \tag{5.16}$$

Eq. (5.16) clearly shows that working with $\Delta H^{0,ave}_{prot}$ or explicitly taking into account the acid strength distribution of the zeolite leads to identical model predictions owing to the nature of the model equations.

The total hydrocracking conversion, the isomerization and the cracking conversion of nonane on the three zeolites (Figure 5-8) and the individual outlet flow rates were simulated satisfactorily. The estimated standard protonation enthalpy increases for the three zeolites, ordered according to their Si/Al$_F$-ratio is shown in Figure 5-10. The highest value of the standard protonation enthalpy increase, corresponding with the weakest average acid strength, was found for the Pt/H-Y-zeolite, as expected. In the dealuminated Pt/CBV-720 sample, the

standard protonation enthalpy was lower reflecting the increase of average acid strength, vide Figure 5-10. Moreover the standard protonation enthalpy increase for Pt/CBV-720 was lower than that of the most dealuminated Pt/CBV-760 sample. Consequently the average acid strength of Pt/CBV-720 was slightly higher than that of Pt/CBV-760. This decrease of the acid strength at very high dealumination levels is in agreement with the commonly observed trends commented in Section 5.1.

5.3.4 Combined effect of carbon number and acid strength

A series of experiments with alkanes ranging from pentane to dodecane have been performed on the Pt/H-Y-zeolite. Hence, both the carbon number and the zeolite were different from the reference case, i.e., octane on Pt/CBV-760. The relative reactivities observed were similar to those for the series of alkanes on Pt/CBV-760, however, the absolute reactivity on the Pt/H-Y-zeolite was much lower. Estimates for the standard protonation enthalpy increase with respect to the reference case were obtained by regression of the corresponding kinetic data, maintaining all the kinetic parameters related to the carbenium ion rearrangements fixed at their reference values. These estimates account simultaneously for the effect of the carbon number, vide Eq. (5.5), Section 5.3.2 and the effect of the average acid strength, vide Eq. (5.9), Section 5.3.3. By comparison with the sum of the values obtained while investigating the two separate effects separately, the additivity of the latter was verified. The altered physisorption behaviour was taken into account via C_{sat} and K_{L,P_i} in Eq. (4.3) (Table 4-1a-c).

A good agreement between experimental and calculated total hydrocracking conversion and isomerization and cracking conversion was observed as well as for the individual outlet flow rates. The estimated values for the standard protonation enthalpy increases are shown in Figure 5-11 and compared with the sum of the two separate effects. Additivity, within the statistical limits, was observed for all the alkanes used in this work, except for hexane. However, since the deviation found for hexane doesn't further increase, but even decreases when pentane is considered, it can be stated that the standard protonation enthalpy increase with the carbon number is independent of the zeolite considered.

The high values for the standard protonation enthalpy increase on the Pt/H-Y-zeolite reflect how difficult acid catalyzed alkene conversion is on Pt/H-Y-zeolite. Hence, other reaction pathways, such as hydrogenolysis, can become dominant. The difficult alkane protonation on Pt/H-Y-zeolite was most obvious for pentane, where hydrogenolysis accounted for about half of the pentane conversion. The average acid strength of a Pt/H-Y-zeolite is too weak for pentene conversion.

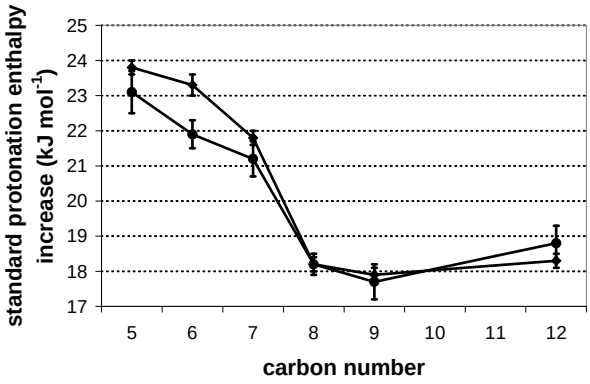

Figure 5-11 Standard protonation enthalpy increases for alkanes on Pt/H-Y-zeolite (reference: octane on Pt/CBV-760). Direct estimation for the combined effect of carbon number and acid strength (♦) compared to the sum of the results for the two separate effects (●)

5.4 Conclusions

The effect of reactant carbon number and average acid strength of zeolites on the hydrocracking activity was investigated via the kinetic modelling of alkane hydrocracking data on three Pt/H-(US)Y-zeolites. Physisorption was explicitly accounted for based on independently obtained information.

The effect of the reactant carbon number was incorporated in the model through the introduction of the standard protonation enthalpy of physisorbed alkenes as only parameter. The estimated standard protonation enthalpies indicate a stabilization of the carbenium ions which increases with the carbon number in the range pentane to octane. The latter is caused by an increase of branching possibilities allowing extra inductive stabilization. For carbon numbers of C_8 and higher, the effect levels out. The carbon number effect on the standard protonation enthalpy is independent of the zeolite.

The standard protonation enthalpy of alkenes also offers a means to quantify the average acid strength of Pt/H-(US)Y-zeolites. Accounting for different average acid strengths could also be achieved by adjustment of the standard protonation enthalpy. The estimated values show a shallow maximum in average acid strength for the Pt/CBV-720 sample, while the average acid strength of Pt/H-Y-zeolite is too weak for pentene protonation.

5.5 References

[1] Kerr, G. T., *Hydrogen Zeolite Y, Ultrastable Zeolite Y, and Aluminum-Deficient Zeolites* **Adv. Chem. Ser.** *121* 219-229 (1973).

[2] Wang, Q. L., Giannetto, G., Torrealba, M., Perot, G., Kappenstein, C., and Guisnet, M., *Dealumination of Zeolites Kinetic study of the dealumination by hydrothermal treatment of a NH4NaY Zeolite* **J. Catal.** *130* 459-470 (1991).

[3] Barthomeuf, D., *Zeolite acidity dependence on structure and chemical environment, correlations with catalysis* **Mat. Chem. Phys.** *17* 49-71 (1987).

[4] Kuehne, M. A., Kung, H. H., and Miller, J. T., *Effect of Steam Dealumination on H-Y Acidity and 2-Methylpentane Cracking Activity* **J. Catal.** *171* 293-304 (1997).

[5] Corma, A., Martinez, A., Pergher, S., Peratello, S., Perego, C., and Bellusi, G., *Hydrocracking-hydroisomerization of n-decane on amorphous silica-alumina with uniform pore diameter* **Appl. Catal. A Gen.** *152* 107-125 (1997).

[6] Kuehne, M. A., Babitz, S. M., Kung, H. H., and Miller, J. T., *Effect of framework Al content on HY acidity and cracking activity* **Appl. Catal. A Gen.** *166* 293-299 (1998).

[7] Morin, S., Ayrault, P., Gnep, N. S., and Guisnet, M., *Influence of the framework composition of commercial HFAU zeolites on their activity and selectivity in m-xylene transformation* **Appl. Catal. A Gen.** *166* 281-292 (1998).

[8] Zhang, W., and Smirniotis, P. G., *Effect of Zeolite Structure and Acidity on the Product Selectivity and Reaction Mechanism for n-Octane Hydroisomerization and Hydrocracking* **J. Catal.** *182* 400-416 (1999).

[9] Yaluris, G., Madon, R. J., and Dumesic, J. A., *Catalytic Ramifications of Steam Deactivation of Y Zeolites : An Analysis Using 2-Methylhexane Cracking* **J. Catal.** *186* 134-146 (1999).

[10] Dempsey, E., *Acid Strength and Aluminum Site Reactivity of Y Zeolites* **J. Catal.** *33* 497-499 (1974).

[11] van Santen, R. A., and Kramer, G. J. *Reactivity theory of Zeolitic Brondsted Acidic Sites* **Chem. Rev.** *95* 637-660 (1995).

[12] Remy, M. J., Stanica, D., Poncelet, G., Feijen, E. J. P., Grobet, P. J., Martens, J. A., and Jacobs, P. A., *Dealuminated H-Y zeolites: Relation between Physicochemical Properties and catalytic Activity in Heptane and Decane Isomerization* **J. Phys. Chem.** *100* 12440-12447 (1996).

[13] Wouters, B. H., Chen, T.-H., and Grobet, P. J., *Reversible tetrahedral-octahedral framework aluminum transformation in zeolite Y* **J. Am. Chem. Soc.** *120* 11419-11425 (1998).

[14] Wang, Q. L., Giannetto, G., and Guisnet, M., *Dealumination of Zeolites III. Effect of Extra-framework aluminum species on the activity, selectivity and stability of Y zeolites in n-heptane cracking* **J. Catal.** *130* 471-482 (1991).

[15] Biaglow, A. I., Parillo, D. J., Kokotailo, G. T., and Gorte, R. J., *A Study of Dealuminated Faujasites* **J. Catal.** *148* 213-223 (1994).

[16] Bamwenda, G. R., Zhao, Y. X. Groten, W. A., and Wojciechowski B. W., *The Effects of EFAl Extraction on 2-Methylpentane Cracking over Steamed HY* **J. Catal.** *157* 209-221 (1995).

[17] Debrabandere, B., and Froment, G. F., *Influence of the hydrocarbon length on the kinetics of the hydroisomerization and hydrocracking of n-paraffins* **Stud. Surf. Sci. Cat.** *106* 379-389 (1997).

[18] Svoboda, G. D., Vynckier, E., Debrabandere, B., and Froment, G. F., *Single-event rate parameters for paraffin hydrocracking on a Pt/US-Y Zeolite* **Ind. Eng. Chem. Res.** *34* 3793-3800 (1995).

[19] Denayer, J. F., Baron, G. V., Souverijns, W., Martens, J. A., and Jacobs, P. A., *Hydrocracking of n-alkane mixtures on Pt/H-Y zeolite: Chain length dependence of the adsorption and kinetic constants* **Ind. Eng. Chem. Res.** *36* 3242-3247 (1997).

[20] Martens, G. G., Marin, G. B., Martens, J. A., Jacobs, P. A., and Baron, G. V., *A Fundamental Model for Hydrocracking of C_8 to C_{12} Alkanes on Pt/US-Y Zeolites* **J. Catal.** *195* 253-267 (2000).

[21] Weitkamp, J., *Hydrocracking, Cracking and Isomerization of Hydrocarbons* **Erdöl Kohle Erdgas P.** *31* 13-22 (1978).

[22] Denayer, J. F. M., and Baron, G. V., *Adsorption of normal and branched paraffins in faujasite zeolites NaY, HY, Pt/NaY and USY* **Adsorption** *3* 1-15 (1997).

[23] Denayer, J. F., Baron, G. V., Vanbutsele, G., Jacobs, P. A., and Martens, J. A., *Evidence for Alkylcarbenium Ion Reaction Intermediates from Intrinsic Reaction kinetics of C6-C9 n-Alkane Hydroisomerization and Hydrocracking on Pt/H-Y and Pt/USY Zeolites* **J. Catal.** *190* 469-473 (2000).

[24] Vansina, H, Baltanas, M. A., and Froment, G. F., *Hydroisomerization and Hydrocracking. 4. Product distribution from n-octane and 2,2,4-trimethylpentane* **Ind. Eng. Chem. Prod. Res. Dev.** *22* 526-531 (1983).

[25] Vynckier, E., and Froment, G. F., *Modelling of the kinetics of complex processes based upon elementary steps*, in: *Kinetic and Thermodynamic Lumping of Multicomponent Mixtures* (G. Astarita and S. I. Sandler, Eds.) **Elsevier,** *Amsterdam* 131-161 (1991).

[26] Corma, A., Lopez Aguado, A., Nebot, I., and Tomas, F., *A kinetic study of the cracking, isomerization, and disproportionation on n-heptane on a chromium-exchanged Y zeolite* **J. Catal.** *77* 159-168 (1982).

[27] Martens, J. A., and Jacobs, P. A., *Conceptual Background for the conversion of hydrocarbons on heterogeneous acid catalysts* in *'Theoretical Aspects of Heterogeneous Catalysis'* (Ed. Moffat, J. B.) **Van Nostrand Reinhold Catalysis Series** (1990).

[28] Yaluris, G., Madon, R. J., Rudd, D. F., and Dumesic, J. A., *Catalytic Cycles and Selectivity of Hydrocarbon Cracking on Y-zeolite-based Catalysts* **Ind. Eng. Chem. Res.** *33* 2913-2923 (1994).

[29] Yaluris, G., Rekoske, J. E., Aparicio, L. M., Madon, R. J., and Dumesic, J. A., *Isobutane cracking over Y zeolites I. Development of a kinetic model II Catalytic cycles and reaction selectivity* **J. Catal.** *153* 54-64 (1995).

[30] Watson, B. A., Klein, M. T., and Harding, R. H., *Mechanistic Modelling of n-Heptane Cracking on HZSM-5* **Ind. Eng. Chem. Res.** *35* 1506-1516 (1996).

[31] Watson, B. A., Klein, M. T., and Harding, R. H., *Catalytic cracking of alkylbenzenes: modelling the reaction pathways and mechanisms* **Appl. Catal. A Gen.** *160* 13-39 (1997).

[32] Watson, B. A., Klein, M. T., and Harding, R. H., *Mechanistic Modelling of a 1-Phenyloctane/n-Hexadecane Mixture on Rare Earth Y Zeolite* **Ind. Eng. Chem. Res.** *36* 2954-2963 (1997).

[33] Dumesic, J. A., Rudd, D. F., Aparicio, L. M., Rekoske, J. E., and Treviño, A. A., *The Microkinetics of Heterogeneous Catalysis* **American Chemical Society,** *Washington DC* (1993).

[34] Boudart, M., and Djéga-Mariadassou, G., *Kinetics of Heterogeneous Catalytic Reactions* **Princeton,** *New Jersey* (1984).

Chapter 6

Single-Event Modelling of Aromatic Hydrogenation

The single-event methodology based upon elementary steps has been developed and applied mainly for acid catalyzed reaction steps such as isomerization, cracking and alkylation of hydrocarbons in the methanol-to-olefins (MTO) process [1], catalytic cracking [2-4] or hydrocracking [5-7], Chapter 4 and Chapter 5. An analogous methodology for metal catalyzed reactions and for (de)-hydrogenation in particular has been suggested by Van engelandt [8] and for (de)-hydrogenation and hydrogenolysis by Verstraete [9]. However, the model has not been applied as such. The model developed by Verstraete [9] is summarized first and subsequently some remarks and comments to this model are formulated.

6.1 Single-Event (De)-Hydrogenation Rate Coefficients

In contrast to the mechanism for the acid catalyzed reactions no literature agreement exists for the mechanism of the metal catalyzed hydrogenation reactions, vide Chapter 7. E.g., for the hydrogenation of aromatic components models with atomic hydrogen addition have been proposed [11-15], while other models assumed molecular hydrogen addition to the aromatic reactant [16,17]. In some models the occurrence of a rate-determining step in the hydrogenation sequence is assumed [14-17], while in others it is not [11-13].

Because of this lack of agreement the single-event methodology for (de)-hydrogenation is related to the global (de)-hydrogenation reaction [9], which is, in fact, not in line with the original single-event philosophy that elementary steps should be considered. The single-event rate coefficient for (de)-hydrogenation corresponds to a rate-determining elementary step, which

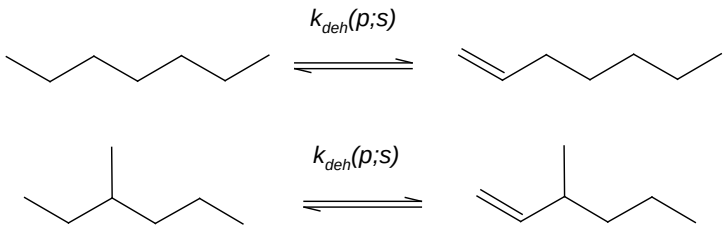

Figure 6-1 Number of identical transformations in (de)-hydrogenation reactions

is assumed to be the surface reaction step. However, no specific structure for the reactant and the activated complex involved in that elementary step is assumed. Hence, the single-event methodology, i.e., the exclusion of the symmetry contribution to the rate coefficient, is applied on the entire hydrogenation sequence. Verstraete [9] used statistical factors instead of symmetry numbers [18,19]. The *number of single-events, n_e,* for an acid catalyzed elementary step being defined as the ratio of the symmetry numbers of reactant and activated complex, is replaced by the *number of identical transformations, n_s,* for a metal catalyzed reaction which is calculated as the ratio of the statistical factors of reactant and product molecule. The use of the *number of identical transformations* is illustrated in Figure 6-1. Both the dehydrogenation of *n*-heptane into hept-1-ene and of 3-methylhexane into 3-methylhex-1-ene involve the formation of a terminal double bond between a primary and a secondary carbon atom. However, in the case of *n*-heptane two identical bonds are available for dehydrogenation leading to hept-1-ene, whereas for 3-methylhexane, only one is available leading to 3-methylhex-1-ene. The use of one rate coefficient to describe both dehydrogenations requires incorporation of the *number of identical transformations* described above.

6.1.1 Dehydrogenation Rate Coefficients

In this and the subsequent paragraphs the development presented by Verstraete [9] will be summarized. The dehydrogenation rate coefficients for saturated hydrocarbons are assumed to only depend on the structure of the double bond which is formed, i.e., whether the carbon atoms involved in the dehydrogenation are primary, secondary or tertiary carbon atoms. An increasing steric hindrance in hydrogen abstraction and an increasing alkene stability with the degree of substitution of the carbon atoms involved in the double bond formation [20] are at the origin of this assumption. This leads to the definition of six reactant independent rate coefficients for dehydrogenation of saturated hydrocarbons, i.e., $\tilde{k}_{deh}(p;p)$, $\tilde{k}_{deh}(p;s)$, $\tilde{k}_{deh}(p;t)$, $\tilde{k}_{deh}(s;s)$, $\tilde{k}_{deh}(s;t)$ and $\tilde{k}_{deh}(t;t)$. In the formation of dienes, the just defined rate coefficients can be used if no conjugation exists between the two double bounds in the diene.

However, the formation of conjugated double bounds is generally favored. This requires extra dehydrogenation rate coefficients because of non-negligible effects of this conjugation on the stability of the diene and, hence, because of an expected non-negligible effect on the activated complex and corresponding activation energy. Six additional parameters are introduced, i.e., $\tilde{k}_{deh}(p;as)$, $\tilde{k}_{deh}(p;at)$, $\tilde{k}_{deh}(s;as)$, $\tilde{k}_{deh}(s;at)$, $\tilde{k}_{deh}(t;as)$, and $\tilde{k}_{deh}(t;at)$, to account for the formation of double bonds involving one allylic carbon atom. Finally, the dehydrogenation of cyclic dienes into aromatic components also requires three additional rate coefficients because both carbon atoms involved in the dehydrogenation are in allylic position in this case and because of the extra resonance stabilization of an aromatic ring. These three rate coefficients are $\tilde{k}_{deh}(as;as)$, $\tilde{k}_{deh}(as;at)$ and $\tilde{k}_{deh}(at;at)$.

6.1.2 Hydrogenation Rate Coefficients

The definition of the dehydrogenation rate coefficients determines the hydrogenation rate coefficients via the thermodynamic consistency, which couples the forward and the reverse rate coefficient via the equilibrium coefficient:

$$K = \frac{k_f}{k_r} \tag{6.1}$$

Hence, if a certain dependence present in the equilibrium coefficient K can be neglected in the forward rate coefficient k_f it has to be present in the reverse rate coefficient k_r and vice versa. In this particular case the dehydrogenation rate coefficient was assumed to be independent of the alkene formed and, hence, the hydrogenation rate coefficient will certainly depend on the alkene involved. This is why the alkene hydrogenation rate coefficients are written as $\tilde{k}_{hyd}(O_{i,j};m;n)$ where $O_{i,j}$ represents the alkene j to be hydrogenated into the corresponding alkane i and m and n the types of the carbon atoms involved the double bond. The hydrogenation rate coefficients for dienes and aromatic components are written in a similar way.

The rate coefficients for (de)-hydrogenation are summarized in Table 6-1. The number of dehydrogenation coefficients was limited to 15, while the number of hydrogenation rate coefficients equals the number of unsaturated components, because the hydrogenation rate coefficients are component dependent. This impracticably high number can, however, be reduced as will be shown in the subsequent paragraph.

Table 6-1 Single-event rate coefficients for (de)-hydrogenation reactions

Dehydrogenation of saturated components		
$\hat{k}_{deh}(p;p)$	$\hat{k}_{deh}(p;s)$	$\hat{k}_{deh}(p;t)$
$\hat{k}_{deh}(s;s)$	$\hat{k}_{deh}(s;t)$	$\hat{k}_{deh}(t;t)$
Dehydrogenation of unsaturated components with one double bond		
$\hat{k}_{deh}(p;as)$	$\hat{k}_{deh}(s;as)$	$\hat{k}_{deh}(t;as)$
$\hat{k}_{deh}(p;at)$	$\hat{k}_{deh}(s;at)$	$\hat{k}_{deh}(t;at)$
Dehydrogenation of unsaturated components with two double bonds		
$\hat{k}_{deh}(as;as)$	$\hat{k}_{deh}(as;at)$	$\hat{k}_{deh}(at;at)$
Hydrogenation of unsaturated components with one double bond		
$\hat{k}_{hyd}(O_{i,j};p;p)$	$\hat{k}_{hyd}(O_{i,j};p;s)$	$\hat{k}_{hyd}(O_{i,j};p;t)$
$\hat{k}_{hyd}(O_{i,j};s;s)$	$\hat{k}_{hyd}(O_{i,j};s;t)$	$\hat{k}_{hyd}(O_{i,j};t;t)$
Hydrogenation of unsaturated components with two double bonds		
$\hat{k}_{hyd}(O_{i,j};p;as)$	$\hat{k}_{hyd}(O_{i,j};s;as)$	$\hat{k}_{hyd}(O_{i,j};t;as)$
$\hat{k}_{hyd}(O_{i,j};p;at)$	$\hat{k}_{hyd}(O_{i,j};s;at)$	$\hat{k}_{hyd}(O_{i,j};t;at)$
Hydrogenation of aromatic components		
$\hat{k}_{hyd}(A_i;as;as)$	$\hat{k}_{hyd}(A_i;as;at)$	$\hat{k}_{hyd}(A_i;at;at)$

6.1.3 Reduction of the number of (de)-hydrogenation rate coefficients

Because the (de)-hydrogenation rate coefficients were defined for the elementary surface reaction step, these coefficients are related to each other by the relationship presented in Eq.

(6.1), which can be expressed in this case as:

$$K_{deh}(P_{i-M};O_{i,j-M}) = \frac{n_{s,deh_{i,j}}\,\tilde{k}_{deh}(m;n)}{n_{s,hyd_{i,j}}\,\tilde{k}_{hyd}(O_{i,j};m;n)} \tag{6.2}$$

Via the chemisorption coefficients of the alkane and the alkene on a metal site, the surface reaction equilibrium coefficient can be replaced by the gas phase equilibrium coefficient:

$$K_{deh}(P_{i-M};O_{i,j-M}) = \frac{K_{O_{i,j}-M}\,K_{deh}(P_i;O_{i,j})}{K_{P_i-M}} \tag{6.3}$$

Hence, the hydrogenation rate coefficient can be written as a function of the dehydrogenation rate coefficient and of equilibrium coefficients which can be calculated or estimated:

$$\tilde{k}_{hyd}\left(O_{i,j};m;n\right)=\tilde{k}_{deh}\left(m;n\right)\frac{n_{s,deh_{i,j}}}{n_{s,hyd_{i,j}}}\frac{K_{P_i-M}}{K_{O_{i,j}-M}\,K_{deh}\left(P_i;O_{i,j}\right)} \tag{6.4}$$

and the number of (de)-hydrogenation rate coefficients is reduced from the number of unsaturated components + fifteen to fifteen only.

Moreover, in the experiments aromatic components were the only unsaturated species observed. The quantities produced of all cycloalkenes and cyclodienes were always below the detection limit of the analytical apparatus and because the estimation of rate coefficients related to the production or consumption of such species would lead to unreliable values, their concentrations were calculated assuming a quasi-equilibrium. For similar reasons one rate-determining step was proposed in the (de)-hydrogenation sequence from cycloalkanes to aromatic components while the remaining steps were assumed to be quasi-equilibrated. The location of the rate-determining step in the (de)-hydrogenation sequence is catalyst dependent [10]. For the catalyst used by Verstraete [9], a Pt-Sn/Al_2O_3 catalyst, the rate-determining step in cycloalkane dehydrogenation to aromatic components was found to be the dehydrogenation of the cycloalkene into the cyclodiene. The remaining (de)-hydrogenation coefficients to be estimated are $\tilde{k}_{deh}\left(s;as\right),\tilde{k}_{deh}\left(s;at\right),\tilde{k}_{deh}\left(t;as\right),$ and $\tilde{k}_{deh}\left(t;at\right)$. However, using only one cycloalkane model component, it was impossible to distinguish between four parallel routes to the same product. Hence, only one rate coefficient was used in the modelling of the (de)-hydrogenation kinetics with the following equation expressing the reaction rate for the hydrogenation of aromatic component *i* [9]:

$$R_{A_i}=\frac{k_{deh}K_{NO_{i,j}-M}K_{deh}\left(N_i;NO_{i,j}\right)C_{t,M}\left(p_{N_i}-\dfrac{p_{A_i}p_{H_2}^3}{K_{deh}\left(N_i;A_i\right)}\right)}{p_{H_2}\left(1+\sum_{i=1}^{n_{nap}}\left(K_{N_i-M}\,p_{N_i}+K_{A_i-M}\,p_{A_i}\right)\right)} \tag{6.5}$$

The surface concentrations of the cycloalkenes and –dienes were found to be negligible and, hence, were removed from the rate equation. This equation contains 6 parameters: 1 rate coefficient, k_{deh}, 3 chemisorption coefficients, K_{6N_i-M}, $K_{6NO_{i,j}-M}$ and K_{A_i-M}, and 2 equilibrium coefficients, $K_{deh}(6N_i,6NO_{i,j})$ and $K_{deh}(6N_i,A_i)$. The dehydrogenation equilibrium coefficients are calculated using thermodynamic data. Because in the rate equation only the product of the rate coefficient and the cycloalkene chemisorption coefficient appears, three adjustable parameters are used in the above equation by Verstraete [9]: 1 composite rate

coefficient, $k_{deh}K_{6NO_{i,j}-M}$, representing the product of the real rate coefficient and the cycloalkene chemisorption coefficient and 2 chemisorption coefficients, K_{6N_i-M} and K_{A_i-M}, for cycloalkanes and aromatic components respectively.

6.2 Application to Aromatic Hydrogenation Kinetics

Some practical and fundamental remarks can be made with respect to the above presented single-event model in aromatic hydrogenation, which may explain why the methodology has been developed but not applied as such so far, nor in this work.

6.2.1 Selection of the Reaction Mechanism

According to the definition of the single-event rate coefficients for (de)-hydrogenation the reaction mechanism for hydrogenation of an aromatic component to the corresponding cycloalkane is postulated to occur via a 1,3-cyclohexadiene and a cyclohexene intermediate. However, it was found from the quantumchemical calculations discussed in Chapter 7 that the addition of the second hydrogen atom to the aromatic ring occurs on the carbon atom in β-position to first hydrogenated carbon atom. Hence, the surface intermediate with two hydrogen atoms added does not necessarily correspond to 1,3-cyclohexadiene nor to 1,4-cyclohexadiene.

These calculations suggest that rate coefficients corresponding to the addition or abstraction of only one hydrogen atom instead of two should be used. The secondary or tertiary character of the carbon atom as well as its participation in a single or conjugated double bond system are possible factors to include in the definition of such single-event rate coefficients for hydrogenation.

6.2.2 Parameter Estimation

In practice, the kinetic scheme developed in paragraph 6.1 leads to indistinguishable parallel routes and, hence, fully correlated kinetic coefficients if the hydrogenation of only one model component is investigated. E.g., in toluene hydrogenation to methylcyclohexane three possible steps from methylcyclohexadiene to methylcyclohexene are potentially rate-determining, i.e., *(s;as), (s;at)* and *(t;as)* but ultimately they all lead to the same observable product, i.e., methylcyclohexane. Hence, only one rate coefficient suffices to describe the hydrogenation behaviour.

A judicious definition of single-event hydrogenation rate coefficients and selection of appropriate model components is required to obtain reliable parameter estimates in the single-event methodology in aromatic component hydrogenation.

6.3 Conclusion

A single-event methodology to metal catalyzed reactions in general and to the (de)-hydrogenation of (un)-saturated cyclic components in particular has been proposed by Verstraete [9]. However, the effective application in the kinetic modelling has not been performed yet. Practical as well as more fundamental reasons limit the applicability of the current methodology and, hence, the hydrogenation kinetics developed within the framework of this thesis are not based on the single-event, but on a general microkinetic methodology.

6.4 References

[1] Park, T. Y., and Froment, G. F., *Kinetic Modelling of the Methanol to Olefins Process. 1. Model Formulation* **Ind. Eng. Chem. Res.** *40* 4172-4186 (2001).

[2] Feng, W., Vynckier, E., and Froment, G. F., *Single-Event Kinetics of Catalytic Cracking* **Ind. Eng. Chem. Res.** *32* 2997-3005 (1993).

[3] Dewachtere, N. V., Santaella, F., and Froment, G. F., *Application of a Single-Event Kinetic Model in the Simulation of an Industrial Riser Reactor for the Catalytic Cracking of Vacuum Gas Oil* **Chem. Eng. Sci.** *54* 3653-3660 (1999).

[4] Beirnaert, H. C., Alleman, J. R., and Marin, G. B., *A Fundamental Model for the Catalytic Cracking of Alkanes on a USY zeolite in the Presence of Coke Formation* **Ind. Eng. Chem. Res.** *40* 1337-1347 (2001).

[5] Svoboda, G. D., Vynckier, E., Debrabandere B., and Froment, G. F., *Single-Event Rate Parameters for Paraffin Hydrocracking on a Pt/US-Y Zeolite* **Ind. Eng. Chem. Res.** *34* 3793-3800 (1995).

[6] Martens, G. G., Marin, G. B., Martens, J. A., Jacobs, P. A., and Baron, G. V., *A Fundamental Kinetic Model for Hydrocracking of C-8 to C-12 alkanes on Pt/US-Y Zeolites* **J. Catal.** *195* 253-267 (2000).

[7] Martens, G. G., Thybaut, J. W., and Marin, G. B., *Single-Event Rate Parameters for the Hydrocracking of Cycloalkanes on Pt/US-Y Zeolites* **Ind. Eng. Chem. Res.** *40* 1832-1844 (2001).

[8] Van engelandt, W., *Reformuleren van Nafta door Selectieve Hydrokraking* **PhD Thesis** *Ghent University* (1998).

[9] Verstraete, J., *Kinetische Studie van de Katalytische Reforming van Nafta over een Pt-Sn/Al_2O_3 Katalysator* **PhD Thesis** *Ghent University* (1997).

[10] Van Trimpont, P. A., Marin, G. B., and Froment, G. F., *Kinetics of Methylcyclohexane Dehydrogenation on Sulphided Commercial Pt/Al_2O_3 and Pt-Re/Al_2O_3 Catalysts* **Ind. Eng. Chem. Fundam.** *25* 544-553 (1986).

[11] Snagovskii, Y. S., Lyubarski, G. Y., and Ostrovskii, G. M., *Kinetics of Benzene Hydrogenation on Nickel. I. Reactions in the Kinetic Region* **Kinet. Katal.** *2* 258-265 (1966).

[12] Van Meerten, R. Z. C., and Coenen, J. W. E., *Gas Phase Benzene Hydrogenation on a Nickel-Silica Catalyst IV. Rate Equations and Curve Fitting* **J. Catal.** *46* 13-24 (1977).

[13] Chou, P., and Vannice, M. A., *Benzene Hydrogenation over Supported and Unsupported Palladium II. Reaction Model* **J. Catal.** *107* 140-153 (1987).

[14] Rahaman, M. V., and Vannice, M. A., *The Hydrogenation of Toluene and o-, m-, and p-Xylene over Palladium II. Reaction Model* **J. Catal.** *127* 267-275 (1991).

[15] Lin, S. D., and Vannice, M. A., *Hydrogenation of Aromatic Hydrocarbons over Supported Pt Catalysts* **J. Catal.** *143* 563-572 (1993).

[16] Kehoe, J. P. G., and Butt, J. B., *Kinetics of Benzene Hydrogenation by Supported Nickel at Low-Temperature* **J. Appl. Chem. Biotechnol.** *22* 23-30 (1972).

[17] Mirodatos, C., Dalmon, J. A., and Martin, G. A., *Steady-State and Isotope Transient Kinetics of Benzene Hydrogenation on Nickel Catalysts* **J. Catal.** *105* 405-415 (1987).

[18] Bishop, D. M., and Laidler, K. J., *Symmetry numbers and structural factors in rate theory* **J. Chem. Phys.** *42* 1688-1691 (1965).

[19] Bishop, D. M., and Laidler, K. J., *Statistical factors for chemical reactions* **Trans. Farad. Soc.** *66* 1685-1687 (1970).

[20] Fessenden, R. J., and Fessenden J. S., *Organic Chemistry* **Brooks/Cole Publishing Company** *Pacific Grove* (1994).

Chapter 7

Vapour Phase Hydrogenation Kinetics of Toluene on Pt/ZSM22

Kinetic experiments on the hydrogenation of toluene were performed on 0.5 wt% Pt/ZSM-22 in a Berty type reactor at the Laboratorium voor Petrochemische Techniek of Ghent University. Construction of a kinetic model was based on a critical evaluation of available literature data on the hydrogenation of aromatic components together with physicochemical studies on the interaction of aromatic components and related hydrogenated products with metal surfaces as well as on quantumchemical calculations. This leads to a general microkinetic model, analogous to the Horiuti Polanyi mechanism for ethylene hydrogenation, with the first 4 H atom addition steps not in quasi-equilibrium. Chemisorption of hydrogen and toluene was assumed to occur on identical sites. No dehydrogenated surface species was taken into account. The preexponential factors were calculated using transition state theory. A model with equal surface reaction rate coefficients for the H addition steps was selected as the best model. The estimated toluene and H_2 chemisorption enthalpies amounted to –70 kJ mol^{-1} and –42 kJ mol^{-1}. An activation energy in the range of 40 to 50 kJ mol^{-1} was found. Under typical reaction conditions, 60 % of the surface is covered by toluene and 20 % by H atoms. The remaining 20 % are free. Negligible amounts of partially hydrogenated species were found to be present on the catalyst surface.

7.1 Introduction

The hydrogenation or saturation of aromatic components is of increasing interest due to the more stringent environmental legislation [1]. Moreover, the removal of aromatic components is beneficial for a diesel's quality as the cetane number increases with decreasing aromatic content [1,2]. In this work, the hydrogenation is approached as a part of the hydrocracking process. Extensive work has already been performed on the hydrocracking of (cyclo)-alkanes [3-5]. Reaction conditions were such that the metal catalyzed (de)-hydrogenation reactions were in quasi-equilibrium. Since hydrogenation of aromatic species is more difficult and, hence, slower than hydrogenation of (cyclo)-alkenes, the hydrogenation equilibrium for aromatic components cannot be assumed a priori.

The hydrogenation of aromatic components has been investigated intensively. Especially in elder work benzene is used as model component [6-21]. More recently other aromatic model components are being used, such as toluene [22-26] and xylene-isomers, ethylbenzene and naphthalene [22,27-34]. Apart from the aromatic model component, also the catalytic material plays an important role. Several metals or their combinations, such as Ni, Pt, Pd, PtPd… can be used. The properties of the support can also have an effect on the hydrogenation behaviour [15,25,35-38]. Lin and Vannice [23,36], Chupin et al. [25] and Rousset et al. [26] have used the same combination of toluene and Pt as used in the present work.

A variety of kinetic models for the hydrogenation of aromatic model components have been proposed [13,15,22,24,27,28,30,36]. Lin and Vannice [15] considered four categories. Distinctive features between the different categories include the selection of a rate-determining step (RDS) in the hydrogenation reaction sequence or not, and the assumption of molecular H_2 or atomic H addition to the aromatic species. The final model of these authors for the hydrogenation of toluene on Pt accounts for atomic H addition to the aromatic molecule with the first H addition as the rate-determining step. In addition, the presence of a partially dehydrogenated product as most abundant surface intermediate was incorporated to account for the formation of carbonaceous species [15].

The assumption of non-competitive chemisorption, i.e., the existence of one type of sites for H_2 chemisorption and another type of sites for the hydrocarbon chemisorption, is prevailing, but not explicitly mentioned. In recent literature [24,27,30,32] competitive chemisorption of hydrogen and the aromatic model component is explicitly dealt with and even selected as the most likely mechanism by Lindfors et al. [24].

Apart from the above kinetic studies, other relevant information concerning the hydrogenation of aromatic components can be obtained from physicochemical studies on the interaction of aromatic species and related hydrogenated products with metal surfaces [39-47] or from first principles [48]. A reaction path analysis based on quantum chemical calculations allows to gain insight in the reaction mechanism and therefore the construction of a more fundamental kinetic model. Ab initio density functional calculation have been used to study e.g. ethylene hydrogenation [48]. Most studies about aromatic components deal with benzene/cyclohexane, however, some information on toluene/methylcyclohexane and ethylbenzene is also available [41,46]. The assumption of the first H atom (or H_2 molecule) addition as the RDS can be related to the breaking of the resonance stabilization of the aromatic species. This seems justified in the vapour phase where the standard enthalpy of formation of cyclohexadiene is higher than that of benzene, cyclohexene and cyclohexane. On a Pt(111)-surface, however, Koel et al. [44] reported that adsorbed cyclohexene and two adsorbed H atoms have the highest standard enthalpy of formation in the benzene hydrogenation sequence.

This Chapter focuses on the hydrogenation of toluene. Kinetic models are developed based on the insight gained from physicochemical studies. Other relevant information for construction of kinetic models was obtained from quantumchemical calculations. Data regression enabled the selection of a model based on statistical and physical interpretation of the results.

7.2 Experimental

The investigated range in experimental operating conditions is shown in Table 7-1. The variation in inlet partial pressures corresponded with molar inlet H_2 to toluene ratios from 5 to 10. The total pressure, i.e., including N_2, was in the range of 1 to 3 MPa. The reactant inlet partial pressure varied from 110 to 360 kPa. During prolonged experimental runs, i.e. 2 to 4 hours, a slight decrease in catalytic activity was observed. Therefore, between 2 experiments a 10 mmol H_2 s^{-1} flow was sent through the reactor to avoid significant catalyst deactivation in the long term. The total number of experiments amounted to 42.

The absence of mass transport limitations in the intercrystalline pores was verified (Weisz moduli ~10^{-2}) [49-51]. Note that intracrystalline diffusion limitations are not relevant, as the hydrogenation is localized at the external crystallite surface [52,53]. Toluene was used as model component since its hydrogenated product, methylcyclohexane, has very limited isomerization possibilities, hence, limiting possible side reactions. The use of benzene, the hydrogenated product of which has even less isomerization possibilities was rejected for an extended set of experiments regarding its carcinogenic character.

Table 7-1 Range of experimental conditions

Temperature (K)	Inlet H_2 Pressure (kPa)	Inlet Toluene Pressure (kPa)	Space Time (kg_{cat} mol^{-1} s^{-1})	Conversion (%)
423 – 498	100 – 300	10 – 60	27 – 82	5 – 45

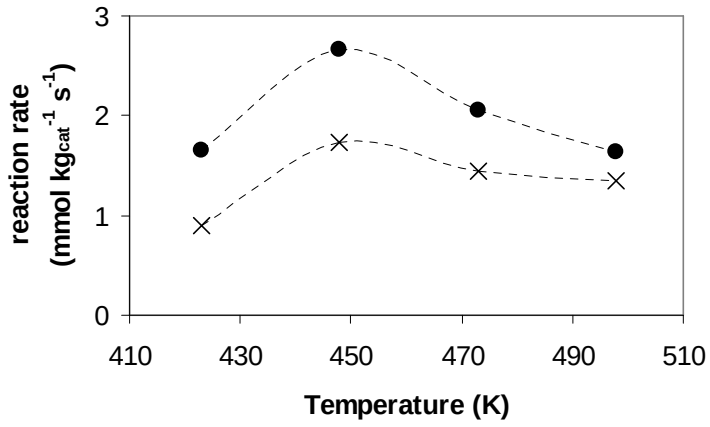

Figure 7-1 Reaction rate as a function of the temperature ($p_{H2,0}$ = 100 kPa, W/F_0 = 82 kg s mol^{-1}), • : $p_{tol,0}$ = 10 kPa; × : $p_{tol,0}$ = 20 kPa

7.3 Experimental Results and Kinetic Model

7.3.1 Effect of the Operating Conditions on the Hydrogenation Rate

The hydrogenation of toluene on 0.5 wt% Pt/ZSM-22 yielded methylcyclohexane as the main product. Small amounts (<5%) of ethylcyclopentane were observed, while only trace quantities of the dimethylcyclopentane isomers were found in the reactor effluent.

The toluene hydrogenation rate showed a maximum as a function of the temperature (Figure 7-1). This phenomenon has already been observed for toluene and other aromatic model components on typical hydrogenation metals, such as Pt, Pd, Ni,… [16,19,22-24,30,31,34]. It is generally accepted that surface coverage effects are at the origin of this maximum. At a certain temperature the increase of the hydrogenation rate coefficient with the temperature is overcompensated by the decrease of the surface coverage of the reaction intermediate involved in the rate-determining step. The intrinsic character of the kinetic data has been verified, vide Section 7.2, and, hence, transport limitations cannot be invoked to explain the phenomenon. Other possible causes, such as thermodynamic limitations, catalyst poisoning or

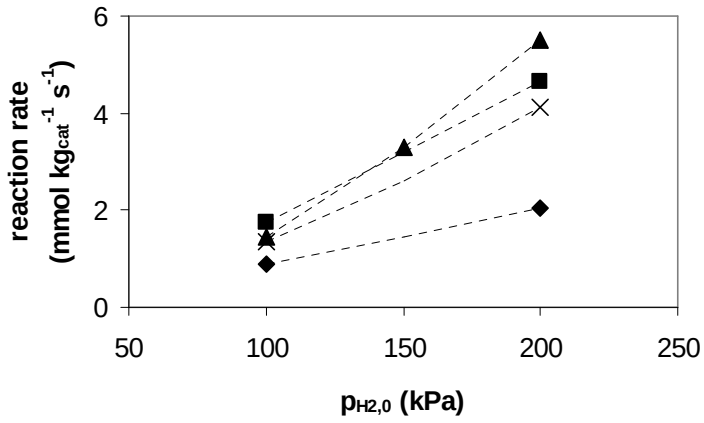

Figure 7-2 **Selected set of experimental data illustrating the effect of H_2 inlet partial pressure on the reaction rate ($p_{tol,0}$=20 kPa, W/F_0 = 82 kg s mol^{-1}), ♦: 423 K; ■ : 448 K; ▲ : 473 K; × : 498 K**

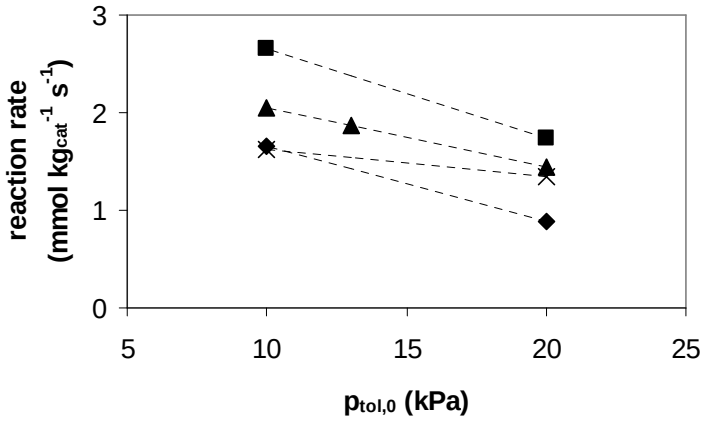

Figure 7-3 **Selected set of experimental data illustrating the effect of toluene inlet partial pressure on the reaction rate ($p_{H2,0}$=100 kPa, W/F_0=82 kg s mol^{-1}), ♦: 423 K; ■ : 448 K; ▲ : 473 K; × : 498 K**

metal particle growth can be discarded [24,34].

Increasing only the H_2 inlet partial pressure and keeping all other experimental inlet variables fixed resulted in an increase of the toluene hydrogenation rate at all temperatures (Figure 7-2), while an increase of only the toluene partial pressure and fixing all other inlet variables leads to a decrease of the toluene hydrogenation rate at all temperatures (Figure 7-3). The partial reaction orders have been determined by a regression of all available data, i.e., not only the data presented in Figure 7-2 and Figure 7-3, at the temperature considered to the equation:

Table 7-2 **H_2 and toluene partial reaction orders and corresponding 95% approximate individual confidence intervals for the temperature range considered estimated by regression of all isothermal experimental data to Eq. (7.1)**

Temperature (K)	m	n
423	-0.2 (± 0.1)	0.6 (± 0.1)
448	-0.2 (± 0.1)	1.1 (± 0.05)
473	-0.1 (± 0.05)	1.8 (± 0.05)
498	0.3 (± 0.1)	1.3 (± 0.05)

$$r^{hyd} = k^{hyd} p_{tol}^{m} p_{H_2}^{n} \tag{7.1}$$

in which *m* and *n* are respectively the toluene and the H_2 partial reaction order. The estimated values are reported in Table 7-2. The H_2 partial reaction order shows an increasing trend with the temperature, in agreement with literature data [14,15,19,22-24,30]. The toluene partial reaction order is negative, except at 498 K (Table 7-2), hence, increasing the inlet partial pressure of toluene, results in a decrease of the hydrogenation rate at most temperatures. This can be understood if the increase in the toluene surface coverage due to the higher toluene partial pressure results in and is overcompensated by a decrease in the H surface coverage due to competition in the chemisorption of toluene and H_2 on the metal surface. Competitive chemisorption has already been reported [7,24,27,30,32], however, most other sources only consider non-competitive chemisorption between the aromatic model component and H_2 [8,10,13,15,22,31,34]. Repulsive interactions between 2 chemisorbed species on neighboring sites exist [48,54-57] and, hence, a certain kind of competition between chemisorbing H_2 and aromatic species can occur, even when different types of sites are involved. The observation of (non)-competitive chemisorption seems to depend on the experimental process conditions. At temperatures lower than those investigated presently the metal surface is completely saturated with aromatic species. However, between the chemisorbed aromatic species, a constant, limited number of sites exist which are available for dissociative H_2 chemisorption [15]. If, at higher temperatures, the saturation of the metal surface by aromatic species is no longer maintained, sites that were previously occupied by an aromatic species are now also available for H_2 chemisorption, explaining the competitive character of the H_2 and aromatic chemisorption at the temperatures investigated in this work. At even higher temperatures surface coverages become so small that no competition is observed.

7.3.2 Kinetic Model Assumptions and Rate Equation

The kinetic modelling of aromatic hydrogenation reactions based on steady state data without in situ characterization of the surface cannot make use of direct information concerning the surface intermediates. This has lead to a variety of possible kinetic models presented for the hydrogenation of aromatic model components, as discussed in Section 7.1. Discrimination among different kinetic models was performed by interpretation of the results of the regression of experimental data to these models. In the present work an alternative model is developed based on insight provided by quantumchemical calculations combined with literature data on the different elementary steps.

a Rate-Determining Step (RDS)

If a RDS is considered, mostly the addition of the first H atom, H_2 molecule or the simultaneous addition of the first 2 H atoms is selected as the RDS [10,14,22,36]. This assumption can, by analogy to gas phase conditions, be related to the breaking of the resonance stabilization of the aromatic species. However, both quantumchemical calculations and experimental results on the interaction of aromatic species with metal surfaces indicate that the presumed analogy between the hydrogenation reaction sequence in the gas phase and on the Pt surface is not valid.

The activation energies for the addition of the first and the second H atom to a benzene ring chemisorbed on a Pt(111) surface were obtained from quantumchemical calculations and amount to 75 and 73 kJ mol^{-1} respectively. The similarity between those values indicates that the rate coefficient of the H atom addition to the chemisorbed benzene species is not significantly different from the rate coefficient of the H atom addition to the cyclohexadienyl species on the surface. If the addition of the first H atom to chemisorbed benzene were breaking the resonance stabilization, a higher value for the activation energy than for that of the second H atom addition would be expected.

The second argument that the analogy between the hydrogenation reaction sequence in the gas phase and on the Pt surface species is not valid is provided in Table 7-3 and Figure 7-4. The chemisorption enthalpies in Table 7-3 were calculated quantumchemically for benzene (B), H_2, and 1,4-cyclohexadiene (CHD) and were taken from literature for cyclohexane (CHA) and cyclohexene (CHE) [41,44]. Experimental support for the quantumchemically calculated values is available [39,41]. No significant differences were found between levels determined based on 1,3- or 1,4-cyclohexadiene, hence, this component will further be addressed as cyclohexadiene. The value found for H_2 represents an average of the variation in H_2

Table 7-3 Chemisorption enthalpies of reactants, product and intermediates during the hydrogenation of benzene

Component	H_2[a]	Benzene[a]	Cyclohexadiene[a]	Cyclohexene[b]	Cyclohexane[b]
ΔH_{chem} (kJ mol^{-1})	70	75[c]	146	71	58
		117[d]			

[a] quantumchemically calculated [b] from literature [41,44] [c] reactive form, [d] non-reactive form

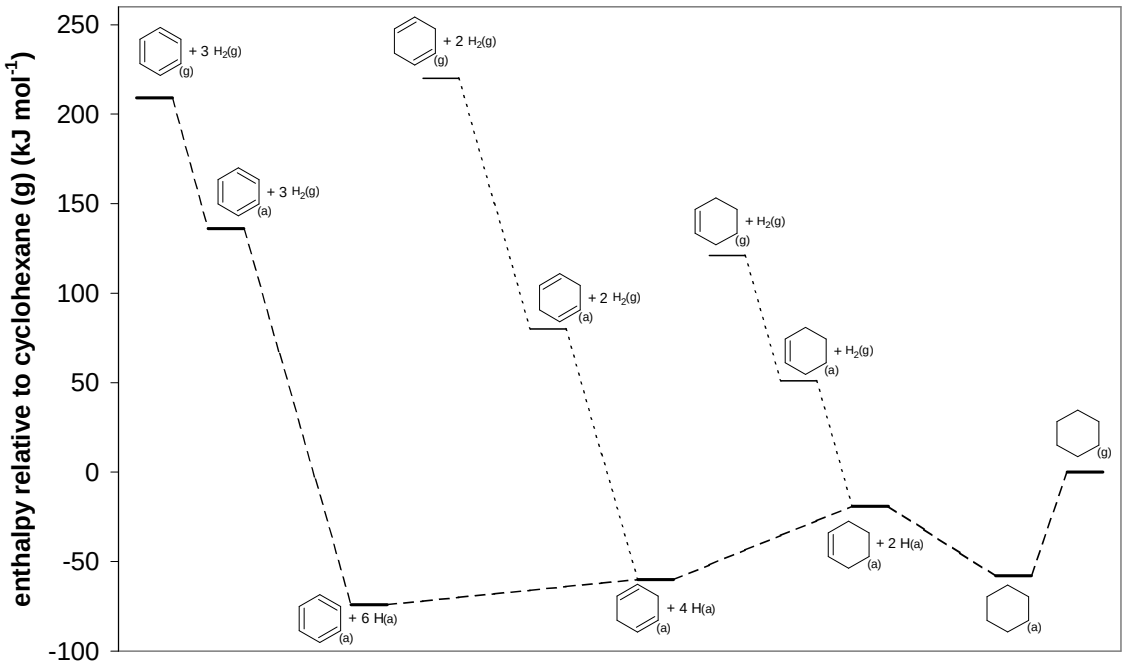

Figure 7-4 Enthalpy levels for the components involved in benzene hydrogenation

chemisorption enthalpy with the surface coverage reported by Podkolzin et al. [56]. For benzene, 2 possibilities were found. A reactive form, mainly occurring at high surface coverages and a non-reactive form, mainly occurring at low surface coverages. The reactive form was used to determine the enthalpy levels in Figure 7-4. For cyclohexadiene only one form was found. Also for cyclohexene and cyclohexane, only one form was reported [41,44]. In Figure 7-4, as a reference, the enthalpy level of gas phase cyclohexane was set to 0. In the gas phase 'CHD + 2 H_2' is at the highest enthalpy level in the hydrogenation reaction sequence. Due to the endothermicity of the dehydrogenation reactions 'CHA' is at a lower enthalpy level than 'CHE + H_2', which on its turn is at a lower level than 'CHD + $2H_2$'. The resonance stabilization of the aromatic ring results in a lower enthalpy level for 'B + $3H_2$' than for 'CHD + $2H_2$'. This resonance stabilization makes hydrogenation in the gas phase very difficult. Once the resonance stabilization has been broken, hydrogenation proceeds very

rapidly to the totally hydrogenated product, i.e., the breaking of the resonance stabilization is the rate-determining step in gas phase hydrogenation. On a Pt-surface, however, this picture is no longer valid. Cyclohexadiene chemisorbs much more strongly than benzene and, hence, the effect of the resonance stabilization with adsorbed benzene is at least weakened, if not entirely lost. Cyclohexene chemisorbs relatively weakly, resulting in the highest enthalpy level for 'CHE + 2H' in the hydrogenation sequence on the surface. Moreover, the enthalpy rise from 'CHD + 4H' to 'CHE + 2H' is higher than from 'B + 6H' to 'CHD + 4H'. If different activation energies for the surface reactions are assumed, then, based on an Evans-Polanyi relationship [58], a higher activation energy is expected for the third or the fourth H addition step. Hence, one of the latter steps is expected to be rate-determining, rather than the addition of the first or second H atom.

Other reaction mechanisms that have been proposed do not assume the existence of a RDS, but consider 2 or all hydrogen addition reactions as being not quasi-equilibrated. Van Meerten and Coenen [13] and Lindfors et al. [24] used the same rate coefficient for all addition steps. Chou and Vannice [15] allowed a linear distribution of standard enthalpies and entropies of activation between the first and the sixth H atom addition step and found a weak decrease and increase respectively. The enthalpy levels during benzene hydrogenation on a Pt-surface, vide Figure 7-4, support such kind of models considering the first to the fourth H atom addition as being not quasi-equilibrated, since it shows an increasing enthalpy level (endothermicity) from benzene up to chemisorbed cyclohexene. Further hydrogenation from cyclohexene to cyclohexane on the surface is exothermic and is more likely to be in quasi-equilibrium.

b Dehydrogenated Surface Species

The minor loss of catalytic activity during hydrogenation can be attributed to the formation of H-deficient carbonaceous species on the metal surface. The coverage of active sites by surface species with an aromatic nature has already been proposed in earlier work [59,60]. In more recent communications especially the group of Vannice considered the inclusion of a dehydrogenation reaction, concurrent to the hydrogenation reactions, involving the aromatic reactant molecule to produce H-deficient species [15,36]. Moreover, Lin and Vannice [15] postulated a single dominant H-deficient species on the surface, i.e., present in much larger amounts than the other possible H-deficient species and the aromatic species. Based on regressions of experimental data to several model equations, each with an other dominant H-deficient species, these authors found that the surface species produced by one H atom abstraction of the chemisorbed aromatic reactant was the most likely dominant surface

a) b)

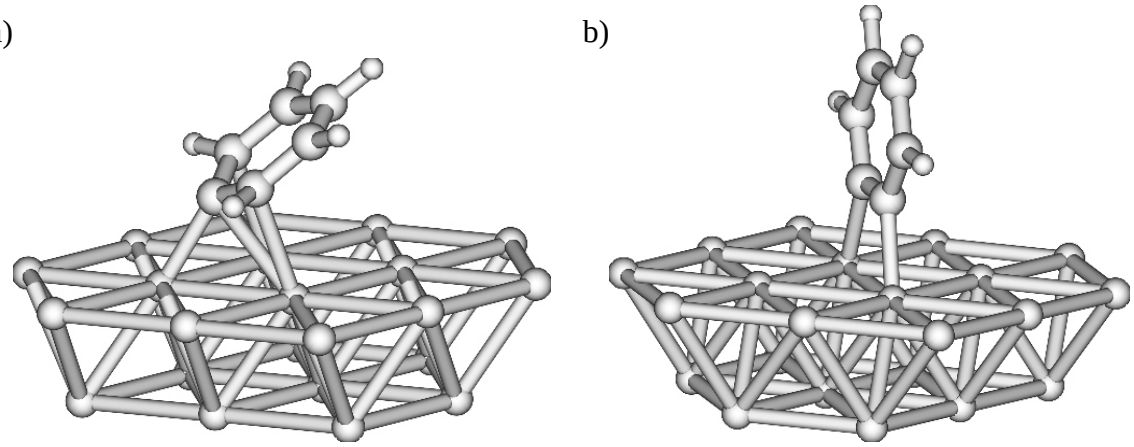

Figure 7-5 Structure of adsorbed a) phenyl and b) benzyne from DFT BP86/double zeta calculations

species.

In a thermochemical study of interaction of benzene and related products with Pt surfaces, Koel et al. [44] also considered H atom abstraction from chemisorbed benzene. Due to uncertainties about the nature of these dehydrogenated species, these authors report two possible enthalpy levels for the latter. One includes extra stabilization of the dehydrogenated species on the surfaces and has an enthalpy level only marginally lower than that of chemisorbed benzene, while the other is more than 100 kJ mol^{-1} higher in enthalpy level [44]. Quantumchemical calculations have been performed to obtain insight in the benzene dehydrogenation reactions. Different pathways were studied. The most stable phenyl and benzyne intermediates are shown in Figure 7-5. The binding of the ring π-system to the Pt surface is broken. The reaction enthalpy for dehydrogenation depends on the hydrogen adsorption energy, which is strongly coverage dependent [56]. The endothermicity of the benzene dehydrogenation to phenyl is between 76 to 102 kJ mol^{-1} and to benzyne between 13 and 66 kJ mol^{-1}. Therefore these ab initio calculations provide evidence for the higher energetic species of the two reported by Koel et al. [44]. Hence, if an equilibrium between the chemisorbed aromatic reactant and its dehydrogenated counterpart is established on the metal surface, it seems unlikely that the H-deficient species would be the most abundant surface intermediate. Also kinetically the dehydrogenation of benzene is limited, since the activation energy has to be higher than 76 to102 kJ mol^{-1}.

c Reactant Chemisorption, Product Desorption and H_2 Spillover

As discussed in Section 7.3.1 the observed toluene partial pressure effect on the hydrogenation rate is believed to originate from competitive chemisorption of the aromatic reactant and H_2 on the metal surface. It is, therefore, necessary to include competitive

chemisorption in the kinetic model. H_2 and toluene chemisorption were assumed to be in quasi-equilibrium, in agreement with other literature models [13,15,22,24,36]. The desorption of methylcyclohexane is assumed to be fast and irreversible since its surface coverage can be assumed to be negligible in accordance with Van Meerten et al. [13]

If hydrogenation reactions are performed on typical hydrogenation metals supported by an acidic carrier, such as an alumina-silicate or a zeolite, a hydrogenation rate enhancement is observed compared to hydrogenation rates on unsupported metals or metals supported by an essentially non-acidic support, such as silica or alumina [15,19,22,23,25,36-38]. Two mechanisms have been proposed to explain this increase in hydrogenation rate. The first mechanism considers metal-support interactions, which modify the electronic state of the metal cluster on the support and make it more active for hydrogenation reactions [35]. The second one, called H_2 spillover, has been developed more recently and has received by now most attention in the literature [15,19,22,23,25,36-38]. Following this mechanism aromatic reactant molecules that are adsorbed on acidic sites 'close' to a metal cluster can be hydrogenated by hydrogen that is 'spilled over' from that metal cluster.

The Pt on the ZSM-22 used in this work is deposited on the external surface of the zeolite, i.e., in the intercrystalline pores, remote from the acid sites. Hence, no rate enhancement due to H_2 spillover is expected to occur.

d Rate Equation

The assumptions about the reaction mechanism based on which the rate equation for toluene hydrogenation was developed are summarized in Table 7-4. These assumptions lead to the following sequence of elementary steps:

$$H_2(g) + 2* \rightleftharpoons 2H* \qquad K_{chem,H_2} \qquad (7.2)$$

$$A(g) + * \rightleftharpoons A* \qquad K_{chem,A} \qquad (7.3)$$

$$A* + H* \overset{k_1}{\rightleftharpoons} AH* + * \qquad K_1 \qquad (7.4)$$

$$AH* + H* \overset{k_2}{\rightleftharpoons} AH_2* + * \qquad K_2 \qquad (7.5)$$

$$AH_2* + H* \overset{k_3}{\rightleftharpoons} AH_3* + * \qquad K_3 \qquad (7.6)$$

$$AH_3* + H* \overset{k_4}{\longrightarrow} AH_4* + * \qquad K_4 \qquad (7.7)$$

1	No RDS exists: the first four H atom additions steps are not quasi-equilibrated, while the fifth and the sixth H atom addition are.
2	H_2 (dissociative chemisorption) and aromatic reactant both chemisorb on identical sites (competitive chemisorption)
3	a) H_2 and aromatic reactant chemisorption are quasi-equilibrated. b) Desorption of the hydrogenated product is fast and irreversible.
4	No dehydrogenated surface species are considered

Table 7-4 Assumptions for the general model analogous to the Horiuti Polanyi mechanism [61]

$$AH_4{*} + H{*} \rightleftharpoons AH_5{*} + {*} \qquad K_5 \tag{7.8}$$

$$AH_5{*} + H{*} \rightleftharpoons AH_6{*} + {*} \qquad K_6 \tag{7.9}$$

$$AH_6{*} \longrightarrow AH_6(g) + {*} \tag{7.10}$$

For finite values of K_5 and K_6, assumption 3b causes the quasi-equilibrium of reactions (7.8) and (7.9) to shift to the right, so that also the AH_4* and AH_5* coverage are negligible. Hence, the net rate of AH_6(g)-production can be written as:

$$R_{AH_6(g)} = C_t k_4 \theta_{AH_3*} \theta_{H*} \tag{7.11}$$

Applying the pseudo steady state approximation for the species *AH**, AH_2*, and AH_3*, the following mass balances can be written for *AH** and AH_2*:

$$0 = k_i\, \theta_{AH_{i\ 1}*}\, \theta_{H*} + \frac{k_{i+1}}{K_{i+1}} \theta_{AH_{i+1}*}\, \theta_* - k_{i+1}\, \theta_{AH_i*}\, \theta_{H*} - \frac{k_i}{K_i} \theta_{AH_i*}\, \theta_* \qquad i = 1,2 \tag{7.12}$$

and for AH_3*:

$$0 = k_3\, \theta_{AH_2*}\, \theta_{H*} - k_4\, \theta_{AH_3*}\, \theta_{H*} - \frac{k_3}{K_3} \theta_{AH_3*}\, \theta_* \tag{7.13}$$

Via expressions for the chemisorption equilibria, surface coverages are related to gas phase partial pressures:

$$\theta_{A*} = \theta_* K_{chem,A}\, p_A \tag{7.14}$$

$$\theta_{H_2*} = \theta_* \sqrt{K_{chem,H_2}\, p_{H_2}} \tag{7.15}$$

A site balance:

$$1 = \theta_* + \theta_{H*} + \theta_{A*} + \theta_{AH*} + \theta_{AH_2*} + \theta_{AH_3*} \tag{7.16}$$

completes the set of algebraic equations. Eq. (2.34) and Eq. (7.11) to Eq. (7.16) describe fully the hydrogenation kinetics in the Berty reactor.

7.4 Modelling Results and Discussion

7.4.1 General Model Analogous to the Horiuti Polanyi Mechanism [61]

In this stage of the model development nine different coefficients are involved. These are four forward rate coefficients (k_1, k_2, k_3, and k_4), three surface reaction equilibrium coefficients (K_1, K_2, and K_3), and two chemisorption coefficients ($K_{chem,A}$ and $K_{chem,H2}$). Hence, for application of the model under non-isothermal conditions 18 parameters have to be determined. This is a large number to be obtained by regression of experimental data since there is only one independent response. Therefore, a reduction of the number of parameters to be obtained by regression is performed by calculation of preexponential factors and by the introduction of extra model assumptions.

The preexponential factors of the four forward reaction rate coefficients can be calculated based on transition state theory [54,55,57,58]. Regarding the uncertainty about the surface mobility of the intermediates, the same value is used for the preexponential factors of the surface reaction rate and equilibrium coefficients. Depending on the assumed surface mobility of the chemisorbed toluene species, a value in the range 10^{-10} Pa^{-1} to 10^{-13} Pa^{-1} is calculated for the preexponential factor of the toluene chemisorption equilibrium coefficient for a mobile and a immobile species respectively. Similar considerations lead to a range from 10^{-8} Pa^{-1} to 10^{-13} Pa^{-1} for the preexponential factor of the H_2 chemisorption equilibrium coefficient. This range is more extended because of the dissociative character of H_2 chemisorption. The preexponential factor for the surface reaction rate coefficient is calculated to be in the range 10^{8} s^{-1} to 10^{13} s^{-1} if all species, i.e., reactants and transition state, are mobile or immobile respectively. However, this range can be even more extended if species with different surface mobilities are involved. Via analogous considerations the value for the preexponential factor of reverse surface reaction rate coefficients amounts to approximately 10^{13} s^{-1}. One single value is reported since the reverse reaction is monomolecular and since the same mobility is assumed for the reactant and the transition state. If the transition state would have a higher mobility than the reactant, a higher value would be obtained. By division of the preexponential factor of the forward and the reverse surface reaction rate coefficient, a range for the preexponential factor of the surface reaction equilibrium coefficients from 10^{-5} to 1 is obtained. Nine parameters are remaining, i.e., four activation energies, three surface reaction

enthalpies and two chemisorption enthalpies. Further reduction of the number of parameters could be performed via an Evans-Polanyi correlation [58] relating the activation energies with the reaction enthalpies, however, this would only reduce the number of parameters from nine to eight and is therefore discarded.

Two possibilities are considered for further reduction of the number of parameters. The preexponential factors of the surface reaction rate coefficients were set equal to each other, i.e., $k^0_{surf}=k^0_i$ for $i=1,2,3,4$, regarding the assumed similarity between the different H atom addition steps. Based on this assumption it is straightforward to assume that also the activation energies of the surface reactions can be set equal to each other. Also the equality of the surface reaction enthalpies can be assumed, leading to a kinetic model with equal surface reaction rate and equilibrium coefficients [13,24]. In such a model no rate-determining step is assumed. On the other hand, based on the enthalpy levels shown in Figure 7-4 and the discussion in Section 7.3.2a, the addition of the third or the fourth H atom could be expected to be rate-determining because of the higher activation energies associated with these steps. Moreover, cyclohexene and cyclohexane dehydrogenation studies provided evidence for a stable π-allylic cyclohexenyl (cC_6H_9) intermediate on the surface [40,43,45]. This could be related to the occurrence of a rate-determining step corresponding to the third or fourth H atom addition step, since in these steps such a species is respectively produced and consumed.

7.4.2 Model Without Rate-Determining Step and With Equal Surface Reaction Rate Coefficients

The rate equation corresponding to the kinetic model with equal surface reaction rate coefficients is obtained by elimination of the surface coverages from the set of equations describing the hydrogenation kinetics, i.e., Eq. (2.34) and Eq. (7.11) to Eq. (7.16). The surface coverage of *AH*, AH_2, and AH_3 can be expressed in terms of the chemisorbed toluene coverage *A** (Eq. (7.12) and Eq. (7.13)):

$$\theta_{AH_3*} = \frac{B\theta_{AH_2*}}{B+1} = \frac{B^2\theta_{AH*}}{B^2+B+1} = \frac{B^3\theta_{A*}}{B^3+B^2+B+1} \tag{7.17}$$

in which $B = K_{surf}\,\theta_{H*}/\theta_* = K_{surf}\sqrt{K_{chem,H_2}\,p_{H_2}}$. The toluene and H atom surface coverage can be related to each other by division of the chemisorption equilibrium expressions:

$$\theta_{H*} = \frac{\sqrt{K_{chem,H_2}\,p_{H_2}}}{K_{chem,A}\,p_A}\,\theta_{A*} \tag{7.18}$$

Combination of Eq. (7.14) and Eq. (7.16) to Eq. (7.18) leads to the following expression for the toluene surface coverage:

$$\theta_{A^*} = \frac{K_{chem,A}\, p_A}{1 + \sqrt{K_{chem,H_2}\, p_{H_2}} + K_{chem,A}\, p_A \dfrac{\left(4B^3 + 3B^2 + 2B + 1\right)}{\left(B^3 + B^2 + B + 1\right)}} \tag{7.19}$$

An analogous equation can be derived for θ_{H^*}, which can then be substituted into Eq. (7.11) resulting in the rate equation:

$$R_{AH_6(g)} = \frac{C_t k_{surf}}{\left(B^3 + B^2 + B + 1\right)} \frac{B^3 K_{chem,A}\, p_A \sqrt{K_{chem,H_2}\, p_{H_2}}}{\left(1 + \sqrt{K_{chem,H_2}\, p_{H_2}} + K_{chem,A}\, p_A \dfrac{\left(4B^3 + 3B^2 + 2B + 1\right)}{\left(B^3 + B^2 + B + 1\right)}\right)^2} \tag{7.20}$$

This rate equation is similar to the one proposed by Van Meerten and Coenen [13]b, however, in this case competitive chemisorption of H_2 and the aromatic reactant is considered and only the first four H atom addition steps are assumed not being quasi equilibrated, instead of all H atom additions.

In the model with equal surface reaction rate coefficients for the H atom addition steps, four parameters or parameter groups are to be obtained by regression: one surface reaction enthalpy (ΔH_{surf}), two chemisorption enthalpies ($\Delta H^0_{chem,A}$ and $\Delta H^0_{chem,H_2}$) and one composite activation energy ($E^{comp}_{A,surf} = E_{A,surf} + \Delta H^0_{chem,A} + 0.5\,\Delta H^0_{chem,H_2}$). Preliminary regressions resulted in an especially low *t* value for the enthalpies contained in the factor B, i.e., $\Delta H^0_{surf} + 0.5\,\Delta H^0_{chem,H_2}$. The insensitivity to the value of this sum of enthalpies indicates that it is close to zero and, hence, that $\Delta H^0_{surf} \approx -0.5\,\Delta H^0_{chem,H_2}$. The factor B has a weak temperature dependence, which is even too weak to be significantly estimated. Several sets of values for the preexponential factors were tested, each corresponding with different assumptions concerning the surface mobility of the H atoms, the hydrocarbon species and the transition states. The optimal set, vide Table 7-5, corresponded with mobile H atoms on the catalyst surface, i.e., two translational degrees of freedom, while the reactant and product hydrocarbon surface species were found to be rather immobile, i.e., no translational degrees of freedom, but one rotational degree of freedom. The transition states were found to have a higher surface mobility than the other hydrocarbon species. This can be related to the conservation of one of the H atom translational degrees of freedom during its addition the hydrocarbon species. A regression with these preexponential factors from Table 7-5 and with an average surface

Table 7-5 Values for the preexponential factors calculated based on transition state theory [73,74,77]

k^0_{surf} (s^{-1})	K^0_{surf}	$K^0_{chem,A}$ (Pa^{-1})	K^0_{chem,H_2} (Pa^{-1})
10^{15}	10^{-2}	10^{-12}	10^{-10}

Table 7-6 Parameter estimates obtained by regression of the three kinetic models used, Eq. (2.34) and Eq. (7.20), respectively Eq. (2.34) and Eq. (7.24) with *i=3,4* and with the preexponential factors from Table 7-5 and corresponding 95% approximate individual confidence intervals

	$E^{comp}_{A,surf}$	$\Delta H^0_{chem,H_2}$	$\Delta H^0_{chem,A}$
		(kJ mol^{-1})	
model with equal surface reaction rate coefficients	-53[a] (± 5)	-42 (± 12)	-70 (± 2)
model with the third H atom addition as the rate-determining step	-51[b] (± 1)	N.S.[d]	-68 (± 1)
model with the fourth H atom addition as the rate-determining step	-59[c] (± 7)	-42 (± 12)	-70 (± 2)

[a] $E^{comp}_{A,surf} = E_{A,surf} + \Delta H^0_{chem,A} + 0.5\,\Delta H^0_{chem,H_2}$, [b] $E^{comp}_{A,surf} = E_A + \Delta H^0_{chem,A} + 1.5\,\Delta H^0_{chem,H_2} + \Delta H^0_1 + \Delta H^0_2$, [c] $E^{comp}_{A,surf} = E_A + \Delta H^0_{chem,A} + 2\,\Delta H^0_{chem,H_2} + \Delta H^0_1 + \Delta H^0_2 + \Delta H^0_3$, [d] Not Significant

reaction equilibrium coefficient for all temperatures leads to the estimates and corresponding 95% approximate individual confidence intervals for the remaining parameters reported in Table 7-6. Although the H_2 chemisorption enthalpy was estimated significantly, the corresponding *t* value was almost a factor 10 lower than the *t* value of the toluene chemisorption enthalpy. However, this is expected when the H atom surface coverage is low compared to the toluene surface coverage and, hence, the model is less sensitive to the H_2 chemisorption parameters. The fractional surface coverages at typical reaction conditions, i.e., T=450 K, $p_{H2,0}$=100 kPa and $p_{tol,0}$=20 kPa, amount to 0.19 for H_2 and to 0.59 for toluene and support the above. The fraction of the surface occupied by other hydrocarbon species is small, i.e., < 0.01. Binary correlation coefficients between the parameters are lower than 0.95, except between the composite activation energy and the H_2 chemisorption enthalpy, where a value of 0.97 is found. This correlation is however in agreement with the lower surface coverage by

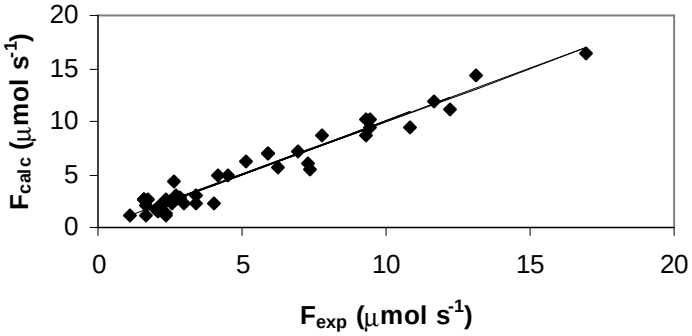

Figure 7-6 **Parity diagram for the methylcyclohexane outlet flow rate; line: experimental, dots: calculated based on the kinetic model with equal surface reaction rate coefficients, Eq. (2.34) and Eq. (7.20) with the preexponential factors from Table 7-5 and the composite activation energy and chemisorption enthalpies from Table 7-6**

H_2. The value of the denominator is relatively insensitive to variations in the H_2 chemisorption enthalpy, while in the numerator such variations strongly affect the value of *B*, vide Eq (7.17), and are compensated by variations in the composite activation energy. The corresponding *F* value for the significance of the regression amounts to 10^4. The parity diagram in Figure 7-6 shows the agreement of the calculated with the experimental methylcyclohexane outlet flow rates. The toluene chemisorption enthalpy, -70 kJ mol^{-1}, is a little less exothermic than the benzene chemisorption enthalpy, -75 kJ mol^{-1} corresponding with the reactive form calculated quantumchemically, vide Table 7-3. The weaker chemisorption of toluene than of benzene explains its lower hydrogenation rate [19,23]. The value for the H_2 chemisorption enthalpy is estimated less negative, i.e., -42 kJ mol^{-1}, than quantumchemically calculated, -70 kJ mol^{-1}. However, the 95% approximate individual confidence interval is rather large and intersects the range of H_2 chemisorption enthalpies reported by Podkolzin et al. [56]. From the value of the composite activation energy, the real activation energy is calculated and amounts to 38 kJ mol^{-1}. This is lower than what was calculated quantumchemically, however, the weak exothermicity estimated for H_2 chemisorption partly accounts for this effect. Using the value reported in Table 7-3, a value closer to the quantumchemically calculated values is obtained, i.e., 52 kJ mol.

7.4.3 Model With a Rate-Determining Step (RDS)

The other possibility mentioned in Section 7.4.1 was the introduction of the third or the fourth H atom addition as the RDS, related to the occurrence of a cyclohexenyl species (cC_6H_9) on the surface. Derivation of the rate equation starts from

$$R_{AH_6(g)} = C_t k_i \theta_{AH_{i-1}*} \theta_{H*} \qquad (i=3,4) \tag{7.21}$$

where i represents the number of the rate-determining H atom addition step. The quasi-equilibrium for the other H atom additions allows us to relate $\theta_{AH_{i-1}*}$ to θ_{A*}:

$$\theta_{AH_{i-1}*} = \left(\prod_{j=1}^{i-1} K_j \right) \frac{\theta_{A*} \theta_{H*}^{i-1}}{\theta_*^{i-1}} \qquad (i=3,4) \tag{7.22}$$

The surface coverages are obtained from the corresponding partial pressures via Eq. (7.14) and Eq. (7.15). Hydrocarbon species other than the aromatic reactant are not considered which is justified by the endothermicity of the first four H atom addition steps (Figure 7-4). Therefore, the site balance, Eq. (7.16) is reduced to:

$$1 = \theta_* + \theta_{A*} + \theta_{H*} \tag{7.23}$$

Combination of Eq. (7.21) to Eq. (7.23) leads to the following rate equation:

$$R_{AH_6(g)} = \frac{C_t k_i \left(\prod_{j=1}^{i-1} K_j \right) K_{chem,A} K_{chem,H_2}^{i/2} p_A p_{H_2}^{i/2}}{\left(1 + K_{chem,A} p_A + \sqrt{K_{chem,H_2} p_{H_2}} \right)^2} \qquad (i=3,4) \tag{7.24}$$

The rate parameters were estimated by a non-isothermal regression of this rate equation for $i=3,4$ to all experimental data. Initial regressions for $i=3$ showed that the model calculations were insensitive to the chemisorption of H_2, such that the H_2 chemisorption term was removed from the denominator. Similar conclusions on the surface mobilities of the species were drawn, so that the same values as in Table 7-5 were used. The remaining parameters are the composite activation energy ($E_A^{comp} = E_A + \Delta H^0_{chem,A} + 1.5\,\Delta H^0_{chem,H_2} + \Delta H^0_1 + \Delta H^0_2$) and the toluene chemisorption enthalpy ($\Delta H^0_{chem,A}$). Their estimates and corresponding 95% approximate individual confidence intervals are reported in Table 7-6. An F value of $5\ 10^2$ was obtained. The agreement between the calculated and experimental methylcyclohexane outlet flow rate is shown in Figure 7-7. The agreement is good, but somewhat inferior to the one obtained with the model with equal surface reaction rate coefficients, which is also reflected in the respective F values. The value obtained for toluene chemisorption enthalpy, -68 kJ mol^{-1}, is in agreement with that obtained with the model with equal surface reaction rate coefficients. Using a H_2 chemisorption enthalpy of 70 kJ mol^{-1} and a 13 kJ mol^{-1}

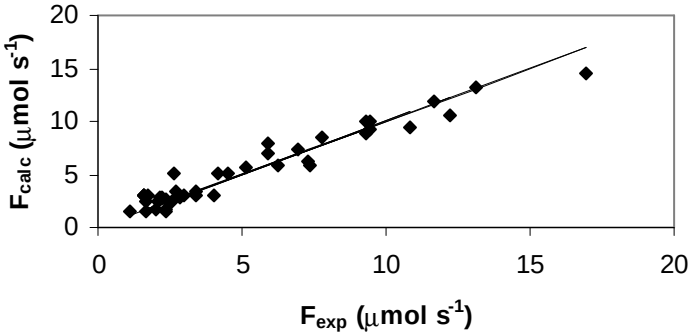

Figure 7-7 **Parity diagram for the methylcyclohexane outlet flow rate; line: experimental, dots: calculated based on the kinetic model with the 3rd H addition as the rate-determining step, Eq. (2.34) and Eq. (7.24) with *i=3* and with the preexponential factors from Table 7-5 and the composite activation energy and chemisorption enthalpies from Table 7-6**

endothermicity between *A** and AH_2* (Figure 7-4), a value of 109 kJ mol^{-1} is obtained for the real activation energy starting from the composite activation energy. Using the weakest H_2 chemisorption enthalpy reported by Podkolzin et al. [56], i.e., 50 kJ mol^{-1}, the value for the real activation energy amounts to 80 kJ mol^{-1}, which is somewhat higher than the values calculated quantumchemically and on the high end of the range reported in the literature [34].

Taking the fourth H atom addition as the RDS, all parameters, i.e., the composite activation energy ($E_A^{comp} = E_A + \Delta H^0_{chem,A} + 2\Delta H^0_{chem,H_2} + \Delta H^0_1 + \Delta H^0_2 + \Delta H^0_3$) and the H_2 and toluene chemisorption enthalpies, could be estimated significantly. The conclusions concerning the surface mobilities of the species were analogous to those mad above and, hence the same values as in Table 7-5 were used. The values and their corresponding 95% approximate individual confidence intervals are reported in Table 7-6. An *F* value of 10^4 was obtained. Figure 7-8 shows the agreement between calculated and experimental methylcyclohexane outlet flow rates. H_2 chemisorption is estimated to be weaker than expected, analogous to the results obtained with the model with equal surface reaction rate coefficients. Using a 30 kJ mol^{-1} endothermicity between *A** and AH_3* (Figure 7-4), a value of 65 kJ mol^{-1} is obtained for the real activation energy starting from the composite activation energy. However, if the relationship $\Delta H_{surf} \approx -0.5\Delta H_{H2}$ obtained based on the model with equal surface reaction rate coefficients is used, then with an endothermicity of 60 kJ mol^{-1} a real activation energy of 35 kJ mol^{-1} is found. Using a value for the H_2 chemisorption enthalpy of –70 kJ mol^{-1} and the same relation as above, the value for the real activation energy amounts to 46 kJ mol^{-1}.

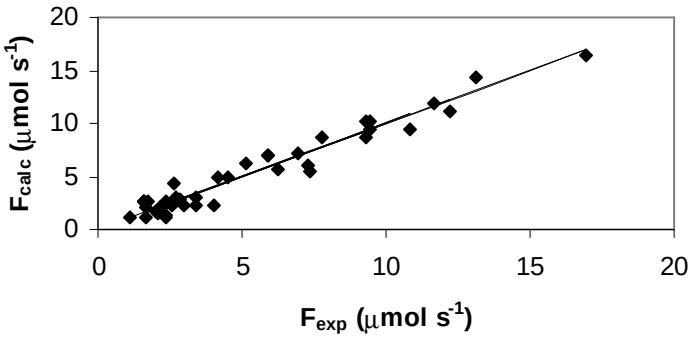

Figure 7-8 **Parity diagram for the methylcyclohexane outlet flow rate; line: experimental, dots: calculated based on the kinetic model with the 4rd H addition as the rate-determining step, Eq. (2.34) and Eq. (7.24) with *i=4* and with the preexponential factors from Table 7-5 and the composite activation energy and chemisorption enthalpies from Table 7-6**

7.4.4 Model Selection

From the three models tested in this work, the model with equal surface reaction rate coefficients and the model with the fourth H atom addition as the rate-determining step have the highest *F* values for significance of the regression. In those two models the chemisorption enthalpies for toluene and H_2 could be significantly estimated simultaneously. Also the parity diagrams for those two models were very similar. This similar behaviour indicates that the model with the fourth H atom addition as the rate-determining step is a limit of the more general model with equal surface reaction rate coefficients. In this limiting case the surface coverage of the partially hydrogenated surface species decreases as the number of added H atoms increases. This effect appears from Eq. (7.17) for values of B which are sufficiently lower than one, but not zero. With sufficiently large differences in surface coverage, also the differences in the forward reaction rates will be large because of the equal surface reaction rate coefficients used. Hence, the forward reaction of the surface species with the lowest surface coverage becomes rate-determining. In that limiting case, the model with equal surface reaction rate coefficients (7.20) becomes mathematically equal to the model with the fourth H atom addition as the rate-determining step, Eq. (7.24) with *i=4*. Because of this more general character of the model with equal surface reaction rate coefficients, this model is selected. A similar conclusion was drawn by Van Meerten and Coenen [13]b.

7.5 Conclusions

Careful consideration of various aspects encountered in the kinetic modelling of aromatic component hydrogenation has yielded important new insights in the hydrogenation reaction mechanism. It was shown that the rate-determining effect of the resonance stabilization in the gas phase is lost upon chemisorption on the catalyst surface. Although a certain loss of catalytic activity occurred, the presence of dehydrogenated species as most abundant surface intermediate in equilibrium with the aromatic reactant can be rejected. An identical type of sites was assumed for H_2 and toluene. A thermochemical analysis of the hydrogenation of benzene on a Pt-surface suggested the quasi-equilibration of the last 2 H atom addition steps.
A model with equal surface reaction rate coefficients for the first four H atom addition steps and assuming quasi-equilibrium for the fifth and the sixth H atom addition was selected as the best model, based on its flexibility. According to this model the hydrocarbon species are relatively immobile on the catalyst surface, while the H atoms have a higher mobility. The surface coverage by H atoms is non negligible, but is lower than the surface coverage by aromatic reactant molecules. The activation energy and chemisorption enthalpies estimated with this model are close to values calculated quantumchemically and reported in literature.

7.6 References

[1] Cooper, B. H., and Donnis, B. B. L., *Aromatic saturation of distillates: an overview* **Appl. Catal. A Gen.** *137* 203-223 (1996).

[2] Allen, L., World Fuels Meeting, Fall 1998, Washington D.C, EAA-World Fuels-98 http://www.criterioncatalysts.com/pdfs/WrldFls98.pdf.

[3] Martens, G. G., and Froment, G. F., *Kinetic modelling of paraffins hydrocracking based upon elementary steps and the single event concept* **Stud. Surf. Sci. Catal.** *122* 333-340 (1999).

[4] Martens, G. G., Marin, G. B., Jacobs, P. A., Martens, J. A., Baron, and G. V., *A fundamental kinetic model for hydrocracking of C_8 to C_{12} alkanes on Pt/US-Y zeolites* **J. Catal.** *195* 253-267 (2000).

[5] Martens, G. G., Thybaut, J. W., and Marin, G. B., *Single-Event Rate Parameters for the Hydrocracking of Cycloalkanes on Pt/US-Y Zeolites* **Ind. Eng. Chem. Res.** *40* 1832-1844 (2001).

[6] Canjar, L. N., and Manning, F. S., *Note on the kinetics of the catalytic hydrogenation of benzene on a supported nickel catalyst* **J. Appl. Chem.** *12* 73-74 (1962).

[7] Germain, J. E., Maurel, R., Bourgeois, Y., and Sinn, R., *Kinetics of the hydrogenation of benzene in the vapour phase on the catalyst Ni-alumina. II. Order with respect to cyclohexane* **J. Chim. Phys.** *60* 1227-1230 (1963).

[8] Snagovskii, Y. S., Lyubarski, G. Y., and Ostrovskii, G. M., *Kinetics of benzene hydrogenation on nickel. I. Reactions in the kinetic region* **Kinet. Katal.** *2* 258-265 (1966).

[9] Zlotina, N. E., and Kiperman, S. L., *Kinetics of benzene hydrogenation over nickel catalysts in a gradientless system. II. Kinetic-isotopic effects of the reaction* **Kinet. Katal.** *6* 1335-1341 (1967).

[10] Jiracek, F., Pasek, J., and Horak, J., *Kinetics of benzene hydrogenation with nickel catalyst on alumina* **Collect. Czech. Chem. Commun.** *33* 3266-3279 (1968).

[11] Roethe, K. P., Roete, A., Rosahl, B., and Gelbin, D., *Comparative study of a model reaction in various experimental reactors* **Chem.-Ingr. Tech.** *42* 805-812 (1970).

[12] Kehoe, J. P. G., and Butt, J. P., *Kinetics of benzene hydrogenation by supported nickel at low temperature* **J. Appl. Chem. Biotechnol.** *22* 23-30 (1972).

[13] a) Van Meerten, R. Z. C., De Graaf, T. F. M., and Coenen, J. W. E., *Gas Phase Benzene Hydrogenation on a Nickel-Silica Catalyst III. Low-Field Magnetization Measurements on Hydrogen, Benzene, Cyclohexene and Cyclohexane Adsorption, and Benzene Hydrogenation* **J. Catal.** *46* 1-12 (1977), b) Van Meerten, R. Z. C., and Coenen, J. W. E., *Gas Phase Benzene Hydrogenation on a Nickel-Silica Catalyst IV. Rate Equations and Curve Fitting* **J. Catal.** *46* 13-24 (1977).

[14] Mirodatos, C., Dalmon, J. A., and Martin, G. A., *Steady-State and Isotopic Transient Kinetics of Benzene Hydrogenation on Nickel Catalysts* **J. Catal.** *105* 405-415 (1987).

[15] a) Chou, P., and Vannice, M. A., *Benzene Hydrogenation over Supported and Unsupported Palladium I. Kinetic Behaviour* **J. Catal.** *107* 129-139 (1987), b) Chou, P., and Vannice, M. A., *Benzene Hydrogenation over Supported and Unsupported Palladium II. Reaction Model* **J. Catal.** *107* 140-153 (1987).

[16] a) Coughlan, B., and Keane, M. A., *The hydrogenation of benzene over nickel-supported Y zeolites. Part 1. A kinetic approach* **Zeolites** *11* 12-17 (1991), b) Coughlan, B., and Keane, M. A., *The hydrogenation of benzene over nickel-supported Y zeolites. Part 2. A mechanistic approach* **Zeolites** *11* 483-490.

[17] Ostrovskii, N. M., Parmaliana, A., Frusteri, F., Maslova, L. P., and Giordano, N., *Analysis of hydrogenation of benzene on an aluminum oxide-supported platinum block catalyst with a honeycomb structure* **Kinet. Catal.** *32* 67-73 (1991).

[18] Reyes, P., Concha, I., Konig, M. E., and Delgado, E., *The kinetics of benzene hydrogenation on a rhodium/yttrium sodium zeolite catalyst* **Bol. Soc. Chil. Quim.** *36* 147-152 (1991).

[19] Lin, S. D., and Vannice, M. A., *Hydrogenation of Aromatic Hydrocarbons over Supported Pt Catalysts I. Benzene Hydrogenation* **J. Catal.** *143* 539-553 (1993).

[20] Au, S. S., Dranoff, J. S., and Butt, J. B., *Nonuniform activity distribution in catalyst particles: benzene hydrogenation on supported nickel in a single pellet diffusion reactor* **Chem. Eng. Sci.** *50* 3801-3812 (1995).

[21] Dobert, F., and Gaube, J., *Kinetics and Reaction Engineering of Selective Hydrogenation of Benzene Towards Cyclohexene* **Ind. Eng. Chem. Res.** *35* 1824-1833 (1996).

[22] a) Rahaman, M. V., and Vannice, M. A., *The Hydrogenation of Toluene and o-, m-, and p-xylene over Palladium I. Kinetic Behaviour and o-Xylene Isomerization* **J. Catal.** *127* 251-266 (1991), b) Rahaman, M. V., and Vannice, M. A., *The Hydrogenation of Toluene and o-, m-, and p-xylene over Palladium II. Reaction Model* **J. Catal.** *127* 267-275 (1991).

[23] Lin, S. D., and Vannice, M. A., *Hydrogenation of Aromatic Hydrocarbons over Supported Pt Catalysts II. Toluene Hydrogenation* **J. Catal.** *143* 554-562 (1993).

[24] Lindfors, L. P., Salmi, T., and Smeds, S., *Kinetics of Toluene Hydrogenation on Ni/Al2O3 Catalysts* **Chem. Eng. Sci.** *48* 3813-3828 (1993).

[25] Chupin, J., Gnep, N. S., Lacombe, S., and Guisnet, M., *Influence of the metal and of the support on the activity and stability of bifunctional catalysts for toluene hydrogenation* **Appl. Catal. A Gen.** *206* 43-56 (2001).

[26] Rousset, J. L., Stievano, L., Cadete Santos Aires, F. J., Geantet, C., Renouprez, A. J., and Pellarin, M., *Hydrogenation of Toluene over g-Al_2O_3-Supported Pt, Pd, and Pd-Pt Model Catalysts Obtained by Laser Vapourization of Bulk Metals* **J. Catal.** *197* 335-343 (2001).

[27] Smeds, S., Murzin, D., and Salmi, T., *Kinetics of ethylbenzene hydrogenation on Ni/Al_2O_3* **Appl. Catal. A Gen.** *125* 271-291 (1995).

[28] a) Huang, T.-C., and Kang, B.-C., *Kinetic Study of Naphthalene Hydrogenation over Pt/Al_2O_3 Catalyst* **Ind. Eng. Chem. Res.** *34* 1140-1148 (1995), b) Huang, T.-C., and Kang, B.-C., *The Hydrogenation of Naphthalene with Platinum/Aluminum-Aluminum Phosphate Catalysts* **Ind. Eng. Chem. Res.** *34* 2955-2963 (1995).

[29] Smeds, S., Murzin, D., and Salmi, T., *Kinetics of m-xylene hydrogenation on Ni/Al_2O_3* **Appl. Catal. A Gen.** *141* 207-228 (1996).

[30] Smeds, S., Salmi, T., and Murzin, D., *Gas phase hydrogenation of o- and p-xylene on Ni/Al_2O_3 - kinetic behaviour* **Appl. Catal. A Gen.** *145* 253-265 (1996).

[31] Keane, M. A., *The Hydrogenation of o-, m-, and p-Xylene over Ni/SiO_2* **J. Catal.** *166* 347-355 (1997).

[32] Smeds, S., Murzin, D., and Salmi, T., *Gas phase hydrogenation of o- and p-xylene on Ni/Al_2O_3 - kinetic modelling* **Appl. Catal. A Gen.** *150* 115-129 (1997).

[33] Quartaro, J., Mignard, S., and Kasztelan, S., *Trends for mono-aromatic compounds hydrogenation over sulfided Ni, Mo and NiMo hydrotreating catalysts* **Catal. Lett.** *61* 167-172 (1999).

[34] Keane, M. A., and Patterson, P. M., *The Role of Hydrogen Partial Pressure in the Gas-Phase Hydrogenation of Aromatics over Supported Nickel* **Ind. Eng. Chem. Res.** *38* 1295-1305 (1999).

[35] Figueras, F., Gomez, R., and Primet, M., *Adsorption and Catalytic Properties of Palladium Supported by Silica, Alumina, Magnesia, and Amorphous and Crystalline Silica-Aluminas* **Adv. Chem. Ser.** *121* 480-488 (1973).

[36] Lin, S. D., and Vannice, M. A., *Hydrogenation of Aromatic Hydrocarbons over Supported Pt Catalysts* **J. Catal.** *143* 563-572 (1993).

[37] Wang, J., Huang, L., and Li, Q., *Influence of different diluents in Pt/Al_2O_3 catalyst on the hydrogenation of benzene, toluene and o-xylene* **Appl. Catal. A Gen.** *175* 191-199 (1998).

[38] Wang, J., Li, Q., and Yao, J., *The effect of metal-acid balance in Pt-loading dealuminated Y zeolite catalysts on the hydrogenation of benzene* **Appl. Catal. A Gen.** *184* 181-188 (1999).

[39] Hugenschmidt, M. B., Diaz, A. L., and Campbell, C. T., *Interaction of Cyclohexadiene with Pt(111) Studied by BPTDS and HREELS* **J. Phys. Chem.** *96* 5974-5978 (1992).

[40] Land, D. P., Erley, W., and Ibach, H., *HREELS investigation of the orientation and dehydrogenation of cyclohexane on Pt[111]* **Surf. Sci.** *289* 237-246 (1993).

[41] a) Xu, C., Tsai, Y.-L., and Koel, B. E., *Adsorption of Cyclohexane and Benzene on Ordered Sn/Pt(111) Surface Alloys* **J. Phys. Chem.** *98* 585-593 (1994), b) Xu, C., Koel, B. E., Newton, M. A., Frei, N. A., and Campbell, C. T., *Dehydrogenation of methylcyclohexane on Pt(111)* **J. Phys. Chem.** *99* 16670-16675 (1995).

[42] Haq, S., and King, D. A., *Configurational Transitions of Benzene and Pyridine Adsorbed on Pt{111} and Cu{110} Surfaces: An Infrared Study* **J. Phys. Chem.** *100* 16957-16965 (1996).

[43] Peck, J. W., and Koel, B. E., *Selective Dehydrogenation of 1,3-cyclohexadiene on Ordered Sn/Pt(111) Surface Alloys* **J. Am. Chem. Soc.** *118* 2708-2717 (1996).

[44] Koel, B. E., Blank, D. A., and Carter, E. A., *Thermochemistry of the selective dehydrogenation of cyclohexane to benzene on pt surfaces* **J. Mol. Catal. A Chem.** *131* 39-53 (1998).

[45] Su, X., Kung, K., Lahtinen, J., Shen, R. Y., and Somorjai, G. A., *Cyclohexene dehydrogenation and hydrogenation on Pt(111) monitored by SFG surface vibrational spectroscopy: different reaction mechanisms at high pressures and in vacuum* **Catal. Lett.** *54* 9-15 (1998).

[46] Ranke, W., and Weiss, W., *Adsorption and thermal decomposition of ethylbenzene and styrene on Pt(111) studied by UPS and XPS* **Surf. Sci.** *465* 317-330 (2000).

[47] Sautet, P., and Bocquet, M.-L., *Shape of molecular adsorbates in STM images: A theoretical study of benzene on Pt(111)* **Phys. Rev. B** *53* 4910-4925 (1996).

[48] Hansen, E. W., and Neurock, M., *First-Principles-Based Monte Carlo Simulation of Ethylene Hydrogenation Kinetics on Pd* **J. Catal.** *196* 241-252 (2000).

[49] Bos, A. N. R., Lefferts, L., Marin, G. B., and Steijns, M. H. G. M., *Kinetic research on heterogeneously catalyzed processes: A questionnaire on the state-of-the-art in industry* **Appl. Catal. A Gen.** *160* 185-190 (1997).

[50] Berger, R. J., Stitt, E. H., Marin, G. B., Kapteijn, and F., Moulijn, J. A., *Chemical reaction kinetics in practice* **CATTECH** *5* 30-60 (2001).

[51] Fovel, I., *Hydrogenering van Tolueen op een Hydrokrakingskatalysator* **Master Thesis** *Ghent University* (2002).

[52] Martens, J. A., Parton, R., Uytterhoeven, L., Jacobs, P. A., and Froment, G. F., *Selective Conversion of Decane into branched Isomers. A Comparison of Pt/ZSM-22, Pt/ZSM-5 and Pt/USY zeolite catalysts* **Appl. Catal.** *76* 95-116 (1991).

[53] Parton, R., Uytterhoeven, L., Martens, J. A., and Jacobs, P. A., *Synergism of ZSM-22 and Y zeolites in the bifunctional conversion of n-alkanes* **Appl. Catal.** *76* 131-142 (1991).

[54] Zhdanov, V. P., *Elementary Physicochemical Processes on Solid Surfaces* **Plenum Press** *New York* (1991).

[55] van Santen, R. A., and Niemantsverdriet, J. W., *Chemical Kinetics and Catalysis* **Plenum Press** *New York* (1995).

[56] Podkolzin, S. G., Watwe, R. M., Yan, Q., de Pablo, J. J., and Dumesic, J. A., *DFT Calculations and Monte Carlo Simulations of the Co-adsorption of Hydrogen Atoms and Ethylidyne Species on Pt(111)* **J. Phys. Chem. B** *105* 8550-8562 (2001).

[57] Boudart, M., and Djéga-Mariadassou, G., *Cinétique des Réactions en Catalyse Hétérogène* **Masson** *Paris* (1982).

[58] Dumesic, J. A., Rudd, D. F., Aparicio, L. M., Rekoske, J. E., and Treviño, A. A., *The Microkinetics of Heterogeneous Catalysis* **American Chemical Society** *Washington DC* (1993).

[59] Voelter, J., Hermann, M., and Heise, K., *Comparative hydrogenation and adsorption of benzene and methylbenzenes on cobalt and rhodium catalysts* **J. Catal.** *12* 307-313 (1968).

[60] Prasad, K. H. V., Prasad, K. B. S., Mallikarjunan, M. M., and Vaidyeswaran, R., *Self-Poisoning and Rate Multiplicity in Hydrogenation of Benzene* **J. Catal.** *84* 65 (1983).

[61] Horiuchi, J., and Polanyi, M., *Exchange reactions of hydrogen on metallic catalysts* **Trans. Faraday Soc.** *30* 1164-1172 (1934).

Chapter 8

Liquid Phase Hydrogenation Kinetics of Toluene on Pt/ZSM22

Kinetic toluene hydrogenation experiments were performed on 0.5 wt% Pt/ZSM-22 in a three-phase Robinson Mahoney type reactor at the Laboratorium voor Petrochemische Techniek of Ghent University. A kinetic model developed based on vapour phase experimental data was used in the liquid phase kinetic modelling. The standard state used in the description of the vapour liquid equilibrium and the reactant chemisorption was the ideal gas state at 1 bar (= 10^5 Pa) and, hence, non ideality in the liquid phase was described in terms of fugacities expressing the deviation from the ideal gas state at 1 bar, rather than in terms of activities expressing the deviation from the ideal liquid. The use of fugacities provides several advantages over the use of activities, from which the most important within the framework of this Chapter is that it allows the comparison of model parameter values in vapour and liquid phase kinetics in a convenient way. The fugacities were calculated using the Peng-Robinson cubic equation of state. Expressions for the surface reaction steps were constructed considering the chemisorbed species as in an ideal dilute solution with the catalyst as solvent and neglecting the interactions of the chemisorbed species with non chemisorbed liquid molecules. A priori simulations with the vapour phase kinetic model adapted for the liquid phase conditions resulted in an overestimation of the toluene conversion. However, regression of the model to a limited set of liquid phase toluene hydrogenation data resulted for the toluene and hydrogen chemisorption enthalpies in values statistically not different at the 95 %

probability level from the values obtained in the vapour phase kinetic modelling of toluene hydrogenation, i.e., -72 ± 4 kJ mol^{-1} and –40 ± 21 kJ mol^{-1} for toluene and hydrogen respectively in the liquid phase and –70 ± 2 kJ mol^{-1} and –42 ± 12 kJ mol^{-1} in the vapour phase. The activation energy for hydrogen addition was found to be higher than under vapour phase conditions, i.e., 52 ± 8 kJ mol^{-1} compared to 38 ± 5 kJ mol^{-1}, which was possibly caused by neglecting the interactions between the chemisorbed species and the non chemisorbed liquid molecules.

8.1 Introduction

Refinery conversion processes such as hydrocracking are typically performed under three-phase conditions [1,2]. Nevertheless, the study of such processes on laboratory scale is frequently performed in vapour phase. A more accurate description of vapour phase conditions is possible and is expected to lead to more adequate kinetic models than models obtained based on three phase experiments. On the other hand, the applicability under liquid phase conditions of a kinetic model developed based on vapour phase experiments needs to be verified and may subsequently lead to guidelines for general model improvement or for model adaptations. This is the philosophy around which Chapter 7 and the current Chapter of this thesis are built. A kinetic model for toluene hydrogenation was constructed based on vapour phase experiments, vide Chapter 7, and is validated for liquid phase conditions in the current Chapter.

Apart from the aspect of kinetic model validation for liquid phase conditions, this Chapter also focuses on the methodology applied in the description of liquid phase kinetics. It is demonstrated that the methodology applied earlier at Ghent University [3,4] accounts for non idealities of both the vapour and the liquid phase with respect to the ideal gas state at 1 bar (=10^5 Pa). The liquid phase fugacities have, however, always been recalculated to the corresponding concentrations and because of the continuous use of concentrations in the liquid phase kinetic models without explicitly referring to the standard state, i.e., ideal gas at 1 bar, it may have seemed that ideal liquid behaviour was assumed and that the standard state used was the pure liquid state. The use of the latter standard state seems self-evident in the description of liquid phase phenomena, however, as demonstrated in Section 8.4.1, the use of the ideal gas at 1 bar as standard state may be preferred above the pure liquid as the standard state [5,6] on the condition that accurate methods are available to calculate liquid phase fugacities.

Table 8-1 Range of experimental conditions

Temperature (K)	Total Pressure (MPa)	Inlet Hydrogen to Toluene Ratio (mol mol^{-1})	Space Time (kg_{cat} mol^{-1} s^{-1})	Conversion (%)
448 – 473	1 – 3	5	26	0.1 - 20

8.2 Experimental

The current Chapter describes the liquid phase analogue of the vapour phase investigations presented in Chapter 7 and, hence, the same catalyst and reactant, i.e., 0.5 wt % Pt/H-ZSM-22 and toluene respectively, are used. The range of investigated experimental operating conditions is shown in Table 8-1. The temperature range reported was chosen to be similar to the range investigated in the vapour phase experiments, vide Table 7-1, in order to compare between vapour and liquid phase hydrogenation data. To have enough liquid under these operating conditions a heavy solvent, c.q., *n*-dodecane, was added. A mixture containing 10 mol % toluene and 90 mol % *n*-dodecane was used in all the experiments. Because conversion in the absence of 0.5 wt % Pt/H-ZSM-22 was observed when using a pure hydrogen gas feed, a gas mixture containing 10 mol % hydrogen and 90 mol % nitrogen was used. The absence of mass transport limitations in the intercrystalline pores was verified (Weisz moduli ~10^{-2}) [7-9]. Note that intracrystalline diffusion limitations are not relevant, as the hydrogenation occurs at the external crystallite surface of ZSM-22 [10,11].

8.3 Results

Methylcyclohexane was the only product observed in the hydrogenation of toluene on 0.5 wt% Pt/ZSM-22 in the liquid phase. Only trace quantities of ethylcyclopentane and the dimethylcyclopentane isomers were found in the reactor effluent.

Transient phenomena observed in the Robinson-Mahoney reactor are visualized in Figure 8-1 using the toluene conversion calculated based on the flashed liquid as a function of the time on stream. This Figure provides the necessary information for an experimental verification of the calculated stabilization time of the set-up [3,9,12]. Because no liquid is contained in the reactor on start-up, the liquid first has to accumulate before it can leave the reactor via the downcomer at the top, vide Figure 2-5. Under the conditions used, the accumulation of the liquid in the reactor requires about 30 ks or 8 h, explaining why the data points in Figure 8-1 are only available from 30 ks on. The highest values for the toluene conversion calculated based on the flashed liquid are obseverved when the accumulation of the liquid has been

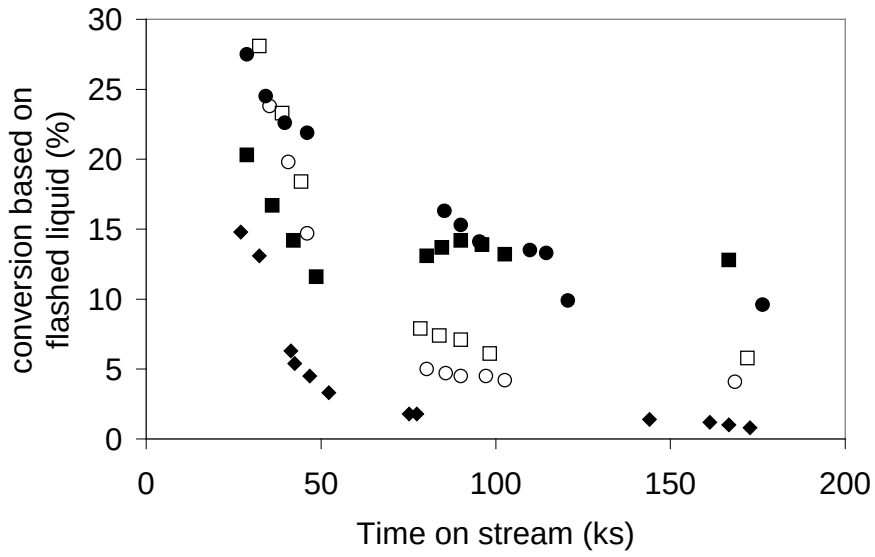

Figure 8-1 Toluene conversion calculated based on the flashed liquid as a function of the time on stream: effect of temperature and total pressure (♦: 1 MPa; ● : 2 MPa; ■ : 3 MPa; open symbols : 448 K; closed symbols : 473 K)

accomplished, i.e., after 30 ks. For higher time on stream values, a decrease of the toluene conversion calculated based on the flashed liquid to the steady state value is observed. The time needed to obtain the steady state toluene conversion calculated based on the flashed liquid, i.e., 90 to 120 ks or 25 to 33 h, corresponds to the stabilization times calculated by Debrabandere [3] and De Waele [9], assuming that under steady state conditions the liquid occupies about 60 vol % of the reactor.

Both temperature and total pressure have a positive effect on the hydrogenation rate in the range of experimental conditions investigated as is illustrated in Figure 8-1. In the same temperature range under vapour phase conditions a decrease in the reaction rate was observed, vide Figure 7-1. This decrease has been related with the decrease in toluene concentration chemisorbed on the metal surface. The decreasing reaction rate observed between 448 K and 473 K in the vapour phase is expected to occur only at higher temperatures in the liquid phase. Because higher reactant concentrations are employed at the fluid-catalyst interface in the liquid than in the vapour phase experiments, higher temperatures are required to significantly reduce the toluene concentration on the metal surface. Apart from the toluene concentration effect a slight increase in hydrogen saturation concentration with the temperature may also contribute to the absence of a decrease in the reaction rate with temperature in the liquid phase experiments [13].

The effect of the total pressure is related to the hydrogen solubility in the liquid phase. The higher the total pressure, the higher the hydrogen partial pressure and, hence, the hydrogen solubility in the liquid phase. A positive partial reaction order with hydrogen then leads to the higher reaction rates observed.

8.4 Kinetic Modelling

8.4.1 Thermodynamic Non Ideality

Whereas thermodynamic non ideality is not often an issue under vapour phase conditions, deviations from thermodynamic ideality are more frequently encountered under liquid phase conditions. The thermodynamic non ideality in a binary mixture containing molecules A and B is typically caused by differences in interactions between molecules of the same type, i.e., A-A and B-B interactions, and of a different type, i.e., A-B interactions [5]. If mixtures of similar components of a similar molecular size are considered, i.e., A resembles B, such as in a benzene and toluene mixture, the A-A and B-B interactions are very similar to the A-B interactions and ideal liquid behaviour may be established. Non ideal behaviour occurs when the A-B interactions differ strongly from A-A and/or B-B interactions, e.g., because of strong H-bond bridges formed between two components of a different type but none or weaker bridges between components of the same type. The binary mixture acetone – chloroform is an example of a strongly non ideal liquid mixture because of the H-bond bridges between acetone and chloroform.

From the above, it may be clear that when describing liquid phase kinetics in a mixture of aliphatic hydrocarbons with a not too broad carbon number range, such as parapur [3], the system can be described as a thermodynamically ideal liquid. If, however, the carbon number range considered is more extended, such as in an industrial three-phase adiabatic fixed bed reactor [4], deviations from thermodynamic ideality can be expected, certainly when aromatic components are incorporated in the feedstock mixture, vide Chapter 9.

Considering the liquid as thermodynamically non ideal, the standard state with respect to which the deviations from ideality are expressed has to be selected. From the discussion above it seems evident to express the non ideality of the liquid with respect to ideal liquid behaviour, i.e., using the pure liquid as the standard state. However, the calculation of a chemical potential, if performed properly, i.e., accounting appropriately for the interactions between the components, is independent of the standard state used:

$$\mu_i = \mu_i^{standard} + RT \ln a_i \tag{8.1}$$

In Eq. (8.1) a_i is a generalized activity the exact interpretation and, maybe even more important, the correct calculation method of which depends on the standard state used, however, the value of the chemical potential μ_i itself is independent of the standard state used. Three standard standard states are often encountered [5]:

- The ideal gas state at 1 bar for gases.
- The pure liquid for components in a mixture and for the solvent in a solution.
- The pure solute experiencing solute – solvent interactions only for the solute in a solution.

A distinction is made between a mixture where all components are present in more or less the same quantities and a solution in which one of the components is present in excess, i.e., the solvent, while the other components are only present in minor amounts.

If accurate methods are at hand to calculate activities in the case that the pure liquid is used as the standard state and if accurate methods are also available to calculate fugacities in case the ideal gas at 1 bar is used as the standard state, a non ideal liquid mixture can be considered as a deviation from an ideal liquid or as a deviation from an ideal gas. The selection of the one or the other standard state then may depend on other criteria, such as the calculation of generalized activities in other phases to be described. The latter may occur when calculating vapour liquid equilibria or when comparing quantitative kinetic behaviour in different phases.

As recommended by Poling et al. [6], the vapour liquid equilibrium calculations for hydrocarbon mixtures are performed using the ideal gas state at 1 bar as the standard state for both the liquid and the vapour phase. As a consequence the generalized activity a_i in Eq. (8.1) represents a fugacity f_i which can be calculated using, e.g., the Peng-Robinson equation of state and the equality of the chemical potentials of all individual components i in a mixture with n components as a requirement for the phase equilibrium is reduced to the equality of the fugacities:

$$\mu_{P_i}^{V} = \mu_{P_i}^{L} \qquad i=1,\ldots,n \tag{8.2}$$

$$f_{P_i}^{V} = f_{P_i}^{L} \qquad i=1,\ldots,n \tag{8.3}$$

Liquid phase kinetics can be described based on activities or on fugacities, depending on the selected standard state. It is clear that the values of the model parameters depend on the selected standard state and, hence, because the aim of this Chapter is the comparison between vapour and liquid phase kinetics, the same standard state as in the vapour phase kinetic modelling, i.e., the ideal gas state at 1 bar, is used for the liquid reactants and in the description of the chemisorption steps. The effect on the rate equations is discussed in Section 8.4.2. In general, equations of state originally developed for describing non ideal gases give

rather poor results for liquid phase fugacities. However, since the system described here only contains hydrocarbons and hydrogen, deviations are expected to be relatively small, certainly when compared to strongly non ideal liquids such as electrolytes and, hence, the Peng-Robinson equation of state is also used to calculate the liquid phase fugacities.

The reactants on the catalyst surface are in a chemisorbed state. The interactions of these chemisorbed species with the catalyst are much stronger than the intermolecular interactions between fluid phase molecules. According to Madon and Iglesia [14], interactions between chemisorbed species and non chemisorbed fluid phase molecules can therefore be neglected. This is in agreement with earlier work by Madon et al. [15] on the liquid phase kinetics of cyclohexene hydrogenation in different solvents. These authors define solvent independent standard states for the fugacities of the empty sites and the chemisorbed species and assume that the fugacities under the working conditions equal those in the standard state:

$$\begin{aligned} f_{*} &= f_{*}^{0} \\ f_{A*} &= f_{A*}^{0} \end{aligned} \tag{8.4}$$

i.e., that the fugacities of the free sites and the chemisorbed species are solvent independent. This assumption was successful for the different solvents used by Madon et al. [15], and was generalized to fluids afterwards [14].

In contrast to this, Singh and Vannice [16], do take into account interactions between chemisorbed species and non chemisorbed liquid molecules. However, these authors assume that the interaction between a chemisorbed species and a liquid phase molecule is the sum of the interactions between two liquid phase molecules and the interactions between a free site and a non chemisorbed liquid phase molecules. This additivity can be questioned because the environment of the chemisorbing species and the chemisorption site changes significantly upon chemisorption. As a result of the changing environment, the additivity of interactions assumed by Singh and Vannice [16] is expected to be no longer valid. Because the earlier assumption that interactions between chemisorbed species and the catalyst are much stronger than those between fluid phase molecules seems more reasonable, the assumption of Madon and Iglesia [14] will be adopted in this work.

The use of fugacities for chemisorbed species and free active sites is not usual and no information was found in the literature. Therefore, for the chemisorbed species and the free active sites a new standard state is defined to be used in the description of the elementary surface reaction steps. An analogy is proposed between chemisorbed species and free sites on a catalyst surface and an ideal liquid. The standard state for the chemisorbed species

corresponds to pure chemisorbed species experiencing only chemisorbed species–catalyst interactions. An analogous definition is used for the standard state of the free active sites. Hence, the chemical potential of the chemisorbed species and the free active sites can be expressed as follows:

$$\begin{aligned} \mu_{A^*} &= \mu^*_{A^*} + RT\ln\theta_{A^*} \\ \mu_{*} &= \mu^*_{*} + RT\ln\theta_{*} \end{aligned} \tag{8.5}$$

In Eq. (8.5) the superscript * indicates that the pure form is concerned while the subscript * denotes the active site. Considering the system as an ideal liquid corresponds to the Langmuir assumption that the chemisorbed species do not influence each other or affect the properties of the free active sites.

In the study of adsorption processes a standard state in which half of the active sites is occupied, i.e., $\theta=1/2$, is generally used for reasons of configurational entropy [17]. The use of such a standard state is of particular importance when a detailed physical interpretation of the entropy values is aimed at. Because in this thesis order of magnitude values have been calculated for the preexponential factors, corresponding to a general picture on the (im)mobility of the involved species, the use of a standard state in which, i.e., $\theta=1/2$, is considered not to be required.

8.4.2 Liquid Phase Kinetic Model

The model with equal surface reaction rate coefficients which was selected as the best model in Chapter 7 and which was developed assuming implicitly ideal gas behaviour for the vapour phase will be used and extended to be also applicable under conditions deviating from ideal gas behaviour in general and for liquid phase conditions in particular. Because the interactions between chemisorbed species and liquid molecules are neglected [14,15], the description of the kinetics on the catalyst surface is independent from the aggregation state of the non chemisorbed reactants. The difference between the description of vapour and liquid phase kinetics is then situated in the chemisorption steps, i.e., the transfer of reactants from the fluid phase to the catalyst surface.

Consider the chemisorption of a component *A* on a surface with sites *:

$$A(g) + * \quad \leftrightarrows \quad A^* \qquad\qquad K_A^f \tag{8.6}$$

for which the following equilibrium relationship can be written:

$$K_A^f = \frac{\theta_{A^*}}{f_A^F\,\theta_*} \tag{8.7}$$

in which the superscript *F* represents the aggregation state of the chemisorbing component, i.e., vapour or liquid. The fugacity coefficient Φ_A of a species *A* is defined via the following relationship:

$$f_A = \Phi_A \, p_A \tag{8.8}$$

in which the partial pressure, p_A, can be replaced by the total pressure, p_t, and the mole fraction of *A*, y_A:

$$p_A = y_A p_t \tag{8.9}$$

The concentration of a species *A* in the liquid phase, C_A^L, can be related to its mole fraction using the molar volume of the liquid, V_m. Doing so, the relationship between the liquid phase concentration of a species *A*, C_A^L, and its fugactiy, f_A^L, becomes:

$$f_A^L = \Phi_A^L p_t V_m^L C_A^L \tag{8.10}$$

A balance over the active sites:

$$1 = \theta_* + \theta_{A^*} \tag{8.11}$$

can be rewritten as follows:

$$1 = \theta_* \left(1 + K_A^f \, f_A^F\right) \tag{8.12}$$

Using Eq. (8.12) the free acid site fraction can be eliminated from Eq. (8.7) resulting in:

$$\theta_{A^*} = \frac{K_A^f \, f_A^F}{\left(1 + K_A^f \, f_A^F\right)} \tag{8.13}$$

For the ideal gas situation Eq. (8.13) is reduced to:

$$\theta_{A^*} = \frac{K_A^f \, p_A}{\left(1 + K_A^f \, p_A\right)} \tag{8.14}$$

using:

$$f_A^F = f_A^V = p_A \tag{8.15}$$

In case of chemisorption from the liquid phase, the fugacity in Eq. (8.13) is replaced by, vide Eq. (8.10):

$$f_A^F = f_A^L = \Phi_A^L p_t V_m^L C_A^L \tag{8.16}$$

the relationship between the liquid phase concentration of *A* and the fractional surface coverage by *A* is obtained:

$$\theta_{A^*} = \frac{K_A^f \, \Phi_A^L p_t V_m^L C_A^L}{\left(1 + K_A^f \, \Phi_A^L p_t V_m^L C_A^L\right)} \tag{8.17}$$

Hence, when using concentrations in the modelling of liquid phase kinetics, the chemisorption coefficient used in vapour phase modelling is replaced by the following liquid phase chemisorption coefficient:

$$K^{L}_{chem,A} = K^{f}_{A}\,\Phi^{L}_{A}\,p_t\,V^{L}_{m} \tag{8.18}$$

to account for the non ideality of the liquid phase with respect to the ideal gas at 1 bar [3,4].

8.4.3 Model Simulations and Regression

The method explained in the previous paragraph has been applied in the kinetic modelling of liquid phase toluene hydrogenation. The liquid phase concentrations were obtained via the vapour liquid equilibrium calculations as explained in Appendix A. The rate equation used was that derived in Chapter 7 for the model with equal surface reaction rate coefficients, Eq. (7.20), in which the chemisorption coefficients for toluene and hydrogen were replaced by Eq. (8.18):

$$R_{AH_6(g)} = \frac{C_t k_{surf}}{\left(B^3+B^2+B+1\right)} \frac{B^3 K^{f}_{A}\Phi^{L}_{A}\,p_t V^{L}_{m} C^{L}_{A} \sqrt{K^{f}_{H_2}\Phi^{L}_{H_2}\,p_t V^{L}_{m} C^{L}_{H_2}}}{\left(1+\sqrt{K^{f}_{H_2}\Phi^{L}_{H_2}\,p_t V^{L}_{m} C^{L}_{H_2}} + K^{f}_{A}\Phi^{L}_{A}\,p_t V^{L}_{m} C^{L}_{A}\,\frac{\left(4B^3+3B^2+2B+1\right)}{\left(B^3+B^2+B+1\right)}\right)^{2}} \tag{8. 19}$$

With the following expression for the factor *B*:

$$B = K_{surf}\sqrt{K^{f}_{H_2}\Phi^{L}_{H_2}\,p_t V^{L}_{m} C^{L}_{H_2}} \tag{8. 20}$$

The total molar methylcyclohexane outlet flow rates obtained experimentally and simulated are compared in the parity diagram shown in Figure 8-2. The simulated total molar methylcyclohexane outlet flow rates are higher than the experimental values.

Improvement of the simulations was pursued by an estimation of the same three adjustable parameters, which were estimated in the final regression of the vapour phase kinetic modelling. It needs to be mentioned that the regression is based on a very limited set of experimental data, however, it is worthwhile to make a qualitative and quantitative comparison with the results obtained based on the vapour phase modelling. Estimates for the composite activation energy, the toluene chemisorption enthalpy and the hydrogen chemisorption enthalpy are reported in Table 8-2. The agreement between the experimental and the calculated molar methylcyclohexane outlet flow rates is shown in Figure 8-2. The relative magnitudes of the 95 % individual approximate confidence intervals are the same as those obtained based on the vapour phase experiments. The broadest confidence interval is observed for the hydrogen chemisorption enthalpy, while the narrowest confidence interval is

Table 8-2 **Parameter estimates obtained by regression of the kinetic model with equal rate coefficients adapted for liquid phase conditions, Eq. (2.34) and Eq. (8. 19), with the preexponential factors from Table 7-5 and corresponding 95% individual approximate confidence intervals**

$E_{A,surf}^{comp}$ (kJ mol^{-1})	$\Delta H_{chem,H_2}^{0}$ (kJ mol^{-1})	$\Delta H_{chem,A}^{0}$ (kJ mol^{-1})
-40[a] (± 8)	-40 (± 21)	-72 (± 4)

[a] $E_{A,surf}^{comp} = E_{A,surf} + \Delta H_{chem,A}^{0} + 0.5\,\Delta H_{chem,H_2}^{0}$

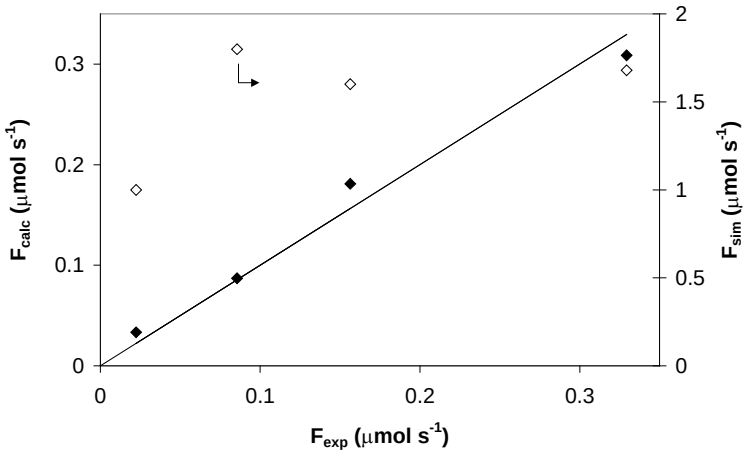

Figure 8-2 **Parity diagram for the methylcyclohexane outlet flow rate for the a priori simulation (open symbols – right *y*-axis) and after regression (closed symbols – left *y*-axis); line: experimental, symbols: calculated based on the kinetic model with equal surface reaction rate coefficients adapted for liquid phase kinetics, Eq. (2.34) and Eq. (8. 19) with the preexponential factors from Table 7-5 and the composite activation energy and chemisorption enthalpies from Table 7-6 (open symbols) or from Table 8-2 (closed symbols)**

observed for the toluene chemisorption enthalpy. This is in agreement with the higher surface coverages calculated for toluene than for hydrogen, resulting in a higher sensitivity of the model to the toluene chemisorption enthalpy than to that of hydrogen. Moreover the values obtained for both chemisorption enthalpies based on the liquid phase experiments, i.e., –72 kJ mol^{-1} for toluene and –40 kJ mol^{-1} for hydrogen, correspond very well with the values obtained based on the vapour phase experiments, i.e., –70 kJ mol^{-1} and –42 kJ mol^{-1} respectively. The *t*-values for the differences between the values of the chemisorption coefficients obtained based on the vapour and the liquid phase modelling amount to 0.87 for the toluene chemisorption enthalpy and 0.16 for the hydrogen chemisorption enthalpy. This

means that the values for the chemisorption enthalpies obtained based on vapour phase and liquid phase kinetic modelling are not significantly different from each other on the 95 % probability level. This supports the assumptions made in the modelling of the chemisorption steps.

The individual 95 % confidence interval for the composite activation energy has a magnitude intermediate to that of the chemisorption enthalpies. The actual value for the composite activation energy based on the liquid phase kinetics is estimated 13 kJ mol^{-1} less negative than that estimated based on the vapour phase experiments. The *t*-value for the difference between the composite activation energy obtained based on the vapour and the liquid phase kinetic modelling amounts to 2.7 and, hence, the difference is considered to be significant on the 95 % probability level. This might indicate that the description of the kinetics on the catalyst surface, to a certain extent, depends on the aggregation state of the fluid phase around the catalyst, in contrast to the assumption made before, vide Section 8.4.1 that interactions between the fluid phase molecules and the reactants chemisorbed on the surface are negligible.

From the composite activation energy and the chemisorption enthalpies for toluene and hydrogen obtained based on the liquid phase kinetic modelling, the real activation energy can be calculated and amounts to 52 kJ mol^{-1}. This is higher than the activation energy obtained based on the vapour phase experiments, i.e., 38 kJ mol^{-1}. Assuming that interactions between fluid phase molecules and chemisorbed species are non negligible, this difference can be interpreted based on differences in the energy of vapour and liquid phase molecules and, hence, based on differences in energy transferred between a vapour phase molecule and a chemisorbed species or between a liquid phase molecule and a chemisorbed species. While an ideal gas molecule contains translational, rotational and vibrational degrees of freedom, it can be assumed for a liquid phase molecule in a stagnant liquid that it only has vibrational degrees of freedom [18]. Because the active sites are located in the macropores of the catalyst, vide Section 2.1.1, the liquid phase in contact with the active sites can indeed be considered as stagnant. Assuming similar vibrational degrees of freedom for vapour and gas phase molecules, the difference in energy between a vapour and a liquid phase molecule corresponds to energy of the vapour phase molecule related to its translational and rotational degrees of freedom, which amount to 3/2kt and kt respectively. At the temperatures used this corresponds to an energy for vapour phase molecules which is about 10 kJ mol^{-1} higher than for liquid phase molecules. When (part of) this extra energy of vapour phase molecules with repsect to liquid phase molecules is exchanged between vapour phase molecules and

chemisorbed species upon collisions, a lower activation energy is expected in the vapour phase kinetic modelling than in the liquid phase kinetic modelling.

8.5 Conclusions

The standard state applied in kinetic modelling determines the meaning of the coefficients used and also determines which generalized activity has to be used in the kinetic expressions. Different standard states can be used in the different elementary steps in a complex reaction mechanism.

In the liquid phase hydrogenation of toluene, the ideal gas state at 1 bar was used as the standard state for describing the vapour liquid equilibrium and the chemisorption of the reactants on the catalyst surface. The equality of the chemisorption enthalpies obtained based on vapour and liquid phase kinetic modelling supports the above methodology when applied to a system containing hydrocarbons and hydrogen. Interactions between fluid phase molecules and reactants chemisorbed on the catalyst surface are significant and lead to a lower activation energy in the vapour phase than in the liquid phase.

8.6 References

[1] Martino, G., Courty, P., and Marcilly, C., *Handbook of heterogeneous Catalysis, Chapter 3.1, Perspectives in Oil Refining* (Eds. Knözinger, Ertl, and Weitkamp) **Wiley – VCH** 1801-1818 (1997).

[2] Scherzer, J., and Gruia, A. J., *Hydrocracking Science and Technology, Chapter 1, 2 & 10, Introduction, Historical Aspects & Hydrocracking Processes* **Marcel Dekker Inc.** *New York*, 1-8, 9-12, 174-199 (1996).

[3] Debrabandere B., *Hydroisomerizatie en Hydrokraking van mengsels koolwaterstoffen op Pt/USY-zeolieten* **PhD Thesis** *Ghent University* (1997).

[4] Martens, G. G., and Marin, G. B., *Kinetics for Hydrocracking Based on Structural Classes: Model Development and Application* **AIChE J.** *47* 1607-1622 (2001).

[5] Atkins, P. W., *Physical Chemistry 3rd ed.* **Oxford University Press** *Oxford* (1987).

[6] Poling, B. E., Prausnitz, J. M., and O'Connell, J. P., *The Properties of Gases and Liquids 5th ed.* **McGraw-Hill** *New York* (2000).

[7] Bos, A. N. R., Lefferts, L., Marin, G. B., and Steijns, M. H. G. M., *Kinetic research on heterogeneously catalyzed processes: A questionnaire on the state-of-the-art in industry* **Appl. Catal. A Gen.** *160* 185-190 (1997).

[8] Berger, R. J., Stitt, E. H., Marin, G. B., Kapteijn, F., and Moulijn, J. A., *Chemical reaction kinetics in practice* **CATTECH** *5* 30-60 (2001).

[9] De Waele, B., *Hydrogenering van tolueen in een 3-fase reactor* **Master Thesis** *Ghent University* (2002).

[10] Martens, J. A., Parton, R., Uytterhoeven, L., Jacobs, P. A., and Froment, G. F., *Selective Conversion of Decane into branched Isomers. A Comparison of Pt/ZSM-22, Pt/ZSM-5 and Pt/USY zeolite catalysts* **Appl. Catal.** *76* 95-116 (1991).

[11] Parton, R., Uytterhoeven, L., Martens, J. A., and Jacobs, P. A., *Synergism of ZSM-22 and Y zeolites in the bifunctional conversion of n-alkanes* **Appl. Catal.** *76* 131-142 (1991).

[12] Muñoz, J. A., *Hydroisomerization and Hydrocracking on Zeolites: Shape Selectivity and Kinetics in Liquid Phase* **PhD Thesis** *Ghent University* (2000).

[13] Rautanen, P. A., Aittamaa, J. R., and Krause, A. O. I., *Solvent Effect in Liquid-Phase Hydrogenation of Toluene* **Ind. Eng. Chem. Res.** *39* 4032-4039 (2000).

[14] Madon, R. J., and Iglesia, E., *Catalytic reaction rates in thermodynamically non-ideal systems* **J. Mol. Catal. A Chem.** *163* 189-204 (2000).

[15] Madon, R. J., O'Connell, J. P., and Boudart, M., *Catalytic Hydrogenation of Cyclohexene: Part II. Liquid Phase Reaction on Supported Platinum in a Gradientless Slurry Reactor* **AIChE J.** *24* 904-911 (1978).

[16] Singh, U. K., and Vannice, M. A., *Kinetic and Thermodynamic Analysis of Liquid-Phase Benzene Hydrogenation* **AIChE J.** *45* 1059-1071 (1999).

[17] de Boer, J. H., and Kruyer, S., *Entropy and Mobility of Adsorbed Molecules I. Procedure, Atomic Gases on Charcoal* **Proc. K. Ned. Akad. Wet.** *56* 451-463 (1952).

[18] Bird, R. B., Stewart, W. E., and Lightfoot, E. N., *Transport Phenomena 2nd ed.* **Wiley & Sons** *New York* (2002).

Chapter 9

Simulation of the Hydrocracking of an Aromatic Containing VGO in an Industrial Reactor

The hydrogenation of aromatic components has been incorporated into the fundamental kinetic model used in the industrial hydrocracker simulation model developed before at Ghent University [1-3]. The rate equations used for the hydrogenation of the aromatic components were those obtained from earlier work on toluene hydrogenation kinetics in vapour and liquid phase, vide Chapter 7 and Chapter 8. One hydrogenation rate equation with a unique set of corresponding parameter values was used for all aromatic components. The effect of the structure of the aromatic reactant on its hydrogenation rate is the subject of ongoing research and is to be incorporated in the simulation model in the future.

Simulations have been performed for the hydrocracking of an aromatic containing vacuum gasoil (VGO). The effects of variations in operating conditions was simulated for inlet temperatures in the range 510 K to 530 K, inlet total pressures in the range 10 to 15 MPa and inlet molar hydrogen to hydrocarbon ratios in the range 20 to 30. In all the simulations the hydrogenation of the aromatic components was found to occur in the first decimeters of the reactor. A hot spot in the liquid phase temperature and important temperature differences between the gas and the liquid phase are observed. In the second part of the reactor, i.e., when all aromatic components are hydrogenated, the liquid and gas phase temperature come close to each other at a level far below the liquid phase hot spot temperature.

9.1 Introduction

Simulation models are very useful tools in the design and operation of chemical reactors. The industrial relevance of a kinetic model is determined to an important extent by its ease of incorporation into a reactor model. As a result, kinetic models with a limited number of lumps representing the major product fractions are frequently used. The drawback of such kinetic models is that the model parameters are often feedstock dependent and need to be redetermined upon each change of feedstock. Fundamental kinetic models, on the other hand, account for the underlying chemistry and, hence, have feedstock invariant parameters. However, the complexity of the reaction networks in fundamental kinetic models and the detailed feedstock analysis required limit their applicability. With the relumped single-event model based on the structural class method, vide Chapter 4, a compromize between lumped and fundamental kinetic models has been developed combining the advantages of both types of models. Because of the lumped nature of the model, the ease of incorporation is guaranteed and no highly detailed feedstock analysis is required. Because of a judicious definition of the lumps, vide Chapter 4, the fundamental character of the model and, hence, the feedstock invariance of the model parameters, is preserved.

Until now the relumped model was handling the hydrocracking of alkanes and cyclo-alkanes [2,3]. The hydrogenation of aromatic components had not been included yet. Because the required experimental data have been obtained as a part of this thesis and have lead to a kinetic model for toluene hydrogenation, vide Chapter 7 and Chapter 8, the hydrogenation of aromatic components has now been incorporated in the simulation model for an industrial hydrocracking reactor.

9.2 Simulation Procedures

9.2.1 Operating Conditions, Feedstock, Products and Physical Properties

The operating conditions used in the simulation of the industrial hydrocracking reactor are reported in Table 9-1. Special attention is given to the range of inlet temperatures considered in these simulations, i.e., 510 to 530 K. This is considerably lower than the inlet temperatures used in industrial hydrocracking reactors which are in the range 573 to 723 K, vide Table 1-4. Such high temperatures are required when less active catalysts, e.g., a CoMo or a NiMo metal phase deposited on an amorphous alumina are used instead of the noble metal loaded zeolite used in the current simulations. Moreover, effects of catalyst poisoning are not included in the

Table 9-1 Operating conditions used in the industrial reactor

Inlet Temperature (K)	Inlet Pressure (MPa)	Inlet Molar Hydrogen to Hydrocarbon Ratio (mol mol^{-1})	Aromatic Content[a] (wt%)	Liquid Hourly Space Velocity (m_L^3 (m^3_{cat} $h)^{-1}$)
510 – 530	10 – 15	20 – 30	0 – 30	4.6

[a] The aromatic content in the feedstock was varied using scaling factors for the aromatic and saturated fractions, maintaining the internal composition of these fractions as reported in Table 9-2

simulations. If catalyst poisoning occurs, higher temperatures are required to maintain the desired activity of the catalyst. As a result, modelling results presented in this Chapter for a temperature range from 510 to 530 K using a fresh, i.e., not poisoned, catalyst with a high activity are considered to be representative for industrial units working at higher temperatures but using a partially poisoned or a less active catalyst. Other operating conditions such as total pressure and molar hydrogen to hydrocarbon ratio fall within the range used industrially, vide Table 1-4 and Table 9-1.

The feedstock composition used in the simulation is that of a partially hydrogenated vacuum gasoil (VGO) [4] and is reported in Table 9-2. It has a density of 0.832 kg m^{-3} at 300 K and a boiling point range of 580-750$^+$K. Weight fractions for *n*-alkanes, *iso*-alkanes, mono- to tetra-ring cycloalkanes and mono- to tri-ring aromatics per carbon number were originally reported based on a GC-MS analysis of the saturated and unsaturated fractions being separated using HPLC. Considering a typical ratio for the weight fractions of monomethyl- to dimethylbranched alkanes in a naphtha, kerosine or VGO [4], the *iso*-alkane weight fractions were split according to a 10:1 ratio while the tribranched alkane content is taken to be zero. The total aromatic content amounts to 17.7 wt%. In simulations with varying aromatic content of the feedstock from 0 to 30 wt% the internal composition of the saturated and the aromatic fraction was maintained by using appropriate scaling factors. The highest aromatic feed fractions used in the simulations lead to a maximum adiabatic temperature rise in the liquid phase of about 60 K. However, because of the high value for the gas phase specific heat capacity, vide Section 9.3.1, the adiabatic temperature rise in the reactor due to the hydrogenation of the aromatic feed content is limited to 2 K only.

Physical properties such as the critical temperature, pressure and volume, the standard enthalpy of formation and the Gibbs enthalpy of formation, and the ideal gas specific heat capacity are calculated for the individual components from which mixture properties can be calculated using well-established mixing rules [5,6]. Values for the individual components are taken from literature when available or estimated using group contribution methods such

Table 9-2 Composition of partially hydrogenated VGO [4]

CN	NPA	MPA	DPA	MNA	DNA	TNA	TEN	MAR	DAR	TAR
14	0	0	0	0	0	0	0	1.239	0.047	0
15	0.002	0	0	0	0	0	0	2.331	0.539	0
16	0.016	0.002	0	0.004	0	0	0	2.707	1.506	0
17	0.077	0.002	0	0.032	0.021	0	0	2.319	1.417	0.323
18	0.167	0.035	0.004	0.128	0.131	0.022	0	1.613	0.915	0.689
19	0.365	0.138	0.014	0.339	0.312	0.109	0.018	0.718	0.335	0.189
20	0.729	0.302	0.030	0.614	0.613	0.247	0.196	0.246	0.168	0.117
21	1.014	0.518	0.052	1.030	1.048	0.541	0.447	0.086	0.113	0.070
22	1.427	0.827	0.083	1.465	1.384	0.650	0.723	0.012	0.020	0.010
23	1.558	1.150	0.115	1.923	1.774	0.873	0.793	0	0	0
24	1.863	1.450	0.145	2.379	2.217	1.243	0.873	0	0	0
25	2.073	1.560	0.156	2.786	2.455	1.366	0.693	0	0	0
26	1.646	1.310	0.131	2.594	2.274	1.089	0.533	0	0	0
27	1.274	1.230	0.123	2.380	2.110	0.897	0.439	0	0	0
28	0.900	1.010	0.101	2.067	1.928	0.615	0.395	0	0	0
29	0.538	0.657	0.066	1.551	1.522	0.403	0.235	0	0	0
30	0.343	0.387	0.039	1.152	1.141	0.163	0.118	0	0	0
31	0.183	0.243	0.024	0.712	0.608	0.090	0.082	0	0	0
32	0.115	0.148	0.015	0.405	0.248	0.092	0.060	0	0	0
33	0.040	0.064	0.006	0.236	0.015	0.125	0.047	0	0	0
Sum	14.33	11.06	1.11	21.80	19.80	8.52	5.65	11.27	5.06	1.39

NPA, MPA, DPA: normal, mono- and dibranched alkanes; MNA, DNA, TNA, TEN: mono-, di-, tri- and tetra-ring cycloalkanes; MAR, DAR, TAR: mono-, di-, and tri-ring aromatics

as Joback's, Fedors' and Benson's. The acentric factor is calculated using the Lee-Kesler method [7]. The reaction enthalpy in the liquid phase, the enthalpy of vapourization, the specific heat capacity and density of the liquid and the gas phase and the fugacity coefficients in the liquid and the gas phase are calculated based on the Peng-Robinson equation of state. Binary interaction parameters for hydrogen in hydrocarbon mixtures were obtained from a correlation proposed by Moysan et al. [8] to account accurately for the hydrogen solubility in the hydrocarbons. Liquid and gas phase viscosities were calculated using the method of Brule and Starling [9].

Table 9-3 Reactor geometry, catalyst properties and inlet conditions used in the simulations

Reactor Geometry	
diameter (m)	2.82
length (m)	7.625
Catalyst Properties	
pellet diameter (m)	$1.3\ 10^{-3}$
porosity ($m_f^3\ m_p^{-3}$)	0.65
density ($kg_{cat}\ m_p^{-3}$)	400
mass (kg_{cat})	19 000
bed bulk density ($kg_{cat}\ m_r^{-3}$)	800
porosity ($m_f^3\ m_{cat}^{-3}$)	0.65
tortuosity	3.7

9.2.2 Reactor Model

Three-phase reactors comprising a gas, a liquid and a solid phase, are industrially used for the hydrocracking of petroleum fractions. The solid phase is constituted by the fixed bed of catalyst pellets, while the gas and the liquid phase flow concurrently downward through the reactor. Most of the feed hydrocarbons are contained in the liquid phase together with dissolved gases such as hydrogen and some light, recycle, hydrocarbons. The gas phase is mainly constituted by hydrogen but also contains light, recycle hydrocarbons and some heavier evapourated feed hydrocarbons. In Table 9-3 the reactor geometry and the catalyst properties are reported. Interaction between the gas and the liquid phase can be low, e.g., in a trickle flow regime, or high, e.g., in a pulse, spray or bubble flow regime. For the conditions used, the reactor operates in the transition regime between trickle flow and pulse flow, however, because of the high total pressures trickle flow is more likely [10]. An important issue in multiphase reactors is which interphase contacts occur and to what extent. When operating an industrial reactor in trickle flow regime complete wetting of the catalyst can be expected when the liquid flow rates are sufficiently high [11]. Most correlations for the wetting efficiency have been developed for high pressure and high temperature laboratory trickle bed reactors [11-13]. When applied to the conditions used in simulations performed within the framework of this Chapter these correlations result in values close to unity. Internal contacting, i.e., the interfacial area between the internal surface of the catalyst and the liquid

phase relative to the total internal surface area of the catalyst, is usually equal to unity because of capillary effects [14].

The reactor is modeled using a one-dimensional heterogeneous model with both gas and liquid phase moving in plug flow through the reactor [1,15]. According to Shah et al. [16] the use of such an ideal flow pattern is allowed for industrial trickle bed reactors. Complete wetting of the catalyst may be assumed when the gas and the liquid are adequately distributed [16]. As a result the molar flow rate of gas phase component *i* can only change due to mass transfer from or to the liquid phase. According to the two film model, the flux of component *i* from the vapour phase to the liquid phase can be written as:

$$N_i = K_L\left(\frac{C_{i,G}}{H_i} - C_{i,L}\right) \tag{9.1}$$

with:

$$\frac{1}{K_L} = \frac{1}{k_G H_i} + \frac{1}{k_L} \tag{9.2}$$

the overall mass transfer resistance, which is composed by a gas, $1/k_G H_i$, and a liquid, $1/k_L$, side mass transfer resistence. The mass transfer coefficients are derived from correlations proposed by Sato et al. [17] for the liquid side and by Reiss [18] for the gas side.

Using the expression for the molar flux from the gas to the liquid phase, the continuity equation for a gas phase component *i* is given by:

$$\frac{1}{\Omega}\frac{d\,F_{i,G}}{d\,z} = -K_L a'_v\left(\frac{C_{i,G}}{H_i} - C_{i,L}\right) \qquad i=1,\ldots,n \tag{9.3}$$

with as inlet condition at $z=0$:

$$F_{i,G} = F^0_{i,G} \qquad i=1,\ldots,n \tag{9.4}$$

The liquid phase is in contact with both the gas and the liquid phase. At the conditions used, the mass transfer resistance from the bulk of the liquid to the catalyst surface is considered to be negligible [19]. The continuity equation for the liquid phase component *i* can then be written as:

$$\frac{1}{\Omega}\frac{d\,F_{i,L}}{d\,z} = \rho_B \sum_{j=1}^{n_{reac}} \eta_j S_{j,i} r_j\left(C_{1,L};\ldots;C_{n,L};T_S\right) + K_L a'_v\left(\frac{C_{i,G}}{H_i} - C_{i,L}\right) \qquad i=1,\ldots,n \tag{9.5}$$

with as inlet condition at $z=0$:

$$F_{i,L} = F^0_{i,L} \qquad i=1,\ldots,n \tag{9.6}$$

with $S_{j,i}$ the stoechiometric coefficient matrix. η_j is the effectiveness factor for reaction *j* and is calculated as the ratio of the reaction rate with internal mass transport limitations, obtained

from integration of the intrinsic reaction rate along the radial profile within the catalyst pellet, and the reaction rate in absence of internal mass transport limitations. Catalyst pellets are assumed to be spherical and, hence, the following continuity equation for component *i* inside the catalyst pellet can be written:

$$\frac{D_{i,e}}{\xi^2}\frac{d}{d\xi}\left(\xi^2\frac{dC_{i,S}}{d\xi}\right)=\rho_B\sum_{j=1}^{n_{reac}}S_{j,i}r_j\left(C_{1,S};...;C_{n,S};T_S\right) \qquad i=1,\ldots,n \qquad (9.7)$$

with as boundary conditions:

$$\begin{aligned} &\xi=0 && \frac{dC_{i,S}}{d\xi}=0 \\ &\xi=\frac{d_p}{2} && C_{i,S}=C_{i,L} \end{aligned} \qquad i=1,\ldots,n \qquad (9.8)$$

The liquid phase diffusivities are calculated using the method of Wilke and Chang [20]. From these liquid phase diffusivities, the effective diffusivities inside the catalyst are calculated taking into account the porosity ε_S and the tortuosity τ_S of the catalyst via:

$$D_{i,e}=\frac{\varepsilon_S}{\tau_S}D_i \qquad (9.9)$$

Adiabatic operation of the reactor is assumed. The catalyst pellets are assumed to be isothermal at the same temperature of the liquid phase [19]. Hence, energy balances need only be constructed for the gas and the liquid phase. The energy transfer between gas and liquid phase has two contributions, the first corresponding to conductive heat transfer and the second to enthalpy transfer induced by mass transfer. The energy consumed or released by vapourization or condensation is assumed to come from or to go to the liquid phase [1]. Hence, an appropriate term is to be included in the liquid phase energy balance only. The liquid phase energy balance can be written as follows:

$$\begin{aligned} u_{s,L}\,\rho_L\,C_{p,L}\frac{dT_L}{dz}=\rho_B\sum_{i=1}^{n_{reac}}\eta_i r_i\left(C_{1,L};...;C_{n,L};T_L\right)\left(-\Delta_r H_i^0\right)+h_L a'_v\left(T_I-T_L\right) \\ +\sum_{i=1}^{n}N_i a'_v\,\Delta_v H_i^0+\sum_{i=1}^{n}N_i a'_v\,C_{p,L,i}\left(T_I-T_L\right) \end{aligned} \qquad (9.10)$$

and the energy balance in the gas phase:

$$u_{s,G}\,\rho_G\,C_{p,G}\frac{dT_G}{dz}=h_L a'_v\left(T_G-T_I\right)+\sum_{i=1}^{n}N_i a'_v\,C_{p,G,i}\left(T_G-T_I\right) \qquad (9.11)$$

with as inlet conditions:

$$\begin{aligned} &z=0 && T_L=T_L^0 \\ &z=0 && T_G=T_G^0 \end{aligned} \qquad (9.12)$$

The interface temperature T_I in Eq. (9.10) and Eq. (9.11) is given by:

$$T_I = \frac{h_G a'_v T_G + h_L a'_v T_L}{h_G a'_v + h_L a'_v} \tag{9.13}$$

which follows from the expressions for the conductive heat fluxes q_G and q_L at both sides of the gas-liquid interphase:

$$\begin{aligned} q_G &= h_G (T_G - T_I) \\ q_L &= h_L (T_I - T_L) \end{aligned} \tag{9.14}$$

h_G and h_L are the heat transfer coefficients in the gas and liquid phase derived from the mass transfer coefficients using the Chilton-Colburn analogy [21]:

$$\begin{aligned} h_G a'_v &= k_G a'_v \rho_G C_{p,G} \left(\frac{Sc_G}{Pr_G} \right)^2 \\ h_L a'_v &= k_L a'_v \rho_L C_{p,L} \left(\frac{Sc_L}{Pr_L} \right)^2 \end{aligned} \tag{9.15}$$

in which *Sc* and *Pr* are the Schmidt and the Prandtl number.

The total pressure drop is calculated from a momentum balance in terms of the single phase pressure drop using Larkins' equation [22]:

$$-\frac{d\, p_t}{d\, z} = (\delta_L + \delta_G) 10^{\left(\frac{0.416}{\left(\log_{10} \sqrt{\frac{\delta_L}{\delta_G}} \right)^2 + 0.666} \right)} \tag{9.16}$$

with as inlet condition:

$$z = 0 \qquad p_t = p_t^0 \tag{9.17}$$

The single phase pressure drops δ_L and δ_G are calculated with the Ergun equation [15].

9.2.3 Kinetic Model

The hydrogenation of aromatic components is incorporated in the earlier developed simulation model for an industrial reactor [1,2]. The reaction network is extended with the hydrogenation of the aromatic pseudo components to the corresponding cycloalkane pseudo components as vizualized in Figure 9-1. Although no tetra-ring aromatic components are contained in the partially hydrogenated VGO, the hydrogenation of tetra-ring aromatic components has been included for the completeness of the reaction network. Because of the high hydrogenation rates compared to acid catalyzed reaction rates, the aromatic components are assumed to be susceptible to any acid catalyzed rearrangement or cracking reaction only

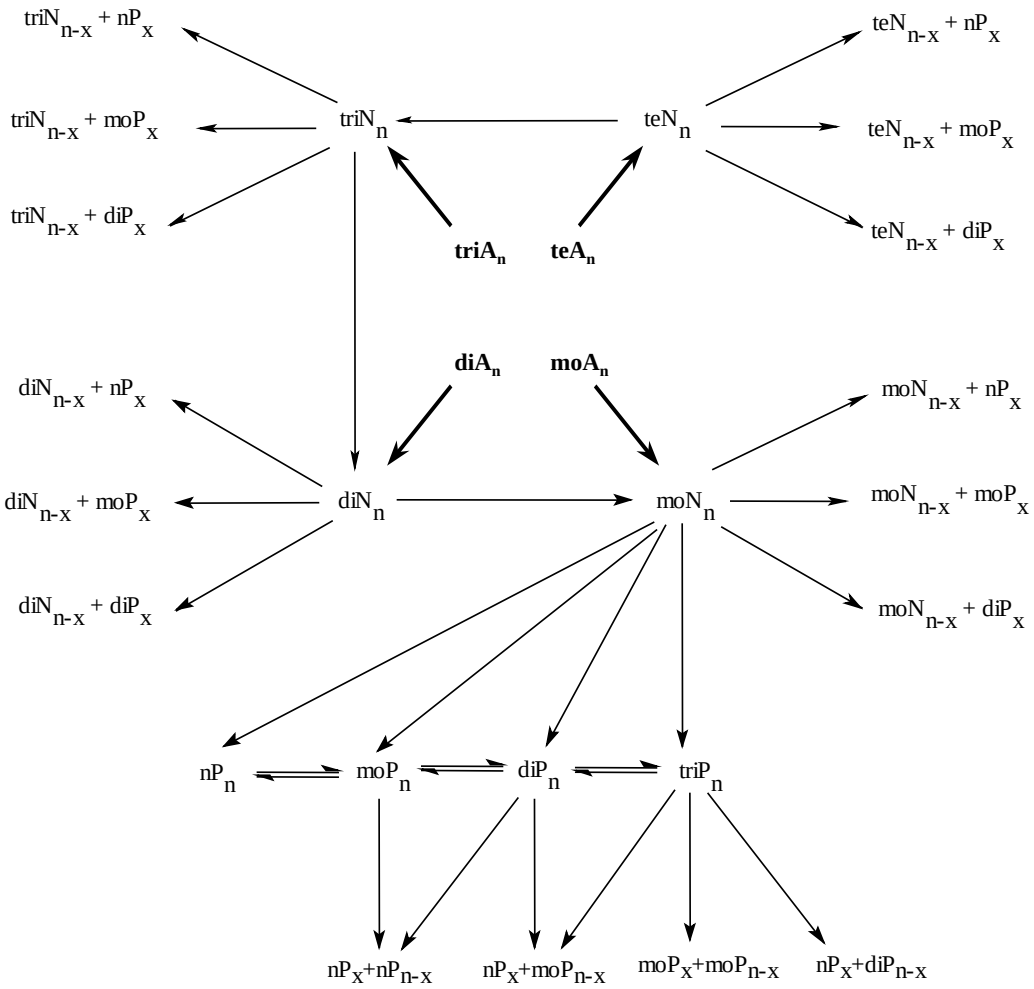

Figure 9-1 Reaction network for hydrocracking of a VGO containing aromatic molecules (newly added reactions are indicated in bold)

after complete saturation. As a consequence cycloalkylaromatic components only occur in the model as intermediates in the hydrogenation sequence of the corresponding aromatic molecule to the corresponding cycloalkane, i.e., no corresponding continuity equations on reactor level are considered.

The rate equation used for hydrogenation is that obtained for toluene hydrogenation adapted to be applicable under liquid phase conditions, vide Chapter 7 and Chapter 8:

$$r_{hyd,A_i} = \frac{C_t k_{surf}}{\left(B^3+B^2+B+1\right)} \frac{B^3 K_{A_i}^f \Phi_{A_i}^L p_t V_m^L C_{A_i}^L \sqrt{K_{H_2}^f \Phi_{H_2}^L p_t V_m^L C_{H_2}^L}}{\left(1+\sqrt{K_{H_2}^f \Phi_{H_2}^L p_t V_m^L C_{H_2}^L}+\sum_{j=1}^{n_{aro}} \frac{K_{A_j}^f \Phi_{A_j}^L p_t V_m^L C_{A_j}^L \left(1+2B+3B^2+4B^3\right)}{B^3+B^2+B+1}\right)^2} \quad (9.18)$$

with:

$$B = K_{surf} \sqrt{K_{H_2}^f \Phi_{H_2}^L p_t V_m^L C_{H_2}^L} \quad (9.19)$$

Compared to Eq. (8. 19) the chemisorption term in the denominator of Eq. (9.18) accounts for the presence of several aromatic components via the summation over all aromatic components instead of the pure aromatic component used in Chapter 7 and Chapter 8. The same rate equation and parameter values are used for all aromatic components. Possible substituent effects and multiple aromatic ring effects are the subject of current research activities at Ghent University and will be incorporated in a further stage.

The reaction network and corresponding rate equations for saturated molecules are identical to those used by Martens and Marin [2,3]. The rate equations for saturated molecules are obtained using the relumped single-event model in which the relumping coefficients are calculated with the structural class based method as discussed in Chapter 4. The adaptation of the model to be applicable under liquid phase conditions is identical to that described in Chapter 8. The details of this adaptation for the acid catalyzed reactions and corresponding relumped methodology are reported by Martens and Marin [2] and by Martens [3].

9.2.4 Integration Methods

The set of ordinary differential equations constituted by the mass, energy and momentum balances in the axial direction is solved using Gear's method [23]. Although the overall mass balance allows to eliminate one of the individual mass balances, all individual mass balances are solved simultaneously, using the overall mass balance as controll only.The intraparticle integration in the calculation of the effectiveness factors is performed with an orthogonal spline collocation method [24]. The initial guess of the intraparticle concentration profiles is updated using a Newton-Raphson method until the required accuracy is obtained. The codes for both integration routines have been implemented based on '*Numerical Recipes'* [25].

The simulations were performed on a desktop PC equipped with a Pentium IV 1 GHz processor and required between 10 and 90 CPU minutes. The calculation of the effectiveness factors is the main CPU time consuming part of the simulation model since reactor simulations with all effectiveness factors fixed to *one* require only a few minutes CPU time.

9.3 Simulation Results and Discussion

9.3.1 Simulation of the Hydrocracking of an Aromatic Component Containing VGO

The hydrogenation of aromatic components is a highly exothermic reaction. As a result, considerable temperature effects are expected when feedstocks contain a non-negligible

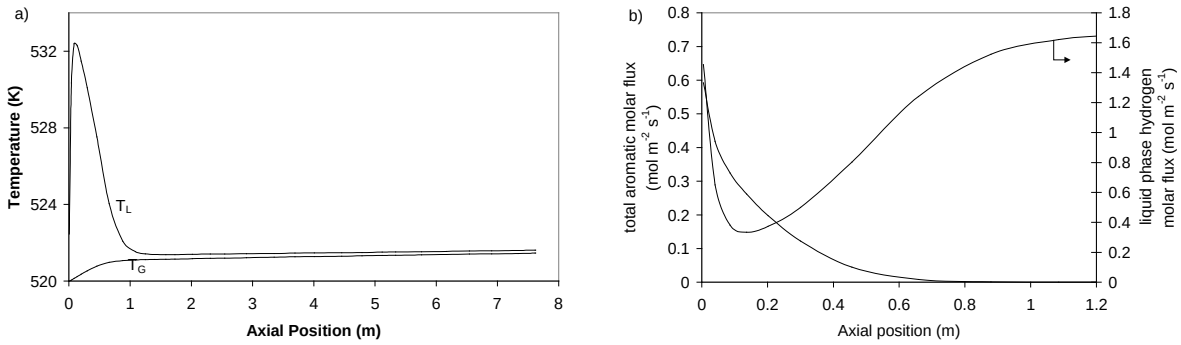

Figure 9-2 **Profiles obtained with a 10 wt% aromatic feed content for a) the liquid, T_L, and the gas, T_G, phase temperature and b) the total aromatic and liquid phase hydrogen molar flux as a function of the axial position in the reactor at 520 K, 12 MPa and a hydrogen to hydrocarbon ratio of 25**

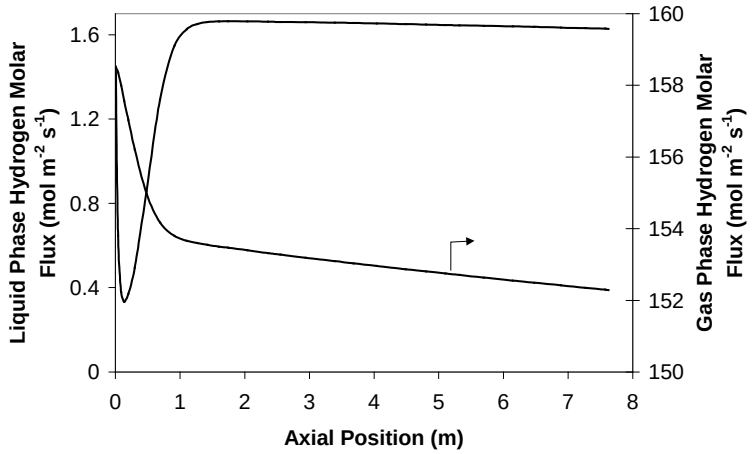

Figure 9-3 **Liquid and gas phase hydrogen molar flux (full lines) as a function of the axial position in the reactor at 520 K, 12 MPa and a hydrogen to hydrocarbon ratio of 25**

aromatic fraction. The simulated gas and liquid phase temperature profiles through the reactor are shown in Figure 9-2a for a temperature of 520 K, a total pressure of 12 MPa and a molar hydrogen to hydrocarbon ratio of 25. The aromatic feed content in this simulation was 10 wt% and was obtained from the original 17.7 wt% by using the appropriate scaling factors, vide Section 9.2.1 and Table 9-1. A higher hydrogen to hydrocarbon ratio is used compared to that used by Martens and Marin [2,3], i.e., 25 compared to 14, because of the considerable hydrogen consumption by the hydrogenation reactions that have been incorporated in this thesis.

An immediate, steep liquid phase temperature rise is observed. A hot spot is reached within the first two decimeter of the reactor, vide Figure 9-2a. Because of the severe decrease in

availability of the hydrogenation reactants, both hydrogen and aromatics, vide Figure 9-2b, the hydrogenation rate decreases. As a consequence the thermal power generated by hydrogenation is reduced and, at the hot spot, i.e., the point of maximum liquid phase temperature, becomes lower than the thermal power transferred from the liquid to the gas phase resulting in a decrease of the liquid phase temperature. In the region of decreasing liquid phase temperature the residual aromatic fraction is hydrogenated and the gas phase temperature increases. The entire aromatic fraction is hydrogenated after 0.6 to 0.8 m and an almost constant difference of about 0.2 K between the gas and liquid phase temperature is established after 1 to 2 meter. Also after 1 to 2 meter the temperature in the reactor is only slightly higher than the inlet temperature because the thermal power generated by hydrogenation is transferred to the vapour phase to a large extent. This is caused by the comparable mass flows in the liquid and the gas phase and the high specific heat capacity of the gas phase compared to the liquid phase. The high gas phase specific heat capacity results from the very low molecular weight of the gas phase molecules compared to the liquid phase molecules. This results in a very moderate temperature effect compared to the inlet temperature after the effect of the aromatic hydrogenation has disappeared. When the constant temperature difference of about 0.2 K between gas and liquid phase is established, a moderate increase of gas and liquid temperature is observed corresponding to the overall exothermicity of the actual hydrocracking process, i.e., without the hydrogenation of aromatic reactants. This constant temperature difference of 0.2 K between the gas and the liquid phase is significantly lower than that of 2.5 K reported by Martens and Marin [2] but can, however, be attributed to the lower hydrocracking severity used in the current simulation, i.e., 520 K, 12 MPa and a molar hydrogen to hydrocarbon ratio of 25, compared to severity used in the simulation by these authors, i.e., 540 K, 12 MPa and a molar hydrogen to hydrocarbon ratio of 14. Differences in gas phase superficial velocities because of the different molar hydrogen to hydrocarbon ratios also contribute to the lower temperature difference between the gas and the liquid phase observed in this work compared to that observed by Martens and Marin [2,3].

Figure 9-3 shows the gas and the liquid phase hydrogen molar fluxes as a function of the axial position in the reactor. The gas phase hydrogen molar flux continuously decreases. It decreases fast in the first meter of the reactor, which is the part of the reactor where the hydrogenation of the aromatic components occurs and then decreases more moderately corresponding to the hydrogen consumed in the actual hydrocracking process. The liquid phase hydrogen molar flux decreases sharply in the first two decimeter of the reactor where hydrogen is consumed much faster by hydrogenation than it can be supplied to the liquid

phase from the gas phase. When a considerable fraction of the aromatic components have been hydrogenated, i.e., after 0.2 to 0.4 m, the hydrogen availability in the liquid phase recovers from the fast initial depletion and the amount of hydrogen absorbed in the liquid phase tends to equilibrium after 1 to 2 m.

9.3.2 Effect of the total aromatic feed content

The effect of variations in the total aromatic feed content on the behaviour of the industrial hydrocracking reactor was simulated at 520 K, 12 MPa and a molar hydrogen to hydrocarbon ratio 25 for an aromatic feed content ranging from 0 to 30 wt%. The corresponding temperature profiles, liquid phase hydrogen molar flux profiles and total aromatic molar flux profiles are shown in Figure 9-4a, b and c. It can be observed from Figure 9-4a that a higher total aromatic feed fraction leads to higher liquid phase hot spot temperatures. The increase in liquid phase hot spot temperature is, however, limited to about 16 K for the higher total aromatic feed fractions, i.e., 20 and 30 wt%. For those higher aromatic feed fractions a shoulder is developed in the peak of the liquid phase temperature profile. The development of such a shoulder depends on which of the two hydrogenation reactants, i.e., hydrogen or the aromatic components, is depleted first. In the case of a low aromatic feed content, i.e., 5 to 10 wt%, a hydrogen excess is still available in the liquid phase when the aromatic components are getting depleted. When the hydrogenation reactions are slowing down because of reactant depletion, the hydrogenation rate tends to *zero* and the hydrogen in the liquid phase recovers from the fast initial depletion In the case of higher aromatic feed fractions, however, liquid phase hydrogen is the limiting reactant. After the initial hydrogen depletion, as long as a considerable amount of aromatic components is left, the hydrogen transfer from vapour to liquid phase is rate-limiting in the hydrogenation mechanism. Hence, when the hydrogenation is slowed down because of reactant depletion, the rate does not immediately drop to *zero*, but to a rate corresponding to the rate of hydrogen transfer between the gas and the liquid phase. As a result also the thermal power generated by hydrogenation is not dropping to *zero* but to a level corresponding to the interphase hydrogen transfer rate, leading to the shoulder observed in the temperature profiles shown in Figure 9-4a for a high aromatic feed content.

Figure 9-4b shows the liquid phase hydrogen molar flux profiles through the reactor. The steep initial decrease corresponds to the development of the liquid phase hot spot temperature. When the aromatic components are becoming the limiting reactant, the liquid phase hydrogen molar flux and corresponding concentration increases rapidly to a value close to the saturation value. In the case of low aromatic feed content, the liquid phase hydrogen molar flux recovers

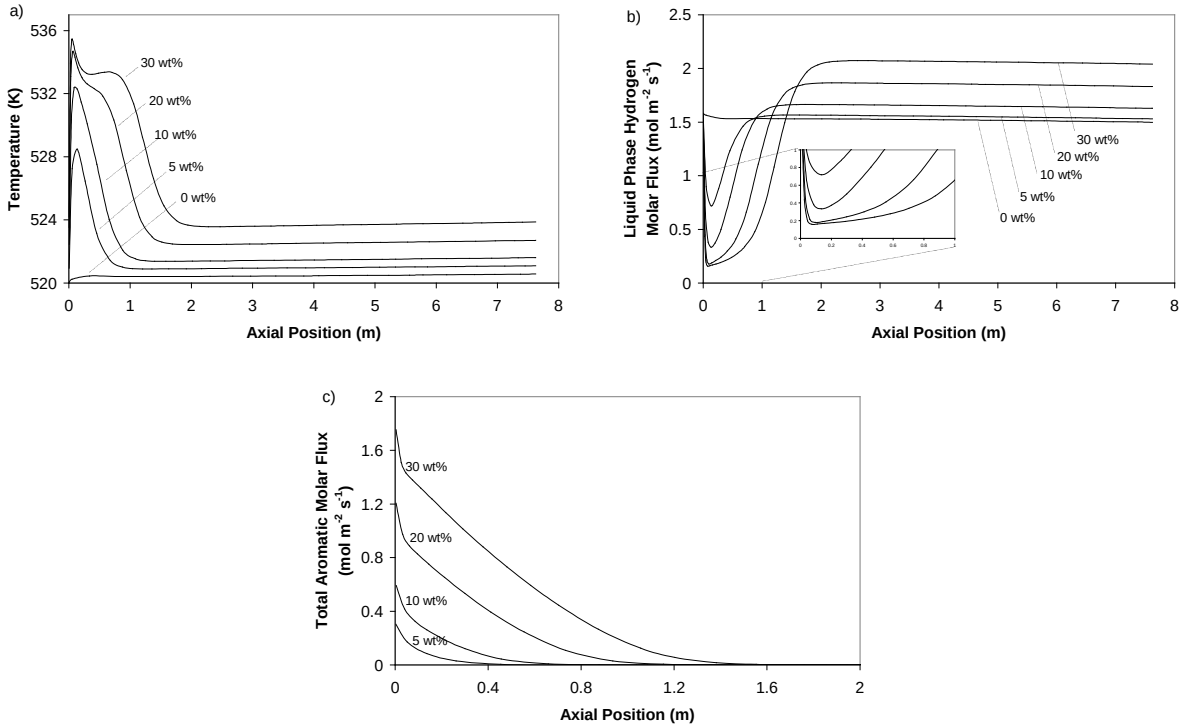

Figure 9-4 **Effect of the total aromatic feed content on: a) the liquid phase temperature, b) the liquid phase hydrogen molar flux and c) the total aromatic molar flux as a function of the axial position in the reactor at 520 K, 12 MPa and a hydrogen to hydrocarbon ratio of 25**

immediately after the initial depletion. However, in the case of a high aromatic feed content, an intermediate region of practically constant liquid phase hydrogen molar flux is developed, corresponding to the regime in which the interphase hydrogen transfer is the rate-limiting step. The differences in liquid phase hydrogen molar fluxes in the second part of the reactor can be attributed to the differences in simulated temperatures. The higher the total aromatic feed fraction and, hence, the higher the temperature in the second part of the reactor, the higher the hydrogen solubility and corresponding hydrogen molar flux in the liquid phase.

Figure 9-4c shows the total aromatic molar flux profiles through the first part of the reactor. The profiles for the low aromatic feed content show an exponential decrease which is expected in the case of reactant disappearence via first order kinetics. The profiles for the high aromatic feed content show a strong initial decrease followed by a more moderate linear decrease. Ultimately the linear decrease of the total aromatic molar flux passes into an exponential decrease. This profile corresponds to the different regimes discussed above in this section. The fast initial decrease of the total aromatic molar flux corresponds to the part of the reactor where none of both reactants is limiting. The moderate linear decrease corresponds to a region where the disappearance of the aromatic components occurs via zero order kinetics,

i.e., the regime where the interphase hydrogen transfer rate is rate-limiting. Ultimately, the aromatic components become the limiting reactant and an exponential decrease similar to the case of the low aromatic feed content is established.

9.3.3 Effect of the Process Conditions

a Total Pressure Effect

The effect of the total pressure was simulated at three different total pressures, i.e., 10, 12 and 15 MPa at 520 K and a molar hydrogen to hydrocarbon ratio 25. Almost no effect of the total pressure on the residue, i.e., C_{18}^{+}, conversion is observed, vide Table 9-4. This results from the opposite effect of the total pressure on the rates of the hydrogenation and the hydrocracking reactions. Hydrogenation rates increase with the total pressure because of the higher hydrogen solubility in the liquid phase at higher total pressures and the positive hydrogen partial reaction order at the conditions used, while *ideal* hydrocracking rates decrease with the total pressure, vide Chapter 3 and simulation results by Martens and Marin [2]. The higher hydrogen solubility at higher total pressures is evident from Figure 9-5a and the corresponding higher hydrogenation rates lead to higher liquid phase peak temperatures, vide, Figure 9-5b. The higher hydrogenation rates at higher total pressures are also reflected by the move towards the beginning of the reactor of the axial position where the total aromatic molar flux drops below 10^{-6} mol m^{-2} s^{-1}, vide Table 9-4. In the second part of the reactor, where all aromatic components are already saturated, higher hydrocracking rates and correspondingly higher C_{18}^{+} conversions are obtained for lower total pressures. For the length of the reactor and the conditions used in the current simulations these two opposite effects almost cancel out and lead to a C_{18}^{+} conversion practically independent from the total pressure.

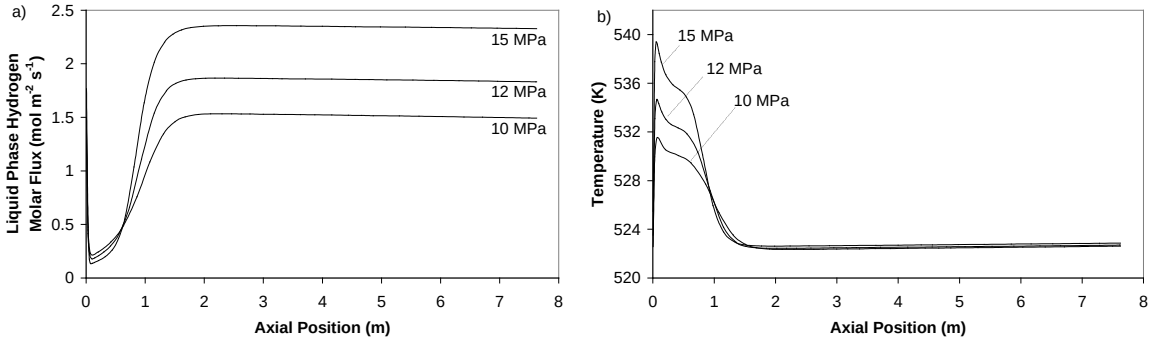

Figure 9-5 Effect of the total pressure on a) the liquid phase hydrogen molar flux and b) the liquid phase temperature as a function of the axial position in the reactor at 520 K and a hydrogen to hydrocarbon ratio of 25

Table 9-4 **Effect of the total pressure on the C_{18}^+ conversion at 520 K and a hydrogen to hydrocarbon ratio of 25**

total pressure (MPa)	10	12	15
C_{18}^+ conversion (wt%)	45.3	43.5	43.4
axial position (m) where total aromatic molar flux drops below 10^{-6} mol m^{-2} s^{-1}	2.8	2.2	1.5

Table 9-5 **Effect of the temperature on the C_{18}^+ conversion and hydrogen consumption at 12 MPa and a hydrogen to hydrocarbon ratio of 25**

Temperature (K)	510	520	530
C_{18}^+ Conversion (wt%)	28.1	43.5	70.6
Hydrogen Consumption (mol s^{-1})	59.8	67.3	80.7

b Inlet Temperature Effect

The effect of the inlet temperature was simulated at three different temperatures, i.e., 510 K, 520 K and 530 K, a total pressure of 12 MPa and a molar hydrogen to hydrocarbon ratio 25. As expected, the C_{18}^+ conversion increases with the inlet temperature. As a result, also the hydrogen consumption increases with the inlet temperature, vide Table 9-5. The liquid phase temperature profile and the liquid phase hydrogen molar flux profile through the reactor are very similar at all inlet temperatures, vide Figure 9-6. For higher inlet temperatures, the liquid phase temperature rise is 0.5 to 1 K higher. The thermal power generation by hydrogenation increases faster with the inlet temperature than the heat transfer to the gas phase. The higher total conversion at higher inlet temperatures leads to higher differences between the liquid

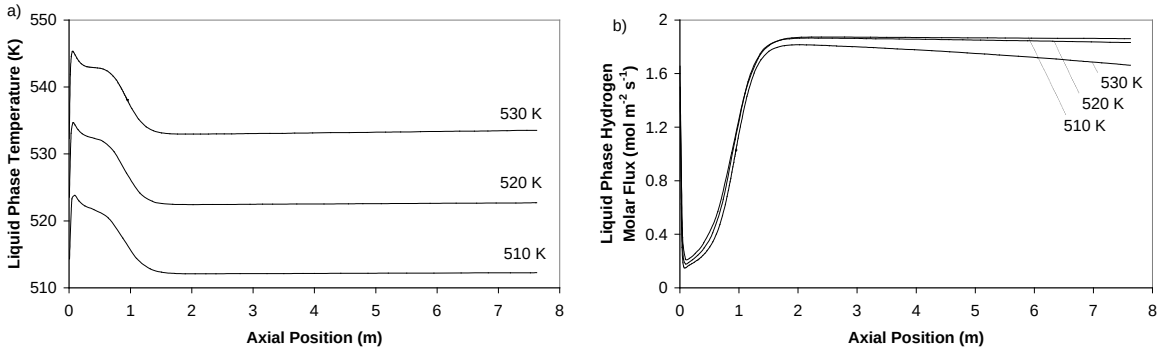

Figure 9-6 **Effect of the inlet temperature on a) the liquid phase temperature and b) the liquid phase hydrogen molar flux as a function of the axial position in the reactor at 12 MPa and a hydrogen to hydrocarbon ratio of 25**

phase temperature at the reactor in- and outlet. The latter effect is, however, limited to about 0.5 to 1 K. The higher hydrogen consumption at higher inlet temperatures is reflected by the lower liquid phase hydrogen molar flux at the outlet of the reactor.

c Hydrogen to Hydrocarbon Ratio Effect

Three different hydrogen to hydrocarbon ratios were used, i.e., 20, 25 and 30, to investigate the effect on the simulation results at 520 K and 12 MPa. A moderate decrease of the C_{18}^{+} conversion with increasing hydrogen to hydrocarbon ratio is observed, vide Table 9-6. Similarly to the total pressure effect, the hydrogen to hydrocarbon ratio has an opposite effect on the hydrogenation and hydrocracking reactions. The rates of the hydrocracking reactions decrease because the (de)-hydrogenation equilibrium tends more to the side of the saturated components when more hydrogen is present, resulting in lower concentrations of unsaturated components and carbenium ions. Because these carbenium ions are the reactants in the rate-determining acid catalyzed steps in hydrocracking, the rate of the hydrocracking reactions decreases. The rate of the hydrogenation reactions increases with the hydrogen availability as can be observed in Figure 9-7a, showing the total aromatic molar fluxes through the reactor. The higher the hydrogen to hydrocarbon ratio, the closer to the inlet of the reactor the aromatic components are depleted. In the second part of the reactor the hydrogen availability in the liquid phase is reversed compared to the first part of the reactor, vide Figure 9-7b. This apparent contradictory result originates from the differences in temperature profiles through the reactor with varying hydrogen to hydrocarbon ratio, vide Figure 9-7c. Because of the lower gas phase superficial velocities with lower hydrogen to hydrocarbon ratios, less heat will be removed from the liquid phase, resulting in the higher liquid phase temperatures observed for lower hydrogen to hydrocarbon ratios. As a consequence of the higher liquid phase temperature, the hydrogen solubility in the liquid phase will be higher for lower hydrogen to hydrocarbon ratios in the second part of the reactor. The decrease in hydrocracking rates because of a higher hydrogen concentration in the liquid phase is,

Table 9-6 Effect of the hydrogen to hydrocarbon ratio on the C_{18}^{+} conversion and hydrogen consumption at 520 K and 12 MPa

Molar Hydrogen to Hydrocarbon Ratio (mol mol^{-1})	20	25	30
C_{18}^{+} Conversion (wt%)	46.7	43.5	41.4

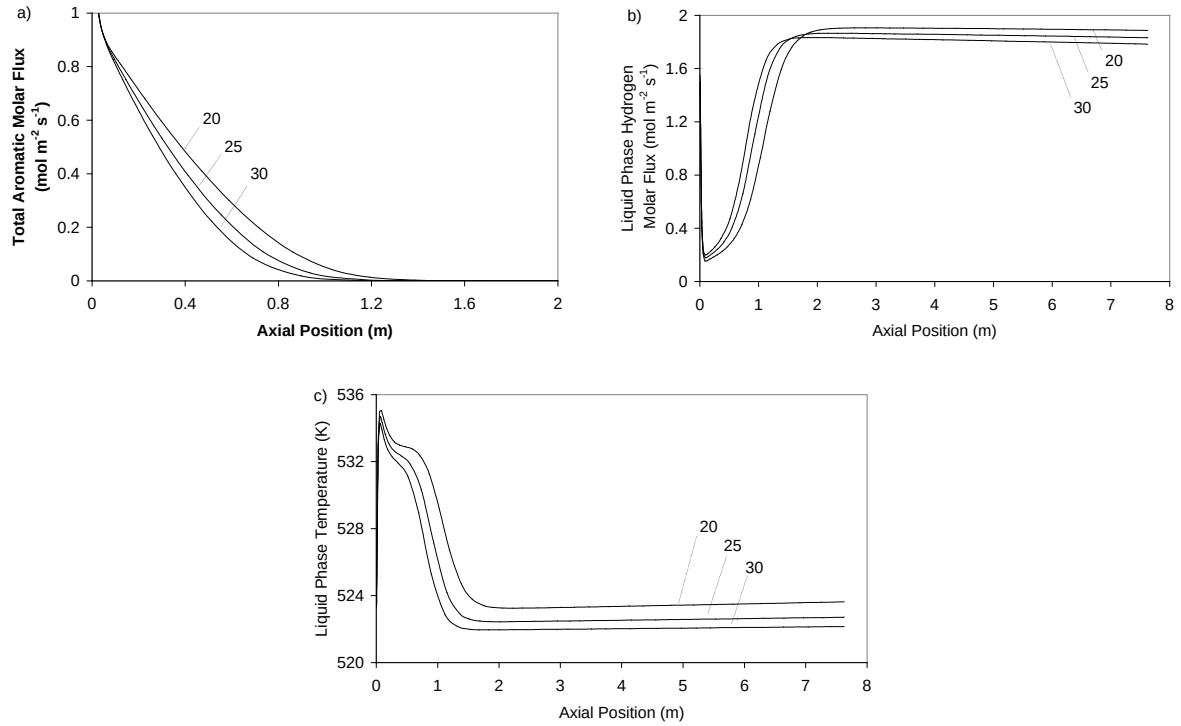

Figure 9-7 Effect of the hydrogen to hydrocarbon ratio on a) the total aromatic molar flux b) the liquid phase hydrogen molar flux and c) the liquid phase temperature as a function of the axial position in the reactor at 520 K and 12 MPa

however, overcompensated by the higher liquid phase temperature. As a consequence, higher C_{18}^{+} conversions are obtained using lower hydrogen to hydrocarbon ratios, vide Table 9-6.

9.4 Conclusions

An existing fundamental kinetic model for hydrocracking of (cyclo)-alkanes has been extended to aromatic components and was used in an adiabatic multiphase fixed bed reactor model for the hydrocracking of an aromatic containing VGO. Parameter values that have been obtained based on vapour phase hydrogenation kinetics and that have been compared to liquid phase hydrogenation kinetics, allowed to simulate the hydrogenation behaviour of the aromatic content of complex feedstock such as a vacuum gas oil.

The simulations revealed that in the first decimeters of the reactor a hot spot occurs. In this part of the reactor, hydrogen consumption is high and the hydrogen absorption in the liquid phase is far from equilibrium. For higher aromatic feed contents, hydrogen absorption in the liquid phase may be so far from equilibrium that the interphase hydrogen transfer from gas to liquid phase becomes the rate-limiting step in the hydrogenation of the aromatic components. The simulation of the effect of the operating conditions on the hydrocracking behaviour show

that a fundamental kinetic model, such as the one used in this thesis, is a powerful tool in the design and the operation of industrial hydroconversion units for the production of environmentally friendly fuels in general and for low aromate fuels in particular.

9.5 References

[1] Froment, G. F., Depauw, G. A., and Vanrysselberghe, V., *Kinetic Modelling and Reactor Simulation in Hydrodesulfurization of Oil Fractions* **Ind. Eng. Chem. Res.** *33* 2975-2988 (1994).

[2] Martens, G. G., and Marin, G. B., *Kinetics for Hydrocracking Based on Structural Classes: Model Development and Application* **AIChE J.** *47* 1607-1622 (2001).

[3] Martens, G., *Hydrocracking on Pt/US-Y zeolites: fundamental kinetic modelling and industrial reactor simulation* **PhD Thesis** *Ghent University* (2000).

[4] Hillewaert L, *De Thermische Kraking van Gasoliën, Experimentele Studie en Modellering* **PhD Thesis** *Ghent University* (1986).

[5] Perry, R. H., Green, D. W., and Maloney, J. O., *Perry's Chemical Engineer's Handbook 6th ed.* **McGraw-Hill** *New York* (1984).

[6] Poling, B. E., Prausnitz, J. M., and O'Connell, J. P., *The Properties of Gases and Liquids 5th ed.* **McGraw-Hill** *New York* (2000).

[7] Lee, B. I., and Kesler, M. G., *A Generalized Thermodynamic Correlation Based on Three-Parameter Corresponding States* **AIChE J.** *21* 510-527 (1975).

[8] Moysan, J. M., Huron, M. J., Paradowski, H., and Vidal, J., *Prediction of the Solubility of Hydrogen in Hydrocarbon Solvents Through Cubic Equations of State* **Chem. Eng. Sci.** *38* 1085-1092 (1983).

[9] Brule, M. R., and Starling, K. E., *Thermophysical Properties of Complex Systems: Applications of Multiproperty Analysis* **Ind. Eng. Chem. Process. Des. Dev.** *23* 833-845 (1984).

[10] Wammes, W. J. A., Mechielsen, S. J., and Westerterp, K. R., *The transition between Trickle Flow and Plug Flow in a Cocurrent Gas-Liquid Trickle-Bed Reactor at Elevated Pressures* **Chem. Eng. Sci.** *45* 3149-3158 (1990).

[11] Al-Dahhan, M. H., and Dudukovic, M. P., *Catalyst Wetting Efficiency in Trickle Bed Reactors at High Pressure* **Chem. Eng. Sci.** *50* 2377-2389 (1995).

[12] Ruecker, C. M., and Akgerman, A., *Determination of Wetting Efficiency for a Trickle-Bed Reactor at High Temperatures and Pressures* **Ind. Eng. Chem. Res.** *26* 164-166 (1987).

[13] Ring, Z. E., and Missen, R. W., *Trickle-Bed Reactors: Tracer Study of Liquid Hold-Up and Wetting Efficiency at High Temperature and Pressure* **Can. J. Chem. Eng.** *69* 1016-1020 (1991).

[14] Al-Dahhan, M. H., Larachi, F., Dudukovic, M. P., and Laurent, A., *High-Pressure Trickle-Bed Reactors: A Review* **Ind. Eng. Chem. Res.** *36* 3292-3314 (1997).

[15] Froment, G. F., and Bischoff, K. B., *Chemical Reactor Analysis and Design 2nd ed.* **J. Wiley,** *New York* (1990).

[16] Shah, Y. T., *Gas-Liquid-Solid Reactor Design* **McGraw-Hill,** *New York* (1979).

[17] Sato, Y., Hirose, H., Takahashi, F., and Toda, M., *Performance of fixed bed catalytic reactor with cocurrent gas-liquid downflow* **1st Pacific Chem. Eng. Congr.** 187 (1972).

[18] Reiss, L. P., *Cocurrent gas-liquid contacting in packed bed columns* **Ind. Eng. Chem. Process. Des. Dev.** *6* 486-498 (1967).

[19] Berger, R. J., Stitt, E. H., Marin, G. B., Kapteijn, F., and Moulijn, J. A., *Chemical reaction kinetics in practice* **CATTECH** *5* 30-60 (2001).

[20] Wilke, C. R., and Chang, P., *Correlations of Diffusion Coefficients in Dilute Solutions* **AIChE J.** *1* 264-270 (1955).

[21] Chilton, T. H., and Colburn, A. P., *Mass Transfer (Absorption) Coefficients. Predictions from Data on Heat Transfer and Fluidum Friction* **Ind. Eng. Chem.** *26* 1183-1187 (1934).

[22] Larkins, R. P., White, R. R., and Jeffrey, D. W., *Two-Phase Concurrent Flow in Packed Beds* **AIChE J.** *47* 231-239 (1961).

[23] Lapidus, L, and Seinfeld, J. H., *Numerical Solutions of Ordinary Differential Equations* **Academic Press** *New York and London* (1971).

[24] Villadsen, J., and Michelsen, M. C., *Solution of Differential Equation Models by Polynomial Approximation* **Prentice Hall** *New Jersey* (1978).

[25] Press, W. H., Teukolsky, S. A., Vetterling, W. T., and Flannery, B. P., *Numerical Recipes* **Camebridge University Press** *Camebridge* (1992).

Chapter 10

Conclusions

The work performed within the framework of this thesis fitted into the ongoing research activities on hydrocracking at the Laboratorium voor Petrochemische Techniek at Ghent University. New subjects such as the hydrogenation of aromatic components in vapour and liquid phase and the detailed carbon number dependence of the single-event kinetic parameters for low carbon numbers have been treated, while other existing subjects such as *non ideal* hydrocracking and the catalyst dependence of the single-event kinetic parameters have been further explored and refined.

The effects of operating conditions on the ideality of the hydrocracking behaviour have been analyzed based on rate equations accounting for potentially rate-limiting reaction steps on the metal and the acid sites. The effects of the operating conditions on the relative importance of the different terms in these rate equations reflect the corresponding effects on the hydrocracking behaviour. The effect of the total pressure, the temperature, the molar hydrogen to hydrocarbon ratio, the reactant's carbon number and the feedstock composition on the ideality of the hydrocracking behaviour can be explained using these rate equations.

The catalyst and carbon number dependence of the single-event rate parameters can be related to the alkene standard protonation enthalpy. For reactant carbon numbers higher than *eight* no differences in standard protonation enthalpy occur, while for lower carbon numbers the standard protonation enthalpy is significantly less negative. Upon dealumination of a Y-zeolite the strength of the acid sites, measured using the alkene standard protonation enthalpy, first increases (Si/Al_F 2.6 $\rightarrow$ 18) and subsequently decreases at high degrees of dealumination (Si/Al_F 18 $\rightarrow$ 60). The effect of the reactant's carbon number and the strength of the acid sites on the alkene standard protonation enthlapy is additive.

Kinetic model development for toluene hydrogenation has been performed based on experimental data, literature information and quantumchemical calculations. One of the major findings was that, in contrast to homogeneous aromatic component hydrogenation in the vapour phase, the resonance stabilization does not lead to the first H atom addition as rate-determining step on a platinum surface. The platinum catalyzed hydrogenation of aromatic components proceeds via a reaction mechanism with equal rate coefficients for the first four hydrogen atom addition steps and quasi equilibration for the last two hydrogen atom additions. The occurrence of dehydrogenated surface species seems very unlikely and has not been accounted for.

A kinetic model for toluene hydrogenation in the liquid phase can be constructed describing the *real* liquid as a deviation from an ideal gas at 1 bar instead of a deviation from an ideal liquid. The former description makes the comparison of the results obtained in the liquid phase with those obtained in the vapour phase much easier. Comparison of vapour with liquid phase kinetics based on fugacities for describing the chemisorption indicates that interactions between chemisorbed species and non chemisorbed fluid molecules have to be accounted for.

The hydrogenation of aromatic components has to be accounted for in order to simulate adequately industrial hydrocracking reactors. The corresponding exothermic effects lead to a hot spot in the first decimeter of the reactor. Moreover, the simulation model for an industrial reactor based on fundamental kinetics provides a powerful tool for the design and optimization of hydroconversion units for the production of fuels meeting the evermore stringent specifications on aromate content.

Further progress on these subjects is of course possible and desirable. The modelling of *non ideal* hydrocracking on a fundamental level is a challenge to be addressed, certainly when the modelling of complex feedstock hydrocracking under industrial operating conditions is aimed at. In this respect an assessment of the carbenium ion concentrations in hydrocracking is required.

The introduction of shape selectivity in single-event modelling is another challenging aspect to be addressed. Plenty of experimental hydrocracking data on Pt/H-ZSM-22 are available but only the first steps in the single-event kinetic modelling of these experiments have been taken, i.e., the pore mouth catalysis in *n*-octane hydrocracking. Next steps include the description of key-lock catalysis, accounting for the cycloalkane hydrocracking behaviour on Pt/ZSM-22, accounting for liquid phase aspects on the shape-selective effects on Pt/H-ZSM-22…

The research with respect to the hydrogenation of aromatic components has been limited in this thesis to toluene hydrogenation. For an adequate quantitative description of the

conversion of the aromatic fraction in a complex feedstock the effect of branched and di- and multi-ring structures needs to be included. Experiments with other model components have already been performed and are expected to provide the necessary information.

To increase the fundamental level of the kinetic modelling of (de)-hydrogenation reactions a single-event model for metal catalyzed reactions should be developed. At least one of the requirements discussed in Chapter 6, i.e., the availability of experiments with more than one model component is fulfilled by now.

Appendix A

Tools in Three-Phase Reactor Simulation and Data Treatment

In addition to the procedures for three-phase reactor simulation and data treatment discussed in Chapter 2, some more detail is provided concerning the calculation of the nitrogen to hydrogen ratio in the gas effluent and the flashed gas effluent and the calculation of the vapour liquid equilibrium.

A.1 Molar Nitrogen to Hydrogen Ratio

The nitrogen in the effluent streams could not be detected in the chromatographic analyses. The FID-detector used for the quantification of the hydrocarbon content is insensitive for nitrogen and on the TCD-detector used for the determination of the hydrogen to methane ratio, nitrogen is used as carrier gas. Selection of another carrier gas, such as helium, would lead to a sensitivity decrease of the detector because of the thermal conductivities of the components involved.

The molar nitrogen to hydrogen ratios in the gas and flashed gas effluent were determined based on an ASPEN [1] flowsheet simulation of the three-phase set-up, vide Figure A - 1. In the case presented in this Appendix reactor temperature and pressure were set at 473 K and 1 MPa respectively. The three feed streams, METHANE, GASFEED and LIQFEED represent the internal standard, the 10%hydrogen/90%nitrogen and the toluene/dodecane feed stream respectively. After mixing these three streams are fed to the reactor. In this flowsheet, the reactor and subsequent phase separation units are represented by one vessel in which the mixed feed stream is separated into a liquid and a vapour stream. GAS corresponds to the gas effluent, while LIQUID is sent to a flash first where temperature and pressure change from

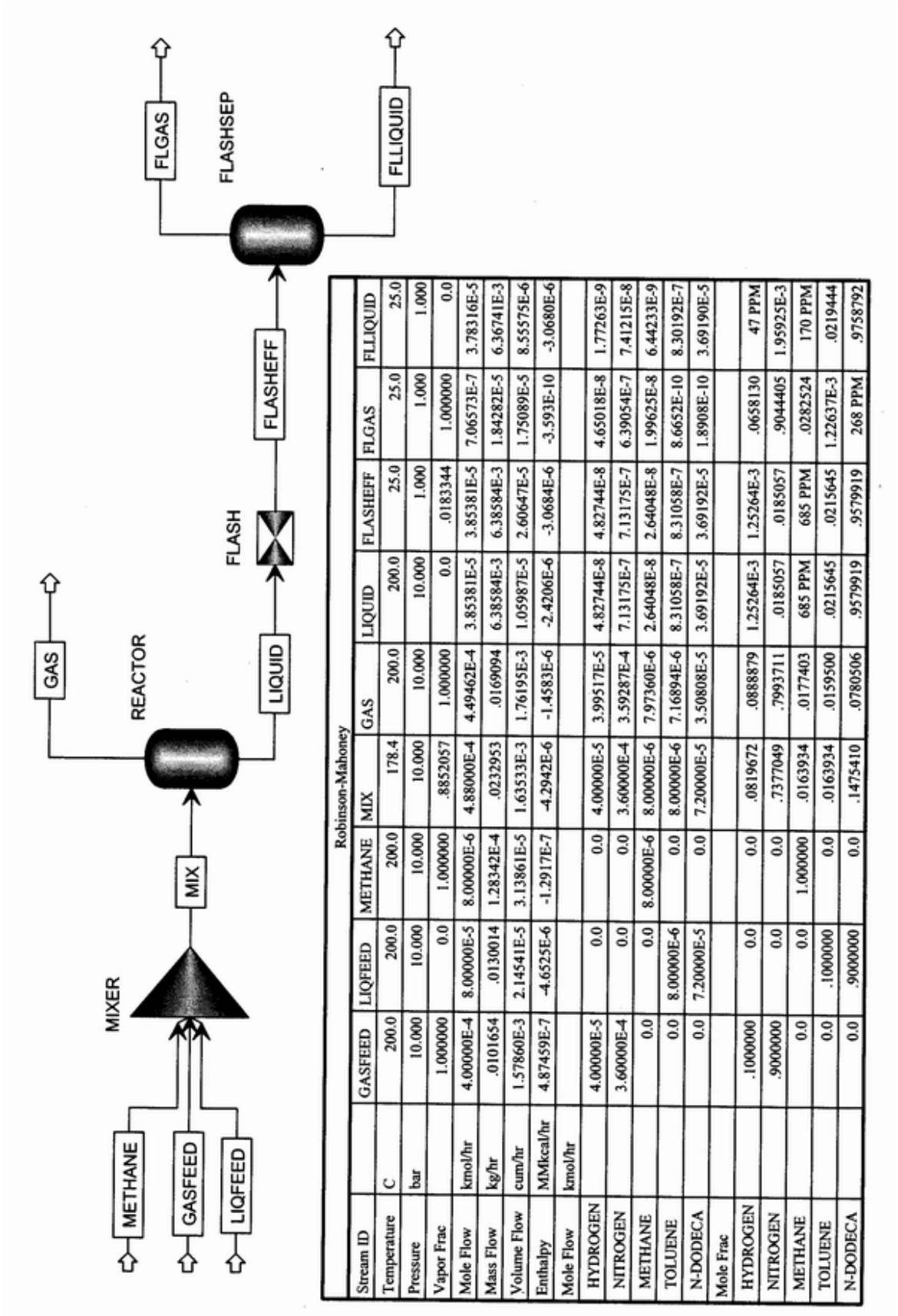

Robinson-Mahoney

Stream ID		GASFEED	LIQFEED	METHANE	MIX	GAS	LIQUID	FLASHEFF	FLGAS	FLLIQUID
Temperature	C	200.0	200.0	200.0	178.4	200.0	200.0	25.0	25.0	25.0
Pressure	bar	10.000	10.000	10.000	10.000	10.000	10.000	1.000	1.000	1.000
Vapor Frac		1.000000	0.0	1.000000	.8852057	1.000000	0.0	.0183344	1.000000	0.0
Mole Flow	kmol/hr	4.00000E-4	8.00000E-5	8.00000E-6	4.88000E-4	4.49462E-4	3.85381E-5	3.85381E-5	7.06573E-7	3.78316E-5
Mass Flow	kg/hr	.0101654	.0130014	1.28342E-4	.0232953	.0169094	6.38584E-3	6.38584E-3	1.84282E-5	6.36741E-3
Volume Flow	cum/hr	1.57860E-3	2.14541E-5	3.13861E-5	1.63533E-3	1.76195E-3	1.05987E-5	2.60647E-5	1.75089E-5	8.55575E-6
Enthalpy	MMkcal/hr	4.87459E-7	-4.6525E-6	-1.2917E-7	-4.2942E-6	-1.4583E-6	-2.4206E-6	-3.0684E-6	-3.593E-10	-3.0680E-6
Mole Flow	kmol/hr									
HYDROGEN		4.00000E-5	0.0	0.0	4.00000E-5	3.99517E-5	4.82744E-8	4.82744E-8	4.65018E-8	1.77263E-9
NITROGEN		3.60000E-4	0.0	0.0	3.60000E-4	3.59287E-4	7.13175E-7	7.13175E-7	6.39054E-7	7.41215E-8
METHANE		0.0	0.0	8.00000E-6	8.00000E-6	7.97360E-6	2.64048E-8	2.64048E-8	1.99625E-8	6.44233E-9
TOLUENE		0.0	8.00000E-6	0.0	8.00000E-6	7.16894E-6	8.31058E-7	8.31058E-7	8.6652E-10	8.30192E-7
N-DODECA		0.0	7.20000E-5	0.0	7.20000E-5	3.50808E-5	3.69192E-5	3.69192E-5	1.8908E-10	3.69190E-5
Mole Frac										
HYDROGEN		.1000000	0.0	0.0	.0819672	.0888879	1.25264E-3	1.25264E-3	.0658130	47 PPM
NITROGEN		.9000000	0.0	0.0	.7377049	.7993711	.0185057	.0185057	.9044405	1.95925E-3
METHANE		0.0	0.0	1.000000	.0163934	.0177403	685 PPM	685 PPM	.0282524	170 PPM
TOLUENE		0.0	.1000000	0.0	.0163934	.0159500	.0215645	.0215645	1.22637E-3	.0219444
N-DODECA		0.0	.9000000	0.0	.1475410	.0780506	.9579919	.9579919	268 PPM	.9758792

Figure A - 1 ASPEN flowsheet describing the flows in the three-phase continuous stirred tank reactor set-up and corresponding stream table

the reactor temperature and pressure to the ambient conditions. This flashed effluent, FLASHEFF, is then separated into the flashed gas, FLGAS, and the flashed liquid, FLLIQUID, corresponding to the measured effluent streams.

From the stream table in Figure A - 1 it is clear that less than 0.5 mole % of hydrogen and nitrogen dissolves in the hydrocarbon mixture. Hence, the molar nitrogen to hydrogen ratio of the gas effluent can be approximated by the molar nitrogen to hydrogen ratio of the gas feed, i.e., 9 in the present case. From the same stream table it can be deduced that nitrogen dissolves a factor 1.64 better in the hydrocarbon mixture than hydrogen, leading to a molar nitrogen to hydrogen ratio in the reactor liquid effluent of 15. Upon flashing of the liquid effluent, hydrogen is preferentially desorbed from the liquid and this causes the molar nitrogen to hydrogen ratio in the flashed gas to slightly decrease, i.e., to 14 instead of 15 in the reactor liquid effluent. As a consequence, the molar nitrogen to hydrogen ratio in the flashed liquid increases to 42, however, the absolute amount of nitrogen and hydrogen in the flashed liquid is negligible.

Simulation at other reactor temperatures and total pressures showed that the molar nitrogen to hydrogen ratio in the gas effluent is always close to the feed ratio, whereas the nitrogen to hydrogen ratio in the flashed gas effluent is somewhat temperature dependent but almost not dependent on the total pressure, vide Figure A - 2.

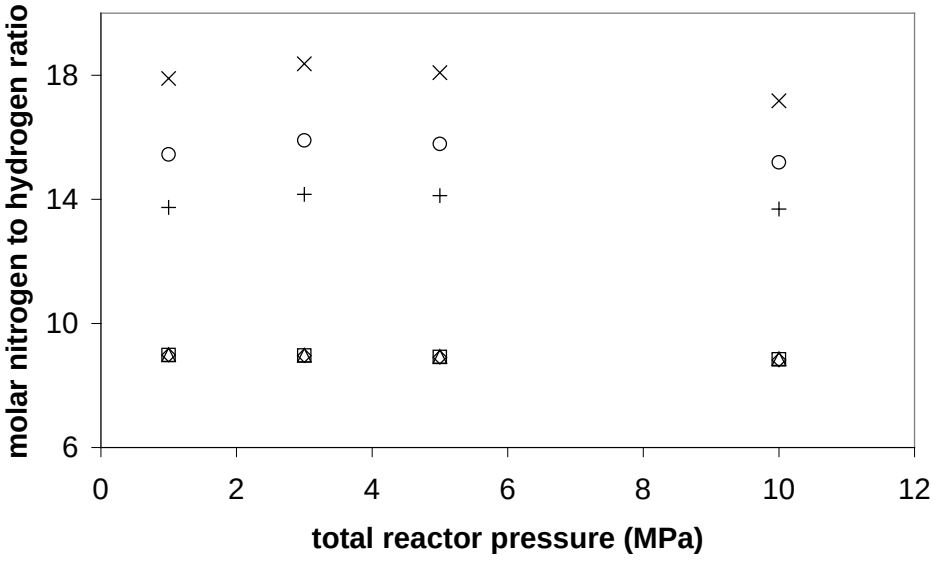

Figure A - 2 Molar nitrogen to hydrogen ratio as a function of the total reactor pressure in the gas effluent for reactor temperatures of 373 K (◊), 423 K (□) and 473 K (Δ) and in the flashed gas effluent for reactor temperatures of 373 K (×), 423 K (○) and 473 K (+)

A.2 Vapour-Liquid Equilibrium

A vapour liquid mixture is equilibrated if at a given temperature T and pressure p_t, the composition of the vapour and the liquid phase are such that the chemical potential for each individual component is the same in the vapour phase as in the liquid phase:

$$\mu_i^g(T, p_t, y_1,.., y_n) = \mu_i^l(T, p_t, x_1,..., x_n) \tag{A.1}$$

Expressing the chemical potential of each component i, for both phases in terms of fugacities:

$$\mu_i^g(T, p_t, y_1,.., y_n) = \mu_i^0(T) + RT \ln f_i^g(T, p_t, y_1,..., y_n) \tag{A.2}$$

$$\mu_i^l(T, p_t, x_1,.., x_n) = \mu_i^0(T) + RT \ln f_i^l(T, p_t, x_1,..., x_n) \tag{A.3}$$

with $\mu_i^0(T)$ the reference chemical potential of component i, i.e., in the ideal gas state at temperature T and a pressure of 1 bar, Eq. (A.1) reduces to :

$$f_i^g(T, p_t, y_{1,}..., y_n) = f_i^l(T, p_t, x_1,..., x_n) \tag{A.4}$$

The fugacity coefficient relates the component's fugacities in both liquid and vapour phase to its mole fraction x_i and y_i in both phases:

$$\begin{aligned} f_i^g(T, p_t, y_1,..., y_n) &= \Phi_i^g(T, p_t, y_1,..., y_n) y_i p_t \\ f_i^l(T, p_t, x_1,..., x_n) &= \Phi_i^l(T, p_t, x_1,..., x_n) x_i p_t \end{aligned} \tag{A.5}$$

Based on Eq. (A.4) and Eq. (A.5) the value for the partition coefficient for component i between vapour and liquid phase, i.e., the so called K-factor, can be obtained as the ratio of the fugacity coefficients:

$$\frac{y_i}{x_i} = K_i = \frac{\Phi_i^l(T, p_t, x_1,..., x_n)}{\Phi_i^g(T, p_t, y_1,..., y_n)} \tag{A.6}$$

The values for the fugacity coefficients Φ_i^l and Φ_i^g are obtained from an equation of state, c.q., Peng-Robinson.

A flash calculation for a mixture of n species and with a total molar flow rate F and composition z_i results in a vapour flow rate F^g and a liquid flow rate F^l with respective compositions y_i and x_i. A set of $2n+2$ equations is involved in this calculation. For each component Eq. (A.6) and the molar balance has to be fulfilled:

$$F\, z_i = F^l\, x_i + F^g\, y_i \tag{A.7}$$

The two remaining equations are the conditions that the sum of the mole fractions must equal one:

$$X = \sum_i x_i - 1 = 0$$
$$Y = \sum_i y_i - 1 = 0 \qquad \text{(A.8)}$$

This set of *2n+2* equations has to be solved iteratively, because the partition coefficients are composition dependent. Initial estimates for the values of the partition coefficients are obtained assuming ideality in both vapour and liquid phase, i.e., $\Phi_i^g = 1$ and $\Phi_i^l = \nu_i^0$, with ν_i^0 the fugacity coefficient for the pure liquid component *i* at the mixture pressure and temperature calculated using the correlation originally proposed by Chao and Seeder [2]:

$$\log_{10} \nu_i^0 = \log_{10} \nu_i^{(0)} + \omega_i \log_{10} \nu_i^{(1)} \qquad \text{(A.9)}$$

$$\log_{10} \nu_i^{(0)} = A_0 + \frac{A_1}{T_{r,i}} + A_2 T_{r,i} + A_3 T_{r,i}^2 + A_4 T_{r_i}^3 + (A_5 + A_6 T_{r,i} + A_7 T_{r,i}^2) p_{r,i} + (A_8 + A_9 T_{r,i}) p_{r,i}^2 - \log p_{r,i} \qquad \text{(A.10)}$$

$$\log_{10} \nu_i^{(1)} = -4.23893 + 8.65808 T_{r,i} - \frac{1.22060}{T_{r,i}} - 3.15224 T_{r,i}^3 - 0.025(p_{r,i} - 0.6) \qquad \text{(A.11)}$$

with $T_{r,i}=T/T_{c,i}$ and $p_{r,i}=p/p_{c,i}$. The values for the coefficients A_i *(i=0,…,9)* for a simple fluid and for hydrogen are taken from literature [2]. Values for the critical properties of each component are obtained from literature or estimated using Fedors' group contribution method for $T_{c,i}$ and Joback's method for $P_{c,i}$ [3]. If no literature data for the acentric factor ω_i are available, it can be estimated from:

$$\omega_i = -\log p_{vpr,i}(T_{r,i} = 0.7) - 1.00 \qquad \text{(A.12)}$$

and using the Lee and Kessler correlation [3] for the reduced vapour pressure $p_{vpr,i}$ at $T_{r,i}=0.7$. Upon combination of Eq. (A.6) and Eq. (A.7) the composition of the vapour and the liquid phase is calculated using the initial values for the partition coefficients :

$$x_i = \frac{z_i}{1 - \varphi + K_i \varphi}$$
$$y_i = \frac{K_i z_i}{1 - \varphi + K_i \varphi} \qquad \text{(A.13)}$$

with $\varphi = F^g/F$. Fast convergence of the iterative procedure is obtained when a good estimate of the vapour fraction φ is available so that both of the conditions (A.8) is fulfilled. Variations of φ for a given set of values for the partition coefficients were found to have a dramatic effect on the values of the function *X* and *Y* in (A.8). Moreover, the more the results for *X* and *Y* deviate from zero, the poorer the convergence behaviour of the calculations. In

some cases, even numerical problems were encountered in the calculation of the fugacities using the Peng Robinson's equation of state. Hence, the method developed by Martens [4] was used to obtain good initial estimates for φ ensuring that both constraints (A.8) are fulfilled.

For an initial guess of $\varphi = 0.5$ and considering (A.13) and the definition of X and Y it can be shown that:

$$X + Y = 0 \tag{A.14}$$

and, hence,

$$\left.\frac{\partial X}{\partial \varphi}\right|_{\varphi=0.5} = \sum_i \left.\frac{z_i(1-K_i)}{[(1-\varphi)+K_i]^2}\right|_{\varphi=0.5} = -\left.\frac{\partial Y}{\partial \varphi}\right|_{\varphi=0.5} = -\sum_i \left.\frac{z_i K_i(1-K_i)}{[(1-\varphi)+K_i]^2}\right|_{\varphi=0.5} \tag{A.15}$$

If now X is positive, and by virtue of (A.15) Y is negative, φ should be increased or decreased, depending on the sign of both $\frac{\partial X}{\partial \varphi}$ and $\frac{\partial Y}{\partial \varphi}$, such that the value of X decreases and that of Y increases. Because for $\varphi = 0.5$ the sign of both derivatives is opposite a variation of φ will have an opposite effect on X and Y as required to force both X and Y to evolve in the appropriate direction. As a result the following procedure is used to obtain a good initial value for φ:

1. Set $\varphi = 0.5$
2. Calculate the molar composition of both phases using (A.13) and the partition coefficients from Chao-Seeder
3. Calculate X, Y and $\frac{\partial Y}{\partial \varphi}$
4. Adapt φ according to the following rules :

   If $\frac{\partial Y}{\partial \varphi} < 0$ $\rightarrow$ $\varphi_n = \varphi_{n-1}/(1-Y)$

   If $\frac{\partial Y}{\partial \varphi} > 0$ $\rightarrow$ $\varphi_n = \varphi_{n-1}(1-Y)$

5. Go back to step 2 and repeat the calculation until the absolute value of both X and Y is smaller than 0.01.

Starting from the initial estimates for the partition coefficients using Chao-Seeder and the initial estimate of φ using the approach above the following iterative calculation procedure is used leading to the solution of the set equations (A.6)-(A.8):

1. Calculate the composition of both phases using (A.13)

2. Calculate Φ_i^g and Φ_i^l using an equation of state, c.q., Peng-Robinson, and the partition coefficients using (A.6).
3. Compare the new K_i^n values with those obtained from the previous cycle K_i^{n-1} using the following error function :

$$E = \sqrt{\frac{\sum_i^n \left(\frac{K_i^n - K_i^{n-1}}{K_i^n} \right)}{n}} \tag{A.16}$$

4. If $E>10^{-6}$ and the number of iterations is smaller than 100 calculate a new value for K_i^n using:

$$K_i^n = \sqrt{K_i^n K_i^{n-1}} \tag{A.17}$$

and go back to step 1.

5. Otherwise calculate X-Y and a new value for the vapour fraction :

$$\varphi_n = \varphi_{n-1} - \frac{(X-Y)\big|_{\varphi_{n-1}}}{\left.\frac{\partial (X-Y)}{\partial \varphi}\right|_{\varphi_{n-1}}} = \varphi_{n-1} - \frac{\sum_i^n \frac{z_i (1-K_i^n)}{1+\varphi(K_i^n - 1)}}{\sum_i^n \frac{z_i (1-K_i^n)^2}{\left(1+\varphi(K_i^n - 1)\right)^2}} \tag{A.18}$$

6. If $|X\text{-}Y| > 10^{-5}$ and the number of iterations is smaller than 100 go back to step 1.

A.3 References

[1] Aspen Technology, Inc. *ASPEN PLUS User Guide* **Aspen Technology, Inc.** (2001).

[2] Chao, K. C., and Seeder, J. D., *A general correlation of Vapour-Liquid Equilibria in Hydrocarbon Mixtures* **AIChE J.** *7* 598-605 (1961).

[3] Poling, B. E., Prausnitz, J. M., and O'Connell, J. P., *The Properties of Gases and Liquids 5th ed.* **McGraw-Hill** *New York* (2000).

[4] Martens, G., *Hydrocracking on Pt/US-Y zeolites: fundamental kinetic modelling and industrial reactor simulation* **PhD Thesis** *Ghent University* (2000).

Appendix B

Reaction Family Significance in Hydrocracking

Several reaction families can occur on acid catalysts, however, not all of them contribute significantly to the observed product distribution. Typical acid catalyzed reaction families encountered in catalytic reforming, catalytic cracking and hydrocracking are (de)-protonation, hydride shift, alkyl shift, PCP-branching, β-scission, oligomerization and hydride transfer. In the single-event model for hydrocracking only alkyl shifts, PCP branching reactions and β-scissions are considered as potentially rate-determining elementary steps which have a significant effect on the observed product distribution. The reasons why (de)-protonation, hydride shift, oligomerization and hydride transfer reactions are not considered as potentially rate-determining elementary steps are discussed in the subsequent paragraphs.

B.1 (De)-Protonation/Hydride Shift

In the original development of the single-event model [1], (de)-protonation and hydride shift reactions were incorporated as potentially rate-determining elementary steps. However, in later work on *n*-octane hydrocracking [2] it was found that the (de)-protonation reactions were potentially fast reactions and, hence, quasi-equilibrium could be assumed for the (de)-protonation reactions. As a consequence, a quasi-equilibrium can also be assumed for the carbenium ion isomers via hydride shifts. This is illustrated in Figure B - 1 with the (de)-protonation of 2-methylhept-2-ene into 2-methylhept-2-yl carbenium ion and 2-methylhept-3-yl carbenium ion. Because quasi-equilibrium, represented by the full arrows, can be assumed between the alkene and the two related carbenium ions quasi-equilibrium,

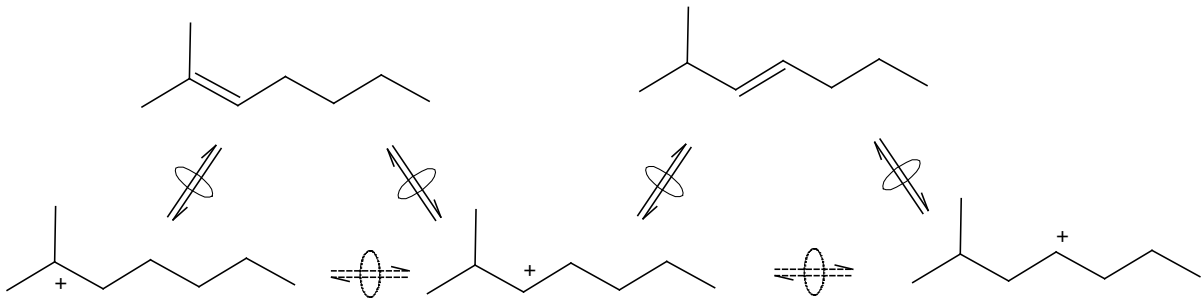

Figure B - 1 Quasi equilibration of hydride shift reactions illustrated based On 2-methylheptane structurally related alkenes and carbenium ions

represented by the dotted arrows, is induced between the two carbenium ions themselves. Moreover, quasi-equilibrium can also be assumed between the above mentioned carbenium ions and the second alkene from which it can be formed via protonation, c.q., 2-methylhept-3-ene for the 2-methylhept-3-yl carbenium ion, as illustrated in Figure B - 1 and 2-methylhept-1-ene for the 2-methylhept-2-yl carbenium ion (not shown). These alkenes may lead to other carbenium ions which are also in quasi-equilibrium with the original carbenium ions as illustrated for the formation of the 2-methylhept-4-yl carbenium ion from 2-methylhept-3-ene. Hence, all carbenium ions which are isomers via hydride shifts are in quasi-equilibrium.

B.2 Oligomerization/β-scission

Oligomerization, as a bimolecular reaction, depends both on the concentration of carbenium ions and of the alkenes.

$$O_{C1} + R^{+}_{C2} \longleftrightarrow R^{+}_{C1+C2} \tag{B.1}$$

The affinity of a reaction measures how strong the oligomerization/β-scission reactions deviate from equilibrium and is an indication of the direction in which the reaction is ocurring, the forward, i.e., oligomerization ($A_r >> 0$) or the reverse, i.e., β-scission ($A_r << 0$).

$$\frac{r_{forward}}{r_{reverse}} = exp\left(\frac{A_r}{RT}\right) \tag{B.2}$$

Taking into account the equilibrium of the (de)-hydrogenation and (de)-protonation reactions, the affinity for the oligomerization/β-scission reaction can be written as a function of hydrogen and alkane partial pressures:

$$A_r = RT \ln K_r \frac{p_{P_{C1}} p_{P_{C2}}}{p_{P_{C1+C2}} p_{H_2}} \tag{B.3}$$

Under the typical conditions of temperature, pressure and molar hydrogen to hydrocarbon ratio applied a value for $A_r = -35\ 10^3\ J\ mol^{-1}$ is found for 99% feed conversion. This

corresponds to a ratio of the forward, oligomerization, to the reverse, cracking, reaction rate of 0.25 10^{-3}. Hence, even at 99% conversion, β-scission reactions proceed more than 1000 times faster than oligomerization, justifying the neglect of oligomerization reactions in the reaction network.

B.3 Hydride Transfer

In the hydrocracking model hydride transfer is kinetically insignificant. If only ideal hydrocracking experiments are considered (quasi equilibrated metal catalyzed reactions) and when the protonation of the alkenes can be assumed to be in quasi equilibrium, quasi equilibrium is established between a carbenium ion and a corresponding alkane. This means that for a hydride transfer:

$$P_1 + R_2^+ \rightleftharpoons R_1^+ + P_2 \tag{B.4}$$

the alkane P_1 is in equilibrium with carbenium ion R_1^+ and the carbenium ion R_2^+ is in equilibrium with alkane P_2. Hence, the molecules involved in hydride transfer are in equilibrium and the eventual occurrence of a slower, rate determining hydride transfer can be neglected compared to the fast (de)hydrogenation and (de)protonation.

Moreover, based on estimated parameter values for catalytic cracking by Beirnaert et al. [3] hydride transfer reaction rates are obtained which are more than 600 times slower than the slowest isomerization or cracking rates. Hence, it is expected that even when (de)hydrogenation and/or (de)protonation are not equilibrated, the rate of the rate determining steps in hydrocracking will still be significantly faster than the rate of hydride transfer.

B.4 References

[1] Vynckier, E., and Froment, G. F., *Modelling of the kinetics of complex processes based upon elementary steps*, in: *Kinetic and Thermodynamic Lumping of Multicomponent Mixtures* (G. Astarita and S. I. Sandler, Eds.) **Elsevier,** *Amsterdam* 131-161 (1991).

[2] Svoboda, G. D., Vynckier, E., Debrabandere, B., and Froment, G. F., *Single-event rate parameters for paraffin hydrocracking on a Pt/US-Y Zeolite* **Ind. Eng. Chem. Res.** *34* 3793-3800 (1995).

[3] Beirnaert, H. C., Alleman, J. R., and Marin, G. B., *A Fundamental Kinetic Model for the Catalytic Cracking of Alkanes on a USY Zeolite in the Presence of Coke Formation* **Ind. Eng. Chem. Res.** *40* 1337-1347 (2001).

Appendix C

Rate Equation Development for Non Ideal Hydrocracking

In the development of the rate equations for *non ideal* hydrocracking, two provisional assumptions for the mathematical simplicity of the equations have been made. A lumped reaction scheme was used in the development of the rate equations, while other more detailed reaction schemes are suggested and used in the literature [1,2]. The second provisional assumption was related to the (de)-hydrogenation reaction mechanism, which was assumed to occur molecularly via an Eley-Rideal mechanism. This and other reaction mechanisms have been proposed for (de)-hydrogenation [3].

This Appendix demonstrates that when both provisional assumptions are abandoned and, hence, a more detailed reaction scheme and other (de)-hydrogenation reaction mechanisms are used, this leads to analogous qualitative interpretations as those made in Chapter 3.

C.1 Reaction Scheme

The lumped reaction scheme used in Chapter 3, vide Figure 3-5, only accounts for the very basic observations in *n*-alkane hydrocracking: the *n*-alkane is first isomerized and, subsequently, can crack to lighter products. A more detailed lumped reaction scheme, such as in Figure C - 1, makes a distinction between mono- and multibranched isomers and, hence, rate equations based on this more detailed lumped reaction scheme more accurately describe the isomer formation from the normal alkane and are able to account for differences in cracking rates from mono- and multibranched isomers. This feature is expected to improve the predicting capabilities of the model, certainly when the range of experimental conversions is extended. The qualitative interpretation of the rate equations, however, is independent of

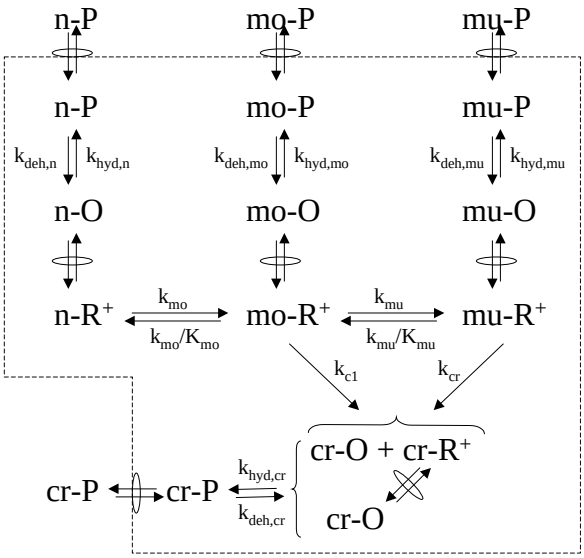

Figure C - 1 Detailed lumped reaction scheme [1,2] used in *non ideal* hydrocracking

the level of detail included in the lumped reaction scheme because very similar terms appear explaining the shift from *ideal* to *non ideal* hydrocracking and vice versa.

Physisorption in the more detailed lumped reaction scheme is accounted for via the same expression, i.e., Eq. (3.1), where *f* stands for normal (*n*), monobranched (*mo*), multibranched (*mu*) or cracked (*cr*). The expressions for the net production rates of the alkanes based on the (de)-hydrogenation reactions are also equivalent to Eq (3.4), vide Chapter 3. The difference between the two lumped reaction schemes is reflected in the expressions based on the steady state approximation for the alkenes and the carbenium ions. One extra alkene pseudo-component has to be considered and, as a consequence, extra reactions have to be accounted for in the reaction scheme. The following equations are obtained for the net rates of formation of the normal, monobranched, multibranched and cracked alkenes:

$$R_{n-O} = k_{deh,n} K^{M}_{n-P} \left(C_{n-P} - \frac{C_{n-O} p_{H_2}}{K_{deh,n}} \right) - k_{mo} K^{A}_{n-O} \left(C_{n-O} - \frac{C_{mo-O_{iso}}}{K_{mo}} \right) = 0 \tag{C.1}$$

$$\begin{aligned} R_{mo-O} = {} & k_{deh,mo} K^{M}_{mo-P} \left(C_{mo-P} - \frac{C_{mo-O} p_{H_2}}{K_{deh,mo}} \right) + k_{mo} K^{A}_{n-O} C_t^{A} \left(C_{n-O} - \frac{C_{mo-O}}{K_{mo}} \right) \\ & - k_{mu} K^{A}_{mu-O} C_t^{A} \left(C_{mo-O} - \frac{C_{mu-O}}{K_{mu}} \right) - k_{c1} K^{A}_{mo-O} C_t^{A} C_{mo-O} = 0 \end{aligned} \tag{C.2}$$

$$\begin{aligned} R_{mu-O} = {} & k_{deh,mu} K^{M}_{mu-P} \left(C_{mu-P} - \frac{C_{mu-O} p_{H_2}}{K_{deh,mu}} \right) + k_{mu} K^{A}_{mu-O} C_t^{A} \left(C_{mo-O} - \frac{C_{mu-O}}{K_{mu}} \right) \\ & - k_{cr} K^{A}_{mu-O} C_t^{A} C_{mu-O} = 0 \end{aligned} \tag{C.3}$$

$$R_{cr-O} = k_{deh,cr} K^{M}_{cr-P} \left(C_{cr-P} - \frac{C_{cr-O} p_{H_2}}{K_{deh,cr}} \right) + 2\left(k_{cr} K^{A}_{mo-O} C_t^{A} C_{mo-O} + k_{cr} K^{A}_{mu-O} C_t^{A} C_{mu-O} \right) = 0 \quad \text{(C.4)}$$

In Eq. (C.1) to Eq. (C.4) and further in Paragraph C.1, the * superscript as defined in Chapter 3, vide Eq. (3.6) and Eq. (3.9), has been omitted for simplicity of the mathematical expressions. In Paragraph C.2 the same notation as in Chapter 3 is used again. The alkene pseudo-component concentrations are the only unknowns in this set of equations, Eq. (C.1) to Eq. (C.3), for the normal and the two isomer alkene pseudo-components, which constitute a linear system of three equations and three unknowns of the following form:

$$\begin{bmatrix} a & b & 0 \\ c & d & e \\ 0 & f & g \end{bmatrix} \begin{bmatrix} C_{n-O} \\ C_{mo-O} \\ C_{mu-O} \end{bmatrix} = \begin{bmatrix} h \\ i \\ j \end{bmatrix} \quad \text{(C.5)}$$

with:

$$\begin{aligned} a &= k_{hyd,n} p_{H_2} + k_{mo} & f &= -k_{mu} \\ b &= -\frac{k_{mo}}{K_{mo}} & g &= k_{hyd,mu} p_{H_2} + \frac{k_{mu}}{K_{mu}} + k_{mo} \\ c &= -k_{mo} & h &= k_{deh,n} C_{n-P} \\ d &= k_{hyd,mo} p_{H_2} + \frac{k_{mo}}{K_{mo}} + k_{mu} + k_{c1} & i &= k_{deh,mo} C_{m-P} \\ e &= -\frac{k_{mu}}{K_{mu}} & j &= k_{deh,mu} C_{mu-P} \end{aligned} \quad \text{(C.6)}$$

which has as solution:

$$\begin{aligned} C_{n-O} &= \frac{efh - dgh + bgi - bej}{aef + bcg - adg} \\ C_{mo-O} &= \frac{cgh - agi + aej}{aef + bcg - adg} \\ C_{mu-O} &= \frac{afi - cfh + bcj - adj}{aef + bcg - adg} \end{aligned} \quad \text{(C.7)}$$

Combination of Eq. (3.4) for the normal, monobranched and multibranched alkenes with Eq. (C.1) to Eq. (C.3) for the normal and the two isomer alkene pseudo-components and substitution of the alkene concentrations by the expressions (C.6) and (C.7) leads to the following expression for the net rates of formation of the alkane pseudo-components:

$$R_{n-P} = \frac{-\left(k_{mo}k_{hyd,m}k_{hyd,mu}p_{H_2}^2 + k_{mo}\frac{k_{mu}}{K_{mu}}k_{hyd,m}p_{H_2} + k_{mo}k_{cr}k_{hyd,m}p_{H_2} + k_{mo}k_{mu}k_{hyd,mu}p_{H_2} + k_{mo}k_{mu}k_{cr} + k_{mo}k_{c1}k_{hy,mu}p_{H_2} + k_{mo}k_{c1}\frac{k_{mu}}{K_{mu}} + k_{mo}k_{c1}k_{cr}\right)}{\begin{aligned} &* k_{deh,n}C_{n-P} + \left(\frac{k_{mo}}{K_{mo}}k_{hyd,n}k_{hyd,mu}p_{H_2}^2 + \frac{k_{mo}}{K_{mo}}\frac{k_{mu}}{K_{mu}}k_{hyd,n}p_{H_2} + \frac{k_{mo}}{K_{mo}}k_{cr}k_{hyd,mu}p_{H_2}\right)k_{deh,m}C_{m-P} + \frac{k_{mo}}{K_{mo}}\frac{k_{mu}}{K_{mu}}k_{hyd,n}p_{H_2}k_{deh,mu}C_{mu-P} \\ &k_{hyd,n}k_{hyd,m}k_{hyd,mu}p_{H_2}^3 + \frac{k_{mu}}{K_{mu}}k_{hyd,n}k_{hyd,m}p_{H_2}^2 + k_{cr}k_{hyd,n}k_{hyd,m}p_{H_2}^2 + \frac{k_{mo}}{K_{mo}}k_{hyd,n}k_{hyd,m}p_{H_2}^2 + \frac{k_{mo}}{K_{mo}}\frac{k_{mu}}{K_{mu}}k_{hyd,n}p_{H_2} + \frac{k_{mo}}{K_{mo}}k_{cr}k_{hyd,n}p_{H_2} \\ &+ k_{mu}k_{hyd,n}k_{hyd,mu}p_{H_2}^2 + k_{mu}k_{cr}k_{hyd,n}p_{H_2} + k_{mo}k_{hyd,m}k_{hyd,mu}p_{H_2}^2 + k_{mo}\frac{k_{mu}}{K_{mu}}k_{hyd,m}p_{H_2} + k_{mo}k_{cr}k_{hyd,m}p_{H_2} + k_{mo}k_{mu}k_{hyd,mu}p_{H_2} + k_{mo}k_{mu}k_{cr} \\ &+ k_{c1}k_{hyd,n}k_{hyd,mu}p_{H_2}^2 + \frac{k_{mu}}{K_{mu}}k_{c1}k_{hyd,n}p_{H_2} + k_{c1}k_{cr}k_{hyd,n}p_{H_2} + k_{mo}k_{c1}k_{hyd,mu}p_{H_2} + k_{mo}\frac{k_{mu}}{K_{mu}}k_{c1} + k_{mo}k_{c1}k_{cr} \end{aligned}} \quad \text{(C.8)}$$

$$R_{m-P} = \frac{\begin{aligned} &\left(k_{mo}k_{hyd,m}k_{hyd,mu}p_{H_2}^2 + k_{mo}\frac{k_{mu}}{K_{mu}}k_{hyd,m}p_{H_2} + k_{mo}k_{cr}k_{hyd,m}p_{H_2} + k_{mo}k_{c1}k_{hyd,mu}p_{H_2} + k_{mo}\frac{k_{mu}}{K_{mu}}k_{c1} + k_{mo}k_{c1}k_{cr}\right) * k_{deh,n}C_{n-P} \\ &-\left(\frac{k_{mo}}{K_{mo}}k_{hyd,n}k_{hyd,mu}p_{H_2}^2 + \frac{k_{mo}}{K_{mo}}\frac{k_{mu}}{K_{mu}}k_{hyd,n}p_{H_2} + \frac{k_{mo}}{K_{mo}}k_{cr}k_{hyd,mu}p_{H_2} + k_{mu}k_{hyd,n}k_{hyd,mu}p_{H_2}^2 + k_{mu}k_{cr}k_{hyd,n}p_{H_2} + k_{mo}k_{mu}k_{hyd,mu}p_{H_2}\right. \\ &\left. + k_{mo}k_{mu}k_{cr}\right) * k_{deh,m}C_{m-P} + \left(\frac{k_{mu}}{K_{mu}}k_{hyd,n}k_{hyd,m}p_{H_2}^2 + k_{c1}\frac{k_{mu}}{K_{mu}}k_{hyd,m}p_{H_2} + k_{mo}\frac{k_{mu}}{K_{mu}}k_{hyd,m}p_{H_2} + k_{mo}\frac{k_{mu}}{K_{mu}}k_{c1}\right) * k_{deh,mu}C_{mu-P} \end{aligned}}{\begin{aligned} &k_{hyd,n}k_{hyd,m}k_{hyd,mu}p_{H_2}^3 + \frac{k_{mu}}{K_{mu}}k_{hyd,n}k_{hyd,m}p_{H_2}^2 + k_{cr}k_{hyd,n}k_{hyd,m}p_{H_2}^2 + \frac{k_{mo}}{K_{mo}}k_{hyd,n}k_{hyd,m}p_{H_2}^2 + \frac{k_{mo}}{K_{mo}}\frac{k_{mu}}{K_{mu}}k_{hyd,n}p_{H_2} + \frac{k_{mo}}{K_{mo}}k_{cr}k_{hyd,n}p_{H_2} \\ &+ k_{mu}k_{hyd,n}k_{hyd,mu}p_{H_2}^2 + k_{mu}k_{cr}k_{hyd,n}p_{H_2} + k_{mo}k_{hyd,m}k_{hyd,mu}p_{H_2}^2 + k_{mo}\frac{k_{mu}}{K_{mu}}k_{hyd,m}p_{H_2} + k_{mo}k_{cr}k_{hyd,m}p_{H_2} + k_{mo}k_{mu}k_{hyd,mu}p_{H_2} + k_{mo}k_{mu}k_{cr} \\ &+ k_{c1}k_{hyd,n}k_{hyd,mu}p_{H_2}^2 + \frac{k_{mu}}{K_{mu}}k_{c1}k_{hyd,n}p_{H_2} + k_{c1}k_{cr}k_{hyd,n}p_{H_2} + k_{mo}k_{c1}k_{hyd,mu}p_{H_2} + k_{mo}\frac{k_{mu}}{K_{mu}}k_{c1} + k_{mo}k_{c1}k_{cr} \end{aligned}} \quad \text{(C.9)}$$

$$R_{mu-P} = \frac{\begin{pmatrix} k_{mo}k_{mu}k_{hyd,mu}p_{H_2} \end{pmatrix} * k_{deh,n}C_{n-P} + \left(k_{mu}k_{hyd,n}k_{hyd,mu}p_{H_2}^2 + k_{mo}k_{mu}k_{hyd,mu}p_{H_2} \right) * k_{deh,m}C_{m-P} \\ \left(\frac{k_{mu}}{K_{mu}}k_{hyd,n}k_{hyd,m}p_{H_2}^2 + \frac{k_{mo}}{K_{mo}}\frac{k_{mu}}{K_{mu}}k_{hyd,n}p_{H_2} + k_{c1}\frac{k_{mu}}{K_{mu}}k_{hyd,n}p_{H_2} + k_{mo}\frac{k_{mu}}{K_{mu}}k_{hyd,m}p_{H_2} + k_{mo}\frac{k_{mu}}{K_{mu}}k_{c1} + k_{cr}k_{hyd,n}k_{hyd,m}p_{H_2}^2 \right. \\ \left. + \frac{k_{mo}}{K_{mo}}k_{cr}k_{hyd,n}p_{H_2} + k_{mu}k_{cr}k_{hyd,n}p_{H_2} + k_{c1}k_{cr}k_{hyd,n}p_{H_2} + k_{mo}k_{cr}k_{hyd,m}p_{H_2} + k_{mo}k_{mu}k_{cr} + k_{mo}k_{c1}k_{cr} \right) * k_{deh,mu}C_{mu-P}}{k_{hyd,n}k_{hyd,m}k_{hyd,mu}p_{H_2}^3 + \frac{k_{mu}}{K_{mu}}k_{hyd,n}k_{hyd,m}p_{H_2}^2 + k_{cr}k_{hyd,n}k_{hyd,m}p_{H_2}^2 + \frac{k_{mo}}{K_{mo}}k_{hyd,n}k_{hyd,m}p_{H_2}^2 + \frac{k_{mo}}{K_{mo}}\frac{k_{mu}}{K_{mu}}k_{hyd,n}p_{H_2} + \frac{k_{mo}}{K_{mo}}k_{cr}k_{hyd,n}p_{H_2} \\ + k_{mu}k_{hyd,n}k_{hyd,mu}p_{H_2}^2 + k_{mu}k_{cr}k_{hyd,n}p_{H_2} + k_{mo}k_{hyd,m}k_{hyd,mu}p_{H_2}^2 + k_{mo}\frac{k_{mu}}{K_{mu}}k_{hyd,m}p_{H_2} + k_{mo}k_{cr}k_{hyd,m}p_{H_2} + k_{mo}k_{mu}k_{hyd,mu}p_{H_2} + k_{mo}k_{mu}k_{cr} \\ + k_{c1}k_{hyd,n}k_{hyd,mu}p_{H_2}^2 + \frac{k_{mu}}{K_{mu}}k_{c1}k_{hyd,n}p_{H_2} + k_{c1}k_{cr}k_{hyd,n}p_{H_2} + k_{mo}k_{c1}k_{hyd,mu}p_{H_2} + k_{mo}\frac{k_{mu}}{K_{mu}}k_{c1} + k_{mo}k_{c1}k_{cr}} \tag{C.11}$$

$$R_{cr-P} = \frac{\left(k_{mo}k_{c1}k_{hyd,mu}p_{H_2} + k_{mo}\frac{k_{mu}}{K_{mu}}k_{c1} + k_{mo}k_{c1}k_{cr} + k_{mo}k_{mu}k_{cr} \right) * k_{deh,n}C_{n-P} + \left(k_{c1}k_{hyd,n}k_{hyd,m}p_{H_2}^2 + k_{c1}\frac{k_{mu}}{K_{mu}}k_{hyd,n}p_{H_2} + k_{c1}k_{cr}k_{hyd,n}p_{H_2} \right. \\ \left. + k_{mo}k_{c1}k_{hyd,mu}p_{H_2} + k_{mo}\frac{k_{mu}}{K_{mu}}k_{c1} + k_{mo}k_{c1}k_{cr} + k_{mu}k_{cr}k_{hyd,n}p_{H_2} + k_{mo}k_{mu}k_{cr} \right) * k_{deh,m}C_{m-P} + \left(k_{c1}\frac{k_{mu}}{K_{mu}}k_{hyd,n}p_{H_2} + k_{mo}k_{mu}k_{cr} \right. \\ \left. + k_{cr}k_{hyd,n}k_{hyd,m}p_{H_2}^2 + \frac{k_{mo}}{K_{mo}}k_{cr}k_{hyd,n}p_{H_2} + k_{mu}k_{cr}k_{hyd,n}p_{H_2} + k_{c1}k_{cr}k_{hyd,n}p_{H_2} + k_{mo}k_{cr}k_{hyd,m}p_{H_2} + k_{mo}k_{mu}k_{cr} + k_{mo}k_{c1}k_{cr} \right) * k_{deh,mu}C_{mu-P}}{k_{hyd,n}k_{hyd,m}k_{hyd,mu}p_{H_2}^3 + \frac{k_{mu}}{K_{mu}}k_{hyd,n}k_{hyd,m}p_{H_2}^2 + k_{cr}k_{hyd,n}k_{hyd,m}p_{H_2}^2 + \frac{k_{mo}}{K_{mo}}k_{hyd,n}k_{hyd,m}p_{H_2}^2 + \frac{k_{mo}}{K_{mo}}\frac{k_{mu}}{K_{mu}}k_{hyd,n}p_{H_2} + \frac{k_{mo}}{K_{mo}}k_{cr}k_{hyd,n}p_{H_2} \\ + k_{mu}k_{hyd,n}k_{hyd,mu}p_{H_2}^2 + k_{mu}k_{cr}k_{hyd,n}p_{H_2} + k_{mo}k_{hyd,m}k_{hyd,mu}p_{H_2}^2 + k_{mo}\frac{k_{mu}}{K_{mu}}k_{hyd,m}p_{H_2} + k_{mo}k_{cr}k_{hyd,m}p_{H_2} + k_{mo}k_{mu}k_{hyd,mu}p_{H_2} + k_{mo}k_{mu}k_{cr} \\ + k_{c1}k_{hyd,n}k_{hyd,mu}p_{H_2}^2 + \frac{k_{mu}}{K_{mu}}k_{c1}k_{hyd,n}p_{H_2} + k_{c1}k_{cr}k_{hyd,n}p_{H_2} + k_{mo}k_{c1}k_{hyd,mu}p_{H_2} + k_{mo}\frac{k_{mu}}{K_{mu}}k_{c1} + k_{mo}k_{c1}k_{cr}} \tag{C.10}$$

In Eq. (C.8), apart from extra terms resulting in a smoother transition from *ideal* to *non ideal* hydrocracking and vice versa, similar terms as in Eq. (3.12) and Eq. (3.15) appear. The first term, i.e., $k_{mo}k_{hyd,mo}k_{hyd,mu}p_{H_2}^2$, is the one dominating the value of the numerator in *ideal* hydrocracking. Several terms, with as common feature that they contain no hydrogenation rate coefficients, become equally important in *non ideal* hydrocracking, i.e., $k_{mo}k_{mu}k_{cr}$, $k_{mo}k_{c1}k_{mu}/K_{mu}$ and $k_{mo}k_{c1}k_{cr}$. Several terms, corresponding to different possible reaction pathways, appear in this case only because of the detailed reaction scheme used compared to the reaction scheme used in Chapter 3. In *ideal* hydrocracking the complexity of the reaction mechanism used has no effect on the number of dominating reaction pathways. Only one reaction pathway, i.e., the formation of (monobranched) isomers, is possible according to both the reaction scheme used in Chapter 3 and the more detailed reaction scheme developed in this Appendix.

As can be observed from the expressions for the terms important in *ideal* and *non ideal* hydrocracking, i.e., $k_{mo}k_{hyd,mo}k_{hyd,mu}p_{H_2}^2$ and $k_{mo}k_{mu}k_{cr}$, $k_{mo}k_{c1}k_{mu}/K_{mu}$ and $k_{mo}k_{c1}k_{cr}$ respectively, the same factors, such as temperature, total pressure, metal surface coverage… determine the shift from *ideal* to *non ideal* hydrocracking and vice versa. Hence, the qualitative interpretation of these rate equations can be expected to be very analogous to the interpretation presented in Chapter 3.

C.2 (De)-Hydrogenation Reaction Mechanism

For simplicity of the rate equations it was assumed in Chapter 3 that the (de)-hydrogenation reaction mechanism occurs via an Eley-Rideal mechanism. In this Section it is demonstrated that other possible assumptions on the (de)-hydrogenation reaction mechanism, such as surface reaction, molecular or dissociative hydrogen chemisorption, molecular or atomic hydrogen addition, first or second hydrogen addition as rate-determining step,… [3] enable analogous qualitative interpretations of the rate equations as presented in Chapter 3. To be as broad as possible, the discussion is not limited to the most likely reaction mechanism selected by Dumez and Froment [3] for the dehydrogenation of 1-butene to butadiene, i.e., molecular chemisorption of hydrogen and subsequent molecular surface reaction.

C.2.1 Molecular Hydrogen Chemisorption and Surface Reaction

Whereas in Chapter 3 an Eley-Rideal mechanism was assumed for (de)-hydrogenation, in this Section rate equations are developed for the case where hydrogen chemisorbs molecularly on

the metal surface prior to hydrogenation. This leads to the replacement in Eq. (3.3) of the hydrogen partial pressure by the hydrogen surface concentration:

$$R_{f-P} = -k_{deh,f}\left(C^M_{f-P}C^M_{*} - \frac{C^M_{f-O}C^M_{H_2}}{K^M_{deh,f}}\right) \tag{C.12}$$

Accounting for the chemisorption on the metal surface, this equation can be rewritten using the concentrations of physisorbed pseudo-components in the pores and the hydrogen partial pressure:

$$R_{f-P} = \frac{-k_{deh,f}K^M_{f-P}\left(C^M_t\right)^2\left(C_{f-P} - \frac{C_{f-O}p_{H_2}}{K_{deh,f}}\right)}{\left(1+K^M_{H_2}p_{H_2}+\sum_g K^M_{g-P}C_{g-P}\right)^2} \tag{C.13}$$

with:

$$K_{deh,f} = K^M_{deh,f}\frac{K^M_{f-P}}{K^M_{f-O}K^M_{H_2}} \tag{C.14}$$

The composite dehydrogenation rate coefficient is defined in this case as follows:

$$k^*_{deh,f} = \frac{k_{deh,f}\left(C^M_t\right)^2}{\left(1+K^M_{H_2}p_{H_2}+\sum_g K^M_{g-P}C_{g-P}\right)^2} \tag{C.15}$$

Compared to the equations derived in Chapter 3 an extra term appears in the denominator accounting for the hydrogen chemisorption and the denominator is squared because two active sites are involved in the rate-determining step.

If the hydrogen surface concentration is low, leading to a negligible chemisorption term for hydrogen, the same chemisorption term remains in the denominator as in the original expression, Eq. (3.6), however, because of the squared denominator the effects discussed in Section 3.4.2e will already occur at lower total pressures.

For higher hydrogen surface concentrations, the composite dehydrogenation rate coefficient, $k^*_{deh,f}$, exhibits an inverse squared dependence on the total pressure and, hence, the linear dependence on the total pressure of the term which dominates the value of the numerator of Eq. (3.18) in the case of *ideal* hydrocracking, $\gamma p_t\, k^*_{deh,iso}/K_{deh,iso}$, changes to an inverse dependence. Because this is in contradiction with the experimental observations, the assumption of high hydrogen surface coverage can be rejected.

C.2.2 Dissociative Hydrogen Chemisorption – First H-Addition as RDS

Assuming dissociative hydrogen chemisorption and the first hydrogen addition as the rate-determining step leads to the replacement of the hydrogen partial pressure in Eq. (3.3) by the atomic hydrogen surface concentration and the replacement of the alkane surface concentration by the surface concentration of the species from which one hydrogen atom has been abstracted:

$$R_{f-P} = -k_{deh,f}\left(C^M_{f-P_{-H}}C^M_* - \frac{C^M_{f-O}C^M_H}{K^M_{deh,f}\left(f-P_{-H};f-O\right)}\right) \tag{C.16}$$

Via the equilibrium between the alkane and the species with one hydrogen atom abstracted, the alkane surface concentration can be introduced:

$$R_{f-P} = -k_{deh,f}\left(\frac{K^M_{deh}\left(f-P;f-P_{-H}\right)C^M_{f-P}\left(C^M_*\right)^2}{C^M_H} - \frac{C^M_{f-O}C^M_H}{K^M_{deh}\left(f-P_{-H};f-O\right)}\right) \tag{C.17}$$

Accounting for the chemisorption on the metal sites, the hydrocarbon concentrations physisorbed in the pores and the hydrogen partial pressure can be introduced:

$$R_{f-P} = \frac{-k_{deh,f}K_{deh}\left(f-P;f-P_{-H}\right)K^M_{f-P}\left(C^M_t\right)^2\left(C_{f-P} - \dfrac{C_{f-O}p_{H_2}}{K_{deh,f}}\right)}{\sqrt{K^M_{H_2}p_{H_2}}\left(1+\sqrt{K^M_{H_2}p_{H_2}}+\sum_g K^M_{g-P}C_{g-P}\right)^2} \tag{C.18}$$

with:

$$K_{deh,f} = K^M_{deh}\left(f-P;f-P_{-H}\right)K^M_{deh}\left(f-P_{-H};f-O\right)\frac{K^M_{f-P}}{K^M_{f-O}K^M_{H_2}} \tag{C.19}$$

and the expression for the composite dehydrogenation rate coefficient becomes:

$$k^*_{deh,f} = \frac{k_{deh,f}\left(C^M_t\right)^2}{\sqrt{K^M_{H_2}p_{H_2}}\left(1+\sqrt{K^M_{H_2}p_{H_2}}+\sum_g K^M_{g-P}C_{g-P}\right)^2} \tag{C.20}$$

As evident from the square root of the hydrogen partial pressure in the denominator of the expression for the composite dehydrogenation rate coefficient, the rate of (de)-hydrogenation reactions will be less dependent on the total pressure than in the original development in Chapter 3.

For low hydrogen concentrations on the metal surface the linear total pressure dependence of the term dominating the value of the numerator of Eq. (3.18) under *ideal* hydrocracking conditions is replaced by a square root dependence of the total pressure. Hence, compared to

the rate equations developed under the simplifying assumptions, higher total pressures are expected to be required for *ideal* hydrocracking to be established under the assumptions discussed in this paragraph.

For higher hydrogen surface concentrations, the linear dependence on the total pressure of the term which dominates the numerator of Eq. (3.18) in the case of *ideal* hydrocracking changes to an inverse square root pressure dependence. Because this is in contradiction with the experimental observation that higher total pressures favor *ideal* hydrocracking, the assumption of high hydrogen surface coverage can be rejected in this case.

C.2.3 Dissociative Hydrogen Chemisorption – Second H-Addition as RDS

Assuming dissociative hydrogen chemisorption and the second hydrogen addition as the rate-determining step leads to the replacement of the hydrogen partial pressure in Eq. (3.3) by the atomic hydrogen surface concentration and the replacement of the alkene surface concentration by the surface concentration of the species to which one hydrogen atom has been added:

$$R_{f-P} = -k_{deh,f}\left(C^M_{f-P}C^M_* - \frac{C^M_{f-P_{-H}}C^M_H}{K^M_{deh}\left(f-P;f-P_{-H}\right)}\right) \tag{C.21}$$

Via the equilibrium between the alkene and the species with one hydrogen atom added, the alkene surface concentration can be introduced:

$$R_{f-P} = -k_{deh,f}\left(C^M_{f-P}C^M_* - \frac{C^M_{f-O}\left(C^M_H\right)^2}{C^M_* K_{deh}\left(f-P_{-H},f-O\right)K^M_{deh}\left(f-P,f-P_{-H}\right)}\right) \tag{C.22}$$

Accounting for the chemisorption on the metal sites, the hydrocarbon concentrations physisorbed in the pores and the hydrogen partial pressure can be introduced:

$$R_{f-P} = \frac{-k_{deh,f}K^M_{f-P}\left(C^M_t\right)^2\left(C_{f-P} - \dfrac{C_{f-O}p_{H_2}}{K_{deh,f}}\right)}{\left(1+\sqrt{K^M_{H_2}p_{H_2}} + \sum_g K^M_{g-P}C_{g-P}\right)^2} \tag{C.23}$$

with

$$K_{deh,f} = K^M_{deh}\left(f-P;f-P_{-H}\right)K^M_{deh}\left(f-P_{-H};f-O\right)\frac{K^M_{f-P}}{K^M_{f-O}K^M_{H_2}} \tag{C.24}$$

In this case the expression for the composite dehydrogenation rate coefficient becomes:

$$k^{*}_{deh,f} = \frac{k_{deh,f}\left(C_t^M\right)^2}{\left(1+\sqrt{K^M_{H_2}p_{H_2}}+\sum_g K^M_{g-P}C_{g-P}\right)^2} \tag{C.25}$$

For low hydrogen surface concentrations this equation is reduced to the same equation as derived in Paragraph C.2.1. For higher hydrogen surface concentrations, an inverse dependence of the composite dehydrogenation rate coefficient on the total pressure is obtained and, hence, the pressure dependence of term dominating the value of the numerator of Eq. (3.18) in *ideal* hydrocracking is cancelled. In this situation the total pressure has no effect on the terms which dominate the value of the numerator of Eq. (3.18) in *(non) ideal* hydrocracking. In such a case, an eventual shift from *ideal* to *non ideal* hydrocracking might be explained similarly to the explanation for the effect of the molar hydrogen to hydrocarbon ratio, vide Section 3.4.2c. However, because the effect of the total pressure on the ideality of the hydrocracking behaviour is rather strong, the situation sketched above seems unlikely.

C.2.4 Dissociative Hydrogen Chemisorption – No RDS

Considering the assumptions discussed in Paragraphs C.2.2 and C.2.3, i.e., the first respectively the second hydrogen atom addition as the rate-determining step in the (de)-hydrogenation reaction mechanism, the assumption that no rate-determining step exists can be considered to be intermediate to these two extremes. If this assumption can be extended to the expression for the rate equation, the following expression for the rate of formation when no rate-determining step exists can be constructed based on the expressions derived for the net rate of formation of the alkane pseudo-components in Paragraphs C.2.2 and C.2.3:

$$R_{f-P} = \frac{-k_{deh,f}K^M_{f-P}\left(C_t^M\right)^2\left(C_{f-P}-\dfrac{C_{f-O}p_{H_2}}{K_{deh,f}}\right)}{\left(K^M_{H_2}p_{H_2}\right)^n\left(1+\sqrt{K^M_{H_2}p_{H_2}}+\sum_g K^M_{g-P}C_{g-P}\right)^2} \tag{C.26}$$

In this equation, the factor $\left(K^M_{H_2}p_{H_2}\right)^n$ in the denominator preceding the squared adsorption term expresses the deviation from the two extreme situations, i.e., from the first or from the second hydrogen addition being the rate-determining step. A value between *0*, corresponding to the second hydrogen addition as the rate-determining step and *0.5*, corresponding to the first hydrogen addition as the rate-determining step is expected for the power *n* in this factor, expressing the intermediate character of the case where no rate-determining step exists between the two extreme situations in which the first or the second hydrogen addition is

assumed to be rate-determining. The effects will be intermediate to the effects discussed in the two preceding Paragraphs. For low hydrogen surface concentrations the linear total pressure dependence of the term dominating the value of the numerator of Eq. (3.18) is reduced to a total pressure dependence with a power *1-n*. Hence, somewhat higher total pressures are expected to be required to establish *ideal* hydrocracking in this case. For higher hydrogen surface concentrations an inverse total pressure dependence with a power *–n*. Because this inverse dependence is in disagreement with the experimental observations, the assumption of high hydrogen surface coverage can be rejected.

C.3 References

[1] Froment, G. F., *Kinetics of the hydroisomerization and hydrocracking of paraffins on a platinum containing bifunctional Y-zeolite* **Cat. Today** *1* 455-473 (1987).

[2] Denayer, J. F., Baron, G. V., Souverijns, W., Martens, J. A., and Jacobs, P. A., *Hydrocracking of n-alkane mixtures on Pt/H-Y zeolite: Chain length dependence of the adsorption and kinetic constants* **Ind. Eng. Chem. Res.** *36* 3242-3247 (1997).

[3] Dumez, F. J., and Froment, G. F., *Dehydrogenation of 1-butene into butadiene. Kinetics, catalyst coking and reactor design* **Ind. Eng. Chem. Proc. Des. Dev.** *15* 291-301 (1976).

Appendix D

Acid Site Coverage

Svoboda et al. [1] derived via parameter estimations that the coverage of the acid sites was low, i.e., the concentration of free acid sites approaches the total concentration of acid sites. This result was used in the derivation of the rate equations in this work after verification with a calculation of the acid site coverage based on known and estimated parameter values.

D.1 Calculation

The energy levels involved in this calculation are schematically shown in Figure D - 1. Under the typical reaction conditions mentioned in Table 5-1 the alkane and hydrogen partial pressure amount to *0.032 MPa* and *0.418 MPa*. From this alkane (Figure D - 1 level 1) partial pressure the corresponding physisorbed alkane (Figure D - 1 level 2) concentration can be calculated according to a Langmuir isotherm. Henry coefficients and saturation concentrations are available [2,3]. Hence, the Langmuir coefficient for a typical alkane such as octane, can

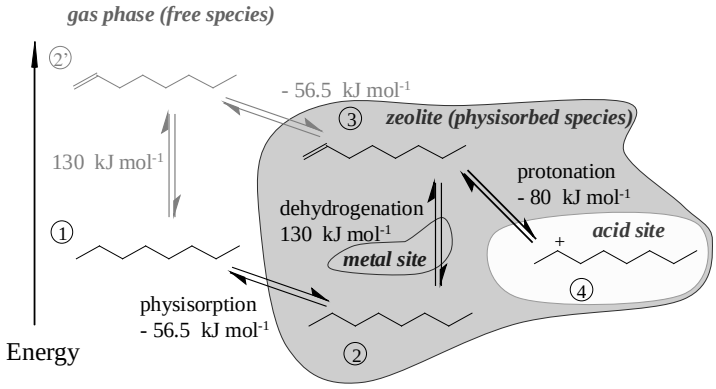

Figure D - 1 Schematic representation of the energy levels involved in carbenium ion formation

be calculated,

$$K_{L,C_8} = 103\ MPa^{-1} \tag{D.1}$$

with which the physisorbed alkane concentration becomes:

$$C_{C_8} = 0.476\ mol\ kg_{cat}^{-1} \tag{D.2}$$

Based on the enthalpies of formation and the absolute entropies of octane, 1-octene and hydrogen a value for the dehydrogenation equilibrium coefficient was calculated at 506 K:

$$K_{deh} = 0.5019\ 10^{-7}\ MPa \tag{D.3}$$

Based on these values the concentration of physisorbed alkenes (Figure D - 1 level 3) amounts to:

$$C_{C_8^=} = 5.72\ 10^{-8}\ mol\ kg_{cat}^{-1} \tag{D.4}$$

A value for the (de)-protonation equilibrium coefficient is not directly available, but a reasonable estimate can be made. The protonation entropy is calculated according to Martens et al. [4] and amounts to *-67 J mol^{-1} K^{-1}*. For the standard protonation enthalpy, values are at hand from quantumchemical calculations [5]. These involve the formation of a σ-bond between the alkene and the active site and, hence, will result in a more negative value for the protonation enthalpy than when an ionic bond is considered. However, in an attempt to calculate the standard protonation enthalpy corresponding with the formation of carbenium ions, Martens et al. [4] arrived at values of *-120 kJ mol^{-1}* and *-150 kJ mol^{-1}* for secondary and tertiary carbenium ions respectively. These values are lower then that obtained via direct quantumchemical calculations, i.e., *-80 kJ mol^{-1}*. They were based on an indirect method, incorporating estimated, tabulated and quantumchemically calculated values and are therefore thought to be less reliable. Hence, the surface concentration of carbenium ions calculated based on the directly quantumchemically obtained value, is considered as an upper limit. The equilibrium coefficient becomes

$$K_{prot} = 57400\ kg_{cat}\ mol^{-1} \tag{D.5}$$

This protonation coefficient provides the link between the concentration of the physisorbed alkenes and the (physisorbed) carbenium ions. It only comprises the formation of an ionic center from a double bond. The van der Waals interactions of the other carbon atoms with the zeolite wall are taken into account via the physisorption coefficient.

The upper limit for the carbenium ion (Figure D - 1 level 4) concentration amounts to

$$C_{R_{tot}^+} = 7.10\ 10^{-4}\ mol\ kg_{cat}^{-1}\ .$$

Compared with the minimum total concentration of acid sites of *0.217 mol* kg_{cat}^{-1}, vide Table 2-1, this maximum concentration of carbenium ions is negligible, justifying the assumption of low acid site coverage.

D.2 References

[1] Svoboda, G. D., Vynckier, E., Debrabandere, B., and Froment, G. F., *Single-event rate parameters for paraffin hydrocracking on a Pt/US-Y Zeolite* **Ind. Eng. Chem. Res.** *34* 3793-3800 (1995).

[2] Denayer, J. F., Baron, G. V., Jacobs, P. A., and Martens, J. A., *Competitive Physisorption Effects in Hydroisomerization of n-Alkane Mixtures on Pt/Y and Pt/USY Zeolite Catalysts* **Phys. Chem. Chem. Phys.** *2* 1007-1014 (2000).

[3] Denayer, J. F. M., and Baron, G. V., *Adsorption of normal and branched paraffins in faujasite zeolites NaY, HY, Pt/NaY and USY* **Adsorption** *3* 1-15 (1997).

[4] Martens, G. G., Marin, G. B., Jacobs, P. A., Martens, J. A., and Baron, G. V., *A Fundamental Model for Hydrocracking of* C_8 *to* C_{12} *Alkanes on Pt/US-Y Zeolites* **J. Catal.** *195* 253-267 (2000).

[5] Kazansky, V. B., Frash, M. V., and van Santen, R. A., *Quantumchemical Study of the Isobutane Cracking on Zeolites* **Appl. Catal. A Gen.** *146* 225-247 (1996).